Florian Lackner

Rydberg States of Alkali-Metal Atoms on Superfluid Helium Nanodroplets

DOCTORAL THESIS

For obtaining the academic degree of
Doktor der technischen Wissenschaften

Doctoral Programme of Technical Sciences
Technical Physics

Graz University of Technology

Supervisor:

Univ.-Prof. Dipl.-Phys. Dr.rer.nat. Wolfgang E. Ernst
Institute of Experimental Physics

Graz, December 2012

Abstract

Rydberg States of Alkali-Metal Atoms on Superfluid Helium Nanodroplets

Since the beginning of atomic physics and quantum mechanics the spectroscopy of Rydberg states played an important role for gaining a deeper understanding of the physics of atoms and molecules as well as the physical properties of matter. The modern technique of helium nanodroplet isolation spectroscopy is a well established method for the investigation of single atoms, molecules, or clusters at a very low temperature of 0.38 K. A combination of these fields of physics, Rydberg state spectroscopy of atoms and molecules on the surface or inside helium nanodroplets, can serve as a tool to explore the physical properties of a special kind of matter: those of a nanosized superfluid.

Rydberg state spectroscopy is used in this thesis to investigate the influence of helium nanodroplets on the Rydberg states and Rydberg series of rubidium (Rb) and cesium (Cs) atoms. For the first time, complete excitation spectra, from the lowest states up to Rydberg states and the ionization threshold, of these two atomic species located on the surface of helium droplets have been recorded.

In this thesis resonance-enhanced multi-photon-ionization time-of-flight (REMPI-TOF) mass spectroscopy and multi-photon laser induced fluorescence (LIF) spectroscopy were used as spectroscopic tools to investigate these Rydberg systems. A special two-step excitation technique was developed, which exploits the fact that Rb and Cs atoms stay bound to the droplet surface upon excitation into their lowest $n^2\mathrm{P}_{1/2}(^2\Pi_{1/2})$ state.

The recorded spectra could be explained within a Rydberg model by using the pseudo-diatomic model for the explanation of the observed transitions. It was found that the ionization threshold is red-shifted due to the influence of the helium droplet, which is caused by polarization effects. The quantum defects obtained for each Rydberg series were found to be lowered by the helium droplet, indicating the screening of the Rydberg electron from the ionic core by the droplet, which acts as a nanosized dielectric.

Rydberg states with electron orbitals much larger than the helium droplet were observed. States with effective principal quantum numbers $n^* < 20$ could be resolved, beyond this region the states form a continuum. Such highly excited Rydberg atoms can accommodate the helium droplet within the orbital of the electron. This finding suggests the formation of a Rydberg system, which is known as Sekatskii-atom: a positive ion solvated in a helium droplet with an orbiting electron.

Kurzfassung

Rydberg-Zustände von Alkaliatomen auf supraflüssigen Helium-Nanotröpfchen

Seit den Anfängen der Atomphysik und der Quantenmechanik kam der Spektroskopie von Rydberg-Zuständen eine wichtige Rolle darin zu das Verständnis der Physik von Atomen und Molekülen sowie den physikalischen Eigenschaften der Materie zu vertiefen. Die moderne Technik der Helium-Nanotröpfchen Matrix-Isolations-Spektroskopie hat sich als gängige Methode zur Spektroskopie kalter (0.38 K) Atome, Moleküle und Cluster etabliert. Eine Kombination dieser beiden Gebiete der Physik, der Spektroskopie von Rydberg Atomen und Molekülen auf Helium-Tröpfchen, kann als Methode zur Erforschung eines speziellen Zustands der Materie dienen, nämlich der einer Supraflüssigkeit im Nanometer-Größenbereich.

In dieser Arbeit wurde die Rydberg-Zustands-Spektroskopie verwendet um den Einfluss eines Helium-Nanotröpfchens auf die Rydberg-Zustände von Rubidium (Rb) und Cäsium (Cs) Atomen zu untersuchen. Zum ersten Mal ist es dabei gelungen ein vollständiges Spektrum, von den niedrigsten Zuständen über Rydberg-Zustände bis zur Ionisationsschwelle, dieser beiden Atome auf Helium-Tröpfchen aufzunehmen.

In dieser Arbeit wurde die Methode der resonanten Multi-Photonen-Ionisations Flugzeitmassenspektroskopie (REMPI-TOF) sowie der Multi-Photonen Laser-Induzierte-Fluoreszenz (LIF) Spektroskopie verwendet um diese Rydberg-Systeme zu untersuchen. Ein spezielles Zwei-Stufen-Anregungsschema wurde entwickelt, welches auf der Tatsache beruht, dass der niedrigste $n^2\mathrm{P}_{1/2}(^2\Pi_{1/2})$ Zustand der beiden Atome bindend ist.

Die aufgenommenen Spektren konnten mit einem Rydberg-Modell erklärt werden, unter Zuhilfenahme des Pseudo-Zweiatomigen Modells zur Erklärung der beobachteten Übergänge. Es wurde herausgefunden, dass die Ionisationsschwelle durch den Einfluß des Tröpfchens rotverschoben ist, was durch Polarisations-Effekte erklärt werden kann. Die Quantendefekte der jeweiligen Rydberg-Serien sind niedriger als im Vergleich zu freien Atomen, was auf eine Abschirmung des Ionenrumpfes vom Rydberg-Elektron durch den Helium-Tropfen zurückzuführen ist, welcher hier die Rolle eines Dielektrikums im Nanometer-Größenbereich spielt.

Rydberg-Zustände mit Elektronen-Orbitalen welche viel größer sind als das Helium-Tröpfchen konnten beobachtet werden. Zustände mit effektiven Hauptquantenzahlen $n^* < 20$ konnten aufgelöst werden, Zustände oberhalb dieses Bereiches bilden ein Kontinuum. Solche hochangeregten Rydberg-Zustände sind groß genug um den Helium-Tropfen innerhalb des Elektronen-Orbitals einzuschließen. Dies stützt die Vermutung, dass sich aus diesen Rydberg-Systemen ein sogenanntes Sekatskii-Atom bildet: Ein positiv geladenes Ion in einem Helium-Tröpfchen umgeben von einem Elektron.

Deutsche Fassung:
Beschluss der Curricula-Kommission für Bachelor-, Master- und Diplomstudien vom 10.11.2008
Genehmigung des Senates am 1.12.2008

EIDESSTATTLICHE ERKLÄRUNG

Ich erkläre an Eides statt, dass ich die vorliegende Arbeit selbstständig verfasst, andere als die angegebenen Quellen/Hilfsmittel nicht benutzt, und die den benutzten Quellen wörtlich und inhaltlich entnommene Stellen als solche kenntlich gemacht habe.

Graz, am …… ……..
(Unterschrift)

Englische Fassung:

STATUTORY DECLARATION

I declare that I have authored this thesis independently, that I have not used other than the declared sources / resources, and that I have explicitly marked all material which has been quoted either literally or by content from the used sources.

…… ……..
date (signature)

Articles related to this work

1. Forming Rb^+ snowballs in the center of He nanodroplets
   M. Theisen, F. Lackner, and W. E. Ernst
   Phys. Chem. Chem. Phys., **12**, 14861-14863, (2010). [1]

2. Two-step excitation of Rb atoms on He nanodroplets
   M. Theisen, F. Lackner, F. Ancilotto, C. Callegari, and W. E. Ernst
   Eur. Phys. J. D, **61**, 403-408, (2011). [2]

3. Rb and Cs Oligomers in Different Spin Configurations on Helium Nanodroplets
   M. Theisen, F. Lackner, and W. E. Ernst
   J. Phys. Chem. A, **115**, 7005-7009, (2011). [3]

4. Cs atoms on helium nanodroplets and the immersion of Cs^+ into the nanodroplet
   M. Theisen, F. Lackner, and W. E. Ernst
   J. Chem. Phys. , **135**, 074306, (2011). [4]

5. Ionization Thresholds of Alkali Metal Atoms on Helium Droplets
   M. Theisen, F. Lackner, G. Krois, and W. E. Ernst
   J. Phys. Chem. Lett., **2**, 2778-2782, (2011). [5]

6. Spectroscopy of nS, nP, and nD Rydberg series of Cs atoms on helium nanodroplets
   F. Lackner, G. Krois, M. Theisen, M. Koch, and W. E. Ernst
   Phys. Chem. Chem. Phys., **13**, 18781-18788, (2011). [6]

7. Rubidium on Helium Droplets: Analysis of an Exotic
   Rydberg Complex for $n^* < 20$ and $0 \leq l \leq 3$
   F. Lackner, G. Krois, M. Koch, and W. E. Ernst
   J. Phys. Chem. Lett., **2**, 2778-2782, (2011). [7]

8. Excited States and Rydberg Series of Alkali Atoms on Helium Nanodroplets
   F. Lackner, G. Krois, and W. E. Ernst
   in preparation, (2012). [8]

Articles [6]-[8] are contained within this work. Articles [1]-[5] are partially contained in this work. Their full content is covered in the PhD thesis of Moritz Theisen.

Contents

List of Tables

List of Figures

Chapter 1

Introduction

1.1 Motivation - Rydberg atoms and helium nanodroplets

The Rydberg states of the hydrogen atom played a crucial role in the birth of quantum mechanics. Today, Rydberg state spectroscopy of atoms, molecules and small clusters continues to be an important tool for gaining a deeper insight into fundamental physical properties of matter [9]. One advantage of Rydberg state spectroscopy is that complicated spectra can be described by one simple formula, the famous Rydberg formula. This allows to order series of electronic transitions in atoms or molecules into so called "Rydberg series". For the description of a Rydberg series one parameter is essential, which is the quantum defect. Furthermore, Rydberg states are stepping stones towards ionization. The ionization threshold and the quantum defects include all information on the electronic structure of an atom or molecule.

Helium nanodroplets are a unique matrix for isolation spectroscopy. They provide an ultra cold (0.38 K) and superfluid environment for foreign atoms and molecules. Helium droplets are transparent from the UV to the IR spectral range and they can be doped with virtually any atom or molecule. Even large and tailored clusters can be formed inside helium nanodroplets. To investigate basic properties of helium nanodroplets and their interaction with foreign atoms and molecules it is advantageous to study atoms or molecules with a simple and well known electronic structure such as alkali atoms.

In this work, the advantages of Rydberg state spectroscopy are used for the investigation of interactions between a nanosized superfluid and alkali atoms. At the beginning of this work, only the lowest two or three excited states of alkali atoms on helium droplets, from Li to Cs, were known. The spectroscopic discovery of more than 40 new energy levels for Rb as well as for Cs on the droplet, from the lowest states up to their ionization thresholds, gives new insights into the interaction between superfluid helium droplets and alkali atoms. The recording of the complete spectra of Rb and Cs on the surface of helium droplets allows a systematic investigation of their Rydberg states. Organizing excited states into Rydberg series allows to draw conclusions far beyond the information which can be drawn from the investigation of isolated transitions. With a Rydberg and Rydberg-Ritz approach the energy levels can be described and calculated and their spectral position is described by the interplay of quantum defect and ionization threshold. The influence of the helium droplet on the quantum defect and the ionization threshold gives additional information on the perturbation of foreign atoms by a nanosized superfluid.

Atoms excited into high Rydberg states have extraordinary properties, for example, a lifetime in the order of μs to ms and orbital radii of several 100 nm to μm. These sizes clearly exceed the size of a helium droplet and suggest the formation of a system where the Rydberg electron surrounds the helium droplet. A system, where the alkali ion core is solvated inside the droplet and the electron is orbiting outside, is often referred to as Sekatskii-atom and is of great interest because it can reveal fundamental information on a nanosized dielectric.

This work extends the understanding of the alkali-helium droplet system to a new level. It illuminates those systems from a new viewpoint with the help of Rydberg state spectroscopy.

1.2 Helium nanodroplet isolation spectroscopy

Helium nanodroplets are superfluid, ultra-cold and transparent from the infrared to the ultraviolet range of the electromagnetic spectrum. These and many other extraordinary properties make them a superior matrix for spectroscopy. In the first part of this short introduction, general properties of helium nanodroplets and basic principles of helium nanodroplet isolation spectroscopy (HENDI) are discussed. Many colleagues from the institute of experimental physics at the TU Graz have presented detailed works on the theoretical concepts behind the production, as well as the history and properties of helium nanodroplets [10–13]. An important emphasis in this thesis lies in the description of the droplet size distribution, since it is a very important ingredient in the study of droplet size dependent effects. This includes the presentation of a more refined model for the calculation of the log-normal droplet distribution and associated parameters.

A complete composition of theoretical and experimental achievements in the field of helium droplets isolation spectroscopy can be found in recent general review articles [14–16] and the special issue of the Journal of Chemical Physics [17]. The state of the art of helium nanodroplet isolation spectroscopy can be found in the book article of C. Callegari and W.E. Ernst in the Handbook of High-resolution Spectroscopy [18].

1.3 Helium

Helium, the second most abundant element in the universe, has extraordinary properties because it shows macroscopic manifestations of quantum mechanical effects. Hence helium is often referred to as "quantum-fluid". It was discovered in 1868 by Jules Jansen [19] in the chromosphere of the sun, which is where the name *helium* comes from ("Helios", the Greek god of the sun). Helium occurs in two stable isotopes, ^{3}He and ^{4}He, where 99.9999% [20] of the helium on earth is ^{4}He. ^{3}He is very rare and expensive and although the physics of ^{3}He is also very extraordinary and interesting, it is not discussed here since only ^{4}He is used in the course of this work. The differences between the two isotopes are caused mainly by the different spin statistics: ^{4}He is a composite boson and ^{3}He is fermionic. The zero point energy of liquid ^{4}He, the energy of a quantum mechanical system in its ground state, is lower than the zero point energy of solid ^{4}He [21]. The consequences of this fact can bee seen in Figure 1.1 where the phase diagram of ^{4}He is shown. Helium is the only element that can not be solidified under normal atmospheric pressure ($p = 1\,\mathrm{atm}$). The pressure has to rise above 25 bar to force ^{4}He into the solid phase. The phase transition from gaseous to liquid of ^{4}He occurs at 4.2 K at ambient atmosopheric pressure.

The first liquefaction of helium was achieved by H. Kammerling Onnes in 1908 [22]. A special feature of helium is that it has two liquid phases, the normal fluid He I and the superfluid He II phase. They are separated by the λ-transition, which is at 2.17 K at ambient atmospheric pressure. The superfluid phase of ^{4}He was discovered in 1938 by P. Kapitsa [23] as well as by J.F. Allan and A. D. Misener [24]. The consequences of the superfluidity of bulk liquid ^{4}He manifests for example in the frictionless flow of the liquid, zero viscosity and entropy, and a non-classical moment of inertia.

Superfluidity is closely related to Bose-Einstein condensation, which was first realized inde-

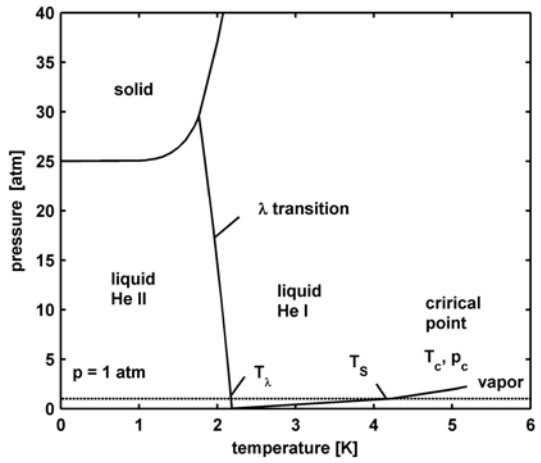

Figure 1.1: Phase diagram of ^{4}He. The data for the preparation of the diagram are taken from references [28–32] The two liquid phases, He I and He II, are separated by the λ-line. Helium has no phase transition from liquid to solid under atmospheric pressure.

pendently by E.A. Cornell and C.E. Wiemann [25] as well as W. Ketterle [26]. Bose-Einstein condensation is a state of matter where a large fraction of bosons occupy the lowest quantum state of the system. In the following the relation between liquid helium droplets and Bose-Einstein condensation is discussed. Comparing the large thermal de Broglie wavelength of liquid helium ($\lambda_{dB} = 0.43\,\mathrm{nm}$ at the boiling point and $p = 1\,\mathrm{atm}$, see Table 2.1 in ref. [13]) with the average interatomic distance ($\mathrm{r}_m = 0.3\,\mathrm{nm}$), it is evident that in the case of liquid He the de Broglie wavelength is the larger quantity. Consequently the helium atoms loose their identity and the bosonic ^{4}He can be described by a common macroscopic wavefunction. The difference between Bose-Einstein condensation and superfluidity is the stronger particle-particle interaction in the superfluid liquid, because of the higher particle density. The relation between the phenomena of superfluidity in helium nanodroplets and Bose-Einstein condensates is discussed by Dalfovo in ref. [27].

1.4 Helium nanodroplets

Clusters are a state of matter which bridge the gap between bulk matter and atoms and molecules. Helium clusters, also referred to as helium nanodroplets because of their liquid state, are an outstanding type of clusters. They have many extraordinary properties, which makes them the ideal host for matrix isolation spectroscopy.

The most common way to produce a continuous helium droplet beam is a free jet expansion [33]. Gaseous helium under high pressure ($20 - 100\,\mathrm{bar}$) and at low temperatures ($2 - 25$) K is expanded through a small nozzle with a typical diameter of 5 μm into vacuum. The first experimental realization of a helium droplet beam produced in a free jet expansion was demonstrated in 1961 by Becker et al. [34]. Depending on the source conditions, different regimes of expansion can be distinguished [35, 36] (see Figure 1.2), where the source temperature is the most important parameter. For example, for a source pressure of p_0 =20 bar and a 5 μm orifice, three qualitatively different regimes are found for (i) $T_0 < 8\,\mathrm{K}$, (ii) $T_0 = 8 - 12\,\mathrm{K}$, and

(iii) $T_0 > 12\,\mathrm{K}$ [35]. These regimes are shown in Figure 1.2. In this Figure the lower section shows the "subcritical" expansion (iii), the middle section corresponds to the "supercritical" expansion regime (ii) and the top section shows the Rayleigh break-up regime (i). The usual mode of operation for obtaining spectra of atoms and molecules is the continuous subcritical expansion. In this regime the mean droplet size is $\bar{N} < 2$ x 10^4 [18]. Larger droplets $\bar{N} > 10^5$ are produced in the "supercritical" expansion regime. Large droplets can be used, for example, for the production of large clusters inside helium droplets [3, 37]. The intensity of a continuous droplet beam is in the order of 2 x 10^{14} droplets $\mathrm{sr}^{-1}\mathrm{s}^{-1}$ (for 20 bar, 10 K and 5 μm, [14]).

The starting point for a subcritical expansion in the helium phase diagram is in the gaseous region. The isentropic expansion cools the helium gas by adiabatic cooling. The finite state lies at temperatures and pressures in the phase diagram where the helium is liquid. Due to this cooling mechanism the helium starts to condensate during the expansion. The atoms start to coagulate and the formation of droplets begins. These initial droplets are rotationally hot, but in the vacuum an evaporative cooling mechanism cools the droplets further down. Hot helium atoms leave the droplet, carrying away an energy of about $5\,\mathrm{cm}^{-1}$ per atom. This cooling process is very fast ($\approx 10^{10}\,\mathrm{Ks}^{-1}$ [38]). A crucial point for the beam production is that the mean free path between the particles must be small compared to the orifice diameter, which can be achieved by high source pressures. In an expansion at these conditions, many collisions between helium atoms lead to a kinetic energy transfer between them, which results in a very narrow velocity distribution ($\Delta v/v = 0.01 - 0.03$ [35]). The helium droplet beam has a velocity in the order of 400 m/s (for $T_0 = 15\,\mathrm{K}$). At distances of about 1000 nozzle diameters from the orifice, hardly any collisions between the atoms occur. The final droplet temperature was experimentally found to be at 0.38 K (for $\bar{N} > 1000$) [39–41]. This temperature was derived from the rotationally resolved infra-red spectrum of the SF_6 molecule inside the helium droplet. By investigations of alkali molecule triplet states it was shown by our group that the temperature on the surface of helium droplets is the same as inside [42]. As can be seen in the helium phase diagram (Figure 1.1) this temperature lies in the superfluid He II phase.

The superfluidity of helium droplets was demonstrated in the so-called "microscopic Andronikashvili experiment" [43]. Sharp rotational lines in the infra-red spectrum, which imply free rotation, of the OCS molecule could be recorded. In recent experiments, small helium droplets ($N < 72$) serve as a tool for the investigation of origin of superfluidity [44, 45].

Pulsed beams of helium droplets have also been developed. They can reach a 100 times higher flux than conventional sources [46].

1.4.1 Helium droplet sizes

The sizes of the helium nanodroplets generated in a jet expansion are determined by three parameters: the stagnation pressure (p_0), the nozzle temperature (T_0) and the nozzle diameter (d_0). The nozzle diameter d_0 in all experiments presented in this thesis is $d_0 = 5\,\mu$m. Thus it is sufficient to describe the droplet size distribution as a function of p_0 and T_0. The size distribution for droplets produced in the subcritical and the supercritical expansion are different. A subcritical expansion results in a logarithmic normal distribution [47] (which can be related to microscopic conditions by a kinetic nucleation theory [48]). In contrast, a supercritical expansion can lead to a linear-exponential [49] or bimodal droplet size distribution [50, 51]. The following discussion deals with droplets which are produced in the subcritical expansion

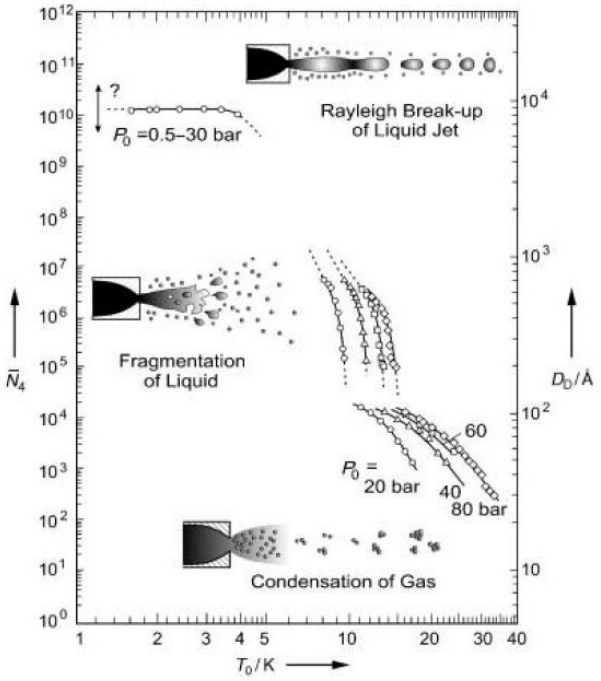

Figure 1.2: Overview of the mean number droplet sizes $\bar{N}$ and liquid-droplet diameters D for ^{4}He droplets formed in different types of continuous modes of jet operation (from: [14]). The lower section ($\bar{N} < 20$ x 10^4) shows the subcritical expansion, the middle section corresponds to the supercritical expansion regime and the top section shows the Rayleigh break-up regime.)

regime.

The mean number $\bar{N}$ of helium atoms per helium droplets which are produced in a subcritical expansion is $\bar{N} = 1000 - 20000$. This is the range of droplet sizes, which was used in the experiments. The mean number $\bar{N}$ of helium atoms is important for experiments where the geometric cross section of the droplets is essential, e.g. electron impact ionization or stray and deflection experiments. In experiments where the droplet itself is only used as a cryo-container without taking part actively in the experiment, e.g. a charge transfer mechanism or similar, the maximum of the distribution is important. These are typically experiments, where the impurity is excited with lasers from the IR to the vacuum UV spectral range, for example laser induced fluorescence or resonance-enhanced multi-photon-ionization experiments, like in the course of this thesis. The droplet size at the maximum of the log-normal distribution is the size where most of the signal originates from. This is, because statistically the most droplets in the beam with atoms or molecules on/in them have this size. Unfortunately the majority of available data in literature are mean number droplet sizes $\bar{N}$. Most probably because the majority of methods for measuring the droplet size are scattering and deflection methods, where the geometric cross section and mean number $\bar{N}$ are important. The most common experimental method for the determination of the droplet size distribution is the deflection of droplets out of the initial beam direction with a secondary atomic beam [47, 52, 53]. Another more recent method is the attenuation of the droplet beam by electron impact ionization [54]. For large droplets, the size distribution was determined by electron attachment [49, 55] and the attenuation of the droplet beam through collisions with noble gas atoms [56]. Information

Table 1.1: Quantities used for the calculation of the droplet size scaling parameter Γ. The following properties are given: the names of the quantity, a short description, the value (or in case of pressure or temperature dependent values, the typical range of the value), the unit and the reference.

quantity	quantity description	value	unit	reference
T_0	source temperature	10 - 25	K	-
p_0	source pressure	10 - 100	bar	-
d_0	source-orifice diameter	5	μm	-
ν	volume per atom in the cluster	27.37	cm^3mol^{-1}	[58]
$a_0(T_0, p_0)$	speed of sound	250 - 500	cm/s	[67]
$n_0(T_0, p_0)$	density	20 - 200	g/cm^3	[67]
s	surface tension	0.35	dyne/cm	[58]
γ	specific heat ratio	5/3	-	[68]
m	mass per He atom	4.0026 x 6.022 x 10^{23}	g/atom	[20]
T_{ref}	reference temperature	3.23	K	[58]
A	vapor-pressure constant	7.8	bar	[58]

about droplet size distributions for continuous sources operated in the super- or subcritical regime can be found in references [14, 41, 47, 49–52, 54–60]. A lot of works have also been published for the characterization of pulsed beam sources [46, 60–66], where a lot of information about size distributions can be found as well. In the following a model for the calculation of all relevant parameters of the log-normal droplet size distribution is presented, which is based on the Knuth model scaling law discussed in references [11, 18].

Droplet size scaling law: the Knuth model

Knuth proposes a scaling law for the mean size of clusters formed in jet-expansions from a nozzle for various gases, including ^{4}He [58]. With two dimensionless parameters, the kinetic parameter K_1

$$K_1(T_0) = n_0(T_0, p_0)\nu \frac{d_0}{a_0(T_0, p_0)} \left(\frac{2s}{\pi m}\right)^{1/2} \left(\frac{T_{ref}}{T_0}\right)^{\frac{1}{2(\gamma-1)}} \tag{1.1}$$

and the thermodynamic parameter K_2

$$K_2(T_0, p_0) = \frac{p_0}{A} \left(\frac{T_{ref}}{T_0}\right)^{\frac{\gamma}{\gamma-1}} \tag{1.2}$$

a simple expression for the scaling parameter Γ can be given:

$$\Gamma(T_0, p_0) = K_1^q(T_0, p_0) K_2^{1-q}(T_0, p_0). \tag{1.3}$$

K_1 and K_2 can be calculated with the quantities summarized in Table 1.1. The parameter q can be found in literature and was set to 0.621 (see reference [18]).

The mean droplet size $\bar{N}$ has roughly a quadratic dependence on the scaling parameter $\Gamma(T_0, p_0)$. The final scaling law is obtained by fitting the experimentally determined droplet

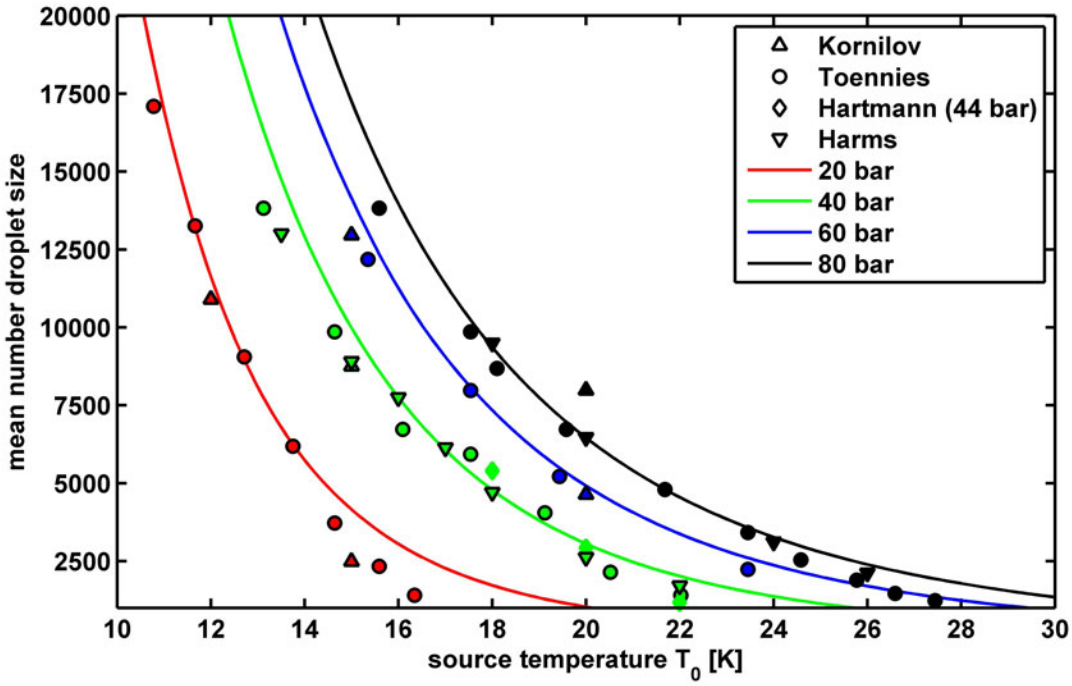

Figure 1.3: Compilation of experimentally determined mean droplet sizes[14, 41, 52, 54]. The solid lines are obtained with Equation 1.4.

sizes from Toennies et al. [14]:

$$\bar{N}(p_0, T_0) = 14.5\,\Gamma^{2.05}(p_0, T_0) \tag{1.4}$$

The two parameters $a = 14.5$ and $b = 2.05$ are the mean values of the obtained fit parameters from the fit of the $p_0 = 20$, 40, 60, and 80 bar data. In Figure 1.3 the fit results are compared to various experimentally determined mean droplet sizes [14, 41, 52, 54]. The scaling law is in good agreement with the data, except for small clusters generated with 20 bar source pressure. The fit procedure includes various source pressures and temperatures in order to give a general scaling law. However, the accuracy of the fit for a certain pressure can be increased by optimizing the fit parameters for a certain pressure. Since the scaling law is obtained by fitting the data from Toennies et al. [14], the result can be compared to other experimental data, e.g. from Harms et al.[52]. For example, the 40 bar mean droplet sizes in [52] are well reproduced by the model (±100 He atoms). When the droplets get smaller (increasing T_0), the accuracy of the model decreases and the uncertainty is about ±300 atoms for $T_0 > 20$ K.

Droplet size distribution

In the above section, a scaling law for the mean droplet size $\bar{N}$ was given (Equation 1.4), which allows the calculation of mean droplet sizes for various source conditions. In order to obtain the full log-normal droplet size distribution, additional information about the half width $\Delta N_{1/2}$ of the distribution is needed. In the following a model is presented, which allows to

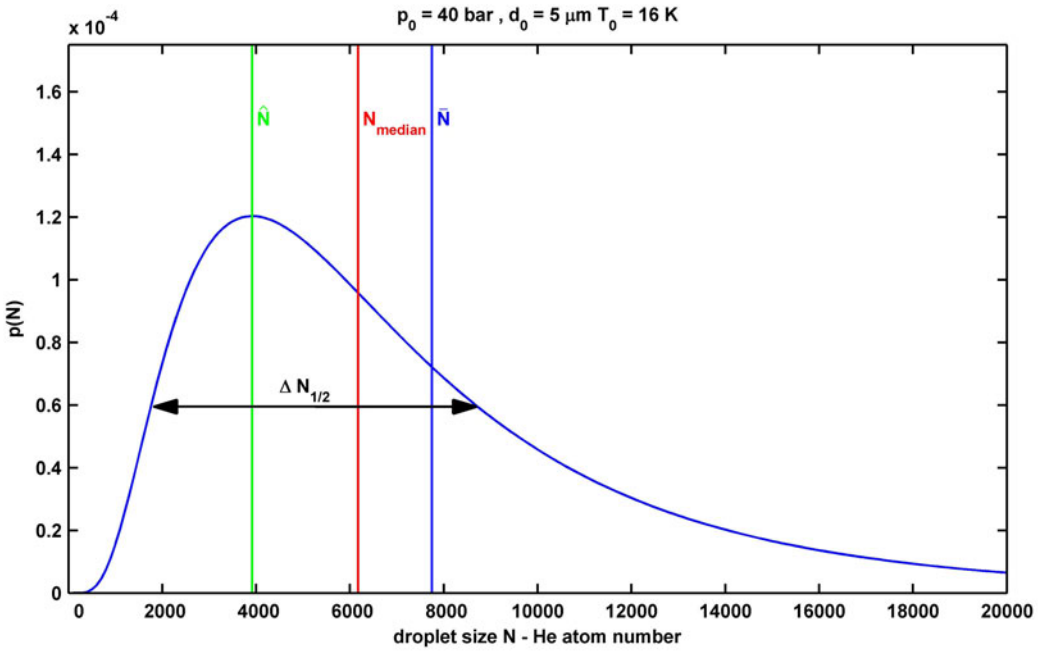

Figure 1.4: Log-normal distribution for source conditions of $p_0 = 40\,\text{bar}$ and $T_0 = 16\,\text{K}$. From this figure the differences between the mean droplet size $\bar{N} = 7749$, the median droplet size $N_{\text{Median}} = 6171$ and the maximum of the distribution $\hat{N} = 3914$ can be seen. The FWHM of the distribution is $\Delta N_{1/2} = 6895$. For comparison, the values given in ref. [52] are $\bar{N} = 7741$, $\Delta N_{1/2} = 6484$, $N_{\text{Median}} = 6248$ and $\hat{N} = 4031$.

calculate all necessary parameters of the log-normal size distribution. The probability $p(N)$ to produce a helium droplet consisting of a certain number N of helium atoms obeys a logarithmic normal distribution, which depends on the source pressure p_0 and source temperature T_0. The log-normal distribution has the following form:

$$p(N) = \frac{1}{N\delta\sqrt{2\pi}} \exp^{-\left[\frac{(\ln(N)-\mu)^2}{2\delta^2}\right]}. \tag{1.5}$$

The parameter μ is the natural logarithm of the median of the distribution (N_{Median}),

$$N_{\text{Median}} = e^{\mu} \tag{1.6}$$

and δ describes the width of the distribution. The mean value $\bar{N}$ is connected to both, μ and δ:

$$\bar{N} = e^{\left(\mu+(\delta^2/2)\right)}. \tag{1.7}$$

For the full width at half maximum (FWHM) $\Delta N_{1/2}$ of the log-normal distribution we can write

$$\Delta N_{1/2} = \exp\left(\mu - \delta^2 + \delta\sqrt{2\ln 2}\right) - \exp\left(\mu - \delta^2 - \delta\sqrt{2\ln 2}\right). \tag{1.8}$$

From this equations we see that, if μ and δ are known, we can calculate all parameters of the distribution. In Figure 1.4 an example of a log-normal droplet size distribution is shown. The mean value $\bar{N}$, the median N_{Median}, the maximum $\hat{N}$ and the FWHM $\Delta N_{1/2}$ are depicted for

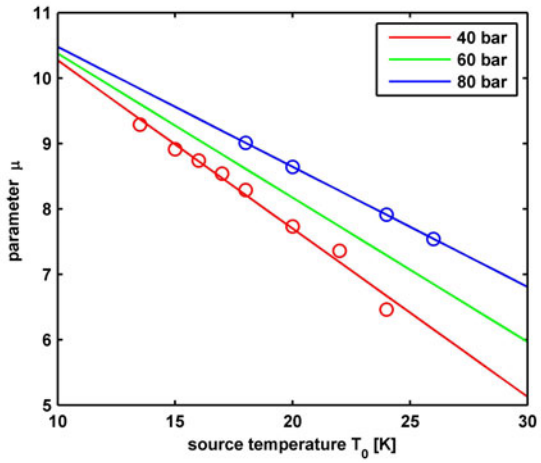

Figure 1.5: Parameter μ as a function of source temperature T_0 for different stagnation pressures p_0. The data points are from reference [52]. The solid lines are obtained from Equation 1.10. The linear dependence of μ on the temperature can be seen in this figure.

a distribution with $p_0 = 40\,\text{bar}$ and $T_0 = 16\,\text{K}$. Due to the asymmetry of the distribution, $\bar{N}$ is always larger than the median and the maximum. The highest probability $p(N)$ to find a droplet with size N is at $\hat{N}$. For subsequent doping this is also the droplet size (neglecting evaporation of atoms after doping) to which most of the foreign atoms are attached, if pick-up conditions for maximum monomer pick-up are chosen. Thus for spectroscopic experiments with impurity atoms the distribution maximum is important, especially in experiments where the influence of the droplet size is investigated. In order to obtain the distribution maximum

$$\hat{N} = e^{\mu - \delta^2} \tag{1.9}$$

the two parameters μ and δ have to be known. Unfortunately there is only one source in literature [52], where the parameters μ and δ are listed and only for a stagnation pressure of 40 and 80 bar. With the scaling law only $\bar{N}$ can be calculated (Equation 1.3). In order to obtain all parameters of the log-normal distribution for various source pressures and temperatures a model is needed, which allows to calculate the two parameters μ and δ from the mean droplet size $\bar{N}$.

In Figure 1.5 the μ parameter from ref. [52] is plotted for different source pressures (40 bar and 80 bar) as a function of the temperature. It can be seen that μ is a linear function of the temperature. Assuming in addition a linear pressure dependence of μ, the following expression for μ is found:

$$\mu = (0.00184\,p_0 - 0.331)\,T_0 + (-0.0133\,p_0 + 13.3747) \tag{1.10}$$

This expression allows the calculation of μ for different source conditions. With Equation 1.7 and 1.10 the parameter δ can now be calculated and the log-normal distribution is known. The great advantage of this model is, that for every pair of source pressure and temperature all parameters of the log-normal distribution can be calculated. However, due to the assumption of a linear pressure dependence of μ, an extrapolation $\leq 30\,\text{bar}$ might not be appropriate. Below 30 bar the ansatz of Kornilov from ref. (Kornilov2009) is used, where a constant value of $\delta = 0.625$ is proposed.

Table 1.2: Calculated parameters for the log-normal droplet size distribution for $p_0 = 60$ bar and different source temperatures T_0. The listed values for $\hat{N}$ and $\hat{R}$ for $p_0 = 60$ bar are the typical source conditions used in the experiments.

T_0	$\bar{N}$	$\bar{R}$ [Å]	$\Delta N_{1/2}$	$\hat{N}$	$\hat{R}$ [Å]	N_{Median}	R_{Median} [Å]	μ	σ
14	17713	58	15171	7432	43	13261	53	9.49	0.76
16	11247	50	9736	4914	38	8534	45	9.05	0.74
18	7342	43	6284	3074	32	5492	39	8.61	0.76
20	4915	38	4053	1828	27	3535	34	8.17	0.81
22	3372	33	2578	1035	22	2275	29	7.73	0.89

In Table 1.2 an example of the calculated values for $p_0 = 60$ bar is given, which is mainly used in the course of this work. More results are presented in the Appendix of this thesis (Section A.1). In Figure 1.6 four examples of the log-normal droplet size distributions from Table 1.2 are shown. For low temperatures it can be seen that the distribution gets very broad. For the log-normal size distribution $\Delta N_{1/2}$ is approximately as large as $\bar{N}$. The model can be used for the subcritical expansion and is valid for $1000 < \bar{N} < 20000$. The accuracy of the calculated values is best in the intermediate region of p_0 and T_0. For example, the experimental values for $p_0 = 40$ bar and $T_0 = 16$ K in ref. [52] are $\bar{N} = 7741$, $\Delta N_{1/2} = 6484$, $N_{\text{Median}} = 6248$ and $\hat{N} = 4031$. The calculated values using the presented model are $\bar{N} = 7749$, $\Delta N_{1/2} = 6895$, $N_{\text{Median}} = 6171$ and $\hat{N} = 3914$, which match the experimental values quite well. At the lower and upper end of the size interval $\bar{N} < \approx 3000$ and $\bar{N} > \approx 15000$ the deviation from experimental values increases (up to $\approx 30\%$). If different values for droplet sizes from literature are compared, their agreement is rather bad. The most important systematic error is the uncertainty of the nozzle diameter, which can deviate from the nominal diameter by about 20% [56]. This deviation explains differences in experimentally determined $\bar{N}$ between different laboratories. Also the different methods which are used for the determination of droplet sizes and uncertainties in the meassurement of T_0 and p_0 can lead to different results. Deviations of up to 20-50% are possible. However, most of the deviations are the result of systematic errors and thus they do not affect conclusions which are derived from the comparison of spectra taken with the same apparatus.

Droplet radius

Assuming spherical droplets, the radius R of a helium droplet can be calculated from the number of helium atoms per droplet N with the following equation [56]:

$$R = \left(\frac{3N}{4\pi\, n_{LHe}} \right)^{1/3}. \tag{1.11}$$

With n_{LHe} =2.18 x 10^{28}, the number density of liquid helium [69], the expression for the radius of a droplet in [Å] is

$$R = 2.22\,(N)^{1/3} \quad [\text{Å}]. \tag{1.12}$$

With this equation the mean radius $\bar{R}$, the median radius R_{Median} and the radius at the maximum of the distribution $\hat{R}$ can be calculated. The radii obtained for $p_0 = 60$ bar and

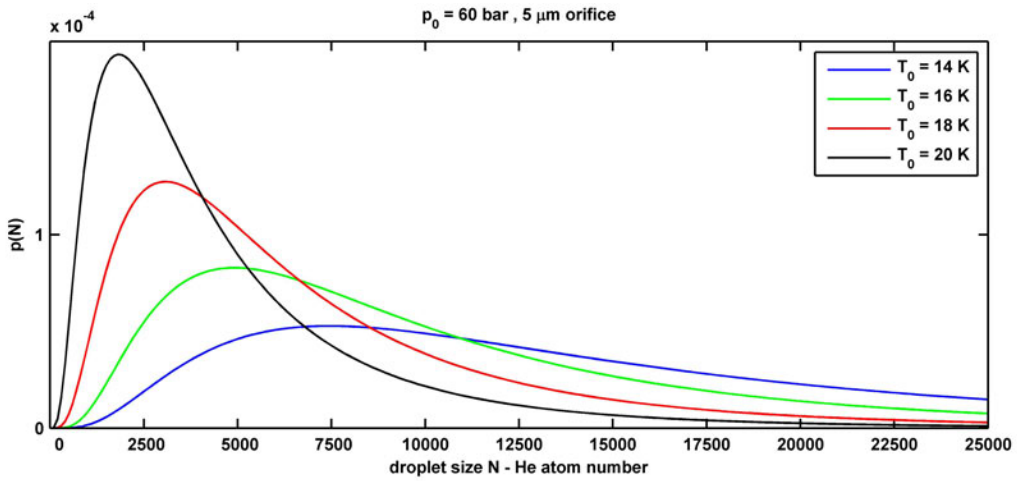

Figure 1.6: Examples of the log-normal distributions for a source pressure of 60 bar and different source temperatures. The corresponding parameters can be found in Table 1.2.

different source temperatures are listed in Table 1.2. In Figure 1.7 the droplet radius in [Å] as a function of the droplet size N is shown. Due to the third root in equation 1.12 the radius changes slowly with the droplet size, except for very small droplets $N < 1000$ where the function $R(N)$ is steep.

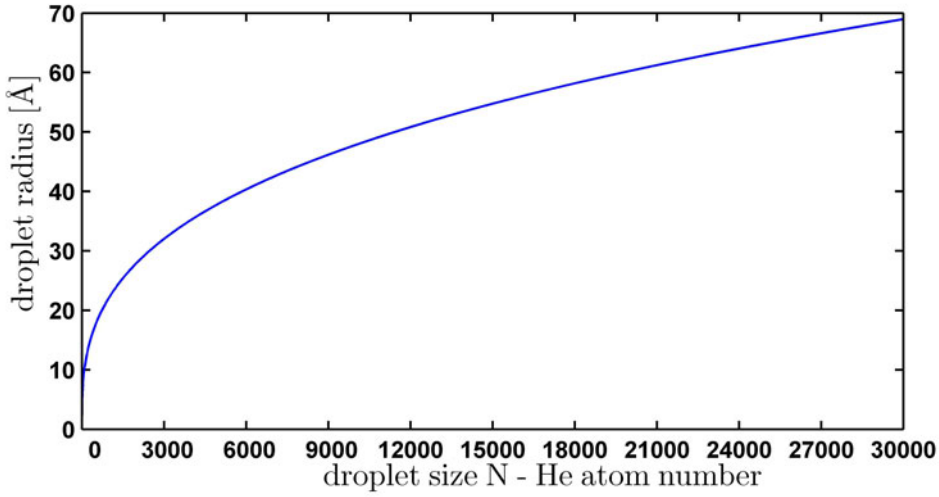

Figure 1.7: Droplet radius in [Å] as a function of the droplet size N as obtained with equation 1.12.

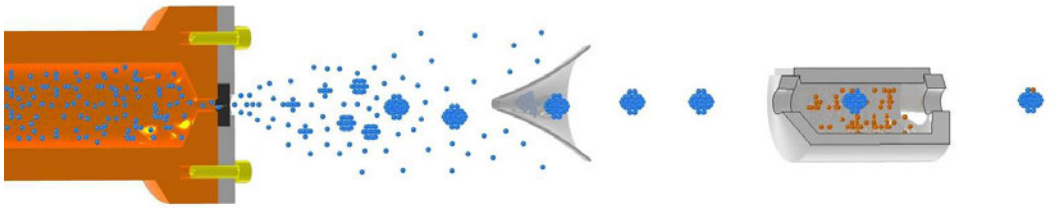

Figure 1.8: Helium droplets are produced in a jet expansion through a small nozzle (left). The beam passes a skimmer (middle) and the pickup cell (right) which is loaded with alkali metal atoms or other species.

1.5 Doping of helium nanodroplets

If an atom or a molecule collides with a helium nanodroplet it is deposited inside or on the surface of the droplet. This ability leads to the development of the so called "pickup" technique for cluster doping. Clusters can be doped with impurity atoms or molecules simply by passing through a zone with increased density of foreign particles. These atoms or molecules can be provided for example by a crossed beam or a pickup cell. The technique was first introduced for the doping of Ar clusters [70]. In 1990 it was shown that this method works also for the doping of helium droplets [71]. In the course of this work only pickup cells designed for alkali metal pickup were used to dope the helium droplets. A scheme of this technique is shown in Figure 1.8. The helium droplet beam, which is generated and skimmed in the source chamber, passes the pickup cell. The cell is loaded with a small amount of alkali metal. By heating the cell, the vapor pressure inside the cell increases and thus the amount of colliding partners for the helium droplets. The cell can also be loaded with gaseous species, where the pressure inside the cell can be adjusted with an inlet leak-valve. In the configuration shown in Figure 1.8, which is used in the experiments, an increased vapor pressure goes along with the production of an effusive beam. The effusive beam is useful for calibration and test measurements. The probability for the droplet to pick up one or more foreign atoms or molecules depends on the pickup cross section, the length of the cell a and is proportional to the pressure in the pickup cell. The pickup statistic for the pickup can easily be calculated with a simple model as shown in the following.
The geometrical cross section of the droplets is a good approximation for the pickup cross section ($\sigma(N,k)$) [14]:

$$\sigma(N,k) = \pi \left(\frac{3N(k)}{4\pi\, n_{LHe}} \right)^{2/3}. \tag{1.13}$$

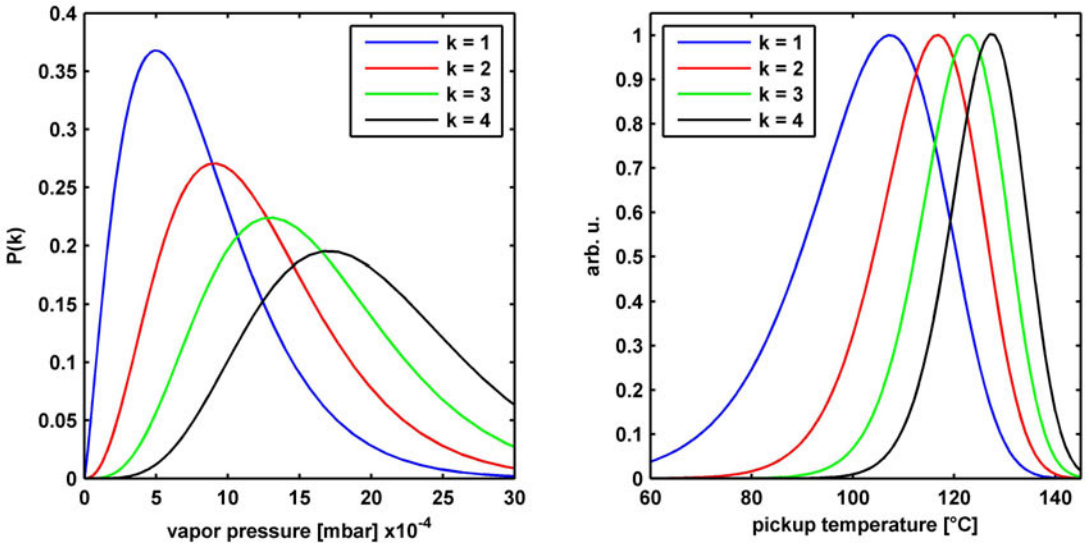

Figure 1.9: Poisson pickup distributions for $k = 1 - 4$ are shown for initial droplet sizes of $N = 7500$. The calculation includes the droplet size shrinking using the values from Table 1.3 on p. 17. The left panel shows the pickup probability as a function of the vapor pressure in the pickup cell. The right panel shows the pickup probability for Rb atoms as a function of the pickup cell temperature. The pickup temperature is offset corrected since the temperature measurement overestimates the real temperature. Hence the right panel is lab specific for ClusterLab I.

The pickup process leads to the deposition of energy into the helium droplet. This changes the pickup cross section for the next impurity, because helium atoms are evaporated from the surface to dissipate the excess energy and to cool down the droplet. This is included in the model by assuming a change of N(k) to N(k+1) in each pickup step. Each evaporated helium atom carries away about $5\,\mathrm{cm}^{-1}$ of energy [10, 72]. The pickup probability of the droplet is known to obey a Poisson distribution [73, 74]:

$$P_k(n,\sigma) = \frac{(an\sigma)^k}{k!} e^{-an\sigma}. \tag{1.14}$$

where a is the length of the pickup cell ($a = 28\,\mathrm{mm}$) and n is the particle density inside the cell. The particle density is proportional to the vapor pressure inside the cell, where the pressure depends on the cell temperature. Particle densities can be calculated from these quantities, where in this model an ideal gas is assumed. Typically pressures in the range of $10^{-5} - 10^{-4}\,\mathrm{mbar}$ are needed to deposit one atom or molecule on the cluster. For alkali atoms, this pressure seems to be slightly higher. In Figure 1.9 the pickup Poisson distributions for $k = 1 - 4$ are shown for an initial droplet size of $N = 7500$ ($T_0 = 14\,\mathrm{K}$ and $p_0 = 60\,\mathrm{bar}$). The calculation includes droplet size shrinking using the values from Table 1.3. On the left panel, the pickup probability is plotted as a function of the vapor pressure in the cell. The right panel shows the pickup probability as a function of the pickup temperature (maxima are normalized to unity) for Rb atoms. Unfortunately the temperature inside the pickup cell is not known exactly. Due to technical reasons the real temperature is lower. This is accounted for in the right panel in Figure 1.9 with a temperature offset of $40\,^\circ\mathrm{C}$ (compared to the left panel). This

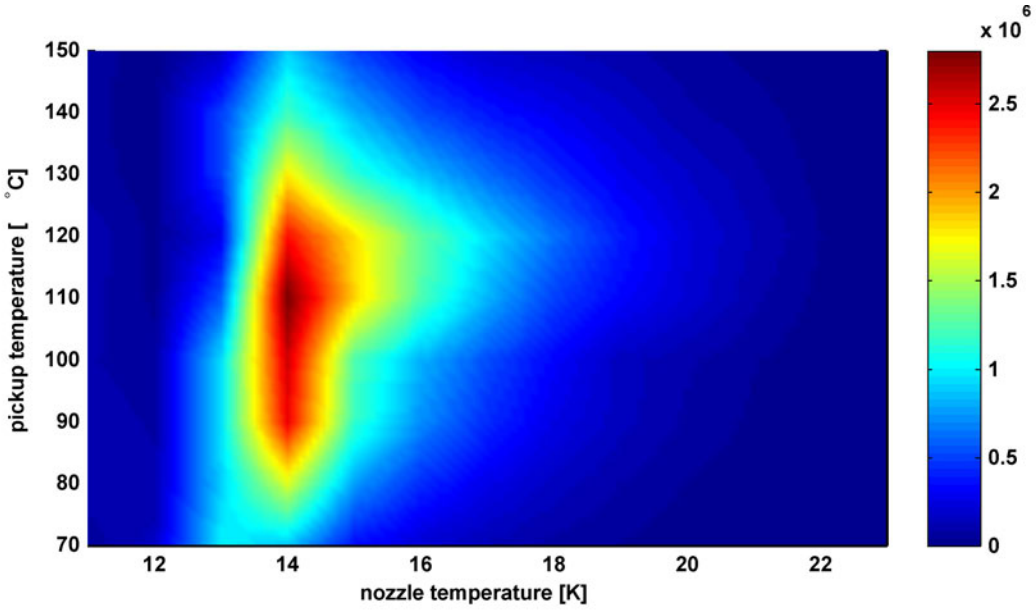

Figure 1.10: Monomer pickup as a function of pickup temperature and nozzle temperature at 60 bar stagnation pressure. The maximum for 14 K ($\hat{N}_{60,14} = 7500$) is approximately at $T_{pup} \sim 100 - 110\,°C$. The signal is obtained by monitoring fluorescence from the Rb–He_N D1 transition as a function of pickup temperature and nozzle temperature.

offset was chosen so that the maximum of the monomer pickup curve fits the experimental obtained maximum at $T_{pup} \sim 100$ - 110 °C as shown in Figure 1.10. Hence it includes also other corrections (see further down) and is probably not equivalent to the real cell temperature. The maximum for 14 K ($\hat{N}_{60,14} = 7500$) in Figure 1.10 is approximately at $T_{pup} \sim 100$ - 110 °C. The signal therein is obtained by monitoring fluorescence light from the Rb–He_N D1 transition as a function of pickup temperature and nozzle temperature, similar to the method presented in ref. [74]. Another reason which causes a deviation of the calculated temperatures from the real pickup temperatures (under-estimation of the temperature in the model) is the implicit assumption in the model, that every collision leads to successful attachment of an atom or a molecule. This can be accounted for by introducing a "sticking coefficient" $f < 1$.

The right panel in Figure 1.9 shows an important feature. Due to the nonlinear dependence of the pickup temperature on the vapor pressure (the following equation for Rb was used here: $\log(p\ [Pa]) = 5.006 + 4.312 - 4040/T$ [20]) the maxima of the pickup curves get more closely together with increasing pickup temperature. It can also be seen (in both panels of the Figure) that the advantage to form small complexes and tailored molecules in helium droplets goes along with the disadvantage that it is not possible to select a single complex size k in the doping process. Another important point which has to be considered is the influence of the broad droplet size distribution on the pickup statistic. This influence is a convolution effect. Equation 1.14 gives the pickup probability for a specific droplet size. Different droplet sizes, as they are always present in the beam, have different cross sections. In the left panel of Figure 1.11 we show the case of $\hat{N} = 7500$, the upper cluster size limit used for spectroscopic experiments in the course of this thesis. The size distribution is approximately as broad as the mean value. Droplet sizes N where the formation probability according to the log-normal

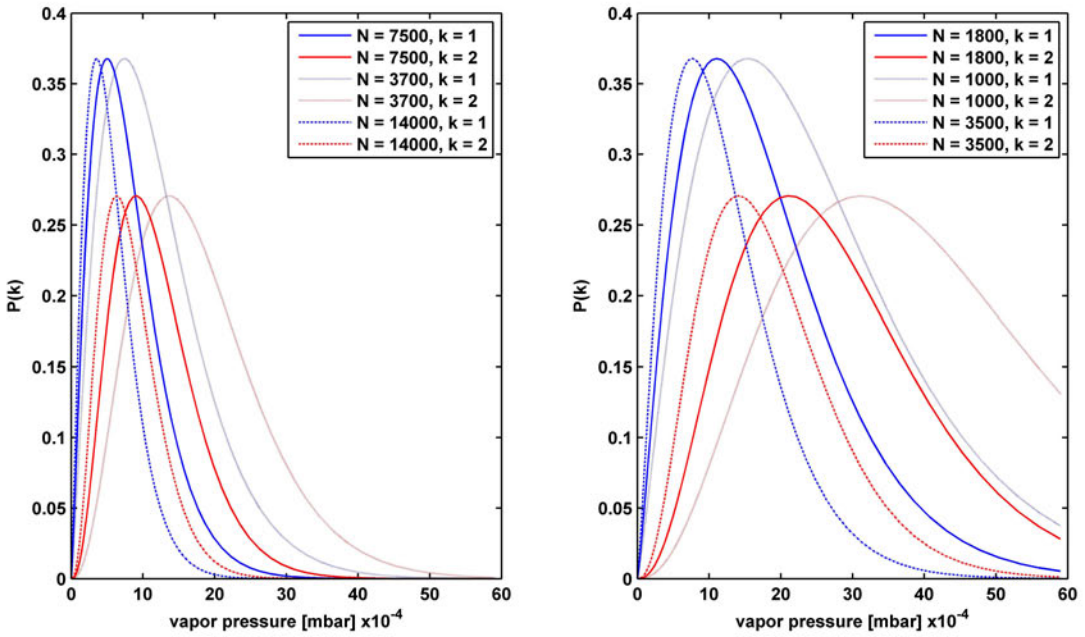

Figure 1.11: Pickup statistic for different droplets with sizes $N = 3700$, 7500, and 14000 (left panel) and $N = 1800$, $N = 1000$ and 3500 (right panel) for $k = 1$ (blue) and $k = 2$ (red).

distribution is decreased to 2/3 of the initial value are $N = 3700$ and $N = 14000$ (see Figure 1.6). From Figure 1.11 one can see that the dimer maximum ($k = 2$) of the $\hat{N} = 14000$ curve requires a lower vapor pressure than the monomer maximum ($k = 1$) of the $\hat{N} = 3700$ curve. As can be seen from Figure 1.6, the log-normal distribution is extremely broad. At conditions optimized for maximum monomer signal it is not possible to dope the droplets specifically with only one atom. There is always a relatively high probability for the formation of dimers at the large droplet fraction of the beam. However, the situation is slightly better if small droplets are used, where the size distribution is narrower (see also ref. [74] Fig. 8, therein the slope of the curves increases with N). This is shown in the left panel in Figure 1.11 for $N = 1800$ and $N = 1000$ and 3500, where the log-normal distribution has reduced to 2/3 of the maximum. The low N monomer and high N dimer curve also overlap here, but not as much as in the left panel. In this case the log-normal distribution does not have an extended large cluster wing. However, the positive effect of a narrow cluster size distribution at small cluster sizes is partly compensated by the fact that the cross section scales with $N^{2/3}$. The best method to avoid dimer and trimer contributions is to reduce the pickup temperature slightly below the monomer maximum.

Droplet shrinking upon capture of foreign atoms and molecules

The shrinking of the helium droplet can be estimated by the amount of energy added to the system by the impurity atom or molecule. According to Lewerenz *et al.* (see Appendix in ref. [73]) the total energy released into the helium droplet can be calculated by

$$E_{pickup} = E_{int} + E_{I-He_N} + E_{I+(k-1)I} + \frac{m_s m_{cluster}}{2(m_s m_{cluster})}(v_s - v_{cluster})^2. \qquad (1.15)$$

Table 1.3: Droplet shrinking upon pickup of rubidium (^{85}Rb) atoms. Exclusive formation of high-spin dimers and trimers [3] is considered in the E_{I-He_N} term. The total shrinking of the droplet is noted in the last column assuming that every evaporated He atom carries $5\,\mathrm{cm}^{-1}$ of energy away [72].

	T_{pup} [°C]	E_{int} [cm^{-1}]	E_{I-He_N} [cm^{-1}]	$E_{I+(k-1)I}$ [cm^{-1}]	$\frac{3k_BT_{pup}}{2}$ [cm^{-1}]	$\frac{m_s v_{cluster}^2}{2}$ [cm^{-1}]	E_{pickup} [cm^{-1}]	$\Delta\mathrm{He}_N$ [N_{He}]	total [N_{He}]
Rb	100	0	10	0	390	570	970	194	194
Rb_2	110	0	10	250	400	570	1230	246	440
Rb_3	120	0	10	939	410	570	1925	385	825

Therein E_{int} is the internal energy of a molecule, which is usually rotationally and vibrationally hot when it is picked up by the droplet. E_{I-He_N} is the binding energy of the impurity atom or molecule to the droplet, which is for alkali atoms about $10\,\mathrm{cm}^{-1}$ [75]. $E_{I+(k-1)I}$ is the energy which is gained by the formation of an impurity dimer ($k = 2$) or trimer ($k = 3$). This is discussed extensively in our article ref. [3] for Rb and Cs oligomers, where the spin-configuration of the formed molecules plays an important role for the released energy. The last term in equation 1.15 accounts for the kinetic energy which is brought into the system because of the relative velocity $v_s - v_{cluster}$ between helium cluster and the scattering partner s. It can be shown that this expression can be greatly simplified because the mass (and thus the kinetic energy) of the droplet is much larger than the kinetic energy of the dopant and by the fact that the velocity distribution of the dopant atoms obey a Maxwell-Boltzmann distribution [74]:

$$E_{pickup} = E_{int} + E_{I-He_N} + E_{I+(k-1)I} + \frac{3k_BT_{pup}}{2} + \frac{m_s v_{cluster}^2}{2}. \tag{1.16}$$

The speed of the droplet depends on the source conditions and is approximately $v_{cluster} = 400\,\mathrm{m/s}$. $E_{int} = 0$ for the pickup of atomic species.

In Table 1.3 an estimation of the droplet size shrinking upon pickup of rubidium atoms is shown. It is assumed that only high-spin dimers and trimers are formed on the droplet for the released binding energy $E_{I+(k-1)I}$. This assumption is based on the results of former experiments, where it was shown that the droplets act as a filter for weakly bound complexes. This ability predestines them for the investigation of high-spin dimers and trimers. A lot of work on this topic has been done in our group [42, 76, 77].

This estimation shows that for single atom doping, the droplet size shrinking can be neglected. The number of approximately 200 evaporated He atoms is small compared to the total number of helium atoms (2000-7500) in the droplet. However, if dimers and trimers are formed and if very small droplets are used, the droplet size decrease should be considered.

1.6 Spectroscopy of doped helium nanodroplets

From the first experimental realization of a helium droplet source in the 1960's [34], it took almost 30 years until the power of helium droplets as matrix for spectroscopy was recognized [71, 78]. Spectroscopy of helium droplets can be subdivided in two main branches: infrared spectroscopy, including rotational and vibrational spectroscopy, and electronic spectroscopy.

Infrared spectroscopy

The first spectroscopic experiments with doped helium nanodroplets were reported by Scoles *et al.* in 1992. In those early infrared spectroscopy experiments, the rotational structure of the SF_6 [79] molecule was investigated. The first high resolution spectra of SF_6 doped helium clusters [80, 81] revealed that molecules can rotate freely in the superfluid helium droplets. Hence helium nanodroplet has been referred to as the ultimate spectroscopic matrix [82], because it combines the advantages of molecular beam spectroscopy and matrix isolation spectroscopy. In helium nanodroplets the preparation of tailored molecules is possible, but the large inhomogeneous line-broadening known from conventional matrix isolation spectroscopy is avoided.

The free rotation was deduced from the observation of sharp lines in the rotational spectra. The only difference to free gas-phase molecules is the smaller rotational constant B, which corresponds to an increased moment of inertia. This was explained by the collective rotation of the first non-superfluid quantum solvation shell, which surrounds the molecule inside the droplet and that follows the rotation of the molecule [83].

Vibrational lines of molecules in helium droplets show in general a slight red-shift $\Delta\tilde{\nu} < 2\,\mathrm{cm}^{-1}$ [14]. This is explained by attractive electrostatic interactions between the helium bath and the molecule. However, also blue-shifts of vibronic lines were observed.

Ro-vibronic spectroscopy of doped helium nanodroplets is reviewed in reference [16].

Electronic spectroscopy

Electronic transitions of atoms or molecules inside or on the surface of helium droplets are in general strongly perturbed. The displacement of the electron upon excitation leads to strong repulsive interaction between the helium atoms and the electron. This causes broad and (in general) blue shifted lines. The smallest linewidths are in the order of a few $10\,\mathrm{cm}^{-1}$ and they are observed in the excitation spectra of lower electronic states of molecules [84]. As will be shown in the course of this thesis, transitions into Rydberg states of alkali atoms on the surface of helium droplets can also be relatively narrow. For transitions of atoms inside helium droplets, linewidths on the order of several $100\,\mathrm{cm}^{-1}$ are reported [85, 86]. The electronic excitation of atoms inside helium droplets leads in general to the ejection of the impurity [87]. For molecules, often sharp peaks (zero phonon line ZPL) are observed close to the gas phase line, which are followed by an energetically higher broad phonon wing [84]. The phonon wing is associated with a simultaneous excitation of the impurity molecule and the liquid helium. The gap between the ZPL and the phonon wing is characteristic for molecules in superfluid matrices, hence this observation provides another proof for the superfluidity of helium nanodroplets. A resent review about electronic spectroscopy (as well as IR-spectroscopy) can be found in ref. [18].

1.6.1 Alkali metal atoms on helium nanodroplets

Probably the best investigated electronic transitions in doped helium droplets are the lowest $n^2P_{1/2,3/2} \leftarrow n^2S_{1/2}$ transitions of the alkali atoms, also known as D1 and D2 lines. Alkali atoms are an exception because they are located at the surface of the droplet. Their binding to the surface is very weak ($\sim$10 cm^{-1} [75]). The equilibrium position of the atom on the surface is determined by the interplay of the Pauli repulsion, between the alkali valence electron and the closed shell helium atoms, and the weak attractive van der Waals interaction. The consequence of this weak interaction is that alkali atoms are located on the surface in a shallow dimple [75, 88]. The D1 and D2 lines are broadened and blue shifted with respect to free atom states [89]. The shifts and linewidths are in the order of several $\sim$10 cm^{-1}, which is lower than compared to alkali atoms in bulk liquid helium [90]. In bulk helium, the atoms are located in a bubble, surrounded by helium. The broadening and blue shift of the D1 and D2 line increases with the ordering number of the alkali atom on the droplet. The properties of single alkali atoms on helium droplets are the main topic of this thesis and will be discussed in more detail in the following sections.

Alkali metal dimers and trimers on helium nanodroplets

The investigation of alkali dimers and trimers on helium nanodroplets were a major research topic in our group. The work on this topic is summarized in the PhD thesis of Gerald Auböck [91] and Johann Nagl [10]. The publications of our group on this topic can be found in refs. [42, 76, 77, 92–94].

On helium nanodroplets the formation of homonuclear alkali molecules as well as the formation of heteronuclear alkali molecules by subsequent pickup of different species is possible. Alkali molecules occur in two different spin configurations: a high spin covalently bond state, with anti-parallel oriented spins of the alkali valence electrons (e.g. dimer: singlet states) and a weakly van der Waals bound molecule with parallel oriented electron spins (high-spin e.g. dimer: triplet states or trimer: quartet states). During the pickup process, where the molecules are formed by successive capture and coagulation of alkali atoms, the binding energy which is gained by molecule formation is released into the droplet. The consequence is that high-spin molecules, where less energy must be dissipated by evaporation of He atoms (which also decreases the droplet size), have a higher probability to stay bound to the surface. The large excess energy of the low-spin systems can destroy these fragile systems. This extraordinary ability offers a possibility to investigate systems, which are difficult to prepare in the gas phase. For example, trimer quartet states have been observed so far only on the surface of helium droplets [95].

Important for this thesis are the Rb and Cs dimers and trimers on helium droplets. Because, as we have seen in section 1.5, the doping process is not monomer selective and hence Rb and Cs dimers (and to a lesser extend trimers) are also formed on the droplet with a certain probability. Thus the contribution to the excitation spectra of the Rydberg states of Rb and Cs atoms must be considered. Excitation spectra related to this molecular species can be found for example for Rb in references [42, 76, 77, 94, 96–99] and for Cs in [100, 101].

Alkali metal clusters on helium nanodroplets

Beyond the formation of dimers and trimers, the formation of larger alkali clusters on helium droplets is possible [3, 102]. We were able to show, by time-of-flight mass spectroscopy, that Rb_n and Cs_n oligomers up to $n = 30$ can be formed on helium droplets. Recent theoretical calculations [103] suggest that at a critical alkali cluster size, the cluster immerses into the helium droplet. This was recently confirmed experimentally for Na_n (submersion for $n > 20$) [104] and K_n (for $n > 80$) [105]. Cs_n is an exception because theoretical calculations suggest that it will not submerge [103].

Chapter 2

Experimental Setup and Experimental Methods

The helium droplet machine was set up by J. Nagl during the course of his diploma thesis (completed 2004) after transfer from the Penn State University. Over the years a lot of new parts were added to the machine and new detection techniques were introduced. This Chapter describes the current status of the droplet machine in the first Section 2.1. The experimental methods and optical setup for the spectroscopy of Rydberg states are described in Section 2.2. Laser induced fluorescence (LIF) spectroscopy and resonant multi-photon ionization (REMPI) spectroscopy are the primarily used methods in the course of this thesis.

2.1 Experimental setup

The helium droplet apparatus consists of three main chambers:

- source chamber
- pickup chamber
- detection chamber

A schematic overview is shown in Figure 2.1. The beam is produced in the source chamber. In the pickup chamber the droplets are doped with foreign atoms and molecules by passing through up to three different pickup cells. The detection chamber hosts the detection equipment and the optical ports for the laser beams.

2.1.1 Source chamber

High purity helium gas (*Air Liquide, Alphagaz 2 He B50L L, grade 6.0 (He* $\geq$ *99.9999%)*) is expanded under high pressure (usually 60 bar) through a cold (typically $14 - 25\,\mathrm{K}$) nozzle with a $5\,\mu$m orifice. The nozzle is cooled with a liquid helium continous flow cryostat. The temperature of the nozzle, which is mounted on an oxigen free copper nozzle holder is monitored by a silicon diode (*Lakeshore DT-471*) and actively stabilized (± 0.3 °C, [10]) by resistive heating (*Lakeshore 330 Autotuning* controller). The temperature measurement is based on the measurement of small voltages and is sensitive to electro-magnetic stray fields. Controllers

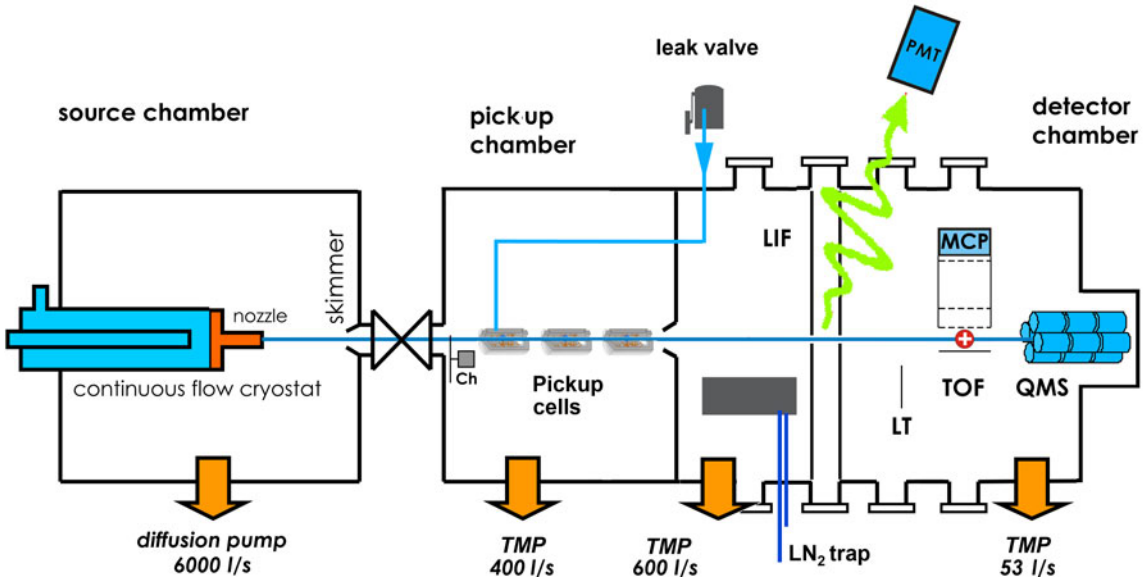

Figure 2.1: Schematic drawing of the helium droplet beam apparatus.

of TMPs or the wires which provide the heating current for the diffusion pump should be kept away from the wires to the silicon diode. The large amount of helium gas which is expanded through the nozzle into the source chamber requires a powerful pump. Therefore a *Leybold DI 6000/10B* (6000 l/s) diffusion pump with a forepump combination consisting of an *Edwards EH 1200* rotary vane pump and an *Edwards E2M80* roots booster is used. A conical skimmer (*Beam Dynamics, model 2*, 400 μm), is located 2 cm downstreem of the orifice at the end of the source chamber. The base pressure in the source chamber is in the lower 10^{-5} mbar range and $4 - 4.5 \times 10^{-2}$ mbar in the foreline without helium expansion. The foreline pressure can be used to diagnose a clogged nozzle: the typical foreline pressure at 14 K nozzle temperature and 60 bar stagnation pressure is $5.8 - 6.1 \times 10^{-2}$ mbar. If the pressure is lower the nozzle is most probably clogged. This happens occasionally and usually the problem can be solved by warming up the nozzle to ~50-60 K while keeping the stagnation pressure at 60 bar. When the droplet beam is present, the pressure in the source chamber reaches typically $1 - 4 \times 10^{-3}$ mbar. The source chamber is connected via a valve (*VAT 01228-KA06, ISO-KF, DN 25*) to the pickup chamber.

2.1.2 Pickup chamber

In the pickup chamber the beam passes at first a chopper, which allows gated counting. The chopper is useful to discriminate laser stray-light from fluorescence light in LIF experiments and it is very important for QMS measurements with the doped droplet beam. In contrast, the chopper is in general not needed for resonant multi-photon ionization experiments and LIF experiments in which a filter is used for the suppression of laser stray-light.

Further downstream, the droplet beam is doped by passing through up to three pickup cells. The interior of the pickup chamber has been modified, which is described in the master thesis of Günter Krois [12]. The pickup chamber can accommodate now a pickup cell for gaseous species, one high temperature pickup cell, suitable to reach temperatures for alkaline-

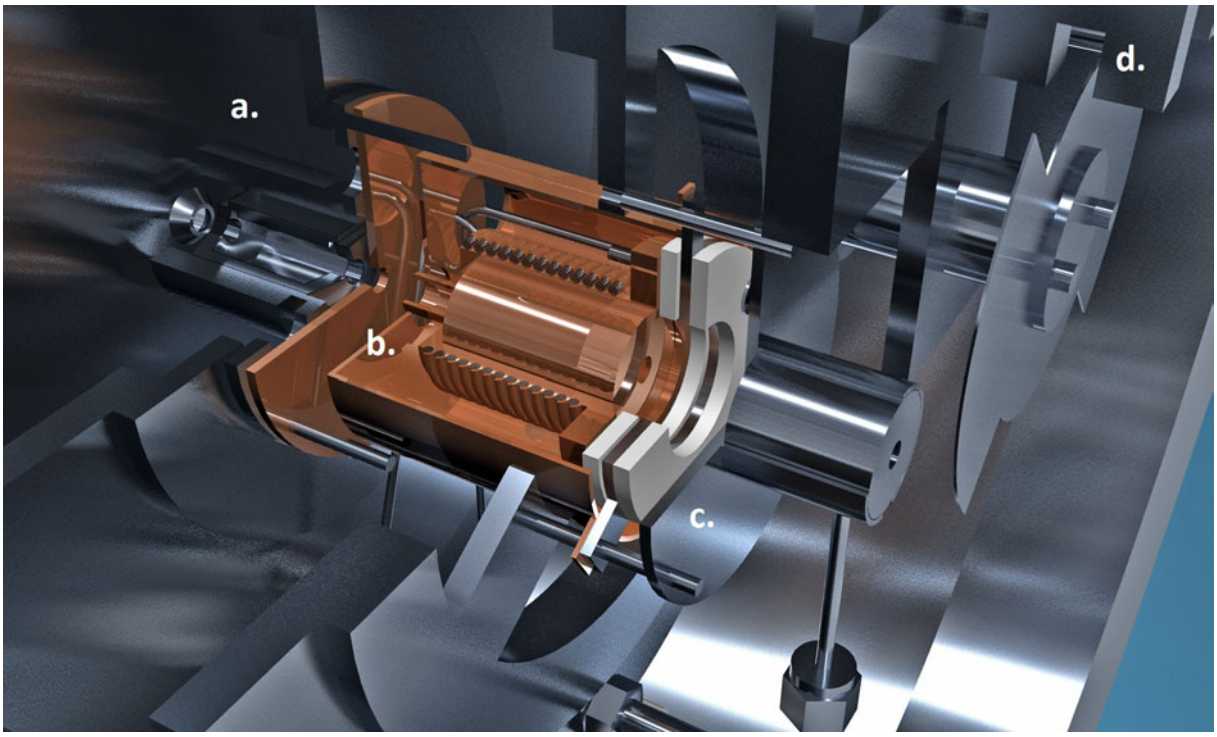

Figure 2.2: Drawing of the pickup chamber of the helium droplet beam apparatus (taken from ref. [12]). It shows the location of the alkali cell (a.), the high temperature cell (b.), the gas pickup cell (c.) and the chopper (d.) in the pickup chamber.

earth metal pickup (which are subject of the PhD-thesis of Günter Krois) and an alkali metal pickup cell. If two high temperature cells are incorporated, the gas pickup cell must be removed from the chamber. For the experiments presented in this thesis, only the alkali pickup cell and the gas pickup cell were used, occasionally in combination. The temperatures used for Rb are in the range of 100-120 °C and for Cs 90-110 °C. A drawing of the pickup chamber (taken from ref. [12]) is shown in figure 2.2. The location of the alkali cell (a.), the high temperature cell (b.), the gas pickup cell (c.) and the chopper (d.) can be seen. The pickup chamber is separated from the detection chamber by a thin stainless steel sheet metal. The doped droplet beam is guided through a 5 mm skimmer into the detection chamber.

The pickup chamber is pumped by a *Leybold Turbovac 361* (354 l/s) with an *Edwards E2M-28* rotary vane forepump. Occasionally the control unit (*Turbotronik NT150/360*) of this TMP has an error and the TMP shuts off automatically. The remaining TMP in the detection chamber is sufficient to pump both chambers and will maintain a pressure of ∼1-3 10^{-6} mbar. If the error occurs during an experiment, the measured signal decreases slowly (10-30 minutes) till the droplet beam is completely destroyed by the high pressure. In roughly 90 % of the cases where a mysterious signal decrease is observed by the experimentalists, it is caused by a TMP error. The TMP control should be checked first and the situation should not be confused with the case where the pickup cell runs out of alkali metal (which might be responsible for 5% of unexplainable signal decreases), which will require to open the vacuum chamber to refill the cell.

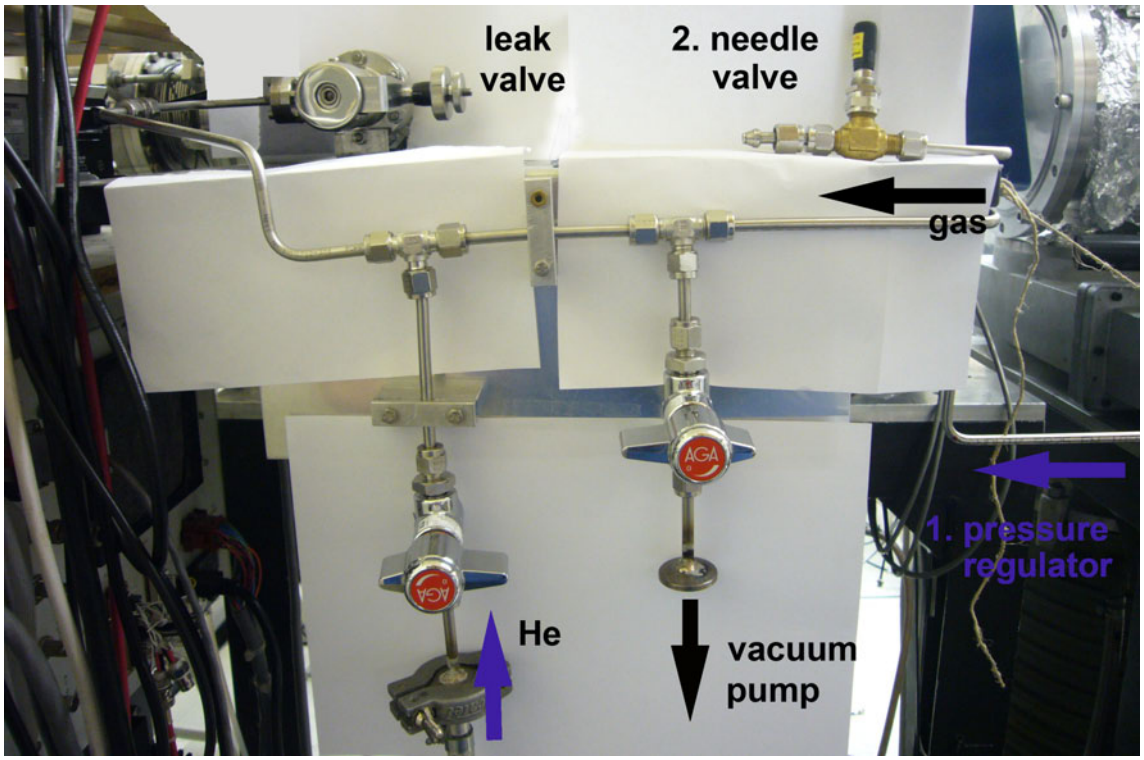

Figure 2.3: Gas inlet system for the gas pickup cell. The system consists of a gas inlet port for He, which is used to flush the system, a port for a diaphragm vacuum pump and an inlet port for the impurity gas. The impurity gas inlet port can be connected to a pressure regulator (1.), mounted on a gas cylinder or a needle valve (2.) connected to a reservoir filled with gas or liquid.

The gas pickup cell

The gas pickup cell is connected via stainless steel tubes to a precision leak valve (*Pfeiffer UDV 046 Ganzmetall-Regelventil DN 40 CF-F/DN 16 CF-R*) outside the chamber. The leak valve is needed in order to accurately adjust the relatively low pressures needed for the gas pickup ($10^{-5} - 10^{-4}$ mbar).

The pickup statistic for gaseous species can be recorded with the quadrupole mass spectrometer (QMS) in the detection chamber. Therefore the droplet beam must be chopped and the difference signal (between the two gates) is monitored on the atomic mass of the gas molecule. As a rule of thumb it can be stated that the valve position where the pickup starts is about one quarter to one half revolution of the adjusting wheel before the pressure in the detection chamber starts to rise. The valve position where the pressure in the detection chamber has raised to $\sim 5 \times 10^{-7}$ mbar should be taken as maximum pickup pressure in the experiments. These high pressures are sometimes needed to produce clusters inside the helium droplets. Too high pickup pressures will destroy the droplet beam and can harm the turbo pumps. The marks on the adjusting wheel are for hydrogen pickup and can be used as an orientation for other gaseous species because the valve positions do not differ significantly for different gaseous species.

The gas inlet system is depicted in Figure 2.3. Before the impurity gas is let into the gas

system, the system must be flushed 2-3 times with helium gas. The system can be evacuated with a diaphragm vacuum pump. This is very important especially if corrosive impurity gases are used. For corrosive gases (e.g. FH, HCl or NH_3) the gas tubes can be heated while evacuating the system with the vacuum pump to pump out the water from the system. The tubes in the system consist of stainless steel and the gasket inside the leak valve consists of copper and sapphire, which should in principle resist aggressive gases if the system is free from water [106].

Two different methods to provide the impurity gas were used for the gas inlet system. The first is straight forward. The free inlet port is connected via a stainless steel tube to a pressure regulator, which is mounted to a gas cylinder. The pressure should be held constant and an excess pressure of 1 bar has proved effective. The second method is used to dope the droplets with species which are liquid under ambient pressure, for example this has proven to work for water, acetone, methanol and ethanol. For this method, the needle valve (2.), which is shown in Figure 2.3, is connected to the gas inlet port instead of the connection to the pressure regulator. The reservoir behind the needle valve (a simple stainless steel tube with one end closed) is filled completely with the liquid. The rest of the system is flushed and evacuated. The diaphragm pump reaches ~3 mbar. If this pressure is below the vapor pressure of the liquid it will go over into the gas phase when the valve is opened. The valve to the vacuum pump must be closed in order to keep the gas in the system. For this method, it is essential that the system is leak-proven and for longer measurements the system must be refilled. Similar to this method, if gaseous species is not available in a gas cylinder, a balloon filled with gas could be put on the end of the gas inlet port behind the needle valve. This provides a gas source which lasts for several hours.

2.1.3 Detection chamber

The experiments take place in the detection chamber. A CAD drawing showing the main parts of the detection and pickup chamber is shown in Figure 2.4 (taken from ref. [12]).
It is equipped with four pairs of optical ports (up to five are possible) which allow the lasers to interact with the droplet beam.

At the end of the chamber a QMS, quadrupole mass spectrometer (Extrel C50-Q), is mounted. It is mounted inline with the droplet beam (Figure 2.1) in a geometry which also allows to use laser ionization instead of electron-impact ionization. At the end of the QMS an optical port is located, which can be used for beam depletion with a counter-propagating laser. The QMS offers a mass range of 1-500 amu. A special feature of this QMS is the unusually low electron impact energy (down to 15 eV), but for usual He droplet experiments 60 eV are recommended.

The detection chamber is equipped with a laser induced fluorescence (LIF) light detection assembly. It consists of a baffle tube and a lens system which guides light from the interaction zone of the droplet beam and the laser to a photo-multiplier tube (PMT) [107] [housing: *Products for research TE210TS-RF*, tube: *Hamamatsu R943-01* with a GaAs photocathode, cathode voltage: -1.4 kV]. The PMT was used in a pulse count mode. Therefore a home made x100 amplifier is placed directly behind the anode (to keep the low signal wire short) and the amplified pulses are counted with a *Stanford Research SR400*. The PMT can be replaced by a fiber bundle which guides the fluorescence light into a modified monochromator (*McPherson*

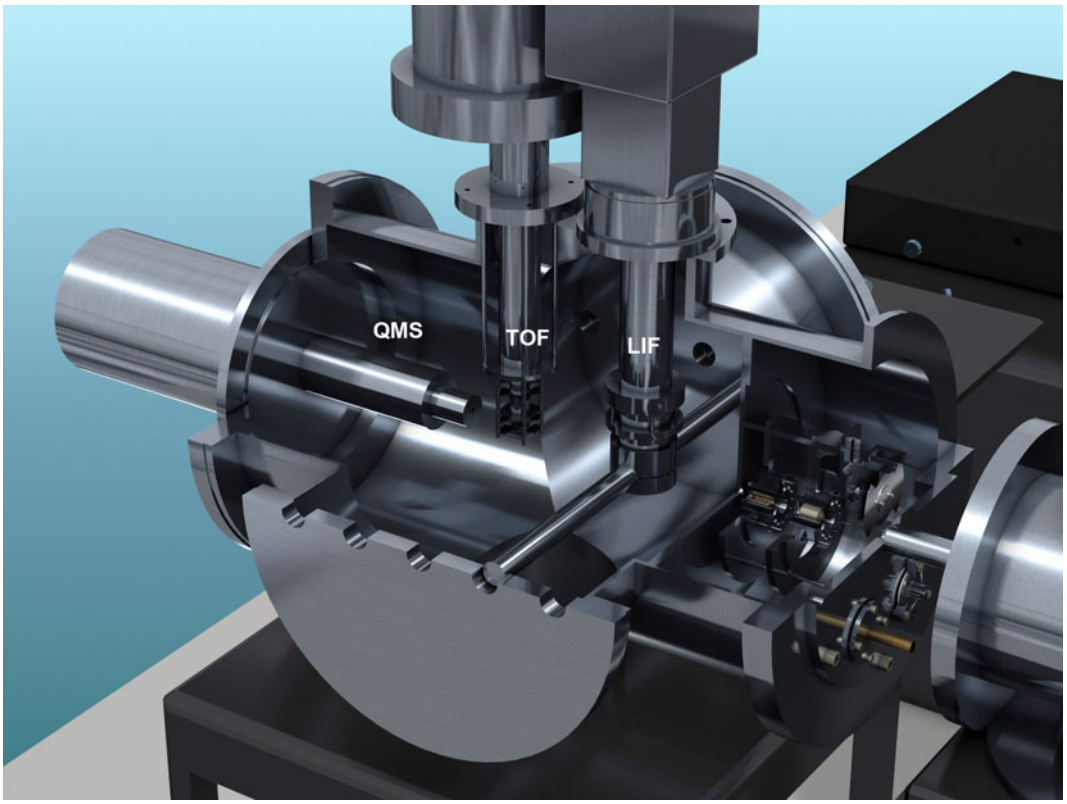

Figure 2.4: CAD drawing of the detection chamber (taken from ref. [12]), showing the location of the QMS at the end of the apparatus, the TOF mass spectrometer (only the extraction region is shown) and the LIF assembly with the baffle tubes and the housing of the lens system. The pickup chamber is connected to the detection chamber and separated by a stainless steel sheet.

EU/700, 0.35 m), where the exit slot is replaced by a water cooled CCD detector (*LOT-Andor iDUS DU401A BR-DD*) in order to monitor dispersed fluorescence emission spectra.

A Langmuir-Taylor (LT) detector mounting can be inserted downstream the LIF assembly [107]. The Langmuir-Taylor detector is used for beam depletion (BD) experiments. The LT detector consists basically of a resistively heated rhenium ribbon. Alkali atoms are ionized with high efficiency on the surface of the ribbon. The ions are accelerated to a shield (negative voltage) where the ion current is monitored with a pico-Ampere meter. If the droplet beam is chopped, the difference current is proportional to the amount of alkali atoms on helium droplets.

A time-of-flight (TOF) mass spectrometer (*Jordan D-850 AREF*) is mounted between the QMS and the LIF assembly [108]. Ions are generated with pulsed lasers. The TOF mass spectrometer can be used in a linear mode for the detection of heavy masses (up to $\sim 10^4$ amu) and a reflectron mode for high resolution measurements.

The detection chamber is pumped by a *Leybold Turbovac TMP600C* (600 l/s) with an *Edwards E2M-28* rotary vane forepump. The pressure in the detection chamber is typically at 1×10^{-7} mbar. Good vacuum conditions are essential for TOF mass spectroscopy in order to provide a long mean free path for the ions and to decrease the background ions. Therefore the TOF was equipped with an additional TMP (*Pfeiffer TMU 64*, 54 l/s with a *Varian 949-9452*

diaphragm forepump), mounted at the flange on the drift tube. To decrease the background signal caused by residual pump oil in the chamber (which becomes a problem below ∼320 nm laser wavelength) two zeolite traps are mounted to the low pressure side of the TMPs in the detection and the pickup chamber. The zeolite in the trap should be changed occasionally or baked out with the heating rods ($< 100\,^{\circ}$C). Therefore the heating rots are connected to the plugbar which is plugged into the regulating transformer (tuned to ∼15%). During this procedure the TMPs should be shut down and the valves to the chambers must be closed while the forepumps are running.

In addition, a cryo pump (liquid N_2 cooled) is located inside the chamber, which reduces the pressure to $\sim 5 \times 10^{-8}$ mbar. The trap enhances the signal to noise ratio (x2) and it is recommended for experiments with UV laser light. The pressure is monitored with a *Granville Phillips GP274* (controller GP307, uncorrected for ionization efficiency).

2.2 Experimental methods

The experimental methods which were primarily used in the course of this thesis are laser induced fluorescence (LIF) spectroscopy and resonance-enhanced multi-photon-ionization time-of-flight (REMPI-TOF) mass spectroscopy. In the following the experimental setup, the laser systems and the optical setup used for this methods are described in detail.

2.2.1 Laser induced fluorescence spectroscopy

For LIF spectroscopy, a laser is guided through the baffle tube (to reduce stray light) of the LIF assembly to the interaction region with the droplet beam. Fluorescence light is collected and guided via a lens system to the PMT. Cw lasers are recommended for LIF spectroscopy, because of the longer duty cycle, compared to pulsed laser systems. However if the desired wavelength is out of cw laser range (which depends on the pump laser) gated photon counting can be used for the detection of fluorescence light. Therefore a gate window is set a few ns after the laser pulse with the SR 400 counter and the control program (LabView) and the photons are collected into this time window.

For the excitation of the D1 and D2 transitions in Rb-He_N and Cs-He_N presented in this work, a Ti:Sapphire (Ti:S) (*Coherent 899-01* cw ring laser) laser was used. In the course of this thesis, the D1 transition is used as a springboard to excite Rydberg states. The laser for this excitation is referred to as L1. The cw Ti:S laser was previously pumped by a *Coherent Innova 200* (used in the early experiments), which is now replaced by a *Coherent Verdi V-18*. The Ti:S laser was operated with two different mirror sets: For the Cs-He_N D1 and D2 (and Rb D1) line the mid-wave optic set (10600-12900 cm^{-1}) was used and for the Rb-He_N D1 and D2 the short-wave optics (11850-14400 cm^{-1}) was used. Because of the relatively broad lines on the droplets, multi-mode operation is sufficient. In the multi-mode operation typically ∼2 W output power are used in the experiments, although up to 5 W output power (@ 12600 cm^{-1} and 18.5 W pump power) are possible with optimum laser adjustment. The birefringent filter was used as tuning element (spectral width ∼10 GHz). The birefringent filter is rotated continuously with a DC motor (typical scan speeds: 0.05-0.4 cm^{-1}/s). The laser wavelength is monitored with either a *Coherent wavemaster* or a *Burleigh WA 1500* (limit accuracy $\pm 1 \times 10^{-7}$). The laser power can be monitored behind the output window

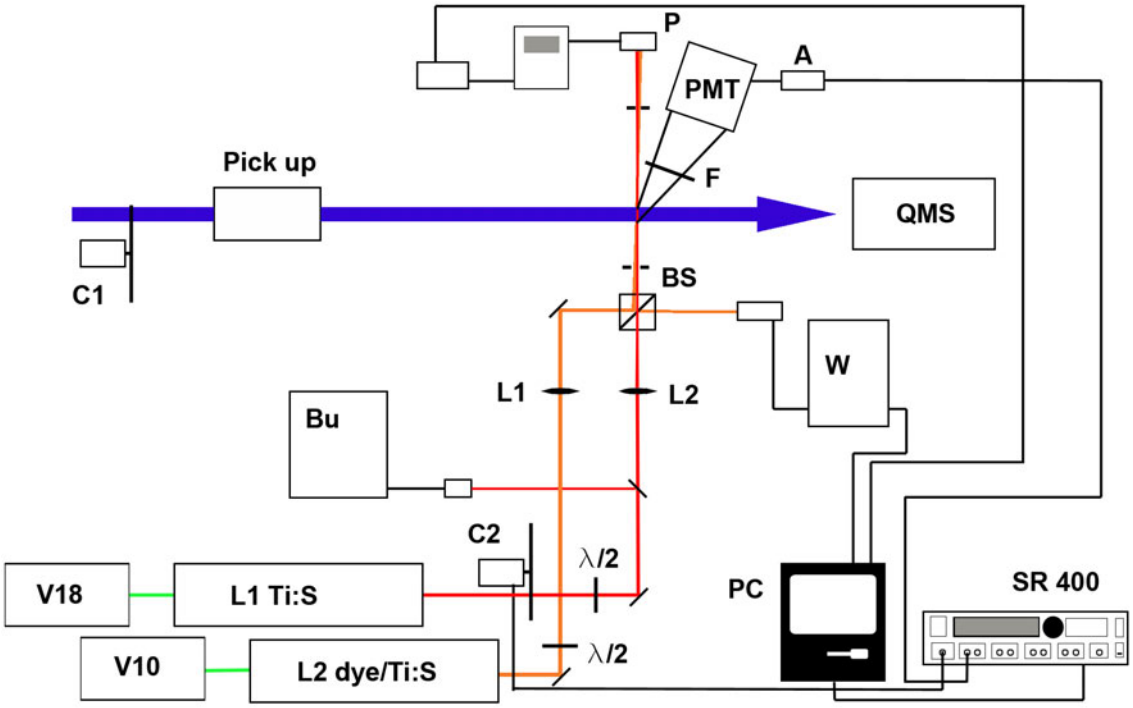

Figure 2.5: Optical setup for cw LIF two-photon spectroscopy: C1...Chopper 1, P...Power sensor, Power meter and SR250, PMT...photo-multiplier tube, A... x 100 amplifier, F...filter, QMS...quadrupole mass-spectrometer, BS...polarizing beam splitter cube, W...Coherent wavemaster, $\lambda/2$...half wave plate, C2...Chopper 2, Bu...Burleigh WA 1500. See text for a description of the measurement scheme.

of the beam apparatus (behind an iris diaphragm to avoid back reflected stray light) with a *Coherent FieldMate* connected to a *Coherent PM-10* thermopile sensor. The analog power meter output is averaged (with a *Stanford Research Model SR 250*) and fed into an analog input of the AD card (*National Instruments PCI-6221*).

To record the excitation spectra of the D1 and D2 transition of Rb-He_N and Cs-He_N, the droplet beam has to be chopped and the difference signal between chopper open (fluorescence + stray light) and chopper closed (stray light) is monitored as a function of the laser wavelength (and corrected for the laser power).

2.2.2 Optical setup for cw LIF two-photon spectroscopy

The optical setup for the cw LIF two-photon spectroscopy experiments is shown schematically in Figure 2.5. For the spectroscopy of Rydberg states, a two step excitation scheme was applied. Therefore, two cw ring lasers with various active medias are used to cover a large spectral range. For the first excitation step the Ti:S ring laser L1 described above was used. The laser is kept at constant wavelength (at maximum two-photon efficiency of the D1 transition), which is monitored with the *Burleigh WA 1500* (Bu). Laser L1 is overlapped with a second laser L2 by using a polarizing beam splitter cube (BS). Therefore the polarization of the linear polarized laser light has to be rotated by using a half wave plate ($\lambda/2$) which is adjusted while the transmitted light is monitored with the power meter (P) until a maximum is reached.

This has to be done for both lasers. Laser L2 excites the atoms from the lowest $n^2P_{1/2}$ state (D1 transition) into a Rydberg state. Laser L2 is either a *Coherent 699 Ring Dye Laser* or a home made cw Ti:S ring laser (borrowed from Prof. L. Windholz). Various laser dyes were used to cover the spectral region from 542 nm to 900 nm (including the Ti:S laser). Fluorescence light is monitored with the photo multiplier tube (PMT), x100 amplified (A) and the photons are counted with the SR 400. A filter (F) is used to suppress stray light, where in the two-step experiments a narrow optical atomic line filter is inserted to monitor the $n^2P_{3/2} \rightarrow n^2S_{1/2}$ transition. Only chopper C2 was used in the two-step experiments. The largest contribution to the background signal arises from fragmenting dimers (and trimers) which are excited by laser L2. In order to distinguish between monomer and background signal, laser L1 is chopped and the monomer signal is the difference between chopper open (monomer + dimer and background) and chopper closed (dimer and background signal only). The open and closed gate of the chopper is monitored with a photo diode which is connected to an oscilloscope. The photo diode monitors the stray light reflected by the chopper disc in the closed phase. The signal from the photo diode is transformed into a TTL signal (using a *Stanford Research DG535* four channel digital delay/pulse generator) and fed into the trigger input of the SR 400 counter. The signal is processed with a LabView program. To ensure that the gate times are exactly the same, the gate window is chosen to be sightly smaller than the duration of the high or low phase of the trigger signal. For example, typically the chopper is open for 0-22 ms followed by a closed phase of 22-44 ms (not exactly because the chopper is not exactly symmetric due to manufacturing reasons). The gate times in this case will by chosen e.g. for gate A: delay: 1 ms, gate open for 20 ms and for gate B: delay 23 ms, gate open for 20 ms. Occasionally the frequency of the chopper wheel drifts, therefore the frequency must be checked from time to time with the photo diode.

The cw laser L2 is scanned by rotating the birefringent filter continuously with a DC motor (scan speeds: 0.05-0.4 cm^{-1}/s) while the two signals (gate A and B) are monitored. The laser wavenumber is recorded with a *Coherent wavemaster* (W). The laser beams terminate in the power sensor, connected to the power meter (P). The laser power is fed via the SR 250 to the PC and is recorded during the measurement. Note that the measured power consists of the power of the chopped laser L1 and L2. This has to be considered, because only the power of L2, which is scanned, is of interest for power corrections of the recorded spectra.

2.2.3 Resonance-enhanced multi-photon-ionization time-of-flight mass spectroscopy

The detection technique used in the multi photon-ionization experiments is time-of-flight (TOF) mass spectroscopy. The TOF mass spectrometer is described and characterized in detail in my master thesis [13]. In the following a short description of the instrument based on ref. [13] is presented. Pulsed lasers are used for ionization which are described thereafter with the optical setup for the resonant three-photon TOF spectroscopy experiments. It should be noted that the TOF mass spectrometer can be operated with a cw laser, thus acting as a simple ion detector (without mass selectivity). Although the ionization efficiency with cw lasers is rather low, the longer duty cycle partly compensates for this disadvantage.

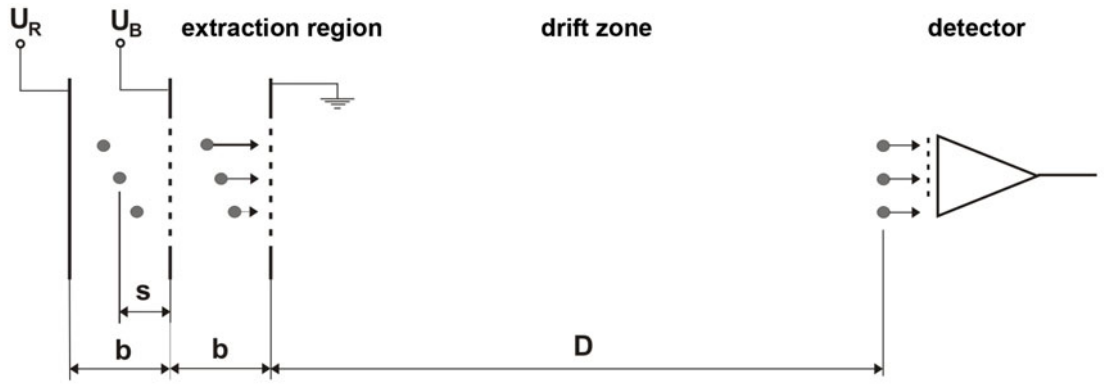

Figure 2.6: Linear TOF mass spectrometer.

Time-of-flight mass spectrometry

The droplet beam apparatus is equipped with a *Jordan D-850 AREF* time-of-flight mass spectrometer. In general, a mass spectrometer determines the mass-to-charge ration (m/z) of ions. In a time-of-flight mass spectrometers this is done by measuring the flight time of the ions. The function principle of a TOF is explained with Figure 2.6. The Figure shows a TOF with a two-stage extraction field region, a so called Wiley-McLaren type arrangement of field plates [109], with the advantage of an improved resolution.

Ions are created by a laser pulse at t_0 (with a suitable source, electron impact ionization would also be possible). In the static electrical field, defined by the voltages applied to the repeller plate U_R and the extraction field plate U_B the ions gain the potential energy eU_S. U_S is the potential at the distance s (see Figure 2.6). The potential energy is converted completely into kinetic energy at the grounded field plate:

$$eU_S = \frac{mv^2}{2}. \tag{2.1}$$

In Equation 2.1 it is assumed that only single ionized ($z = 1$) ions are created by the laser pulse, which is certainly true for alkali atoms on helium droplets. The ions enter the field-free drift region with the velocity v. From Equation 2.1 it can be realized that v depends on the mass of the ion. This is the most important point in the principle of TOF mass spectroscopy. Ions with different masses are separated in time from each other in the drift region. The flight time is given by

$$t = D\sqrt{\frac{m}{2eU_S}}, \tag{2.2}$$

or in the form which is of more practical interest:

$$m = d + ct^2. \tag{2.3}$$

The two constants are determined from spectra of known ions (for the calibration of the instrument see ref. [13]). The parameter d accounts for a time delay between trigger signal and laser pulse.

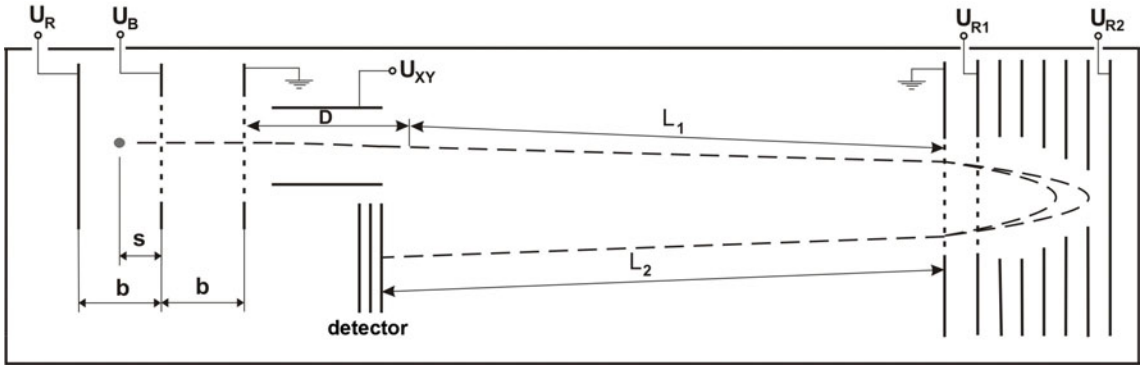

Figure 2.7: TOF mass spectrometer with reflectron.

Equations 2.3 and 2.1 explain the working principle of a TOF mass spectrometer: Ions of different masses pass the drift-region and arrive at the detector at different times because of their different velocities (but equivalent kinetic energy) which they gain in the extraction region. From Equation 2.3 it follows that, in principle, the longer the flight time, the better is the mass separation and thus the resolution:

$$\frac{m}{\Delta m} = \frac{1}{2}\frac{t}{\Delta t}. \tag{2.4}$$

This extended flight time can be achieved by using a reflectron.

However, due to the spatial extension of the laser at the ionization region, additional theoretical effort must be included into this considerations. Ions are generated in a small region $\pm\Delta s$ around the distance s. Hence the ions generated at $+\Delta s$ gain more potential energy and are thus faster in the drift region than the electrons generated at $-\Delta s$. However, at a certain distance D, the fast ions overtake the slower ones. At this focal point the spatial expansion of the ionization region has the smallest influence on the resolution and it is the distance where in a linear TOF usually the detector is located [110] to achieve the best resolution. The focal length D depends on U_R and U_B (first order focus) and can be further improved by optimal chosen distances b, s and D (second order focus, see ref. [110–112]). A reflectron can be used in order to improve the resolution of the instrument due to an increase of flight times for the ions. A TOF with a reflectron is shown schematically in Figure 2.7. The reflectron acts as a mirror for the ions and it keeps the advantage of spatial and energy focusing. The focal point at D acts as a virtual source of ions. At the distance $L1$, the ions enter the reflectron (if their kinetic energy is higher than eU_{R1}). Fast ions with a higher kinetic energy penetrate the reflectron deeper and spend thus a longer time in it. Slower ions are repelled closer to entrance and overtake the fast ions. At the distance $L2$ the ions with different kinetic energies are again focused (first and second order) [113]. At this focal point the detector is located.

Many effects affect the achievable resolution of the TOF. Some of them can be decreased with spatial and energy focusing and the reflectron as described above. Other effects can not be corrected easily, for example, the field distortions caused by the grids in the extraction field plates [114]. The size of the detector has also an influence on the resolution. This effect can be partly compensated by an Einzel-lens, which focuses the ions onto the detector. Another effect is the Coulomb repulsion between the created ions, which becomes important for particle densities higher than 10^{11} ions/cm^3 [115]. This effect can be compensated by increasing the

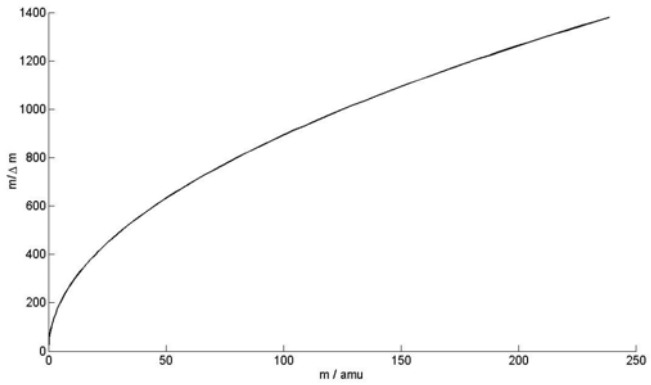

Figure 2.8: Mass dependent resolution $m/\Delta m$ according to Equation 2.4 for a laser pulse duration of $t = 29\,\text{ns}$.

laser cross section at the interaction volume and thus decreasing the ion density (the larger Δs can is compensated by the reflectron). The most important influence, which limits the resolution of the Jordan D-850 AREF, is the laser pulse duration. This effect is mass dependent and can be calculated (using Equation 2.4), which is depicted in Figure 2.8 for a laser pulse duration of $t = 29\,\text{ns}$ (Indigo-S laser). According to the manufacturer $m/\Delta m = 1500$ should be possible (in isolated cases $m/\Delta m = 4000$ is reported). Resolutions achieved with the Jordan D-850 AREF in the calibration measurements are $m/\Delta m = 280$ for ^{39}K and $m/\Delta m = 500$ for ^{85}Rb [13]. This values are only slightly lower than the values estimated with Equation 2.4.

The Jordan D-850 AREF

A technical drawing of the Jordan D-850 AREF is shown in Figure 2.9 (taken from reference [116]). It is equipped with a two stage Wiley-McLaren type extraction field region (A1 and A2) and can be operated in a linear mode and a reflectron mode. The reflectron mode is recommended for general measurements. The linear mode is recommended for the detection of heavy ions (up to several thousand amu), i.e. the detection of Ak^+–He_N. The use of the Einzel-lens, which focuses the ions onto the detector, is recommended for the detection of heavy ions in the linear mode (voltage provided by an external *Heinziger HNLCs 500-20*). The extraction field region is followed by a field-free drift tube. In the case of the linear mode, R1 and R2 are grounded and the 18 mm MCP at the top of the instrument is used. In the reflectron mode voltages are applied to the reflectron (R1 and R2), where VR2 must be higher than U = VA2+(VA1-VA2)/2. In the reflectron mode the 40 mm MCP detector is used. As a rule of thumb, the discrimination voltage VR1 should be chosen as 75 % of U. XY1 and XY2 compensate the initial velocity of the ions. It is important that the VXY wire is plugged into the VXY1 BNC connector if heavy ions should be detected and into VXY2 if lighter ions should be detected. In Table 2.1 recommended voltages, as used in the experiments, are listed. The anode of the multichannel plate (MCP) is connected to a x100 amplifier and the pulses are counted with the SR 400 counter or a home made multi channel analyzer (MCA).

Table 2.1: Recommended voltages for the Jordan D-850 AREF. VA1 and VA2 are the voltages for the extraction field plates. The VXY wire has to be plugged in to the VXY1 or VXY2 port, depending on the mode. VD is the detector voltage, FOC is the voltage applied to the Einzel-lens and VR1 and VR2 are the voltages applied to the reflectron.

Mode	VA1	VA2	VXY	VD	FOC	VR1	VR2
heavy masses linear	4550	3100	50 (VXY1)	4000	-450	-	-
linear	2000	1600	50 (VXY2)	3700	-	-	-
reflectron	1000	700	50 (VXY2)	3700	-	700	1200

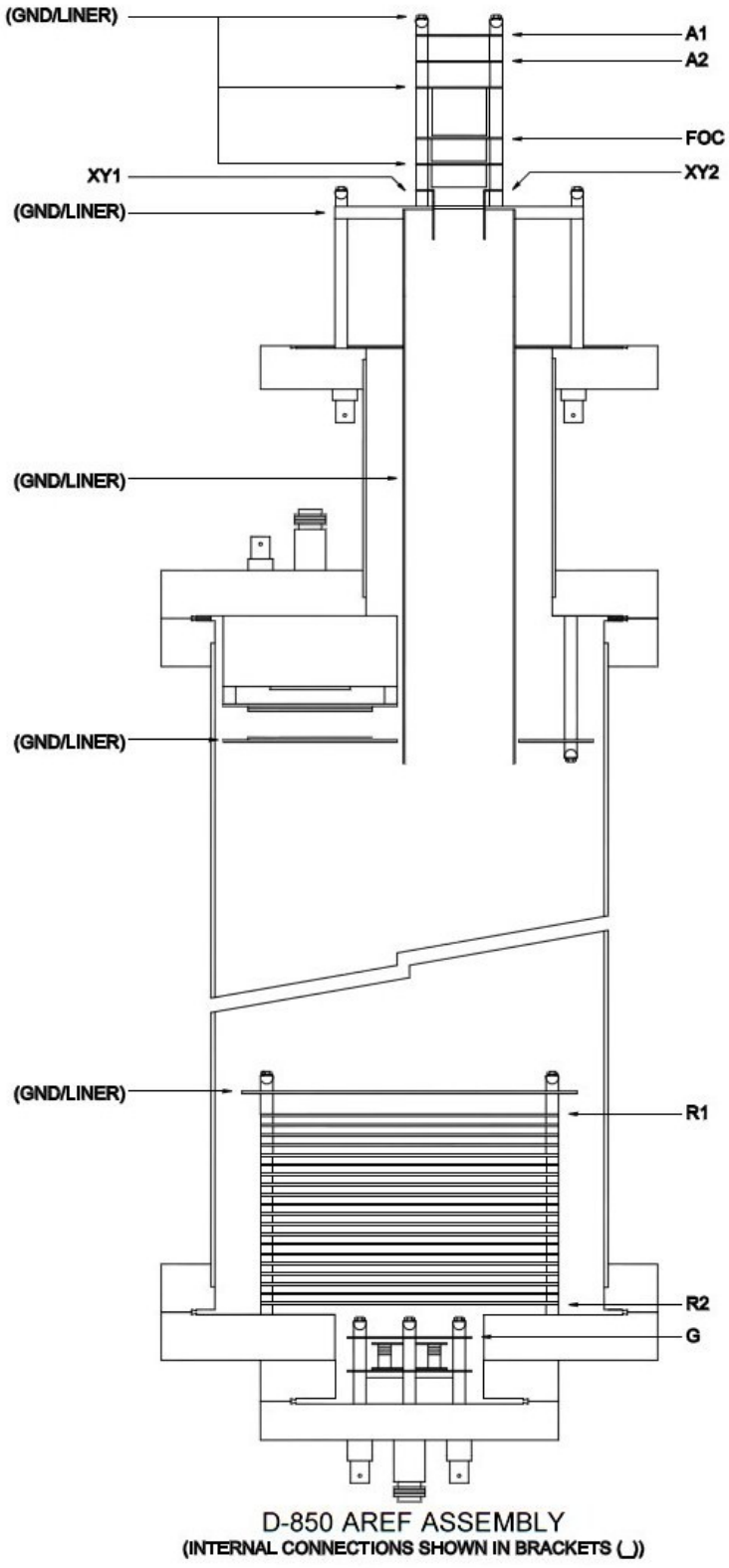

Figure 2.9: Drawing of the Jordan D-850 AREF, taken from reference [116].

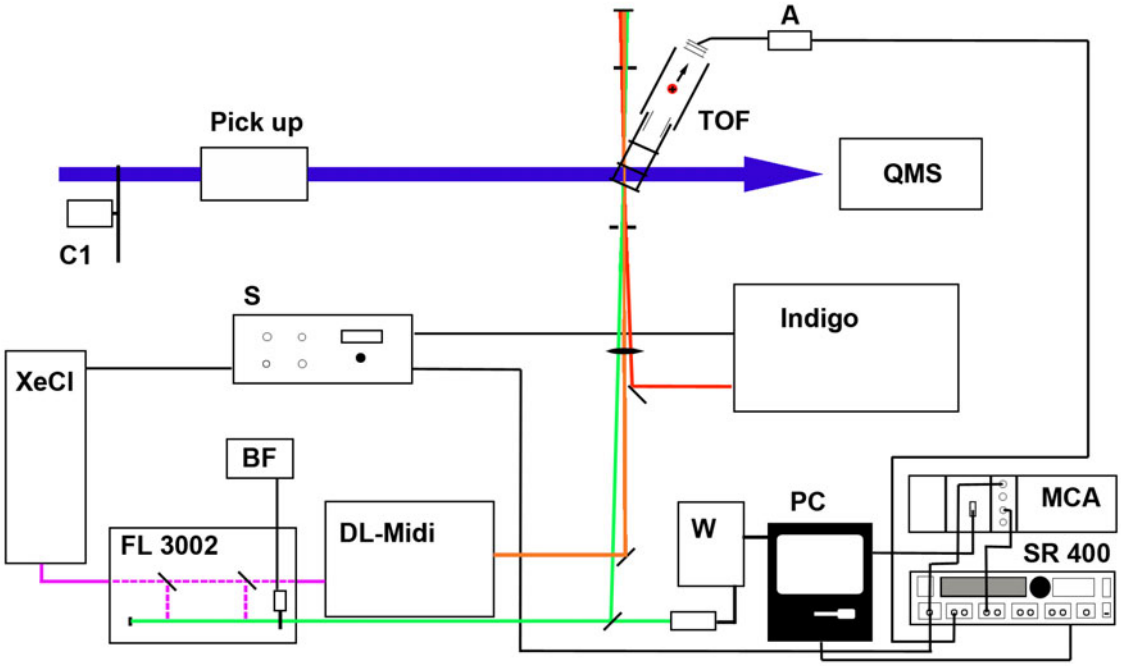

Figure 2.10: Optical setup for resonance-enhanced multi-photon-ionization time-of-flight mass spectroscopy. The lasers are spatially overlapped and synchronized (using the home made synchronization device (S)) and guided into the chamber. A coherent wavemaster (W) monitors the laser wavelength. Ions are detected with the Jordan D-850 AREF (TOF) mass spectrometer and amplified (A). A SR400 counter or a multichannel analyzer (MCA) is used to count the ions.

2.2.4 Optical setup for resonance-enhanced multi-photon time-of-flight mass spectroscopy

The optical setup for resonance-enhanced multi-photon-ionization time-of-flight (REMPI-TOF) mass spectroscopy is shown in Figure 2.10. A variety of pulsed lasers is available for REMPI-TOF spectroscopy. They can be used solely (one-color, one- two- or three-photon ionization spectroscopy) or all together (synchronized) for multi-color multi-photon ionization spectroscopy.

Laser systems

The Indigo-S laser system consists of a 5 kHz Nd:YLF (*Coherent Evolution 15*) pumped Ti:S laser (*Coherent Indigo-S*) (fundamental: 750-920 nm, i.e. 10870-13330 cm^{-1}, ~150 μJ) and can be frequency doubled (SHG, 375-460 nm, i.e. 21740-26665 cm^{-1}, ~50 μJ) and tripled (THG, 250-307 nm, i.e. 32570-40000 cm^{-1}, < 10 μJ). The laser has a pulse duration of approximately 29 ns. This system is described in ref. [117]. The disadvantage of this laser is that it can not be continuously scanned and it has a relatively low pulse energy. However, the 5 kHz repetition rate is an advantage and increases the signal (cps). It should be noted that the

fundamental (of which a fraction passes the SHG crystal unhindered) and the SHG output can be overlapped with each other, which can be useful for some experiments.

The Indigo-S laser can be synchronized with a *Radiant Dyes RD-EXC-200* XeCl 100 Hz excimer laser (25 ns pulse duration) with a home made synchronization device (S). Every 50th pulse of the Indigo-S laser triggers the Excimer laser, which therefore runs with 100 Hz. The nominal output power is 200 mJ, but in order to increase the lifetime of the laser only low voltages (16 kV) are used, which results in a output pulse energy of 70 mJ. This laser pumps simultaneously a *Lambda Physik FL3002* and a *Radiant Dyes DL-Midi* pulsed dye laser. Therefore 50% of the pump power for the main amplifier stage of the FL3002 are taken (using a beam splitter) to pump the DL-Midi laser. If only one pulsed dye laser is needed, the beam splitter can be taken out of the beam path to increase the pump power for the FL3002 main amplifier stage. Since both lasers are pumped with the same laser, they are running synchronously (neglecting the small delay 1 ns/30 cm caused by different beam path). Additionally a small portion of the 308 nm XeCl pump laser can be spatially overlapped with the other lasers. The fixed 308 nm of the XeCl laser with a relatively high pulse energy are useful as an ionizing photon, especially if it is focused into the chamber.

The FL3002 laser is equipped with a frequency doubling stage (FL 35), which is (after calibration) continuously tunable. This enables output wavelength down to 190 nm with several 100 μJ (up to a few mJ) pulse energy, depending on the frequency doubling crystal and pump power.

Optical setup

The lasers for the multi-photon ionization experiments are spatially overlapped in the interaction region with the droplet beam. To ensure spatial overlap, a mirror is inserted (at a reproduceable position) in front of the entrance window and the laser beam is guided through a pinhole located at the distance of the interaction region. A flat incidence angle of the lasers is required in order to spatially overlap the lasers without additional optical components, which will decrease the pulse energy and beam quality. It is possible to overlap the lasers just with mirrors, as schematically shown in Figure 2.10. A lens (or a combination of several lenses) can be used to focus the lasers into the chamber. However, it should be mentioned that the signal is sometimes better if the focus is not exactly at the ionization region. This depends on the transition which is investigated and has to be tested before the experiment is started. In general, the stronger the transition, the less photon density is needed.

If two 100 Hz pulsed lasers are combined, selective chopping of one laser is sometimes desired. Therefore a beam flag (BF), operated with 50 Hz, synchronized with the laser can be used. The motor of a Galvo-plate of a Coherent 699 ring dye laser is taken to build such a beam flag. The Galvo-plate motor is driven by a TTL signal, which is generated by the *Stanford Research DG535* four channel digital delay/pulse generator. The pulse generator is triggered by the laser. The TTL pulse duration is adjusted (delay and pulse width) so that every second laser pulse is blocked by a piece of stiff paper mounted to the Galvo-plate motor (BF). This is monitored with a fast photo diode and an oscilloscope. This selective chopping setup is not restricted to 100 Hz but also works for lower frequencies.

2.2.5 Optical setup for R3PI-TOF Rydberg state spectroscopy of alkali atoms on helium droplets

For the R3PI-TOF spectroscopy of Ak–He_N Rydberg states, which is presented in the course of this thesis, the fundamental output of the Indigo-S laser is synchronized and spatially overlapped with the FL 3002 pulsed dye laser. The Indigo-S laser L1 excites the first step ($n^2P_{1/2}$ ($^2\Pi_{1/2}$), Rb: $n = 5$, Cs: $n = 6$) and the FL3002 laser L2 provides the photon for the excitation of a Rydberg state. Laser L2 is scanned across the Rydberg states and a third photon (either from the Indigo-S or the FL3002) ionizes the complex. The experimental setup is shown in Figure 2.10. The laser wavelength of the scanned laser is monitored with a *Coherent Wavemaster* (W). The ions are monitored with the time-of-flight mass spectrometer (TOF) operated in the reflectron mode and amplified with a x100 amplifier (A). The ions are counted either with the SR 400 counter or a home made multi-channel analyzer (MCA). The advantage of the SR 400 counter is that signal processing is faster which increases the signal to noise ratio for a given scan speed. The disadvantage is that only two time windows (channel A and B) can be recorded simultaneously. In the early Rydberg state spectroscopy experiments channel A was set to the Ak monomer masses and channel B to the Ak-He_m exciplex masses. The advantage of the MCA is that many mass windows can be recorded at the same time. This goes along with an increased duration of signal processing (due to the communication of the MCA with Matlab via the RS232 interface). The MCA was built in the electronic workshop at the institute of experimental physics. The Matlab Program was written by Markus Krug [118] and improved by Günter Krois. The use of the SR400 as a counter is recommended for measurements of relatively low signals or for measurements where no mass resolution is needed, e.g. the detection of heavy ions as a function of laser wavelength. If the MCA is used to count the ions, the SR400 must be operated as a discriminator (discriminator level 15 mV) before the signal is fed into the MCA.

2.3 Pulsed field ionization

Rydberg states are very fragile and sensitive to external electrical fields. To investigate high Rydberg states it is required to excite them under field-free conditions. This is achieved with a home made pulsed extraction field voltage power supply, which replaces the static voltages provided by the TOF power supply. This device was implemented in the apparatus and characterized. The working principle of the pulsed field is explained in the following.

The main part of the pulsed field power supply (PFS) is a fast MOSFET switch (*Behlke Push-Pull switch, HTS 161-06-GSM*). The PFS input voltages U1 and U2 are provided by two external power supplies (*FUG HCN 14 M - 12500* and *FUG HCN 35 - 3500*, respectively). The maximum input for the higher of the two voltages (U1) is recommended with 4550 V. This is the maximum voltage which can be applied to the field plates with the original TOF power supply and it is recommended to do not apply higher voltages. The PFS is constructed for a maximum frequency 100 Hz. The PFS provides two output voltages connected to the VA1 and VA2 BNC connector at the TOF. During the field free time, VA1 is kept at the same potential as VA2 (VA2 = VA1). A TTL signal (from the laser) triggers the PFS, which switches the potential at the VA1 output from U2 to U1 in ∼50-100 ns (depending on the voltages). At this moment, the ions are accelerated towards the extraction field plate and the TOF is working similar to

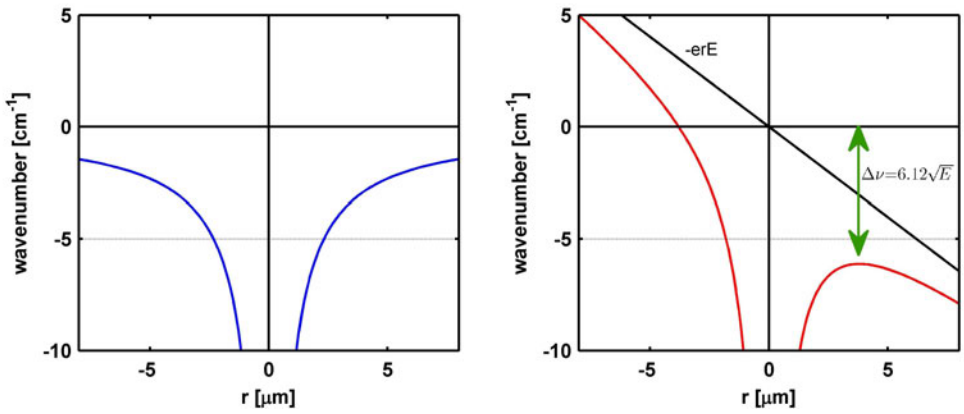

Figure 2.11: Coulomb potential (left) and effective potential $V(r)$ in an electrical field according to Equation 2.5. The depicted potential is calculated for $E = 1\,V/cm$.

the static field mode. The output voltages are measured during the experiment with a voltage divider connected to an oscilloscope. The output voltages are not exactly the same as the input voltages. For example for VA1 = 4.5 kV and VA2 = 3.5 kV: U1 = 3.94 kV and U2 = 3.5 kV or for VA1 = 2 kV and VA2 = 1.6 kV: U1 = 1.82 kV and U2 = 1.87 kV. It is very important to strictly follow the turning on and off procedure: U2 must be always higher than U1. Otherwise the PFS can be damaged. This means that U2 is always turned on first and turned off at last (see instructions on the PFS housing).

The delay of the pulsed field with respect to the TTL trigger signal provided by the TTL output of the excimer laser or the synchronization device can be adjusted in two different intervals. If the TTL trigger signal is connected to the Synch A port, the delay can be adjusted from 1.5 to 100 μs and in the Synch B port from 0.3 to 5.5 μs. Since the laser itself has a delay of a few μs to the TTL trigger signal it is possible to choose the delay so that the excitation takes place at field-on conditions, which is sometimes useful to compare between field-free and field-on excitations with exactly the same extraction field voltages VA1 and VA2.

Best signals were obtained for delays 1-2 μs between laser (measured with a fast photo diode) and extraction field. Note that the ions have a speed of $\sim$0.4 mm/μs in the direction of the droplet beam. For delays longer than approximately 15-20 μs they leave the extraction region of the TOF and can no longer be detected. This effect can lead to miss-interpretations of the observed signals. The decrease of the signal as a function of the delay of the field does not correspond only to the lifetime. Moreover the decreasing signal is caused by ions which leave the extraction field region of the TOF. Differences in the velocity distributions of free atoms and atoms on the droplet beam can also cause an unwanted background signals at longer delay times.

2.3.1 Field ionization

A constant external electrical field E acts as an additive term to the potential ($V(r)$) experienced by an electron (at the distance r from the nucleus and with the elementary charge e) in

the Coulomb-field of an atom:

$$V(r) = -\frac{1}{4\pi\epsilon_0}\frac{e^2}{r} - erE. \tag{2.5}$$

The calculated Coulomb potential and the potential according to Equation 2.5 are shown in Figure 2.11. This function has a maximum ($\frac{dV}{dr} = 0$) which corresponds to the lowering of the ionization threshold. The lowering of the ionization threshold can be calculated with

$$\Delta\nu = 6.12\sqrt{E} \qquad [cm^{-1}], \tag{2.6}$$

where E must be inserted in [V/cm]. The E-field can be calculated from (VA1-VA2)/s, where $s = 1.27\,\mathrm{cm}$ is the distance between the repeller and extraction field plate. Due to the high dipole moment of Rydberg states, they are affected by the Stark effect in an electrical field. This leads to field strength dependent splittings and shifts of the excited states and also to the lifting of selection rules. Hence for the investigation of high Rydberg states, field-free conditions are required. A comparison between field-free and field-on excitation of Rydberg states ($n \geq 24$) is shown in Figure 2.12 for bare Cs atoms. In the field-free signal only sharp lines are observed, which correspond to the $n^2\mathrm{D}_{3/2} \leftarrow 6^2\mathrm{P}_{1/2}$ and $n^2\mathrm{S}_{1/2} \leftarrow 6^2\mathrm{P}_{1/2}$ transitions, where the latter one has less intensity. It can be seen that the lines in the field-on signal are increasingly broadened (Stark-effect) and also the forbidden $n^2\mathrm{P}_{1/2,3/2} \leftarrow 6^2\mathrm{P}_{1/2}$ transitions are observed for these high Rydberg states (not for lower ones). This demonstrates the advantage of the pulsed field for Rydberg state spectroscopy.

However, the pulsed field seems not to work perfectly. Residual fields are present in the extraction field region on the order of ~10 V/cm (estimated from test measurements with free atoms). This causes a shift of the threshold of approximately $20\,\mathrm{cm}^{-1}$ and must be considered in the experiments. This effect also depends on the experimental conditions e.g. the applied voltages to the field plates. This restricts excitations of Rydberg states to $n < 75$. The highest states which could be observed in experiments with free atoms are around $n = 50$. Due to this slight disadvantage it is recommended to take reference spectra of free atoms, which can be compared with term energies from literature. For the determination of the droplet induced shifts of the ionization threshold (measured directly, not extrapolated from Rydberg states) it is recommended to measure the relative shift between free atoms and atoms on droplets under exactly the same field conditions, without changing U1 and U2 between the experiments.

2.3.2 Field ionization versus multi-photon ionization

The high pulse energy of pulsed lasers causes a competition between field ionization and multi-photon ionization. This must be considered by the experimentalist. Multi-photon ionization is proportional to the square (two-photon transition) or the third power (three-photon transition) of the laser intensity (e.g. see ref. [119]). In contrast, less intensity is required to excite an Rydberg state, without ionization. Therefore the pulse energy of the laser has to be decreased in the pulsed field experiments if the majority of atoms should be ionized by field-ionization. This is shown in Figure 2.13 for different laser pulse energies. The Indigo-S laser which excites the intermediate $6^2\mathrm{P}_{1/2}$ state was attenuated to 18 mW (measured with a cw PM-10 sensor). The pulsed dye laser was attenuated to approximately 0.2 mJ. The different regimes of field-ionization and multi-photon ionization can be seen in this Figure. The free atom and the

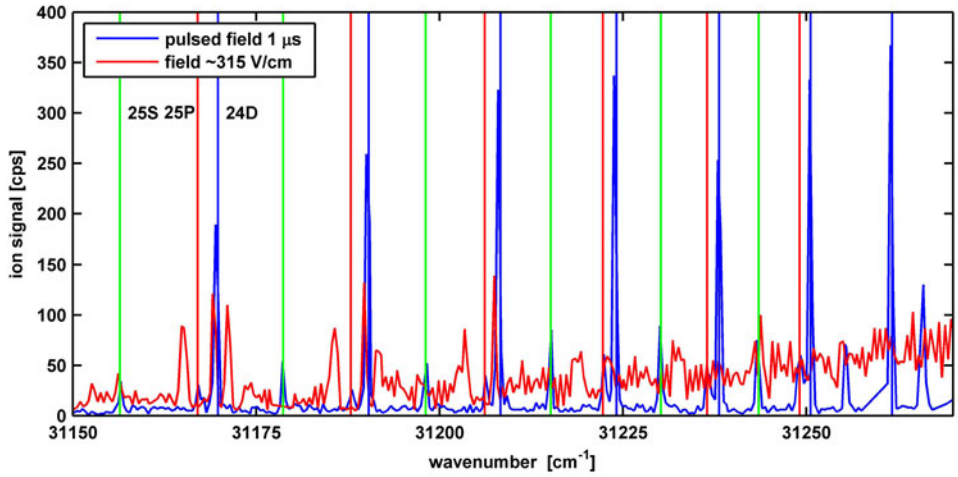

Figure 2.12: Field-free (blue) versus field-on (red) ion signal of bare Cs atoms excited via the $6^2P_{1/2}$ intermediate state. Atomic transitions are shown as vertical lines (nS: green, nP: red, nD: blue). The pulsed field was switched on 1 μs after the laser pulse. The Cs ionization threshold is at 31406.47 cm^{-1}.

calculated field corrected ionization thresholds are shown as vertical lines. It can be seen from Figure 2.13 that the relation between the field ionization and multi-photon ionization depends on the laser pulse energy. It is possible to decrease the pulse energy to a value where no multi-photon ionization occurs (not shown in Figure 2.13). The field-ionization region begins slightly above the calculated field-corrected threshold. In addition the signal quality increases at lower pulse energies.

However, transitions on the droplet have lower transition probabilities and require much higher laser intensity than the atomic transitions shown here. But this effect should also be considered and investigated if the PFS is used for these experiments.

The effect of a residual field can be seen from Figure 2.13. The signal decreases abruptly about 20 cm^{-1} below the ionization threshold at 31406.47 cm^{-1}. This corresponds to a residual field of about 10 V/cm.

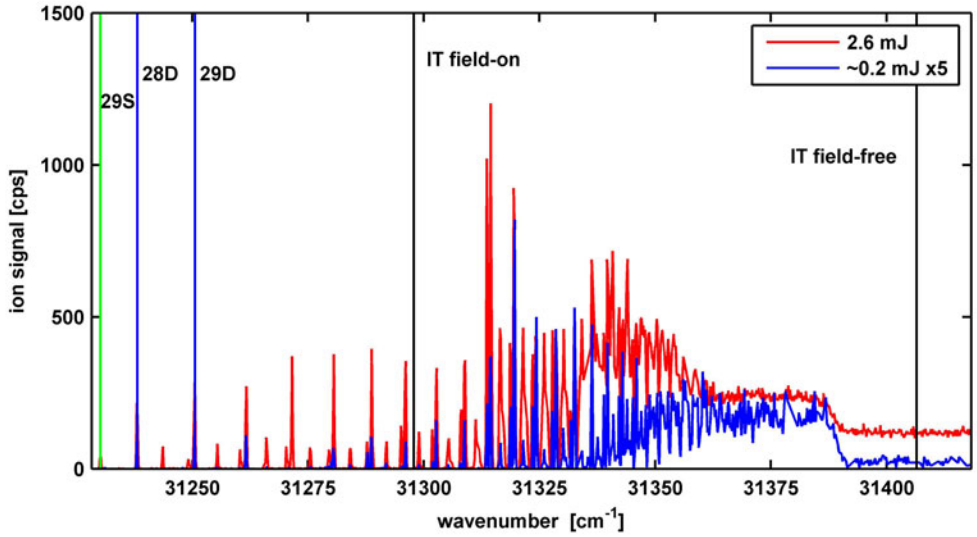

Figure 2.13: Field-free ion signal of bare Cs atoms for different laser pulse energies. The pulsed field was switched on 2 μs after the laser pulse. The field-free and the field corrected Cs ionization thresholds are shown as vertical black lines. The pulse energy of laser L2 for the excitation of a Rydberg state is given in the legend.

Chapter 3

Theoretical Concepts - Ryberg States and Rydberg Series

Rydberg states and Rydberg series are important in many areas of physics, from atomic physics to condensed matter physics. In this chapter the Rydberg concept is explained and discussed. Starting from the simplest Rydberg system, the hydrogen atom, basic properties and principles are deduced. The quantum defect is introduced and its physical meaning is explained within the scope of quantum defect theory. Molecular Rydberg states represent a more complicated system, to which the Rydberg concept applies. Especially Rydberg states of diatomic molecules are important for surface bound atoms on helium droplets, which represent a so-called pseudo-diatomic molecule. From the well-known atomic and diatomic systems the required know-how for the implementation of the Rydberg concept to our new system is obtained, which enables the application of the ideas to the alkali atom - helium nanodroplet system (Ak–He_N). The spectroscopic investigation of Ak–He_N Rydberg states is subject of the following chapters 5 and 6. Chapter 7 is focused on theoretical concepts of Ak–He_N Rydberg states and applies the ideas elaborated in this chapter to Ak–He_N Rydberg states in more detail.

3.1 Rydberg states and Rydberg series

Rydberg atoms are atoms in states of high principal quantum number n [120]. The "high n" in this definition is a somewhat vague term, but there is no defined quantum number because it depends on the atomic (or molecular) species. Rydberg states have many extraordinary properties, most noticeable: the large size of the atomic orbital, the long lifetime, the low binding energy of the electron and the large dipole moment. Rydberg states are closely related to the Coulomb potential in which the electron moves. The energy levels E_{nl} of a Rydberg atom depend only on the principal quantum number n, the orbital angular momentum l and the quantum defect d_l and are described by the famous Rydberg formula:

$$E_{nl} = IT - \frac{Ry}{(n - d_l)^2}. \tag{3.1}$$

The Rydberg constant Ry and the ionization threshold IT are constant for each atom. The Rydberg formula is an empiric equation, but it can be deduced from quantum mechanics, as will be shown later.

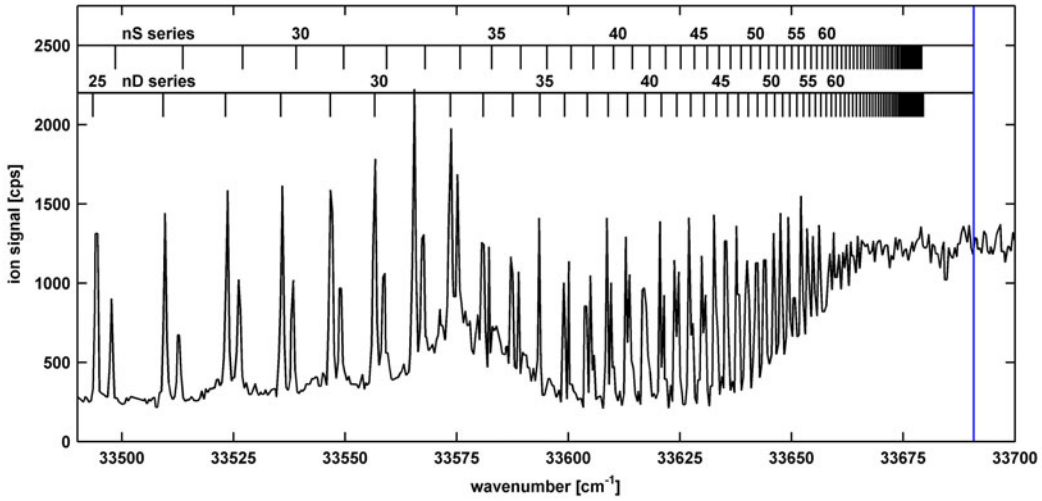

Figure 3.1: Rubidium atom nS and nD Rydberg series, recorded by resonant three-photon ionization spectroscopy (via the $5^2P_{1/2}$ state). The vertical line represents the ionization threshold.

In the special case of the hydrogen atom, which is the only atomic system with a simple Coulomb field, the quantum defect is $d = 0$ and the ionization threshold IT and the Rydberg constant Ry are $Ry = IT = R_\infty = 109737.31568160(16)\,\mathrm{cm}^{-1}$ [121] (in the infinite mass approximation). The Rydberg states form a series where the principal quantum numbers n of each consecutive member differs by one. Such a series is called a "Rydberg series". A Rydberg series is the spectral signature of an independent electron [122]. An example of a Rydberg series is shown in Figure 3.1 for the sharp (nS) and diffuse (nD) series of the Rb atom. The spectrum was recorded with R3PI spectroscopy using a pulsed extraction field (i.e. field free conditions) where the lower intermediate state was the $5^2P_{1/2}$ state. For many-electron atoms, the situation is more complicated. If an atom is excited into a state where the excited electron spends most of its time far away from the inner-shell and the other valence electrons, it will experience an effective charge defined by the charge of the nucleus minus the charge of the core electrons, i.e. one atomic unit of charge. If the electron is promoted to high enough n, the energy levels can be calculated with the Rydberg formula and Rydberg series are observed (e.g. Figure 3.1). The hydrogen Rydberg formula must be modified by introducing the quantum defect d (Equation 3.1) which accounts for the non-zero probability to find the electron inside the core. This reduces the problem essentially to a one-electron problem, very similar to the hydrogen atom.

Alkali atoms have a very compact core due to the closed inner-shell and the single valence electron. Hence, Rydberg series in alkali atoms start already at the first excited states at low principal quantum numbers (they are referred to as "low Rydberg states"). Other systems with one outer electron are for example Cu, Ag and Au (this elements have a closed d shell and one electron in a ns state). There are by far more atomic systems which exhibit Rydberg series in some range of their spectrum than do not [122].

From the fact that the formation of Rydberg states is in the nature of a charge which moves in a Coulomb potential and that non-Coulombic short range parts of the potential can

be accounted for with the quantum defect, it follows obviously that the Rydberg concept does not apply exclusively to atomic systems. For instance, if an electron in a molecule is excited into an orbital with a size much larger than the internuclear separations, it will experience essentially the Coulomb field of the positive molecular core and Rydberg series will emerge. However, this is not restricted to small molecules. Rydberg series have been observed in the C_{60} molecule or in molecules on van der Waals clusters [123]. A more exotic example of a Rydberg systems is the "heavy Bohr atom", a H^+H^- system where the electron is replaced by a much heavier hydrogen ion [124, 125]. Other examples of heavy Rydberg states are muonium [126] and positronium [127]. Rydberg states have also been investigated in the antihydrogen atom [128].

The Rydberg formula also finds application in condensed matter physics. If an electron is promoted from the valence band slightly below the conduction band in a solid, a bound electron-hole pair is formed, where the electron and the hole experience a mutual Coulomb attraction [122]. The bound electron-hole system is referred to as "exciton". The energy levels of this "quasiatom" can be described with the Rydberg formula using a modified Rydberg constant (in the meV range instead of eV in an atom) which accounts for the effective mass of the electron and the hole. There are two different types of excitons, which are Wannier and Frenckel type excitons.

As a concluding remark of this paragraph, another definition of Rydberg states is presented: Rydberg state are excited states of a system whose energy levels fit into a Rydberg series and can hence be described by the Rydberg formula. The condition which has to be provided for the formation of a Rydberg series is that one electron must be excited into a region of space where it can become "dynamically independent" of the other electrons. Many-electron interactions, which are determined inside the core, are subsumed into the value of the quantum defect.

3.1.1 Historic roots of Rydberg states

Rydberg states played an important role at the beginning of atomic physics and the birth of quantum mechanics. The first appearance of a Rydberg atom is in the Balmer series of the hydrogen atom [120]:

$$\lambda_n = \frac{b\,n^2}{n^2 - 4}, \tag{3.2}$$

where $b = 3645.6\,\text{Å}$ and λ_n gives the observed transition wavelength from high n levels into $n = 2$. Balmers formula is a special case of the Rydberg formula. He analyzed four hydrogen lines (H_α, H_β, H_γ and H_δ, all members of the "Balmer series"), measured by A.J. Ångstrom, and he found a mathematical expression (Equation 3.2) which describes the spectral position of the observed lines. He published his formula in 1885 [129].

Independent from J.J. Balmers research, the Swedish physicist Johannes (Janne) Robert Rydberg was focused on the search for a system to arrange spectral lines. At that time, the end of the 19th century, R.W. Bunsen and G.R. Kirchhoff have already been performing spectral analyses of many elements and a wealth of wavelength data was available [130]. Rydberg discovered that the spectral lines of a certain element can be arranged in a series where consecutive lines follow each other with a regularly decreasing difference and intensity. Rydberg tried to find a simple formula that includes integers and which expresses the observed wavenum-

bers. He finally succeeded and derived the Rydberg formula (Equation 3.1), which was first published in 1889 [131] (and printed in 1890). The Rydberg formula expresses the wavelength of a line as the difference of two terms of the same form (in the above form one of them is the IT) where the denominator is a quadratic function and the numerator is a constant. Rydberg realized the remarkable relation between various elements, the generality of the constant for all chemical elements. This constant was named after him, the Rydberg constant Ry. It is currently one of the most accurately known fundamental physical constants [121]. It was also Rydberg who introduced the spectroscopic unit wavenumber [cm^{-1}], which he used to express the Rydberg constant. Rydberg derived his formula purely from his analysis of spectroscopic data. Several years later, at the beginning of the 20th century, the development of quantum mechanics and modern atomic theory gave the theoretical frame for the Rydberg formula. Hence Janne Rydberg is truly one of the great pioneers of atomic physics.

3.2 Rydberg atoms

In this section the quantum mechanical origin of the Rydberg formula is presented and the physical meaning of the quantum defect in the scope of quantum defect theory is explained. As mentioned above, Rydberg states and Rydberg series are characteristic for effective one-electron problems. Therefore, the best starting point for the discussion of those systems is *the* one-electron problem, the hydrogen atom. After the presentation of some important basics of the hydrogen problem, the discussion is extended to the effective one-electron system within the scope of quantum defect theory. As we will see, both problems are quite similar and the results for the hydrogen atom Rydberg states anticipate most of the results in quantum defect theory for Rydberg states in other atoms.

3.2.1 The hydrogen Rydberg atom

The discussion of the hydrogen atom in this section is kept rather short. The problem is subject of every standard atomic physics and quantum mechanics book, e.g. [132–135]. For the one-electron problem in context with Rydberg states the books of T.F. Gallagher [120], J.-P. Connerade [122] and M.S. Child [136] are recommended.

The one-electron hydrogen problem consists of an electron in a spherically-symmetric Coulomb field of a proton. The size of the proton can be neglected, since it is very small compared to the electron orbital and thus the field experienced by the electron is purely Coulombic. The Coulomb potential is given by

$$V_C(r) = -\frac{Ze^2}{4\pi\epsilon_0 r}, \tag{3.3}$$

where the nuclear charge $Z = 1$ for a neutral species. e is the elementary charge, ϵ_0 the vacuum permitivity and m_e is the mass of the electron. The aim of this section is to obtain energy level eigen values, which will lead to the Rydberg formula. Furthermore the electronic eigen wavefunctions are derived, from which many properties of Rydberg atoms can be deduced. In order to do so, we need to solve the Schrödinger equation

$$H\Psi = \left[-\frac{\hbar^2}{2m_e}\Delta + V(r)\right]\Psi = E\Psi. \tag{3.4}$$

By introducing polar coordinates and by separating the complete eigenfunction of the electron ($\Psi_{nl}(r,\Theta,\Phi)$) in radial and angular coordinates

$$\Psi_{nl}(r,\theta,\phi) = R_{nl}(r)Y_{lm}(\theta,\phi), \quad u_{nl}(r) \equiv rR_{nl}(r) \tag{3.5}$$

the Schrödinger equation for the hydrogen atom can be rewritten to the form

$$H\Psi =$$

$$Y_{lm}(\theta,\phi)\left[-\frac{\hbar^2}{2m_e}\frac{1}{r^2}\frac{\partial}{\partial r}\left(r^2\frac{\partial}{\partial r}\right)+V_C(r)\right]R(r) - \frac{R(r)}{2m_e r^2}\hbar^2\left[\frac{1}{\sin\theta}\frac{\partial}{\partial\theta}\left(\sin\theta\frac{\partial}{\partial\theta}+\frac{1}{\sin^2\Theta}\frac{\partial^2}{\partial^2\phi}\right)\right]Y_{lm}(\theta,\phi)$$

$$= E_n\frac{u_{nl}(r)}{r}Y_{lm}(\theta,\phi). \tag{3.6}$$

Equation 3.6 consists of two independent terms, R and Y. The equation can be solved by using a product ansatz (Equation 3.5). Therefore a separation constant λ is introduced. This constant is best chosen with $\lambda = \hbar^2 l(l+1)$, the eigenvalue of the square of the orbital angular momentum operator $\hat{l}$. We get two independent differential equations for the angular part and the radial part. The angular part can be written by using the ansatz $Y(\phi,\theta) = \Theta(\theta)\Phi(\phi)$ for the angular function:

$$\frac{1}{\sin\theta}\frac{\partial}{\partial\theta}\left(\sin\theta\frac{\partial\Theta}{\partial\theta}+\frac{1}{\sin^2\theta}\frac{\partial^2\Phi}{\partial^2\phi}\right) = -l(l+1)\Phi\Theta. \tag{3.7}$$

The solutions to this equation are the normalized spherical harmonics:

$$\Theta(\theta)\Phi(\phi) = Y_{lm}(\theta,\phi) = \sqrt{\frac{(l-m)!}{(l+m)!}\frac{2l+1}{4\pi}}P_l^m(cos\theta)e^{im\phi} \tag{3.8}$$

where P_l^m(x) is the unnormalized associated Legendre polynomial and m is the magnetic quantum number.

The radial Schrödinger equation can be written as:

$$-\frac{\hbar^2}{2m_e}\frac{\partial^2 u_{nl}}{\partial r^2}+\left(\frac{\hbar^2 l(l+1)}{2m_e r^2}-\frac{e^2}{4\pi\epsilon_0 r}\right)u_{nl} = E_n u_{nl} \tag{3.9}$$

It can be seen that the energy eigenvalues E_n of the hydrogen atom depend only on the radial part of the Schrödinger equation. The energy eigen values E_n are obtained by solving equation 3.9 which gives also the radial wavefunctions u_{nl}. The E_n are $(2l+1)$-fold degenerate in the angular momentum l and n^2-fold in magnetic sublevels m. The m degeneracy is an essential degeneracy because equation 3.9 is independent of m. This degeneracy survives any central field. The l degeneracy is a characteristic of the central Coulomb field and it is referred to as accidental degeneracy.

From equation 3.9 we can immediately deduce another important property. The second term in equation 3.9 consists of two parts. The Coulomb potential V_C(r) and a centrifugal potential, $\frac{\hbar^2 l(l+1)}{2r^2}$. The sum of both is the effective potential (V_{eff}) in which the electron moves. This

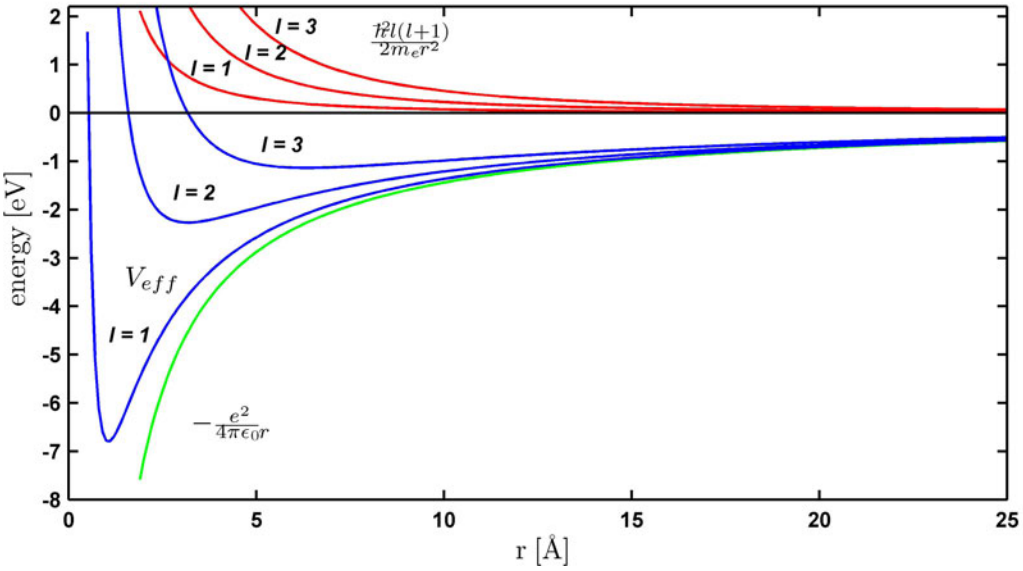

Figure 3.2: Coulomb (green) and centrifugal (red) potentials are summed to give the effective potential V_{eff} (blue). The electron moves in the effective potential, which is shown for orbital angular momenta $l = 1, 2$ and 3.

is shown in Figure 3.2 for orbital angular momenta $l = 1, 2$ and 3. We see that the centrifugal term determines the position of the minimum in the effective potential. It follows that the (classical) inner turning point (see section 3.3.3) of the electron is located at higher r if the orbital angular momentum l is large. It is convenient to switch to atomic units now ($m_e = 1$, $e = 1$, $\hbar = 1$ and $\frac{1}{4\pi\epsilon_0} = 1$). The bound state ($E < IT$, E is negative) solutions of equation 3.9 in the special case of the hydrogen atom must fulfill the boundary conditions (i) $\Psi \to 0$ for $r \to 0$ (i.e. the function must be regular at the origin) and (ii) $\Psi \to 0$ for $r \to \infty$ (the function must be normalizable). These requirements are satisfied by an equation of the form [137]:

$$u_{nl}(r) = r^{l+1} e^{-\sqrt{-2E}} F(r). \tag{3.10}$$

Using this substitution $x = 2\lambda r$, $a = l + 1 - 1/\sqrt{-2E}$ and $b = 2(l+1)$, $u_{nl}(r)$ are solutions of the radial Schrödinger equation 3.9, if $F(r)$ in equation 3.10 are the confluent hypergeometric functions:

$$\begin{aligned} F(a,b,x) = 1 + \tfrac{a}{b}x + \tfrac{a(a+1)}{b(b+1)}\tfrac{x^2}{2!} + \tfrac{a(a+1)(a+2)}{b(b+1)(b+2)}\tfrac{x^3}{3!} + \ldots \\ + \tfrac{1(a+1)\cdots(a+k-1)}{b(b+1)\cdots(b+k-1)}\tfrac{x^k}{k!} + \ldots . \end{aligned} \tag{3.11}$$

with the asymptotic behavior

$$F(a,b,x) \to \frac{\Gamma(b)}{\Gamma(a)} e^x x^{a-b} \left[1 + O(|x|^{-1})\right], \tag{3.12}$$

for large |x|. Equation 3.12 will grow exponentially with x. In order to fulfill the boundary condition (ii), the coefficient of the exponential in equation 3.12 must vanish, which is obtained for $\Gamma(a) = \infty$ (since $\Gamma(b) \neq 0$). The Gamma function has its poles ($\Gamma(a) = \infty$) at $a = 0$ and negative integer values of a. Thus, normalizable wavefunctions which fulfill the boundary

conditions are only possible if $a = -n_r = 0, -1, -2, \ldots$. The confluent hypergeometric functions reduce to a polynomial of degree n_r which is equal to the number of nodes of the radial wavefunction. Now with

$$a = l + 1 - \frac{1}{\sqrt{-2E}} = -n_r \tag{3.13}$$

and the definition $n = n_r + l + 1$ of the principal quantum number n we can write down for the energy eigenvalues

$$E = E_n = -\frac{1}{2(n_r + l + 1)} = -\frac{1}{2n^2}. \tag{3.14}$$

Switching from atomic units to the SI system we get

$$E_n = -\frac{m_e e^4}{8\epsilon^2 h^2 n^2} = -\frac{hcR_\infty}{n^2}. \tag{3.15}$$

This is the hydrogen Rydberg formula and it is equivalent to Equation 3.1. We see that the Rydberg constant can be expressed in physical constants.
For every E_n, n distinct eigen functions exist (for $l = 0, 1, ..., n-1$). The energy eigenvalues form a Rydberg series with regularly decreasing distance and the principal quantum number n of each consecutive series member increases by one. In the case of hydrogen, we have shown that n must be a positive integer.

The radial wavefunctions $u_{nl}(r)$ are given by

$$u_{nl}(r) = N_{nl}(2r/n)^{l+1} e^{r/n} F(-n + l + 1, 2l + 2, 2r/n) \tag{3.16}$$

with the normalization constant

$$N_{nl} = \frac{1}{n(2l+1)!}\sqrt{\frac{(n+l)!}{(n-l-1)!}} \tag{3.17}$$

Note that many text books (e.g. [132–135]) use a notation of equation 3.16 with Laguerre polynomials. The Laguerre polynomials can be defined in terms of hypergeometric functions, so both formulations are equivalent.

3.2.2 Quantum defect theory

In the last section we have deduced the hydrogenic Rydberg formula and wavefunctions. On the basis of these results we extend the model to many-electron atoms. In the following the physical meaning of the quantum defect d and the origin of the Rydberg formula will be explained, which are crucial for this thesis.
The quantum defect can be defined from a slight modification of the Rydberg formula. This will be a purely empiric introduction of d. However, it is also possible to introduce the quantum defect due to a modification of the Coulomb potential at small r, when the electron is close to the core of the atom. This semi-empirical approach will give insight into the physics behind the quantum defect. To do so, we need to consider the theory behind the quantum defect which is quantum defect theory (QDT). In order to not to go beyond the scope of this thesis

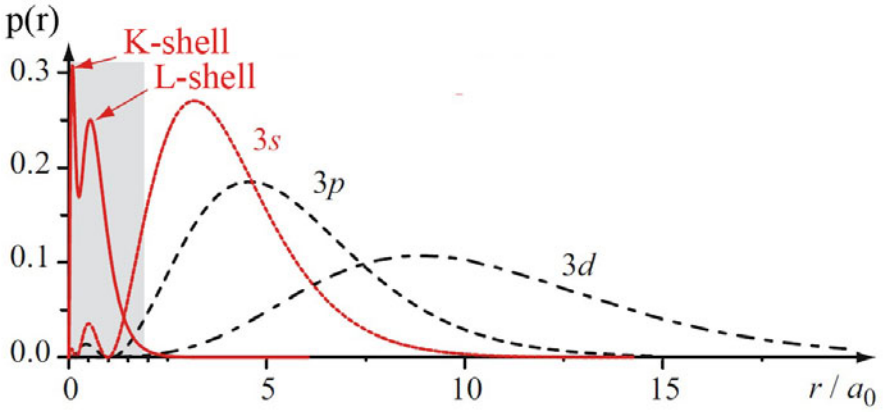

Figure 3.3: This plot shows the cumulative electron density (divided by 40) of the core (Na^+, $Z = 11$) electrons and the radial probability distribution $|R_{nl}(r)|^2$ of the valence electron of Na. The valence electron can penetrate the core. The figure is taken from reference [133].

(which deals only with alkali atoms) and the aim of this chapter, we restrict the discussion to single channel QDT. Single channel QDT is used for systems with a compact core and an outer electron which is excited independently from the other electrons. Single channel QDT leads to unperturbed Rydberg series and constant quantum defects. Such a system is represented for example by the alkali atoms. In QDT the Rydberg series as a whole together with the adjoining continuum are known as an *excitation channel*.
If an atom has more valence electrons, or if molecules are considered, many-body interactions are more important. Different excitation channels can be coupled to each other and thus the Rydberg series can be perturbed and auto-ionization of Rydberg states might occur. This is described by multi channel quantum defect theory (MQDT). An introduction in MQDT can be found in [122], detailed discussions of single channel QDT and MQDT can be found in references [136, 138, 139]. QDT has its origin in the 1950's and 1960's and was developed by M.J. Seaton, U. Fano. (see e.g [140, 141]) and later by C.H. Greene and C. Jungen [139, 142] to name some of the great pioneers of QDT.
The difference between the hydrogen atom and the effective one-electron system is the compact core. This causes a short-range potential experienced by the electron, which differs from the pure Coulomb potential at small distances r close to the core. Considering hydrogenic wavefunctions (see section 3.16), the electron has a certain probability to be found inside the core. The electron can penetrate the core which increases the attraction it experiences because the core electrons do not screen the nuclear charge fully. This is shown in Figure 3.3 where the cumulative electron density for the electron core is plotted together with the radial probability distribution $|R_{nl}(r)|^2$ for the Na atom.

Analytic approach to the quantum defect

A possible approach to account for the short range difference of the effective potential and the Coulomb potential is to introduce an effective potential which differs from the Coulomb potential at short range and goes over into a Coulomb potential at long range.
A special case of this approach will be to add a $\frac{\alpha}{r^2}$ dependent term to equation 3.3 (see [122]).

The long range potential will remain a Coulomb potential, since the additive term decreases rapidly with r. This gives the following effective potential

$$V(r) = -\frac{Ze^2}{4\pi\epsilon_0 r} + \frac{\hbar^2}{2m_e}\frac{\alpha}{r^2}, \tag{3.18}$$

where α is an adjustable parameter. The radial Schrödinger equation changes to

$$-\frac{\hbar^2}{2m_e}\frac{\partial^2 u_{nl'}}{\partial r^2} + \left(\frac{\hbar^2 l'(l'+1)}{2m_e r^2} - \frac{e^2}{4\pi\epsilon_0 r}\right) u_{nl'} = E_n u_{nl'}, \tag{3.19}$$

where $l'(l'+1) = l(l+1) + \alpha$. Now we introduce the quantum defect with $l' = l - d_l$. Using this definition of d_l, the energy eigenvalues which are obtained from equation 3.14 (now with l' instead of l) are

$$E_{nl} = -\frac{1}{2(n_r + l' + 1)} = -\frac{1}{2(n_r + l - d_l + 1)} = -\frac{1}{2(n - d_l)^2}. \tag{3.20}$$

From this elegant approach we learn two things about the quantum defect: (i) the quantum defect is a consequence of the non-Coulomb short range part of the effective potential, i.e. from the interaction of the electron and the core. (ii) The quantum defect depends on l, which is not surprising since the penetration of the electron into the core depends on the centrifugal barrier (due to the centrifugal potential $\frac{\hbar l(l+1))}{2m_e r^2}$), which depends on l. This is also evident from Figure 3.2. From this insight we can derive the ordering of the quantum defects:

$$d_s > d_p > d_d > d_f \cong 0 \ . \tag{3.21}$$

Single channel quantum defect theory

Quantum defect theory rests on the idea that the exchange and correlation interaction of a Rydberg electron and the compact core act over a relatively short range. At large distances, where the electron spends most of its time, the effective field is purely Coulombic. One therefore thinks of the scattering effect of the non-Coulomb core on the Coulomb wavefunctions. For large distances, the Coulomb wavefunctions are still solutions to this effective one-electron problem. We will show that as a result of the non-Coulomb potential the phases of the wave functions change with respect to the hydrogenic wave functions, where the phases are determined by matching to the inner wavefunctions at the core boundary. As already mentioned we restrict here to single channel QDT. A detailed discussion can be found for example in references [136, 138].

The quantum defect results from the short range part of the non-Coulombic effective potential. Thus we suppose that the core region, which is governed by complicated many-body interactions, is small and confined within a small radius r_0. Since r_0 is so small we are more concerned about the solution outside r_0 than inside. The potential in which the electron moves is spherically symmetric and thus the angular part of the solution to the Schrödinger equation 3.6 does not change.

We start the discussion by finding solutions to the Schrödinger equation for arbitrary energies. For the sake of convenience we use the "natural" units introduced by M.J. Seaton [138], which avoids the appearance of the reduced mass in the radial Schrödinger equation:

$$\epsilon = \frac{E - IT}{Ry}. \tag{3.22}$$

with

$$Ry = \frac{m}{m_e} R_\infty. \tag{3.23}$$

With these definitions the radial Schrödinger equation 3.6 can be rewritten

$$-\frac{\partial^2 u_{\epsilon l}}{\partial r^2} + \left(\frac{l(l+1)}{r^2} - \frac{2}{r}\right) u_{el} = \epsilon u_{el}. \tag{3.24}$$

For the hydrogen atom, we were looking for solutions which vanish at the origin because of the (i) ($\Psi \to 0$ for $r \to 0$) boundary condition. The solutions we found were the so called regular Coulomb functions $f_l(\epsilon, r) \propto r^{l+1}$ for $r \to 0$. Now we lose this boundary condition because we exclude the region $r < r_0$ for our solutions. Consequently we must consider the so-called irregular Coulomb function $g_l(\epsilon, r)$, which diverges as $r \to 0$, as a solution of equation 3.24. The open channel solutions ($E > IT$), which are solutions with positive energy, oscillate towards the asymptotic limit $r \to \infty$ [136, 138]:

$$\begin{aligned} f_l(\epsilon, r) &\sim \tfrac{1}{\pi k} \sin\left[kr + k^{-1} \ln 2kr - l\pi/2 + \eta_l(E)\right] \\ g_l(\epsilon, r) &\sim -\tfrac{1}{\pi k} \cos\left[kr + k^{-1} \ln 2kr - l\pi/2 + \eta_l(E)\right] \end{aligned} \tag{3.25}$$

where $k = \sqrt{(E - IT)/Ry}$ and η, the so called Coulomb phase is given by

$$\eta_l(E) = \arg\Gamma(l + 1 - i/k). \tag{3.26}$$

We are interested in solutions for bound states, where $E < IT$. Therefore we introduce the effective quantum number n^*, which is defined by $\epsilon = \frac{E-IT}{Ry} = -1/n^{*2}$. For $n^* > l + 1$ we can express the Coulomb wavefunctions in the following standard form [136, 138]:

$$\begin{aligned} f_l(\epsilon, r) &= \sin\beta_l(E) F^+(\epsilon, l, r) - \cos\beta_l(E) F^-(\epsilon, l, r) \\ g_l(\epsilon, r) &= -\cos\beta_l(E) F^+(\epsilon, l, r) - \sin\beta_l(E) F^-(\epsilon, l, r) \end{aligned} \tag{3.27}$$

where

$$\beta_l(E) = [n^*(E) - l]\pi = \left[\sqrt{Ry/(IT - E)} - l\right]\pi. \tag{3.28}$$

The functions $F^+(\epsilon, l, r)$ and $F^-(\epsilon, l, r)$ differ in the asymptotic behavior where $F^+(\epsilon, l, r)$ increases and $F^-(\epsilon, l, r)$ decreases for $r \to \infty$ (see [138] p. 183, note that Seaton uses the symbols $s_l(\epsilon, r)$ and $-c_l(\epsilon, r)$ instead of $f_l(\epsilon, r)$ and $g_l(\epsilon, r)$ used by Fano [141], Greene [142] and in the book of Child [136]). The $F^+(\epsilon, l, r)$, which is contained in $f_l(\epsilon, r)$ and $g_l(\epsilon, r)$ diverges asymptotically. Thus for a normalizable solution, the coefficients of $F^+(\epsilon, l, r)$ must vanish. From equation 3.27 and 3.28 it is evident that this is the case for
integer ($\sin\beta_l$) and half-odd integer ($\cos\beta_l$) values of $n^* - l$.

In general, the outer part of the wavefunction is a linear combination of $f_l(\epsilon, r)$ and $g_l(\epsilon, r)$, which depends on the strength of the influence of the non-Coulomb core. Important is that bound states occur at energies where the coefficients of the divergent terms cancel. Considering the electron as an classical particle which moves on elliptical Bohr-Sommerfeld orbits (e.g. see [143] p. 122 ff), according to the second Kepler law the electron's speed is highest close to the inner turning point (close to the core). If it experiences a higher nuclear charge Z in the core region, its speed (or impulse, or kinetic energy) will be higher than in the pure Coulomb

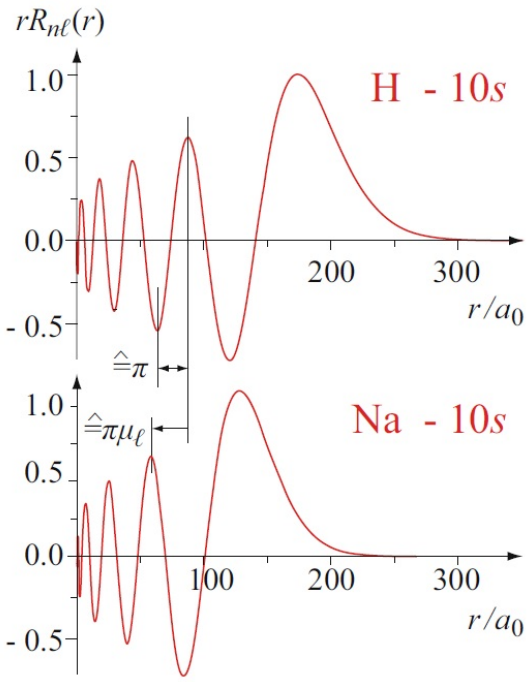

Figure 3.4: This plot shows the radial wavefunction rR_{nl} of the 10s hydrogen orbital and the 10s Na orbital. The phase shift $\pi\mu_l = d_l$, which corresponds to the quantum defect is depicted. The figure is taken from reference [133].

field with $Z = 1$. Quantum-mechanically this corresponds to a reduction of the de Broglie wavelength ($\lambda_{dB} = h/mv$) in the core region ($r < r_0$), thereby causing a phase change in the outer region ($r > r_0$) compared with the corresponding hydrogenic wavefunction. This phase change corresponds to the quantum defect d_l. This is shown in Figure 3.4 where the phase shift $\pi\mu_l = d_l$ between the hydrogen 10S wavefunction and a Na 10S wave function is depicted.

For $r > r_0$ the solution of the radial Schrödinger equation 3.24 can be expressed as a phase shifted linear combination of the regular and irregular Coulomb functions:

$$u_l(\epsilon, r) = \cos \pi d_l f_l(\epsilon, r) - \sin \pi d_l g_l(\epsilon, r). \tag{3.29}$$

With equation 3.25 it follows that

$$u_l(\epsilon, r) \sim \sin\left[\beta_l(\epsilon) + \pi d_l\right] F_l^+(\epsilon, r) - \cos\left[\beta_l(\epsilon) + \pi d_l(\epsilon)\right] F_l^-(\epsilon, r). \tag{3.30}$$

Again we have to eliminate the coefficients of the exponential divergent terms with equation 3.28, which leads to the quantization condition

$$\beta_l(E) + \pi d_l = \left[\sqrt{Ry/(IT - E)} - l + d_l\right] \pi = [n - l]\,\pi. \tag{3.31}$$

which can be easily converted to

$$E_{nl} = IT - \frac{Ry}{(n - d_l)^2}. \tag{3.32}$$

This is the Rydberg formula, deduced from quantum defect theory.

We see that QDT tells us about the physical meaning of the quantum defect, where d corresponds to a phase shift of the outer part of the radial wavefunction compared to the hydrogenic wavefunction. Thus the quantum defect provides a measure of the differences between energy levels of many-electron atoms and energy levels of hydrogenic systems. The quantum defect parameter accounts for all interactions and many-body effects which take place in the core. This means that the complex interactions in the core region can be expressed by just one parameter. Here we assumed that d is constant for a given orbital angular momentum l, i.e. a Rydberg series. In fact d depends slightly on n for lower states and is nearly constant for higher n (see section 3.4). Another important finding is that in a Rydberg series, the effective quantum number n^* differs (nearly) by integer values for different series members because of $n^* = n - d$ and the (nearly) constant quantum defect. The fact that outside the core the wavefunction remains a phase shifted hydrogen wavefunction shows that many properties of Rydberg atoms can be derived from Coulomb wavefunctions.

3.3 Properties of Rydberg atoms

In this section some of the extraordinary properties of Rydberg atoms are discussed. Note that as far as results which are derived from the properties of Coulomb wavefunctions are concerned, n can be substituted by n^* and vise versa.

Important for many properties of Rydberg atoms is the normalization of the Coulomb wavefunctions. Remember: normalization means to ensure that the integral over the entire space of the square of the wavefunction must be unity (the electron must be *somewhere* in space). It can be shown (e.g. ref. [136]) that (using equation 3.28)

$$\int_0^\infty \Psi_{nl}^2(r)dr = \frac{1}{\pi}\left(\frac{d\beta}{d\epsilon}\right) = \left(\frac{dn^*}{d\epsilon}\right) = \frac{n^{*3}}{2Ry} \tag{3.33}$$

This means that the normalization constant decreases as $n^{*-3/2}$, which carries important consequences for scaling properties of Rydberg states.

3.3.1 The size of Rydberg atoms

One property of Rydberg states with high n is that they are very large. The production of atoms with a radius in the micrometer range is possible, which makes them macroscopic objects. Such macroscopic atom sizes have been observed experimentally by measuring the transmission of a Rydberg atom beam through micrometer size slits [144].

The size of a Rydberg atom is defined by the expectation value $\langle r\rangle$ of the radius. From the solution $u_{nl}(r)$ the radial expectation value of the electron's orbit can be calculated analytically by

$$\langle r\rangle_{nl} = N_{nl}^2\left(\frac{n}{2}\right)^2 \int_0^\infty dx x^{2l+3}e^{-x}F^2(-n+l+1, 2l+2, x) \tag{3.34}$$

which gives

$$\langle r\rangle_{nl} = \frac{1}{2}\left[3n^2 - l(l+1)\right], \tag{3.35}$$

Table 3.1: Lifetime parameters for Rb and Cs atoms (from ref. [120]).

		s	p	d	f
Rb	τ_0 (ns)	1.43	2.76	2.09	0.76
	α	2.94	3.02	2.85	2.95
Cs	τ_0 (ns)	1.43	4.42	0.96	0.69
	α	2.96	2.94	2.93	2.94

in units of the Bohr radius a_0 ($a_0 = 0.529177\,\text{Å}$), since this is the length unit in the atomic unit system. The orbital radius and thus the size of a Rydberg atom increases rapidly for Rydberg states because it scales with the square of the principal quantum number $\sim n^2$. This is the reason why Rydberg atoms are so large. For example, an atom with $l = 0$ has an orbital radius of $r = 0.1\,\text{nm}$ for $n = 2$. For $n = 10$ the expectation value is $r = 2.65\,\text{nm}$ and for $n = 200$ it increases to $r = 1.06\,\mu\text{m}$.

3.3.2 Lifetimes of Rydberg atoms

High Rydberg states have very long radiative lifetimes τ_{nl}, which can be on the order of several 100 μs and higher. Lifetimes are related to transition probabilities (the inverse of the Einstein coefficient A). Thus they are related to the inverse of the square of the radial transition-matrix element $|\langle i|r|f\rangle|^2$ between the lower state $|i\rangle$ and the Rydberg state $|f\rangle$. Only the part of the Rydberg wavefunction which spatially overlaps with the lower state wavefunction contributes to the radial matrix element. The Rydberg wavefunction scales as $n^{*-3/2}$ (equation 3.33) and thus the lifetime (for high n) scales as

$$\tau_{nl} \propto n^{*3}. \tag{3.36}$$

In Table 3.1, experimentally measured parameters for the lifetime scaling law for Rb and Cs according to the more general formulation

$$\tau = \tau_0 n^{*\alpha} \tag{3.37}$$

are given (from ref. [120]), where the parameter $\alpha \approx 3$. More recent experimentally measured lifetimes can be found in ref. [145]. Therein, for example, the lifetime of the Rb $45^2\text{S}_{1/2}$ state is given with $\tau = 50\,\mu\text{s}$.

3.3.3 Classical turning points

Classically the electron is thought to move on elliptical trajectories [143], where the core is located at one of the foci. An elliptical orbit has an inner turning point and an outer turning point, the apoapsis and the periapsis, respectively. The turning points separate the classically forbidden and classically allowed regions, where in the allowed region u_{nl} is oscillating and in the forbidden region it is evanescent. The classical turning point is located at distance r at which the total potential energy (the sum of the Coulomb and centrifugal potential) is equal to the bound-state energy (compare to equation 3.9 and 3.14, in atomic units):

$$\frac{l(l+1)}{2r^2} + V(r) = E_n \qquad \Rightarrow \qquad \frac{l(l+1)}{2r^2} - \frac{1}{r} = -\frac{1}{2n^2}. \tag{3.38}$$

This equation can be transformed to the quadratic equation

$$r^2 - 2rn^2 + l(l+1)n^2 = 0 \tag{3.39}$$

where the two solutions can be associated with the inner r_i and outer turning point r_o

$$\begin{aligned} r_i &= n^2 - n\sqrt{n^2 - l(l+1)} \\ r_o &= n^2 + n\sqrt{n^2 - l(l+1)}. \end{aligned} \tag{3.40}$$

These are the turning points for the electron of the hydrogen atom in atomic units. To convert this into SI units, r_i and r_o have to be multiplied with the Bohr radius a_0. The formulas for the turning points, especially the inner turning point, can only be applied with some reservations to atoms with a confined core. The inner turning point for small l is located close or inside the core of the atom (or molecule), hence in this case the equation is no longer valid, but can probably give a rough estimation. From this equation it can be shown that for high n the inner turning point converges to a certain value, which depends on l. This is related to the fact, that the centrifugal potential is very steep and does not change much with energy.

3.3.4 Core penetrating and core non-penetrating Rydberg states

The valence electron of a many-electron atom can penetrate the confined core. If l is low, which goes along with a small r_i, the electron has a certain probability to be found inside the core. In contrast, if l is high, the electron does not penetrate the core. Note that in the case of $l = n - 1$ the classical elliptical orbit turns into a circular orbit. The case where the electron does not penetrate the core is called a *core non-penetrating* state and the other case is referred to as *core penetrating* state. Penetrating states are characterized by a high quantum defect (interactions inside the core). In contrast, the quantum defect of core non-penetrating is very low (close to zero). For example, the lowest l core non-penetrating states in the cesium atom are the nF states. In the sodium atom, also the nD states are non-penetrating [146]. Table 3.2 shows an example for inner turning points r_i, outer turning points r_o and radial expectation values $\langle r \rangle$ for various n and l in [Å]. It can be seen that at higher n, r_i is nearly constant for a fixed l.

3.4 The Rydberg-Ritz formula

The Rydberg formula discussed in the previous section assumes a constant quantum defect. In fact the quantum defect depends slightly on n and is only nearly constant. In effective one-electron systems, like in that of alkali atoms, the variation of the quantum defect is highest at low n and converges to an asymptotic value for high n. Hence, the easiest way to obtain the quantum defect therefore would be to exclude the lowest members of a Rydberg series from a fit of the measured energy levels to the Rydberg formula. However, since the lower series members include important information, an approach which accounts for the deviation of lower members would be preferable. This is accounted for with the Rydberg-Ritz formula, which is valid for unperturbed Rydberg series. The Rydberg-Ritz formula was introduced by

Table 3.2: Examples for the inner turning points r_i, outer turning points r_o and radial expectation values $\langle r \rangle$ for the hydrogen atom. The values are given in [Å] for $n = 5, 10$, and 25.

$n = 5$				
	s	p	d	f
r_i	0	0.54	1.70	3.69
$\langle r \rangle$	19.8	19.3	18.3	16.7
r_o	26.5	25.9	24.8	22.8
$n = 10$				
	s	p	d	f
r_i	0	0.53	1.61	3.28
$\langle r \rangle$	79.4	78.8	77.8	76.2
r_o	105.8	105	104.2	102.6
$n = 25$				
	s	p	d	f
r_i	0	0.53	1.59	3.19
$\langle r \rangle$	496	496	495	492
r_o	662	661	660	658

Walter Ritz in 1903 in his inaugural Dissertation (see [147] p. 290). The formula can also be derived by quantum mechanics [148, 149]. The Rydberg-Ritz formula has the form

$$E_n = IT - \frac{Ry}{(n - d_l(n))^2} \tag{3.41}$$

where d_l is a function of n. It was pointed out by Martin [150], who proposed series formula for the spectrum of sodium atoms, that the following form of the quantum defect $d_l(n)$ is of most practical interest

$$d_l(n) = a + \frac{b}{(n-a)^2} + \frac{c}{(n-a)^4} + \frac{d}{(n-a)^6} + \frac{e}{(n-a)^8} + \ldots \ . \tag{3.42}$$

The Rydberg-Ritz formula with this expression of the quantum defect is known as the modified Rydberg-Ritz formula. The constants $a, b, c, d, e, \ldots$ are the modified Rydberg-Ritz coefficients and a is the asymptotic quantum defect d_l. A compilation of modified Rydberg-Ritz coefficients for alkali atoms can be found in reference [151]. The lowest Rydberg series members determine the Rydberg-Ritz coefficients $b - e$, while the asymptotic value $a = d_l$ is determined by higher series members. A fit of recorded energy levels to the Rydberg-Ritz formula, e.g. with a least squares fit procedure, gives the ionization threshold, the asymptotic quantum defect and the Rydberg-Ritz coefficients. The order of the terms in the modified Rydberg-Ritz formula which should be used in a fit routine depends on the amount of data points and the accuracy of the measured transitions. For energy levels of Rydberg states obtained with high resolution spectroscopy it is useful to use coefficients up to d or e [151]. For low resolution spectra, e.g. atoms on helium droplets, it is sufficient to use the second order coefficient b. Different Rydberg-Ritz formula fit routines are discussed in ref. [152].

Figure 3.5 shows the quantum defects of the atomic cesium $n^2S_{1/2}$, $n^2P_{1/2,3/2}$, $n^2D_{3/2,5/2}$ and $n^2F_{5/2,7/2}$ states. Closer inspection of the Figure reveals differences between the lowest members of core-penetrating and core non-penetrating series [153, 154]. The $n^2S_{1/2}$ and $n^2P_{1/2,3/2}$ quantum defects (Figure 3.5 panel (a)) follow smooth, asymptotically decreasing curves. This is characteristic behavior of series for which the penetration of the valence electron into the core is the primary contributor to the quantum defect. The quantum defect settles down at about $n = 10$ to the asymptotic value a where it remains constant. In contrast, the $n^2F_{5/2,7/2}$ (and also $n^2G_{7/2,9/2}$, see [153]) quantum defects show a smooth asymptotical increase with n (Figure 3.5 lowest panel). This is characteristic for states where the shift of the energy levels E_{nl}, compared to hydrogen energy levels E_n, is dominated by the polarization of the core in the field of the non-penetrating valence electron. This effect causes a decrease of the energy levels at low n and can be accounted for with an additive term in the hydrogen Rydberg formula (Equation 3.14) [120]

$$E_{n,l} = -\frac{1}{2n^2} - \frac{d_l}{n^3}. \tag{3.43}$$

The term exhibits an n^{-3} scaling (which is related to the normalization of the radial wavefunction). The quantum defect for non-penetrating high l states is proportional to l^{-5} and can be calculated with [120]

$$d_l \cong \frac{3\alpha_d}{4l^5}, \tag{3.44}$$

where α_d is the dipole polarizability of the ionic core.

The lower $n^2D_{3/2,5/2}$ states in the cesium atom exhibit an unusual behavior. The quantum defect increases rapidly from $n = 6$ to 7. Weber and Sansonetti reported [153] that closer inspection of high resolution spectroscopy data reveal that the quantum defect reaches a maximum at $n = 10$ and slightly decreases asymptotically for $n > 10$. They attribute this unusual behavior to a result from the competition between polarization and penetration effects [155].

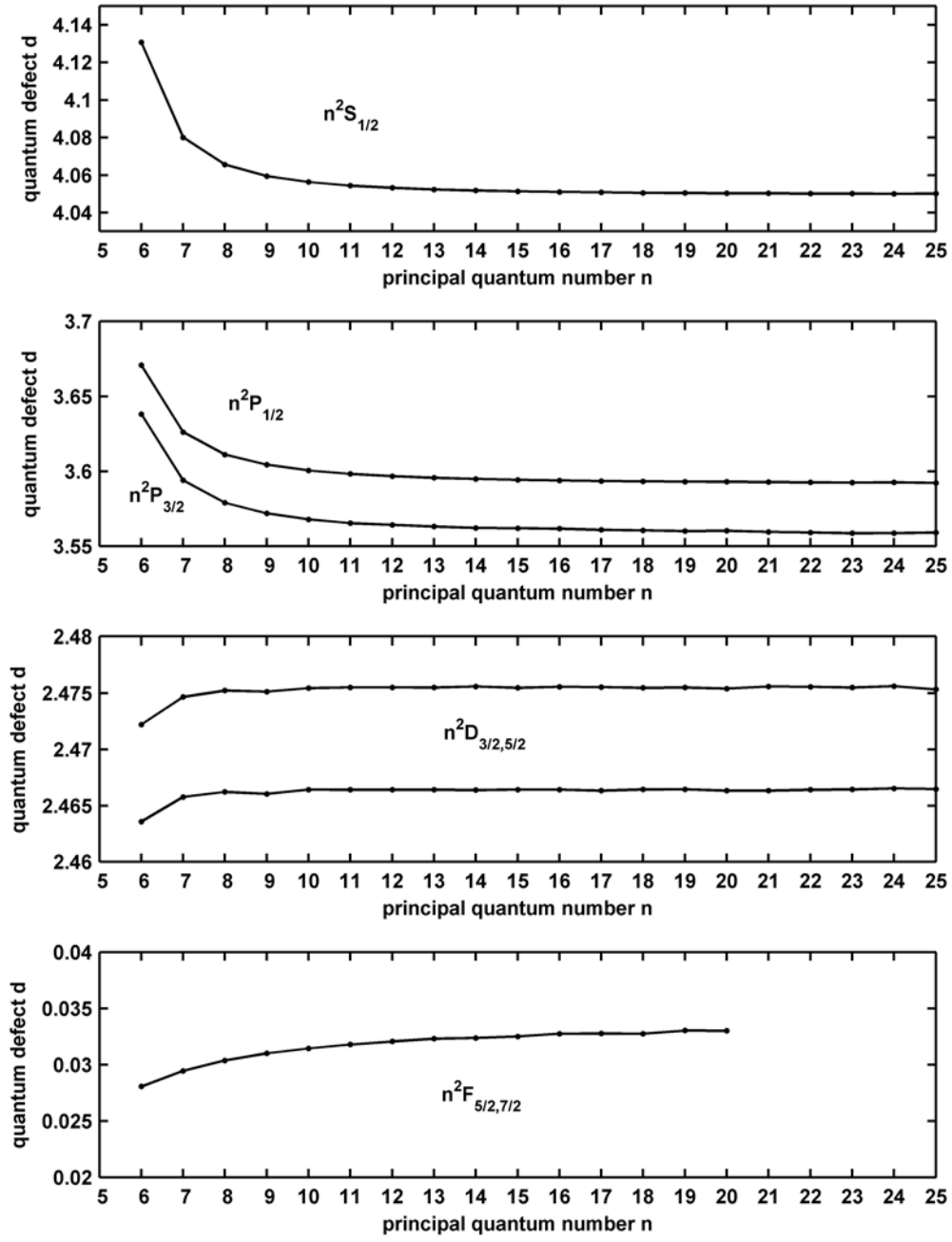

Figure 3.5: Quantum defects of Cs $n^2S_{1/2}$ (upper panel), $n^2P_{1/2,3/2}$ (upper middle panel), $n^2D_{3/2,5/2}$ (lower middle panel) and $n^2F_{5/2,7/2}$ (lower panel) states. Calculated from energy levels given in reference [153].

3.5 Rydberg molecules

As remarked earlier, the Rydberg concept does by no means exclusively apply for atoms, it also finds application in molecules. Rydberg molecules and Rydberg atoms are similar in many ways [122, 156, 157]. In principle, any assembly consisting of an electron and a positive charged core can exhibit stable Rydberg states as long as (i) the electron's wavefunction can spread into free space and (ii) the singly ionized assembly is stable [122]. Note that these conditions are also fulfilled by Ak atoms on helium nanodroplets: (i) for sufficiently high states the overlap between the droplet and the electron's wavefunction (depending on the orientation of the orbital) is very small. In addition, (ii) it is known that the Ak^+–He_N complex is stable.

For molecular spectroscopy, two different classes of excited states are distinguished. States with orbital sizes comparable to the internuclear distance are referred to as "valence states". In molecular "Rydberg states" the orbital sizes are large compared to the internuclear distance. The core of the molecule consists of several atoms and differs from the hydrogenic core. This causes, similar to many electron atoms, a difference to the Coulomb field. For diatomic molecules AB a Rydberg state is in general characterized by $(AB^+)nl\lambda$. Hence the concept of the quantum defect and Rydberg series does also apply to molecules, but their spectra are much more complicated.

In diatomic molecules it is possible that expected molecular orbitals of low members of a Rydberg series (valence orbitals), where much electron density is between the two atoms, are anti-bonding orbitals. If n increases and becomes larger than the interatomic separation, the character of the orbital changes into a binding orbital. This is related to a phenomen known as "Rydbergization" of valence orbitals [158] which describes the smooth change from valence to Rydberg character of an orbital as a function of the internuclear distance. This phenomen explains the absence of stable lower members of molecular Rydberg series.

A similar scenario could be the Rydbergization of an Ak–He_N complex which is excited into a high Rydberg states. This Rydbergization process would correspond to the transition from desorbing Rydberg states to bound Rydberg states and the formation of a Sekatskii-atom (see Section 7.4), where the electron density between Ak atom and droplet decreases with n.

Chapter 4

Alkali Atoms on He Nanodroplets

In this chapter the properties of alkali atoms, especially Rb and Cs, on the surface of helium nanodroplets are discussed. The results obtained for the Rb $5^2P_{1/2,3/2} \leftarrow 5^2S_{1/2}$ and Cs $6^2P_{1/2,3/2} \leftarrow 6^2S_{1/2}$ transitions on the droplet are presented. The non-desorption of Rb and Cs atoms upon excitation of the D1 transition is essential for the development of the two-step excitation scheme, which is used in this work for the excitation of Rydberg states. This chapter includes the detailed discussion of the two-step excitation scheme, which is included in reference [8]. This chapter is also related to ref. [4], in which we showed the non-desorption of Cs atoms from the droplet upon excitation of the D1 transition, and to ref. [2] in which the feasibility of a two-step excitation scheme was demonstrated on the example of the Rb $5^2D_{3/2} \leftarrow 5^2P_{1/2}$ transition.

4.1 Introduction

The $n^2P_{1/2,3/2} \leftarrow n^2S_{1/2}$ transitions of alkali (Ak) atoms on He_N (the D1 and D2 line) are well known since the early days of helium nanodroplet isolation spectroscopy and belong to the best investigated electronic transitions in doped He_N. The first spectroscopic results on the D lines of the alkali metals Li, Na and K, on helium droplets were presented in 1996 [159]. Experimental results for Rb and Cs were published later, in 2001 [160] and in 2004 [101], respectively. An overview of the alkali metal D lines is given in reference [89].

Ak atoms on He_N have the advantage of a relatively simple electronic structure and the accessibility of excited states with lasers in the visible spectrum. Low pickup temperatures are sufficient to reach the necessary vapor pressures, which simplifies the doping process. The first excited P states of the Ak-He_N systems have been studied in detail experimentally as well as theoretically. In contrast, much less research has been done on higher excited states and Rydberg states of the Ak-He_N systems. Very recently, in 2010, the first results on higher excited states were published [161], where parts of the data where acquired with our droplet beam apparatus and lasers [117, 162]. Since that time, the field attracts increasing attention and several groups are currently working on this topic. This thesis includes the first results on Rydberg states and Rydberg series of the Rb-He_N and Cs-He_N systems. Currently spectroscopic data of higher excited and Rydberg states (beyond the D lines) of the following alkali atoms are available: Li [163], Na [164, 165], K [161], Rb [2, 161, 166] and Cs[6, 161]. So far, only the Na, Rb, and Cs spectra on He_N were recorded completely. The most frequently

used method to record excitation spectra is multi-photon ionization spectroscopy and, for lower Rydberg states, laser induced fluorescence spectroscopy. All excited states investigated so far are known to be broadened and shifted with respect to bare atom states. Individual Rydberg states of Ak–He_N systems can be followed up to principal quantum numbers $n \approx 20$. At higher states the observed transitions start to overlap and the excitation spectrum forms a continuum. This will be discussed in more detail in the next chapters. In the following the properties of alkali atoms on helium droplets, especially those of the heavy alkali atoms Rb and Cs, which are important for the two-step excitation of Rydberg states in this thesis are presented.

Surface location of alkali atoms on helium droplets

As already mentioned, alkali atoms reside on the surface of He_N. The location of an impurity inside (solvated state) our outside (surface state) the helium droplet is determined by the interplay of the energy, which is gained by the bond between the helium and the solvent and the energy, which is needed for the creation of a bubble. The bubble formation costs energy because the helium must be evacuated around the impurity in order to accommodate the solvent inside the droplet. If it is energetically favorable to stay on the surface, the foreign atom or molecule will not submerge into the helium droplet. The energy cost for the bubble creation depends on the surface tension σ and the density ρ of the liquid helium (see e.g. [167]). The interaction energy which is gained upon the bond formation between the impurity and a helium atom depends on the pair potential, which is characterized by the potential well depth ϵ and equilibrium separation r_{min}. Ancilotto *et al.* proposed a dimensionless parameter λ [88], which can be calculated from these four quantities. The parameter λ provides a measure of the relative energy gain and hence indicates the surface location or the solvation of the impurity:

$$\lambda = \rho \epsilon r_{min}/(\sigma 2^{1/6}). \tag{4.1}$$

The impurity is located on the surface if $\lambda < 1.9$. Alkali atoms and helium atoms interact only very weakly and therefore ϵ is very small. Hence the energy gain upon submersion would be very small and the surface state is energetically favorable for the alkalis. For example, the parameter λ for Rb is $\lambda = 0.729$ and for Cs $\lambda = 0.659$ (from ref. [88]). Besides the alkali atoms, the only known species which are at (or near) the surface are the alkaline-earth metals [168, 169]. Surface atoms reside in a shallow, "dimple"-like deformation of the helium surface [75]. The form of the dimple depends on the impurity species. The dimple is deeper for alkaline-earth metals than for alkali metals (e.g. see ref. [89], Fig. 3).

4.1.1 The pseudo-diatomic model

The pseudo-diatomic model (PDM) [159, 161] for surface state atoms is a well established model for the assignment and calculation of excited states of atoms on the surface of helium droplets. In the course of this thesis it is used to assign the recorded transitions. It turned out that the PDM is suitable to assign Rydberg states, as long as they appear as individual transitions. Higher Rydberg states ($\approx n > 12$) start to overlap and an assignment within the PDM is no longer appropriate.

In the PDM the helium atom is treated as one atom in a diatomic molecule. The molecular axis in this diatomic-like molecule is defined by the connection between the center of the

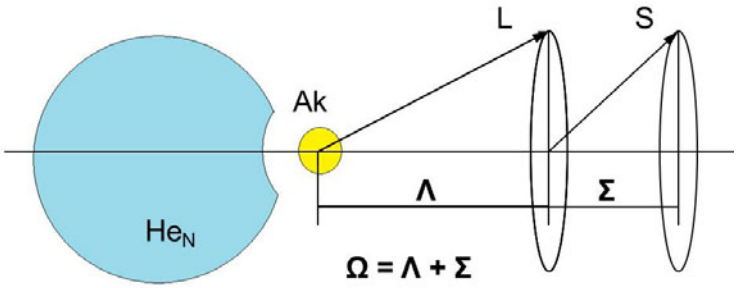

Figure 4.1: Hunds case (a) coupling scheme in the pseudo diatomic model for alkali atoms on helium droplets.

droplet and the nucleus of the alkali atom. This is shown schematically in Figure 4.1 where the position of the Ak atom, the helium droplet and the molecular axis are depicted. The molecular axis defines a quantization axis for the orbital angular momentum L and the Spin S of the atom. Since the helium atoms have a closed shell, the only electron which has to be considered in this diatomic system is the alkali valence electron. Due to the lower symmetry of the Ak–He_N system, L is no longer a conserved quantity. In contrast, the projection Λ of L onto the molecular axis is conserved. The Hunds case (a) coupling scheme is suitable to describe the observed transitions in Rb–He_N and Cs–He_N. The notation in Hunds case (a) is: ${}^{(2S+1)}\Lambda_\Omega$ (see e.g. [170]). S is the spin of the atom ($S = 1/2$ for alkali atoms) and $(2S + 1)$ is the multiplicity, which is 2 for one electron systems. Ω is defined by $\Omega = |\Lambda + \Sigma|$, where Σ is the projection of the spin onto the molecular axis. For alkali atoms $\Sigma = \pm S = \pm 1/2$. For example, the Rb $5^2P_{1/2}$ and $5^2P_{3/2}$ atomic states will split into the ${}^2\Pi_{1/2}$, ${}^2\Pi_{3/2}$ and ${}^2\Sigma_{1/2}$ diatomic substates. The splitting can be seen in Figure 4.2 for the case of Rb–He_N. To assign the excited states unambiguously, the diatomic states are denoted in brackets after the atomic state (in the notation ${}^{(2S+1)}L_J$ of the LS coupling scheme) from which they are arising (e.g. $5^2P_{1/2}$ (${}^2\Pi_{1/2}$)). For higher states, where spin-orbit splitting could not be resolved Ω is neglected.

In the course of this thesis it will be shown that the diatomic electronic selection rules $\Delta\Lambda = 0, \pm 1$ apply for transitions in Rb–He_N and Cs–He_N. According to the diatomic selection rules, it is expected to observe transitions on the droplet, which are forbidden in the free atom. It will be shown in this thesis, that such transitions are experimentally observed, for example the transitions from the nS ground state into the lowest $(n-1)$D states, or the transitions from the nP(Π) state into higher $(n+k)$P(Π, Σ) states.

4.2 The D1 and D2 lines of alkali atoms on helium nanodroplets

The $n^2P_{1/2,3/2} \leftarrow n^2S_{1/2}$ transitions in the alkali atoms are historically known as D1 and D2 transitions. If an alkali atom approaches the surface of a helium droplet, according to the PDM splitting into molecular substates is expected because of the lifting of the spherical symmetry of the atom. This is shown in Figure 4.2 on the example of Rb-He_N potential energy curves (from ref. [91]) for the ground state and the first excited P states. The closer the atom

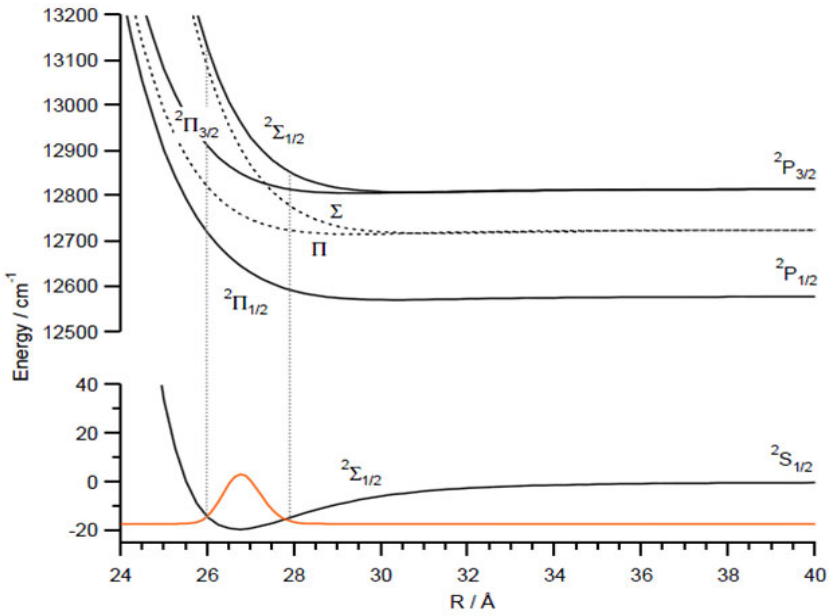

Figure 4.2: Rb-He_N potential energy curves with spin-orbit coupling (solid lines, Hund's case (a)) and without spin-orbit coupling (dashed lines). The nuclear wavefunction of the lowest vibronic level of the ground state is shown in red. (from ref. [91])

is to the surface, the stronger is the (repulsive) interaction and the splitting of the substates arises. In the $5^2S_{1/2}(^2\Sigma_{1/2})$ ground state, the atom is bound to the surface of the droplet at the equilibrium distance. It resides about 3-5 Å above the surface in a dimple (dimple depth according to ref. [88] Tab. 3 $\approx$ 2 Å). According to the Franck-Condon principle, the atom is most probably excited into the repulsive part of the potential. This is the explanation for the broad and shifted transitions. The repulsive interaction is caused by the Pauli-repulsion between the electron and the helium. An intuitive explanation for the steep $5^2P_{1/2}(^2\Sigma_{1/2})$ potential, which exhibits the strongest blue shift of the three P-substates, is shown schematically in Figure 4.3. In the case of the $5^2P_{3/2}(^2\Sigma_{1/2})$ state, the atomic P orbital is oriented to the droplet surface so that one lobe points towards the droplet (right panel). Since the repulsive part is caused by the short-range electron-helium interaction, the increased electron density between the droplet and the atom upon excitation results in a steeper interaction potential in the Franck-Condon region. In contrast the P orbitals of the two Π states are oriented parallel to the droplet surface (left panel). Also important for the number of observed components in the spectrum is the strength of the spin-orbit interaction. The spin-orbit splitting between the $n^2P_{1/2}$ and $n^2P_{3/2}$ states increases with the atomic number of the atom from Li to Cs. The excitation spectrum of the Li-He_N shows only one broad structure, because the droplet induced line broadening is larger than the spin-orbit splitting. In contrast, the heavy alkali atoms Rb and Cs have a well separated spin-orbit structure. This can be seen in Figure 4.5 where the LIF and BD excitation spectrum of the D1 and D2 transitions, as well as the two-step excitation efficiency (see Section 4.3) for Rb–He_N and Cs–He_N are shown (Rb–He_N LIF and BD data are taken from ref. [91]). In both panels of this Figure, the wavenumber scale

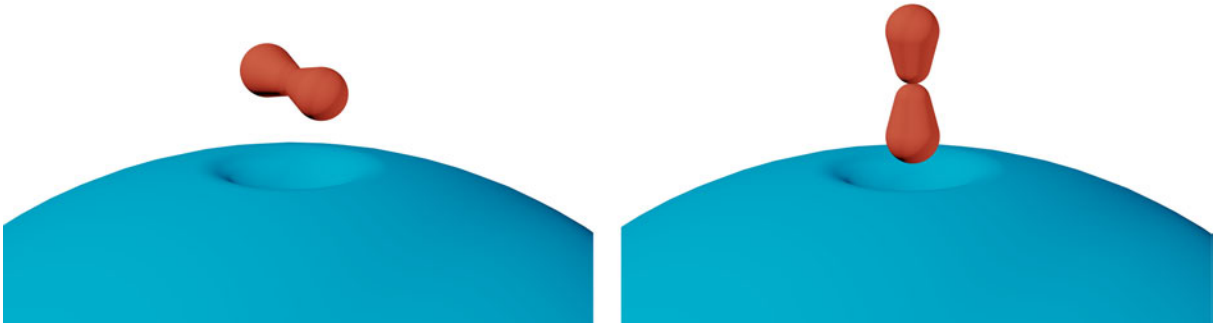

Figure 4.3: Schematic drawing of the spacial orientation of P orbitals to the droplet surface. The orbitals of the two Π states are orientated parallel to the droplet surface (left panel). For the P orbital of the Σ states, one lobe points towards the droplet (right panel).

is the same and the $n^2P_{1/2}$ atomic lines are at the same position. Besides the well resolved spin-orbit splitting, three molecular substates can be identified, which are the $^2\Pi_{1/2}$, $^2\Pi_{3/2}$ and $^2\Sigma_{1/2}$ diatomic substates, in agreement with the PDM. The $^2\Sigma_{1/2}$ state appears as a broad shoulder in the $^2\Pi_{3/2}$ state. The reason for the absence of a pronounced $^2\Pi_{3/2}$ state in the spectrum of Cs–He_N is related to the exciplex formation process upon excitation which is explained in the following.

Exciplex formation

Exciplexes are excited Ak* atoms with several helium atoms attached to it. Excitation into the $^2\Pi_{3/2}$ state causes the desorption of atoms and exciplexes from the surface. Exciplex formation depends on the orientation of the atomic orbital to the helium droplet (Λ) of the excited state [160, 171–173]. This is shown schematically in Figure 4.3, where the different spacial orientations of the P orbital are depicted. In case of a P(Π) state (left panel), where the molecular orbital is oriented parallel to the surface, the helium atoms can be accommodated around the waste of the orbital. In contrast, in the case of the P(Σ) state (right panel), one lobe of the molecular orbital points straight into the helium and the probability of exciplex formation is decreased. This picture is in agreement with TOF mass spectroscopic measurements. Figure 4.4 shows a TOF mass spectrum obtained by ionizing Cs atoms on the droplets via the Cs-He_N $6^2P_{1/2}$ ($^2\Pi_{1/2}$), $6^2P_{3/2}$ ($^2\Pi_{3/2}$) and $6^2P_{3/2}$ ($^2\Sigma_{1/2}$) intermediate states at $\tilde{\nu_1} = 11197\,\mathrm{cm}^{-1}$, $\tilde{\nu_2} = 11745\,\mathrm{cm}^{-1}$ and $\tilde{\nu_3} = 11835\,\mathrm{cm}^{-1}$, respectively. In this experiment, the fundamental output of the Indigo-S laser was used for the first excitation step. The fundamental laser was spatially overlapped with the SHG output of the Indigo-S laser, which provided the ionizing photon. The low pulse-energy (50 μJ) of the SHG is the reason for relatively low signal. The signal was recorded for droplets of size $\hat{N}_{30,15} = 6200$. The 133 amu signal is scaled to unity. This allows to compare the formation probability of exciplexes for the three different cases. The Figure shows that the formation of Cs*-He is about 5 times higher if the ionization path includes the $^2\Pi_{3/2}$ state than compared to an ionization via the $^2\Sigma_{1/2}$ state. Also a small amount of Cs*-He_2 exciplexes is observed, where this signal is higher for the $^2\Pi_{3/2}$ state. We found the same behavior for Rb–He_N, which was published in ref. [1]. The absence of a

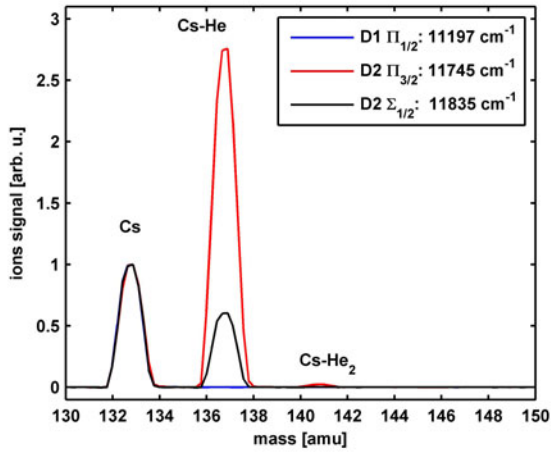

Figure 4.4: TOF mass spectrum obtained by ionizing via the transitions into the Cs-He$_N$ $6^2P_{1/2}$ ($^2\Pi_{1/2}$), $6^2P_{3/2}$ ($^2\Pi_{3/2}$) and $6^2P_{3/2}$ ($^2\Sigma_{1/2}$) states at $\tilde{\nu} = 11197\,\mathrm{cm}^{-1}$, $\tilde{\nu} = 11745\,\mathrm{cm}^{-1}$ and $\tilde{\nu} = 11835\,\mathrm{cm}^{-1}$, respectively. The 133 amu signal is scaled to unity. The exciplex formation is enhanced at the D2 line, and most pronounced for the ionization via the $^2\Sigma_{1/2}$ state.

pronounced $^2\Pi_{3/2}$ peak in the Cs-He$_N$ LIF spectrum (Figure 4.5) can now be explained and it has a technical reason. Cs*-He$_n$ exciplexes emit fluorescence light, which is red-shifted to the atomic lines [159]. The sensitivity of the PMT (Hamamatsu R943-01 with GaAs photocathode), which is used for the LIF experiments, decreases below $11600\,\mathrm{cm}^{-1}$ and cuts off at $11100\,\mathrm{cm}^{-1}$. This means that the transition is there, but our detector is blind at the emitted fluorescence wavelengths. This explains the differences between the R2PI spectra in ref. [101] and our LIF spectra (Figure 4.5).

Non-desorption of Rb and Cs upon excitation of the D1 transition

In contrast, hardly no Cs*-He exciplexes are observed if Rb and Cs atoms are ionized is via the D1 transition. This is in agreement with the results in ref. [101]. Usually an excitation of Ak atoms on He$_N$ induces a desorption process and single excited Ak* atoms or Ak*-He$_m$ exciplexes leave the He$_N$ surface, as we have seen for the D2 excitation in Cs–He$_N$. The formation of an exciplex leads to an energy release into the fragile system due to the relatively strong bond of the Ak-He potential. Exciplex formation at the $^2\Pi_{1/2}$ state of Cs-He$_N$ (and Rb-He$_N$, see ref. [160]) is prevented by a barrier in the A$^2\Pi_{1/2}$ Cs*(Rb*)-He potential (single He atom - Ak* potential, of the exciplex). If the photon-energy of the excitation laser is not

Figure 4.5 *(facing page)*: D1 and D2 transition of Rb and Cs on helium nanodroplets ($\hat{N} = 7500$), recorded wit LIF (red) and BD (blue) spectroscopy. The black data points represent the two-step excitation efficiency. In both panels of the Figure, the wavenumber scale is the same and the $n^2P_{1/2}$ free atom lines are at the same position. Besides the well resolved spin-orbit splitting, three molecular substates can be identified, which are the $^2\Pi_{1/2}$, $^2\Pi_{3/2}$ and $^2\Sigma_{1/2}$ diatomic substates, in agreement with the PDM.

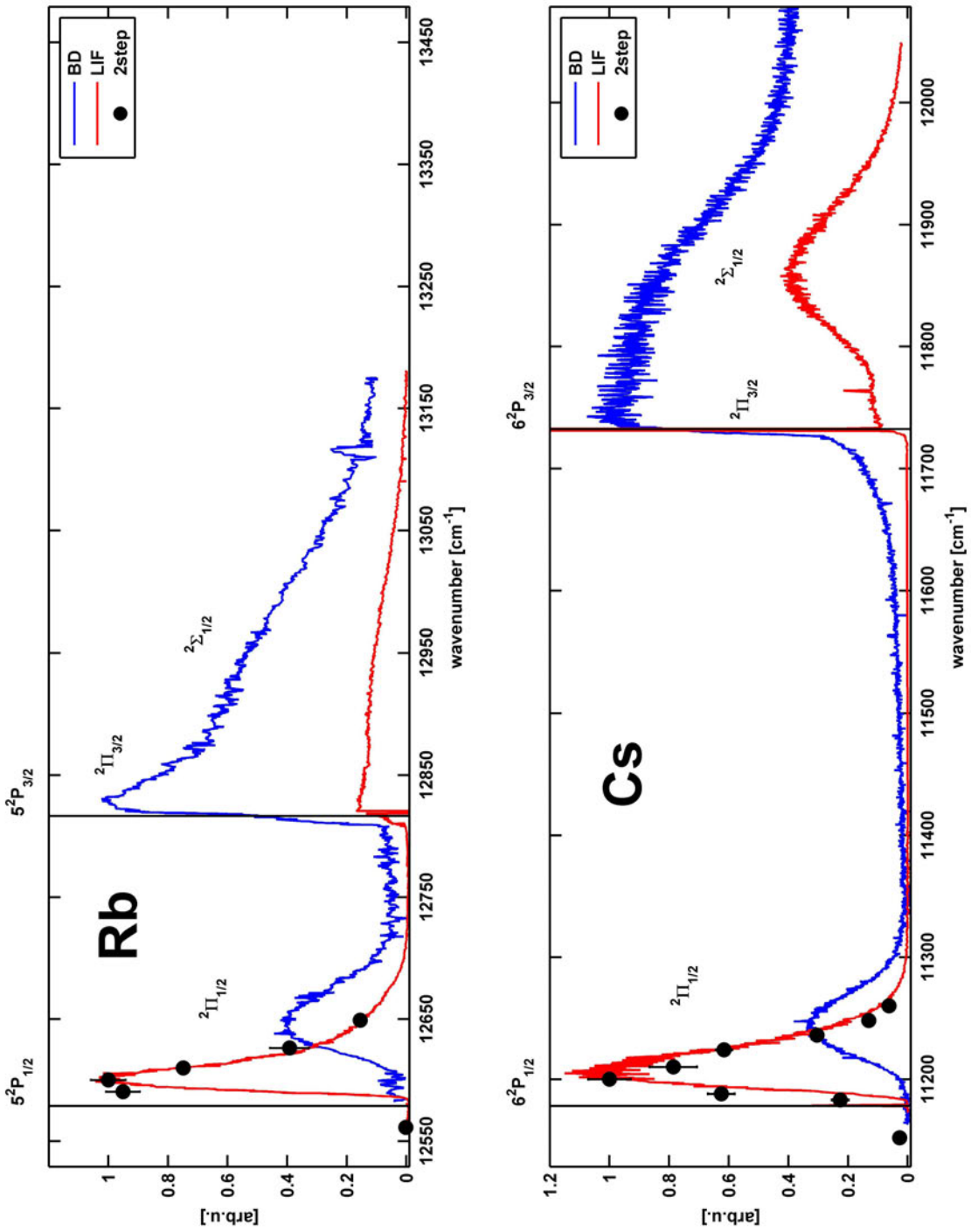
Rb
Cs
BD
LIF
2step
$5^2P_{1/2}$
$5^2P_{3/2}$
$6^2P_{1/2}$
$6^2P_{3/2}$
$^2\Pi_{1/2}$
$^2\Pi_{3/2}$
$^2\Sigma_{1/2}$
wavenumber [cm^{-1}]
[arb.u.]

high enough to overcome the barrier, the atom can stay on the droplet (no energy is released). Only a small amount of exciplexes is expected, from the contributions of atoms which tunnel through the barrier. If the photon-energy is higher, the Cs(Rb) atom on He_N is excited into the repulsive part of the potential, which causes the desorption of atoms, predominantly without helium atoms attached. If the barrier is absent, which is usually the case, the formation of exciplexes is energetically favorable and, depending on the symmetry of the excited state, the atom will in general desorb from the surface as single atom or with one or more He atoms attached to it.

Hence the $5^2P_{1/2} \leftarrow 5^2S_{1/2}$ transition [174] in Rb–He_N and the $6^2P_{1/2} \leftarrow 6^2S_{1/2}$ transition [4] in Cs–He_N are an exception, because the atoms remain bound to the surface upon excitation. This opens a possibility to multiply excite the same atom on He_N, which allows electron spin pumping [174] and two-step excitation experiments [2].

The non-desorbing character of the D1 transitions could be verified by a comparison between BD and LIF spectra. This is shown in Figure 4.5. The BD signal is only sensitive for desorbed atoms, independent of their desorption as free atoms or exciplexes. In contrast, LIF spectroscopy is sensitive to desorbed atoms as well as to atoms on the surface, because the fluorescence emission of the atoms on the surface differs only by a few wavenumbers from the atomic emission and is hence detected by the PMT. Thus from the difference in the two spectra, conclusions about surface states of the atom can be drawn. If the LIF signal is high and no BD signal is detected, the fluorescence light must be emitted by atoms which stay bound to the surface. It can be seen in Figure 4.5 that this is the case for excitation wavelengths close to the atomic D1 line. Also the two-step excitation (see next section) works most efficient in this wavelength range. This is discussed in more detail for Rb–He_N in [174] and in our work on Cs–He_N in ref. [4].

4.3 The two step excitation scheme

The excitation of unstable intermediate states can serve as a tool for the preparation of systems, which are otherwise difficult to access. This has been used for the spectroscopy of Ag Rydberg states [87], Cr autoionizing states [175] or the investigation of RbHe [173] for example.

Sequential two-step excitation of foreign atoms (or molecules) inside or on the surface of He_N is possible if the complex has a bound intermediate state. Such states are rare, but they can be used to investigate the interaction between the droplet and the atom or molecule.

The two Ak–He_N complexes Rb–He_N and Cs–He_N provide systems with a bound intermediate state. Beside these two species, experiments with Ba-He_N [176, 177] suggest that sequential excitation might be possible with alkaline-earth metal doped He_N as well, at least for Ba. In the two-step excitation experiments with Rb and Cs, the energetically lowest $n^2P_{1/2}$ state serves as springboard for the excitation into higher states. Calculations show that the $5^2P_{1/2}(^2\Pi_{1/2})$ potential of Rb [174] and the $6^2P_{1/2}(^2\Pi_{1/2})$ potential of Cs [4, 89] have a very shallow minimum, both with a depth of less than $10\,cm^{-1}$. In the ground state the binding energies are in the order of $15\,cm^{-1}$ for both species. The excitation energy in our experiments are higher than the energy of the free-atom D1 transition by $21\,cm^{-1}$ for Rb and $22\,cm^{-1}$ for Cs. Taking into account the binding energies of the ground states, the atoms are excited into the repulsive part of the $^2\Pi_{1/2}$ potential slightly above the minimum. The excitation path in

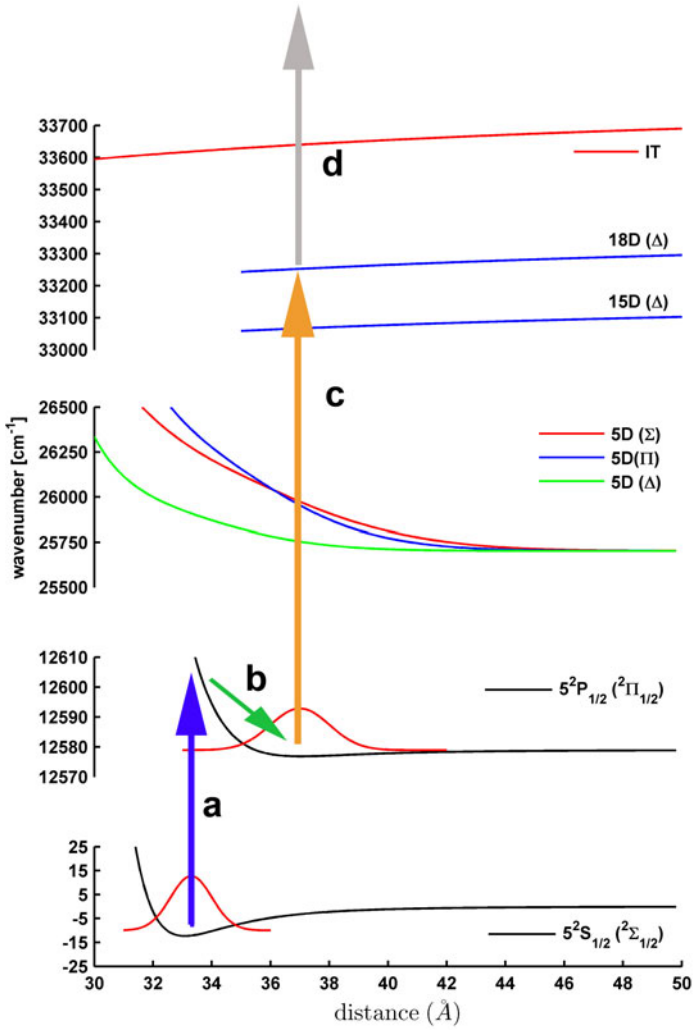

Figure 4.6: Rb-He_N potential energy curves from the ground state to the IT. The excitation path is shown for the case of resonant three photon ionization: The intermediate $5^2P_{1/2}(^2\Pi_{1/2})$ state (a) is excited. The system relaxes (b) and a second laser excites a Rydberg state (c). From this state, the system is ionized (d, REMPI) or fluorescence light is collected (LIF).

the two-step excitation scheme is shown in Figure 4.6 for Rb–He_N. The excitation scheme is similar for the Cs–He_N system, except that n of the involved states is increased by one. The potentials in Figure 4.6 for the ground state, the first excited P states and the 5D states are the same as used in reference [2], which are described in more detail in reference [178]. The excitation with laser L1 (a) is followed by rapid vibronic relaxation of the atom in the excited state (b). This process is very fast and takes place on a few- or sub-nanosecond timescale. Previous experiments [2, 4, 174] suggest that the population distribution of vibronic states reaches thermal equilibrium, before the second laser L2 excites a higher state. This means that the majority of the Rb(Cs)–He_N is in the vibronic ground state (v'= 0) of the $^2\Pi_{1/2}$ potential. From the intermediate state, Rydberg states are excited with a second laser L2 (c). As shown in Figure 4.6 lower states are blue shifted whereas higher Rydberg states and the ionization threshold (IT) are red-shifted. The potentials for the 15D (Δ), 18D (Δ) and the

IT are drawn through the two known points of each potential: the asymptotic energy values (energy levels of the free atom) and the red-shifted energy values (maxima of the peaks in the spectra). The energy values on the droplet are determined experimentally at the equilibrium distance of the intermediate $5^2P_{1/2}(^2\Pi_{1/2})$ state (vertical excitation assumed, Franck-Condon principle). Excitations of Rydberg states from the ground state in future experiments would enable the experimental determination of the form of the Rydberg potentials, because the equilibrium position of the ground state is closer to the droplet. Hence such experiments will provide a third point of the potential curve.

Upon the Rydberg excitation, the atoms desorb from the droplet surface as free atoms or as exciplexes. In the case of REMPI-TOF spectroscopy, the resulting complex is ionized by a third photon (d), which is detected by the MCP of the TOF mass spectrometer. In the case of LIF spectroscopy, which works best for lower Rydberg states, the fluorescence light emitted by the atoms is collected. Taking into account the PMT sensitivity, the major part of the detected fluorescence is emitted by atoms (not exciplexes). In Figure 4.7 we show

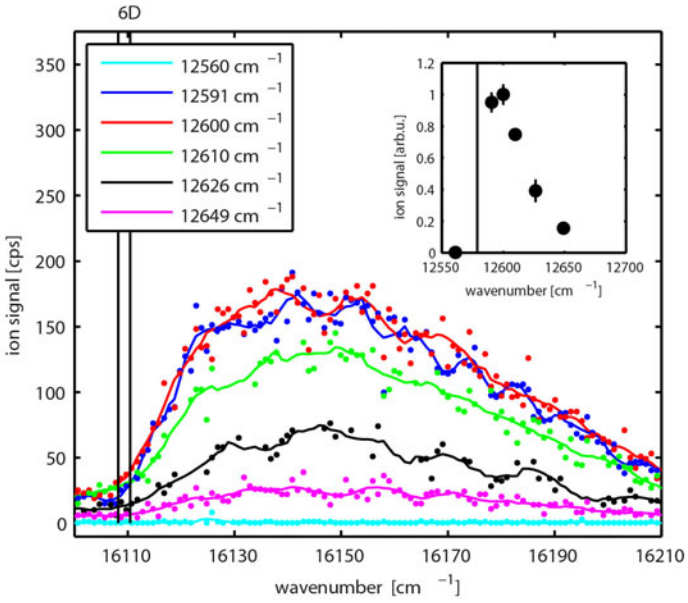

Figure 4.7: Rb–He_N excitation spectrum as obtained by monitoring the Rb^+-He_m ($m = 1-6$) signal as a function of L2 of the Rb–He_N 6D(Δ) state for different wavenumbers of laser L1, which excites the intermediate $5^2P_{1/2}(^2\Pi_{1/2})$ state. The inset shows the relative ion signal at the peak maximum as a function of the L1 wavenumber. Atomic states are indicated by vertical lines, where the line in the inset represents the $5^2P_{1/2}$ state.

an investigation of the intermediate state on the example of the Rb–He_N 6D(Δ) state. The state was recorded by monitoring the Rb^+-He_m ($m = 1-6$) ion yield as a function of the wavenumber of laser L2 (Figure 4.6 (b), for different wavenumbers of laser L1 (Figure 4.6 (a)), which excites the intermediate $5^2P_{1/2}(^2\Pi_{1/2})$ state. The inset shows the relative ion signal at the peak maximum as a function of the L1 wavenumber. This signal is also shown in the upper panel of Figure 4.5, where it can be compared to the LIF and BD spectra. From these Figures we see that the two-step excitation works most effective in a small range close to the

free atom line. In this range the majority of atoms is available for a second excitation step with laser L2. Best signals were obtained at $\tilde{\nu}_{L1} = 12600\,\mathrm{cm}^{-1}$ for Rb and $\tilde{\nu}_{L1} = 11200\,\mathrm{cm}^{-1}$ for Cs–He_N. For comparison, the Rb and Cs free atom transitions are at $12578.960\,\mathrm{cm}^{-1}$ $11178.270\,\mathrm{cm}^{-1}$, respectively. The higher the wavenumber of L1, the larger the fraction of atoms, which desorb from the droplet. Those desorbed atoms are visible in the Rb^+ signal (not shown), when the wavenumber of L2 coincides exactly with the $6^2D_{3/2} \leftarrow 5^2P_{1/2}$ free atom transition. This atomic Rb^+ signal is more pronounced when laser L1 is set to the blue side of the D1 transition because the contribution of Rb^+, which are generated after the excitation into the 6D(Δ) Rb–He_N state, decreases in comparison to the signal from the atoms which desorbed before the second laser can excite the atom. This means that the fraction of Rb^+ ions from the first excitation step in comparison to the fraction of Rb^+ ions from the second excitation step at the free atom $6^2D_{3/2} \leftarrow 5^2P_{1/2}$ transition increases with the wavenumber of L1, the laser for the first excitation step. From this observation we conclude that in the case with L1 at high wavenumber, the atoms leave the droplet predominantly as free, excited atoms in the $5^2P_{1/2}$ state, before the second laser L2 resonantly ionizes them via the $6^2D_{3/2}$ state. In contrast, when the L1 wavenumber is close to the free atom transition, the majority of the atoms is on the droplet surface in the $5^2P_{1/2}$ ($^2\Pi_{1/2}$) (v'= 0) state, and the observed Rb^+ and Rb^+-He_m ions origin from atoms, which leave the He_N after the excitation into the 6D(Δ) Rb–He_N state.

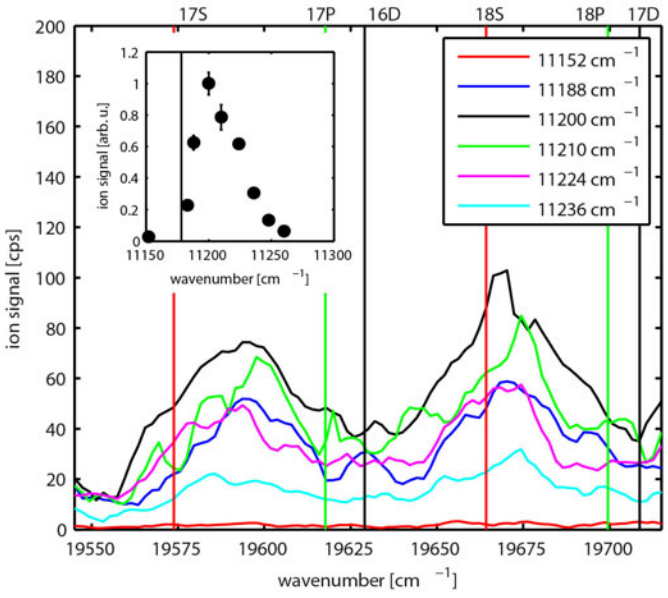

Figure 4.8: Cs–He_N excitation spectrum as obtained by monitoring the Cs^+-He_m ($m = 1-6$) signal as a function of L2 in the range between the free-atom 15D and 17D states for different wavenumbers of laser L1. Laser L1 excites the intermediate $6^2P_{1/2}(^2\Pi_{1/2})$ state. The inset shows the relative ion signal in the observed range as a function of the L1 wavenumber. Atomic states are indicated by vertical lines, where the line in the inset represents the $6^2P_{1/2}$ state.

The Cs–He_N system is similar to the Rb–He_N system. In Figure 4.8 the dependence of high Rydberg states in the range between the free-atom 15D and 17D states on the wavenumber of laser L1 is presented. Individual diatomic states can not be resolved for these transitions. No significant influence of different L1 wavelength on the peak positions is found in the excitation spectrum, which demonstrates the vibronic relaxation of the Cs–He_N system in the $6^2P_{1/2}$ ($^2\Pi_{1/2}$), similar to Rb–He_N. For example, if we assume that the system would not relax, the difference between the signal taken with L1 at 11188 cm^{-1} and 11224 cm^{-1} should be 36 cm^{-1}. This relatively large shift is not observed in Figure 4.8. The inset in Figure 4.8 shows the relative height of the signal. This signal, which is a measure for the two-step excitation efficiency, is also shown in Figure 4.5 together with the LIF and BD spectrum. The two-step excitation is most efficient close to the $6^2P_{1/2}$ free atom state.

With this discussion, we can explain the differences in the LIF, BD and the photo-ion signal in the inset in Figure 4.7, which appears slightly red-shifted compared to the two other signals. Each atom can contribute only once to the sequential two-step signal and only if it stays on the surface of the droplet in the intermediate state. This is the difference to the LIF signal, where also desorbed atoms, that are not bound can contribute to the signal by the emission of a photon and those which are bound can contribute several times (if the laser power is sufficient). However, the LIF and two-step efficiency signals differ only slightly and appear almost identical. In Figure 4.5 it seems, if the maximum of the two signals are scaled to one, that the rising edge of the two-step efficiency signal is red-shifted in comparison to the LIF signal. In contrast, the two-step signal is complementary to the BD signal, which is only sensitive to desorbed atoms.

The small energy range close to the D1 line where the sequential two-step excitation works most efficiently and the very shallow, binding potential of the $^2\Pi_{1/2}$ state are the reason that no significant droplet size dependent effects for different excitation energies of L1 are observed. As theoretical calculations show (see Figure 4.2), due to the presence of the He_N close by the Ak atom, the potential is very steep in the repulsive part. Because the valence electron's wavefunction radius is small compared to the droplet radius used in the experiments, the potential should not vary much with the droplet size. This behavior changes when Rydberg states with large orbitals are excited. The Rydberg potentials are flat and the electron wavefunctions are more sensitive to the droplet size [7]. Experimental results of dispersed fluorescence emission spectra of the Rb(Cs)–He_N $5(6)^2P_{1/2}$ ($^2\Pi_{1/2}$)→$5(6)^2S_{1/2}$ ($^2\Sigma_{1/2}$) transition have an FWHM of just a few (5-8) cm^{-1}, even for large droplets ($N_{14,60}$ = 7500) and are well explained by theoretical calculations of droplets with N= 1000. We thus conclude that the energy of the ($^2\Pi_{1/2}$) (v'= 0) state does not differ much for different droplet sizes, because effects larger than $3-5\,cm^{-1}$ would have been noticed in the experiments [4, 174]. Also the fact that the rising edge in Figure 4.7 does not depend on the energy of L1 strengthens this statement.

This is verified by the two-step ionization spectrum of the Cs–He_N D1 transition for different droplet sizes in Figure 4.9. The transition changes only slightly with the droplet size. The peak maximum moves slightly closer to the free atom line with decreasing droplet size. The left panel shows the difference of the absolute signal, whereas the right panel shows the scaled signal, for a better comparability. Despite this small differences, the peak shapes are essentially the same. Hence the first excitation step is not droplet size selective and in the two-step excitation experiments, the starting point for the excitation of Rydberg states can be treated

(in good approximation) as droplet size independent. However, one has to bear in mind that when excited states of doped He_N states are compared to free atom states, regardless of the dopant atom being excited sequentially by two steps or directly from the ground state, the resulting spectrum has an offset of an energy corresponding to the binding energy of the atom to the He_N in the ground-state or the intermediate state if the system relaxes. This offset is in the range of only a few wavenumbers for the Ak-He_N systems, but it can be larger if the foreign atom is strongly bound.

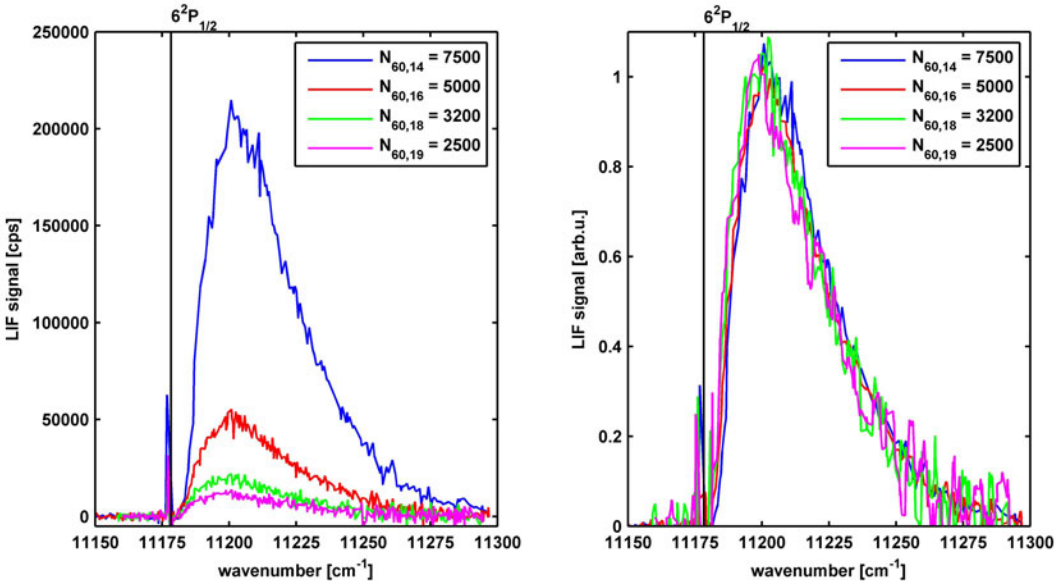

Figure 4.9: Droplet size dependence of the Cs-He_N D1 transition. The peak moves slightly closer to the free atom line with decreasing droplet size (left panel, absolute signals are shown), but if the peaks a scaled to one (right panel), it can be seen that the peak shape does not change significantly with the droplet size.

Chapter 5

Spectroscopy of Cs atom Rydberg States on He Nanodroplets

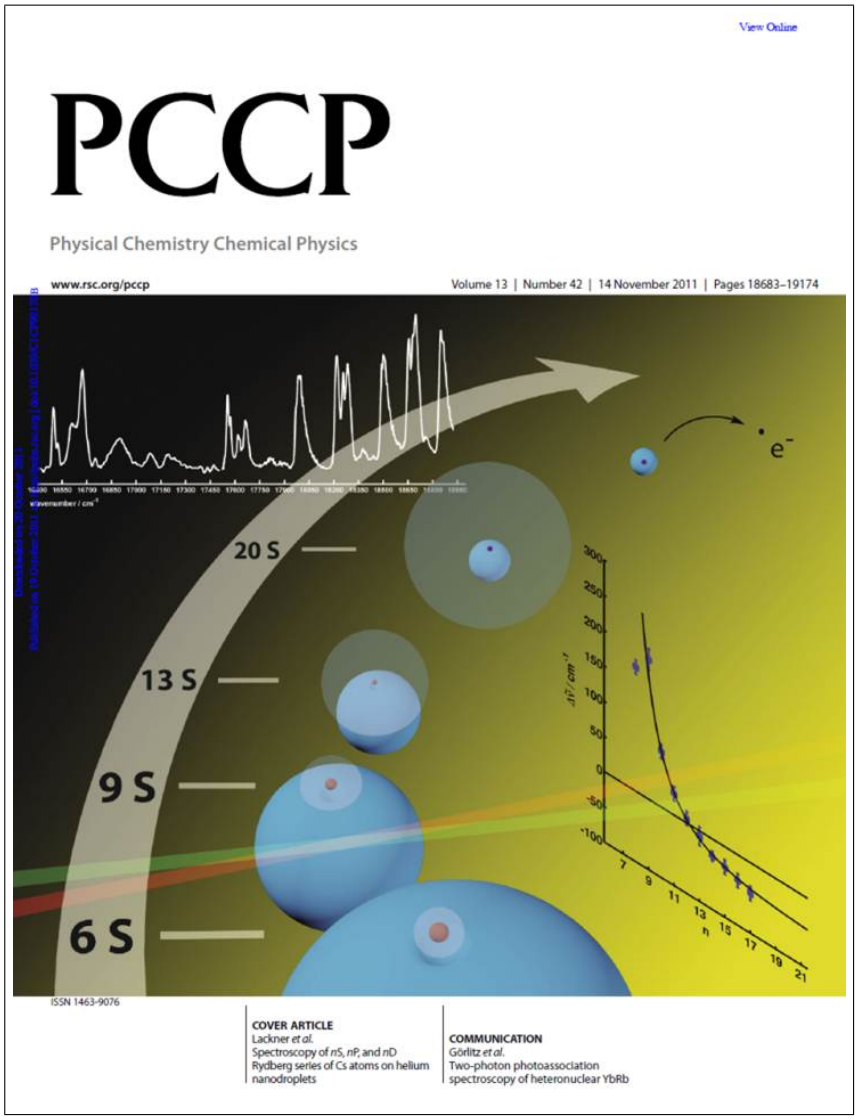

The main part of this chapter corresponds to the Phys. Chem. Chem. Phys. ***13****, 18781-18788 (2011) cover article (ref. [6]). This work includes the complete Cs-He$_N$ excitation spectrum and it demonstrates the Rydberg character of this system. Excitation spectra are obtained by using laser induced fluorescence spectroscopy and reonance-enhanced multi-photon-ionization time-of-flight mass spectroscopy. This is presented in the first section. The following sections include additional studies of the dynamics and the droplet size dependence of excited Cs-He$_N$ states, as well as detailed two-photon ionization studies of the 7P states, which will be published in ref. [8].*

5.1 Spectroscopy of nS, nP, and nD Rydberg series of Cs atoms on helium nanodroplets

The preparation of an artificial superatom consisting of a positive charge inside a superfluid helium nanodroplet and an electron in an orbital surrounding the droplet is of fundamental interest and represents an experimental challenge. In this work, nanodroplets of several thousand helium atoms are doped with single cesium (Cs) atoms. While on the droplet, the Cs valence electron is excited in two steps through an intermediate state into nS, nP, and nD states. The excitation is monitored by laser induced fluorescence or, for high principal quantum numbers, by resonant three-photon-ionization. On-droplet Rydberg excitations are resolved up to about $n = 20$. The energies are compared with those of free Cs atom Rydberg states and quantum defects as well as the on-droplet ionization threshold are derived.

5.1.1 Introduction

Helium nanodroplet isolation spectroscopy has been developed as a powerful tool to study basic properties of single, isolated atoms, molecules, and clusters [18] in an ultracold (0.38 K [39]) environment. In many cases the interaction of the superfluid helium nanodroplet (He_N) with the dopant is a question of fundamental interest.

Alkali-metal (Ak) atoms reside on the surface of the He_N [75, 159] and are very weakly bound. The Ak–He_N system is an ideal test system, because of the simple generation and the accessibility of electronic transitions with tunable lasers. Thus the lowest electronic transitions $n^2P_{1/2} \leftarrow n^2S_{1/2}$ and $n^2P_{3/2} \leftarrow n^2S_{1/2}$, historically known as D1 and D2 lines, respectively, are well characterized. The D1 and D2 lines have been investigated experimentally for Li [159], Na [159, 171, 179], K [159, 171, 172], Rb [160, 174], and Cs [101]. The spectral lines of Ak atoms are broadened due to the interaction with the He_N and the atoms desorb upon excitation in most cases. In addition, the lines are blue-shifted with respect to the transitions of the free atom and this shift increases with the size of the atom (e.g. 50 cm^{-1} for the Cs D1 line [101]). For K, Rb, and Cs, spin-orbit (SO) interaction causes a clearly resolvable line-splitting. The D1 line of Rb and Cs is an exception in that upon excitation the atom does not desorb from the droplet surface for excitation energies close to the atomic line [4, 174]. The non-desorption of the Rb atom in the $5^2P_{1/2}$ state was shown by Auböck *et al.* [174] where it has been used to induce an electron spin polarization by optical pumping. This mechanism is also used for electron spin resonance (ESR) experiments in doped helium nanodroplets [180–182]. New measurements show that this non-desorption is also true for the $6^2P_{1/2}$ state of Cs

atoms on He_N [4]. A fraction (depending on the photon energy) of Cs atoms, when excited into the $6^2P_{1/2}$ state, does not desorb and relaxes into the $6^2S_{1/2}$ state on the droplet.

In spite of the favorable experimental conditions, relatively few experiments have investigated higher excited states of Ak atoms on He_N [161, 164, 165]. For K, Rb, and Cs the $(n{+}1)$p$\leftarrow$ ns ($n = 4, 5, 6$, respectively) transitions as well as the Rb 5d$\leftarrow$5s two-photon transition are discussed. The Rb $5^2D\leftarrow5^2P_{1/2}\leftarrow5^2S_{1/2}$ transition was studied in a two-step excitation experiment [2] where it was shown that due to the non-desorption of Rb in the $5^2P_{1/2}$ intermediate state a two-step excitation of higher states is possible. For Na, experimental data for lower excited states [165] and for Rydberg states [164] is available. Calculated potential energy curves for lower excited states of Na, K, Rb, and Cs on He_N are also provided [178]. However, the highest calculated potential curves for Cs correspond to the 6^2D (Σ, Π, and Δ) states. Transitions to higher states, investigated so far, also show a line-broadening due to the perturbation by the He_N.

When Ak atoms on the surface of He_N are excited to Rydberg states, where the spatial distribution of the valence electron becomes comparable in size to the diameter of the droplet, the question of the structure of the Ak*–He_N system naturally arises (the * denotes an excited atom). It is known that upon photoionization Rb ions immerse into the droplet [1], and new experiments show that this is also true for Cs [4]. Theoretical considerations predict bound electron states for a charged He_N [183]. The formation of a system consisting of an Ak ion-core immersed into a He_N and the electron in an orbital outside, which we refer to as "superatom", would represent such a situation.

In this work, for the labeling of the higher electronically excited states of the Ak–He_N system, three different notations are introduced (for a detailed explanation see Pifrader *et al.* [161]). (i.) Commonly used is the notation of the bare atom with SO coupled atomic orbitals, where the helium droplet is treated as a perturbation: $^{2S+1}L_J$, where L is the orbital angular momentum and J is the total electronic angular momentum and S is the Spin of the electrons (2S+1 is the multiplicity, which is 2 for Ak atoms). (ii.) The second notation takes the diatomic character of the Ak–He_N system into account [159]. The helium droplet is treated as one atom in a diatomic molecule with the molecular axis connecting the center of the droplet with the alkali nucleus. For states with strong SO interaction Hund's case (a) seems appropriate. The standard notation is: $^{2S+1}\Lambda_\Omega$, where Λ is the projection of L on the molecular axis and Ω is the projection of J on the molecular axis. (iii.) For higher states with small spin-orbit interaction compared to the Ak–He_N interaction, the spin can be neglected. This leads to the third notation, where only spinless molecular states (i.e. Λ) are denoted. For example a S state can be denoted as $^2S_{1/2}$ (i.), $^2\Sigma_{1/2}$ (ii.), or Σ (iii.) state. Because the molecular notation is ambiguous, the corresponding atomic state from which the molecular state arises is denoted and the molecular state is set in brackets (e.g. $6^2S_{1/2}$ ($^2\Sigma_{1/2}$)). We call states of Cs atoms on He_N "on-droplet" states and states of bare atoms as "free-atom" states.

In this work the $6^2P_{1/2}$ ($^2\Pi_{1/2}$) state is used as springboard to reach highly excited states and Rydberg states of Cs atoms on He_N.

5.1.2 Experimental

The droplet generation and doping section of the experimental setup has been described in detail in Chapter 2. In brief, the helium nanodroplets are produced in a supersonic jet expan-

Table 5.1: Summary of the lasers used in the experiment. Given are the wavenumbers, peak power or pulse energy, and the observed transitions in the spectrum in Figure 5.2. For the sake of clarity atomic nomenclature is used.

laser	active medium	mode	wavenumber (cm^{-1})	peak power/ pulse energy	observed transitions
L1a	Ti:S	cw	fixed: 11197	2 W	$6^2P_{1/2} \leftarrow 6^2S_{1/2}$
L1b	Ti:S (fundamental)	pulsed	fixed: 11197	150 μJ	$6^2P_{1/2} \leftarrow 6^2S_{1/2}$
L2a	Ti:S	cw	11300-13500	800 mW	$6^2D \leftarrow 6^2P_{1/2}$
					$8^2S \leftarrow 6^2P_{1/2}$
L2b	DCM	cw	14500-16100	800 mW	$8^2P \leftarrow 6^2P_{1/2}$
					$7^2D \leftarrow 6^2P_{1/2}$
					$9^2S \leftarrow 6^2P_{1/2}$
L2c	Rhodamine 6G	cw	16400-17500	1.2 W	$9^2P \leftarrow 6^2P_{1/2}$
					$8^2D \leftarrow 6^2P_{1/2}$
					$10^2S \leftarrow 6^2P_{1/2}$
L3	Ti:S (SHG)	pulsed	21000-22850	50 μJ	$7^2P \leftarrow 6^2S$
L4a	Coumarin 153	pulsed	17500-19150	6 mJ	10^2P to 14^2S states
L4b	Coumarin 307	pulsed	19150-20400	6 mJ	14^2P states to the *IT*

sion of high purity helium gas through a cold 5 μm nozzle into vacuum (nozzle temperature typically 14 K, stagnation pressure 60 bar). Under these conditions droplets with an average number of about 10^4 helium atoms and a diameter of $\sim$ 10 nm are generated. The droplet size at distribution maximum is $\hat{N}_{60,14} = 7500$. The droplet beam is doped by means of a resistively heated pickup cell (80°C to 100°C) loaded with Cs metal.

In order to investigate excited states of Cs atoms on helium droplets, two different spectroscopic methods are used. For lower states laser induced fluorescence (LIF) spectroscopy is used, for Rydberg states resonant three-photon-ionization time-of-flight (R3PI-TOF) spectroscopy is applied. Both schemes exploit the fact that Cs atoms remain on the He_N when excited into the $6^2P_{1/2}$ ($^2\Pi_{1/2}$) state. This non-desorbing state is used as intermediate state for further excitations with a second laser. The two lasers in both types of experiments are spatially overlapped with a beam splitter cube. However, the two methods require different lasers and detectors, and are described separately in the following. Figure 5.1 shows an energy level diagram together with the investigated excitations. The lasers and the corresponding active media for the individual transitions are listed in Table 5.1.

(i) The setup of the LIF scheme is comparable to the one in our previous work [2]. In the present work we use for the first excitation step a Coherent 899-01 Ti:S cw ring laser (L1a), which is pumped with a Coherent Verdi-V18. L1a is kept at a fixed wavenumber (11197 cm^{-1}) and excites the Cs atom into the $6^2P_{1/2}$ ($^2\Pi_{1/2}$) on-droplet state. This non-desorbing intermediate state is used as a springboard to excite higher states. For the second excitation step tunable cw lasers (L2a-L2c) with different active media are used. At higher wavenumbers a cw dye laser (Coherent 699 Ring Dye Laser) and at lower wavenumbers a home made cw Ti:S ring laser is used. Both lasers are pumped with a Coherent Verdi V-10. Due to line broadening caused by the helium droplet it is sufficient to operate all cw lasers in multi-mode. L2 is scanned by rotating the birefringent filter. For the direct excitation of the 7^2P state manifold a pulsed frequency doubled Ti:S laser L3 (Coherent Indigo-S) with a

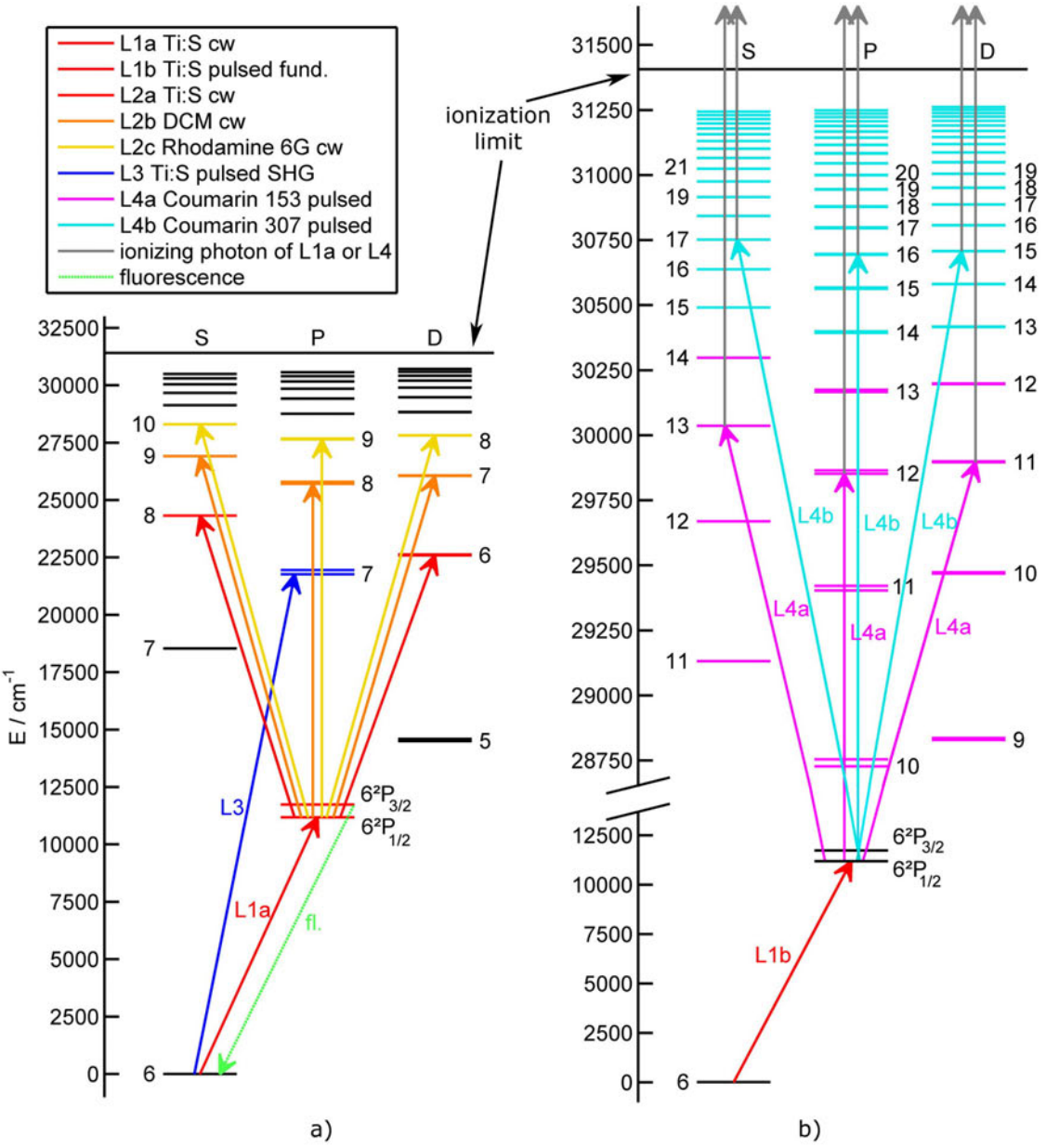

Figure 5.1: Energy level diagram of the bare Cs atom for the illustration of the LIF and the R3PI-TOF scheme. a) LIF spectroscopy: the red arrow indicates the laser L1a for the first excitation step. The arrows starting from the $6^2P_{1/2}$ state represent the laser L2 for the second step as listed in Table 5.1. The levels and arrows are color coded to assign different active media. Laser L3 indicates the direct excitation of the 7P state (blue arrow). Fluorescence light is detected from the $6^2P_{3/2} \rightarrow 6^2S_{1/2}$ transition (green arrow). b) R3PI-TOF spectroscopy: the red arrow indicates the pulsed laser L1b for the first excitation step. The arrows starting from the $6^2P_{1/2}$ state represent the laser L4 for the second step as listed in Table 5.1. A second photon either from the dye laser or the Ti:S laser ionizes the highly excited Cs atom (gray arrows).

repetition rate of 5 kHz and 30 ns pulse duration is used.

Laser induced fluorescence from the $6^2P_{3/2} \rightarrow 6^2S_{1/2}$ transition is collected at the interaction region of the droplet beam and the laser beams and monitored with a Peltier cooled photomultiplier tube (Hamamatsu R943-01). The fluorescence photons are counted with a Stanford Research SR 400 counter. For efficient stray light suppression, a transmission filter is used (max. transmission $\lambda = 8521$ Å, FWHM $= 4$ Å) in order to detect only fluorescence light in a small region around the $6^2P_{3/2} \rightarrow 6^2S_{1/2}$ (D2 line) transition. For direct excitation into the 7^2P states and the two-step excitation into the 6^2D states the filters Schott RG9 and BG39 are used, respectively.

Intensities of the obtained spectral lines can not be compared, because many additional effects influence the signal. Most important, different excited states relax back to the ground state via different fluorescence channels. For example, after an excitation into the $6^2D_{3/2}$ state, according to dipole selection rules for bare atoms, the decay via the $6^2D_{3/2} \rightarrow 7^2P_{3/2} \rightarrow 7^2S_{1/2} \rightarrow 6^2P_{3/2} \rightarrow 6^2S_{1/2}$, the $6^2D_{3/2} \rightarrow 6^2P_{3/2} \rightarrow 6^2S_{1/2}$ and the $6^2D_{3/2} \rightarrow 7^2P_{3/2} \rightarrow 5^2D_{5/2,3/2} \rightarrow 6^2P_{3/2} \rightarrow 6^2S_{1/2}$ channel can contribute to the detected signal. Other channels (e.g. via the $6^2P_{1/2}$ state or the $7^2P_{3/2,1/2} \rightarrow 6^2S_{1/2}$ transition) are suppressed when the D2 transmission filter is inserted. The intensities of the peaks in the LIF spectra are scaled such as to allow all significant bands to be depicted in Figure 5.2. This applies explicitly to states from 7^2P to 8^2S. A differential counting scheme is used in order to get a monomer selective fluorescence signal. This is necessary because the observed fluorescence light is not only generated by single Cs atoms on He_N but also by Cs_2–He_N and Cs_3–He_N, as they are always present in the beam. A part of the excited dimers and trimers fragments and emits fluorescence light of bare excited atoms, decaying via the $6^2P_{3/2} \rightarrow 6^2S_{1/2}$ transition, which cause a background signal [100, 101]. Because the dimer and trimer contribution to the LIF signal arises only from laser L2, L1a is chopped and the counts obtained with the laser L2 only are subtracted from the counts obtained with both lasers. Since L1 has a fixed wavelength, the contribution due to stray light is constant, which is accounted for in the spectrum.

(ii.) For R3PI-TOF spectroscopy two pulsed lasers are used, which cross the droplet beam in the ionization region of a time-of-flight mass spectrometer (Jordan D-850 AREF). The laser setup and the TOF mass spectrometer are described in Chapter 2. A pulsed Ti:S laser L1b (5 kHz repetition rate, 30 ns pulse duration) excites the Cs atom into the $6^2P_{1/2}$ ($^2\Pi_{1/2}$) state. The atom is excited further into higher states with a pulsed dye laser L4 (Lambda Physik FL 3002), pumped by a XeCl Excimer laser (Radiant dyes RD-EXC-200, 100 Hz repetition rate, 26 ns pulse duration). A second photon either from the dye laser or the Ti:S laser ionizes the highly excited atom and the ions are detected with the TOF mass spectrometer. The excitation scheme is shown in Figure 5.1 (b). A home-made synchronization device guaranties the time overlap of two laser pulses of L1b and L4. Every 50^{th} pulse of the 5 kHz L1b (master) coincides with one L4 pulse (slave). A time-resolved counter (Stanford Research SR 400), which is triggered by the synchronization device is used to count the pulses, which are obtained from the multichannel-plate detector in a certain time window, corresponding to a mass range. Mass selective spectroscopy is thus realized and the best signal was obtained when monitoring a time window corresponding to the Cs–He_n ($n = 1 - 8$) masses as a function of the dye laser (L4) wavelength. The Cs mass is not included in the selected time window in order to avoid contributions of fragmented dimers or trimers to the signal.

Figure 5.2 *(facing page)*: Excitation spectrum of Cs–He_N observed with LIF spectroscopy (red) and R3PI-TOF mass selective spectroscopy (blue). The vertical lines indicate transitions of free-atoms. The zero point of the abscissa is the $6^2P_{1/2}$ atomic state. L1 for the first excitation step is kept fixed at $11197\,cm^{-1}$. Data-binning is used to improve the signal and the solid line in the LIF spectrum is obtained by data-smoothing. The LIF signal is the difference signal of the counts obtained with the laser L2 only and the counts obtained with both lasers as a function of the wavenumber of the second laser L2. LIF data are recorded by applying the two-step excitation scheme except for the 7^2P state manifold, which is excited directly by L3 (green). The observed atomic transitions (see text) are plotted as red circles and are at the same positions as the free-atom lines. The R3PI-TOF spectrum starts at the 10^2P states. The Cs–He_n ($n = 1 - 8$) ion signal is plotted as a function of the pulsed dye laser L4 wavelength. The dashed line indicates the calculated ionization threshold of the free atom, corrected for the electrical field in the ion-extraction region of the TOF mass spectrometer.

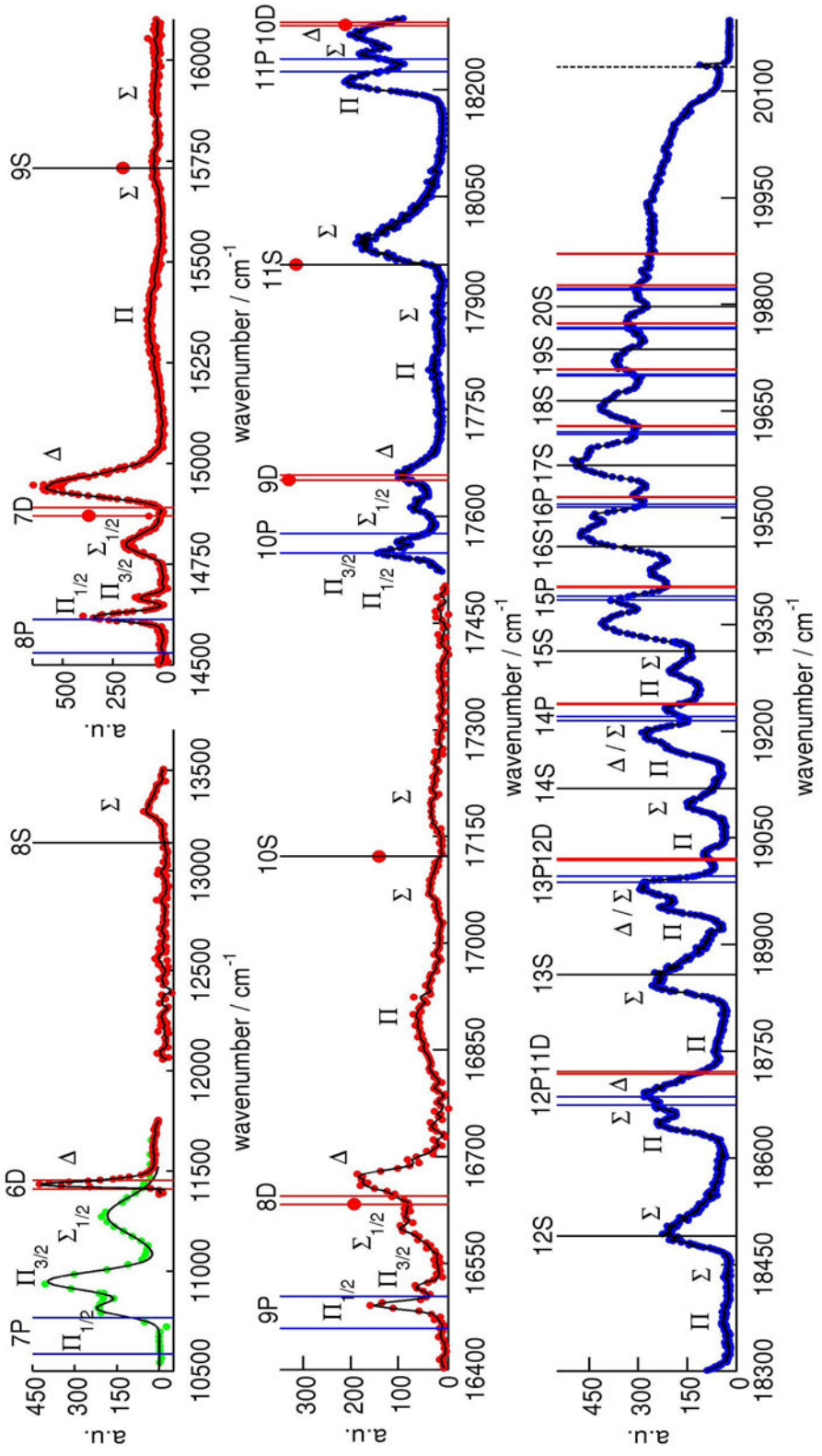
a.u.
wavenumber / cm-1
7P
6D
8S
9S
7D
8P
9P
8D
10S
9D
10P
11S
11P
10D
12S
12P
11D
13S
13P
12D
14S
14P
15S
15P
16S
16P
17S
18S
19S
20S
Π
Σ
Δ
Π1/2
Π3/2
Σ1/2

5.1.3 Results and Discussion

The excitation spectrum of Cs–He_N is depicted in Figure 5.2. The spectrum observed with the LIF scheme (green and red) starts at the 7^2P states and although data have been collected up to the 10^2D (Δ) state, they are displayed just up to the 10^2S state. The R3PI-TOF (blue) data are connected with the LIF data and cover the range from the 10^2P states to the ionization threshold. Note that in addition to nS, and nD levels also excitations into nP levels are observed. The corresponding atomic states are drawn as vertical lines in the spectrum. Data binning is used to enhance the signal to noise ratio and smoothing (solid line) is applied to the LIF data. The 7^2P state manifold is reached by direct excitation (green). The obtained data of the 7^2P states are offset corrected and scaled to match the other spectra. The offset arises most probably due to a dimer signal [161]. The 7^2P peaks are fitted with three Gaussian functions. Note that the binding energy of the ($6^2S_{1/2}$ ($^2\Sigma_{1/2}$)) ground state ($< 15\,cm^{-1}$ [178]) is neglected. One has to be careful when comparing the two-step and directly excited states [2]: The excitation takes place at different Cs-to-He_N distance and therefore, according to the Franck-Condon principle, the peak positions should be blue shifted when directly excited in comparison to the peaks obtained with two-step excitation according to calculations for lower excited states of Callegari and Ancilotto [178]. This behavior of the shift can change for higher excited states. A detailed study of the 7P state manifold is presented in the next section.

The data reflect the situation of the second excitation step from the intermediate state (L2 or L4). Experiments on Rb doped He_N [2] have shown that an excited atom in the $5^2P_{1/2}$ ($^2\Pi_{1/2}$) state relaxes rapidly into the vibronic ground state. For Cs–He_N, this means that the second excitation step can be seen as an excitation from the lowest vibronic state of the $6^2P_{1/2}$ ($^2\Pi_{1/2}$) state into higher electronic states [4]. Comparing the LIF data of the 10^2P states (not shown) with the corresponding R3PI-TOF data, no significant difference in the peak position was observed, which leads to the conclusion that vibrational relaxation takes place in the subnanosecond range (L4 laser pulse-duration is 26 ns). The zero point for the free-atom lines in the spectra is chosen as the $6^2P_{1/2}$ free-atom state. Note that the Cs–He_N complex is weakly bound in the $6^2P_{1/2}$ ($^2\Pi_{1/2}$) state and thus the starting point for the second excitation step lies deeper in energy by a few wavenumbers [4] than the free-atom $6^2P_{1/2}$ state. This has to be taken into account when comparing the position of free-atom lines with the on-droplet peaks.

Atomic Transitions

One spectral feature in the presented spectrum is the observation of sharp atomic transitions in the LIF spectrum. Some of the vertically drawn atomic lines coincide with data points, depicted as red circles in the spectrum. This signal is only observed in the on-period of L1 and thus has to be related to Cs–He_N. Initially bare atoms are not excited due to the blue-shift of the D1 line of Cs on He_N. As the spectral response to L2 is very sharp, this signal has to originate from bare Cs atoms, which detach from the He_N upon excitation with L1, and are further excited from the free-atom $6^2P_{1/2}$ state into higher states. Note that this free-atom $6^2P_{1/2}$ state is energetically higher than the bound on-droplet $6^2P_{1/2}$ ($^2\Pi_{1/2}$) state.

These atomic transitions reflect the free-atom dipole selection rules, only the $n^2S_{1/2} \leftarrow 6^2P_{1/2}$ ($n = 9 - 11$) and $n^2D_{3/2} \leftarrow 6^2P_{1/2}$ ($n = 7 - 10$) transitions are observed. Since L2 runs in

multi-mode, the signal is only observed when the laser wavelength coincide with the sharp atomic transition wavelength. The $6^2D_{3/2} \leftarrow 6^2P_{1/2}$ and $8^2S_{1/2} \leftarrow 6^2P_{1/2}$ free-atom transitions are not observed in the LIF spectrum, because the wavelength of the Ti:S laser L2a is not sufficiently stable. This conclusion is supported by the fact that in the R3PI-TOF experiment where the 6^2D state was investigated (data not shown), the $6^2D_{3/2} \leftarrow 6^2P_{1/2}$ atomic transition was observed. The observation of atomic Cs without attached He in the TOF mass spectrum upon ionization via the $6^2P_{1/2}$ on-droplet and $6^2D_{3/2}$ free-atom states leads to the conclusion that these signals are indeed due to desorbing atoms.

S States

S states could be observed from $n = 8$ to $n = 17$. Their LIF detection is difficult because of the low intensity compared to the other states. This is different in the R3PI-TOF experiments. The most significant difference in LIF and R3PI-TOF spectra is in the intensity of the S (Σ) peak resulting from different transition probabilities of the cascading steps. The on-droplet S peaks have an asymmetric shape with a steeper slope at lower energy. The highest S (Σ) state, which can be separated from others, is the 17^2S (Σ) state.

Later experiments with Rb atoms on helium droplets (next Chapter) suggest that the difference between LIF and R3PI spectra might be caused by a contribution of nF states to the ion signal. In the case of Cs, S and F states are very close to each other (e.g. the 7F state is $16\,cm^{-1}$ above the 11S state, this is much less than separations of comparable states shown in the next chapter for Rb (Rb e.g.: 6F is $129\,cm^{-1}$ above the 9S state)), so it is possible that the S states are overlaid by F states in the R3PI spectrum, but the small energy separation makes it difficult to distinguish between them. As will be shown in the next chapter, atoms in F states predominantly desorb as exciplexes. This could explain the higher R3PI signal, where the Cs mass was excluded, than the LIF signal, which is sensitive to atomic emission.

P States

The lower P states split into three diatomic substates: the $^2\Pi_{1/2}$, $^2\Pi_{3/2}$, and $^2\Sigma_{1/2}$ states, according to Hund's case (a). The labeling of the three molecular states arising from nP levels is done on the basis of calculations [161, 178] for lower P states and by taking into account the interpretation of the $6^2P_{1/2,3/2} \leftarrow 6^2S_{1/2}$ on droplet transitions. The P states show always the same pattern: the lowest state in energy is the $^2\Pi_{1/2}$, then comes the $^2\Pi_{3/2}$ state, and the highest is the $^2\Sigma_{1/2}$ state. The Π states are narrower than the Σ states and with increasing principal quantum number n the peak width decreases. It is also evident that the peaks move closer to each other with increasing n. Comparing the $^2\Pi_{1/2}$ and $^2\Pi_{3/2}$ states of different n, they can be easily separated up to $n = 9$. At $n = 10$ the $^2\Pi_{3/2}$ state appears as a shoulder of the $^2\Pi_{1/2}$ state and at $n = 11$ the two states can not be separated anymore. This can be explained by the fact that for the higher P states the SO interaction is small compared to the Cs–He_N interaction. Therefore we change the notation from the diatomic notation with SO interaction from case (ii.) to the diatomic notation without SO interaction (iii.) (see Section 5.1) for the description of P states above $n = 10$ and neglect the spin.

For high Rydberg states, at $n = 13$, the P (Σ) and D (Δ) are no longer distinct peaks. At the 15^2P state, the P (Π) and P (Σ) can not be resolved and appear as one peak together

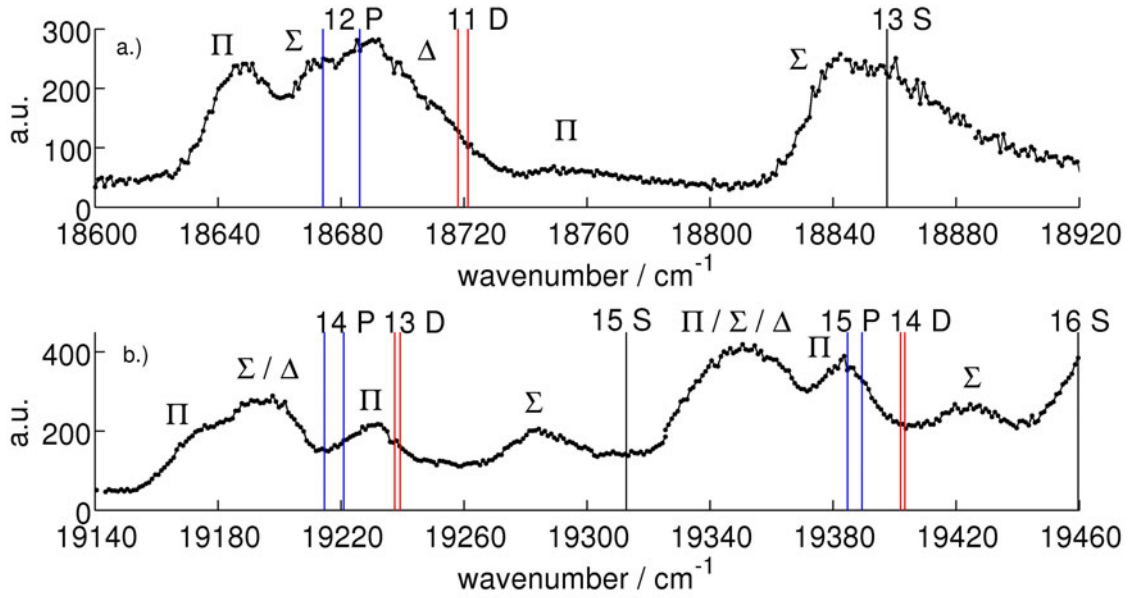

Figure 5.3: Detail of the spectrum in Figure 5.2 from 18600 cm^{-1} to 18920 cm^{-1} and from 19140 cm^{-1} to 19460 cm^{-1}. a.) shows the highest state where the P (Σ) and D (Δ) state can be separated. b.) shows the highest state where the P (Π) and the P (Σ) / D (Δ) state can be separated. From the 15^2P / 14^2D free-atom states on the 15^2P (Π), 15^2P (Σ) and 14^2D (Δ) on-droplet states are only noticeable as one peak.

with the D (Δ) state. The transitions where these Rydberg states start to overlap are shown in Figure 5.3.

D States

The D states split into three different molecular states: Δ, Π, and Σ. We neglect the spin because of the small SO interaction compared to the droplet induced line broadening. We start the discussion with the lower D states observed by LIF spectroscopy. The assignment of the three states is not straight forward, but calculations [178] suggest that the energy sequence of the 6^2D molecular states is $\Delta < \Pi < \Sigma$. However this sequence depends on the Cs-to-$\mathrm{He_N}$ distance in the diatomic model and examples are known in which the Σ and Π potentials cross near the Franck-Condon vertical excitation region [2, 161, 165]. For the 6^2D states, not all data points are shown in the spectrum. The corresponding spectral region is difficult to record because of the different roles the two lasers can play. The $6^2\mathrm{P}_{3/2}$ state lies almost at half the energy of the 6^2D states. Scanning L2 in order to excite the $6^2\mathrm{D} \leftarrow 6^2\mathrm{P}_{1/2}$ transition interferes with a direct excitation of $6^2\mathrm{P}_{3/2} \leftarrow 6^2\mathrm{S}_{1/2}$. This is the reason why a small portion of the spectrum from 11750 cm^{-1} to 12050 cm^{-1} is excluded in Figure 5.2.

The atomic SO splitting between the $6^2\mathrm{D}_{3/2}$ and $6^2\mathrm{D}_{5/2}$ states (42.9 cm^{-1}) [184] is comparable to that between the $9^2\mathrm{P}_{1/2}$ and $9^2\mathrm{P}_{3/2}$ state (44.7 cm^{-1}) [185], where the spin-orbit interaction can be resolved on $\mathrm{He_N}$. Thus the SO splitting should be taken into account for the 6^2D states. With SO splitting the on-droplet 6^2D states split into five substates: $^2\Delta_{5/2}$, $^2\Delta_{3/2}$, $^2\Pi_{3/2}$, $^2\Pi_{1/2}$, and $^2\Sigma_{1/2}$. Considering the selection rules (see next section) only the last

four can be reached from the $6^2P_{1/2}$ ($^2\Pi_{1/2}$) state.

On basis of this discussion, we expand this notation to higher D states. We attribute the intense peak next to the atomic D states to the Δ state. By comparing the 6^2D (Δ) with the 7^2D (Δ) state, this approach seems appropriate, because the peaks have the same asymmetric form. The energetic sequence of the Π and Σ states remains uncertain. So far, we identify the Σ state with the highest in energy (based on ref. [178]). Detailed theoretical calculations of higher excited states could contribute to a better understanding of the assignment of the states.

In the R3PI-TOF spectrum the last D (Δ) state, which can be separated from the P states, is the 13^2D (Δ) state. For lower states, in the overlapping range of LIF and R3PI-TOF data (not shown) no significant difference in the peak position was observed. The state, which is attributed to a molecular Π state, is very broad for lower states ($<12^2D$), which indicates a very steep, repulsive Cs–He_N interaction potential at the Cs-to-He_N distance during the time of excitation. The intensity increases from 12^2D (Π) to 13^2D (Π). This is also visible when comparing 11^2D (Π) to 13^2D (Π) in Figure 5.3. It goes along with a decrease of the widths of the peaks, when the position of the peak moves below the energy of the free-atom state. In contrast, the intensity of the D (Σ) state decreases and the peak disappears for the 11^2D state. The D (Π) state can be separated from the (Δ) state up to 15^2D. Above this, the P and D states are only noticeable as one peak. The highest resolved peak can be attributed to the $20^2D/21^2P$ states, probably the 22^2S state is also part of this band. Note that the assignments in Figure 5.2 refer to free-atom states. At the energy of free atom 20^2S the on-droplet 21^2S (Σ) state lies at about the same energy.

The Pseudo-Diatomic Model for Higher Excited States

So far, the Ak–He_N complex has always been treated in the pseudo-diatomic model. Based on the presented data of higher excited states and Rydberg states, this picture can be discussed in terms of the dependence of decreasing spin-orbit interaction and higher principal quantum numbers. The spectrum in Figure 5.2 agrees well with the pseudo-diatomic model. Here, n'p$\leftarrow$ np transitions are presented for the first time for Ak–He_N complexes. The two-step excitations into higher nP levels demonstrate that the pseudo-diatomic model is also applicable to higher electronically excited Ak atoms on He_N. Electric-dipole selection rules for bare atoms forbid transitions with $\Delta L = 0$. According to the molecular electric-dipole selection rules ($\Delta\Lambda = 0, \pm1$ and $\Delta\Omega = 0, \pm1$) it is possible to excite from the $6^2P_{1/2}$ ($^2\Pi_{1/2}$) state into $^2\Sigma_{1/2}$, $^2\Pi_{1/2}$, $^2\Pi_{3/2}$, and $^2\Delta_{3/2}$ states. In the pseudo-diatomic model the appearance of higher nP levels in the spectrum is thus expected and confirmed.

Furthermore, the diatomic molecule selection rules explain the fact that it was not possible to excite directly (with one photon) from the $6^2S_{1/2}$ ($^2\Sigma_{1/2}$) ground state into the 6^2D (Δ) state. In the two-step experiment, in contrast, this is possible. This is shown in Figure 5.2 at wavenumbers between 11400 cm^{-1} and 11650 cm^{-1} where the measurements of the directly excited $7^2P_{3/2}$ ($^2\Sigma_{1/2}$) state (green circles) and the 6^2D (Δ) state (red circles) overlap. One has to be careful when comparing these two states because of the different excitation schemes. The excitation takes place at different Cs–He_N distances and this influences peak positions in the spectrum.

For high Rydberg states this model loses significance, but as long as individual peaks are

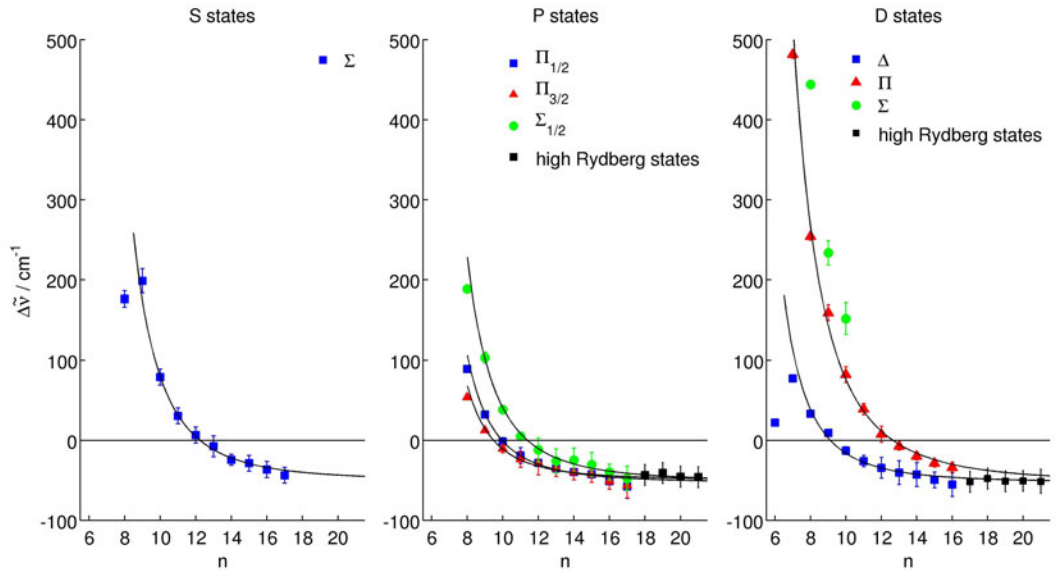

Figure 5.4: Shifts $\Delta\tilde{\nu}$ of the on-droplet peak centers with respect to the corresponding free-atom lines as a function of the principal quantum number n. The on-droplet line positions are obtained from Gaussian fits. The black lines are the results of non-linear least squares fits of Equation 5.1.

separable from each other, they can be attributed to pseudo-diatomic states.

Trends Towards the Ionization Limit

The spectrum presented in Figure 5.2 allows to follow the dependence on the principal quantum number of the shift of individual on-droplet spectral peaks with respect to the corresponding free-atom lines. Therefore, the individual on-droplet peaks are fitted with Gaussian functions and individual line shifts $\Delta\tilde{\nu}$ are obtained as differences of the positions of the Gaussian centers and the corresponding free-atom line positions. These shifts are displayed in Figure 5.4 as function of n, grouped corresponding to the free-atom states from which they originate. $\Delta\tilde{\nu}$ is negative when the energy of the on-droplet peak center is lower than that of the free-atom state, indicating that the Cs*–He_N potential has an attractive character. It can instantly be seen that all peaks move closer to the free-atom lines for increasing n, and that, above a certain value of n, the on-droplet excited states lie energetically below the free-atom states. This red-shift of the on-droplet peaks appears for principal quantum numbers greater that $n \approx 10$: $\Delta\tilde{\nu}$ is negative for S states at $n > 12$, for P states at $n > 9$ (Π states, for $n > 11$ the SO-splitting is neglected) and $n > 11$ (Σ states), and for D states at $n > 9$ (Δ states) and $n > 12$ (Π states). In general, the on-droplet peaks become narrower with increasing n, but at higher Rydberg states, when the peaks in the spectrum start to merge, position and width can not be determined unambiguously. Consequently, for $n > 12$ we obtain the same value for $\Delta\tilde{\nu}$ for the P (Σ) and the D (Δ) states (c.f. Section 5.1.3). Also, above $n = 17$ the Σ, Π, and Δ on-droplet states can not be separated anymore (c.f. Figure 5.2) and are thus plotted as black squares in Figure 5.4. In order to extrapolate towards the ionization limit we fit the shift $\Delta\tilde{\nu}$ as function of n. The energy of both the free-atom states and the on-droplet

Table 5.2: Parameters for the on-droplet part of the fit function given in Equation 5.1, as obtained from a non-linear least squares fit to the data points shown in Figure 5.4. $E_{\mathrm{I,dr}}$ is the ionization energy of the Cs–He_N system, Δd_{dr} is the change of the quantum defect (on-droplet minus free-atom). While the free-atom and the on-droplet quantum defect, $d_{\mathrm{at}}(n)$ and $d_{\mathrm{dr}}(n)$, are n-dependent in the simulation, here only the asymptotic values d_{at} and d_{dr} for $n \to \infty$ are given. The uncertainty in the last digit is given in parentheses.

state	$E_{\mathrm{I,dr}}$ / cm^{-1}	Δd_{dr}	d_{dr}	d_{at}
S (Σ)	31356(2)	-0.128(5)	3.92(1)	4.049 [153]
P ($\Sigma_{1/2}$)	31355(3)	-0.114(4)	3.44(1)	3.559 [185]
P ($\Pi_{1/2}$)	31353(2)	-0.063(3)	3.53(1)	3.592 [153]
P ($\Pi_{3/2}$)	31357(3)	-0.047(3)	3.51(1)	3.559 [185]
D (Π)	31354(7)	-0.26(1)	2.21(1)	2.476 [184]
D (Δ)	31354(3)	-0.071(5)	2.40(1)	2.476 [184]

states is assumed to be given by the Rydberg formula $E_{\mathrm{n}} = E_{\mathrm{I}} - R_\infty/(n-d)^2$, where E_{I} is the ionization energy, R_∞ is the Rydberg constant, and d is the quantum defect [120]. To simulate $\Delta\tilde{\nu}$ we simply take the difference of the Rydberg energies of the on-droplet states and that of the free-atom states:

$$\Delta\tilde{\nu}(\mathrm{n}) = E_{\mathrm{I,dr}} - \frac{R_\infty}{\left(n - d_{\mathrm{dr}}(n)\right)^2} - \left(E_{\mathrm{I,at}} - \frac{R_\infty}{\left(n - d_{\mathrm{at}}(n)\right)^2}\right). \tag{5.1}$$

In the free-atom part we take the known value for the ionization energy $E_{\mathrm{I,at}} = 31406.5\,\mathrm{cm}^{-1}$, and n-dependent values for $d_{\mathrm{at}}(n)$ [153, 184, 185]. In the on-droplet part, the parameter $E_{\mathrm{I,dr}}$ represents the ionization limit of the Cs–He_N system. The corresponding quantum defect $\Delta d_{\mathrm{dr}}(n)$ includes the n-dependent quantum defect of the free atom and a constant change, which accounts for the He_N perturbation: $d_{\mathrm{dr}}(n) = d_{\mathrm{at}}(n) + \Delta d_{\mathrm{dr}}$. $E_{\mathrm{I,dr}}$ and Δd_{dr} are taken as free parameters in a non-linear least squares fit. The results of the fits for the S (Σ), P (Σ, Π), and D (Π, Δ) states are displayed as black lines in Figure 5.4, and the obtained fit parameters are listed in Table 5.2. The first one or two data points are omitted for each of the fits and only data points up to $n = 16$ are used. However, it can be seen in Figure 5.4 that from $n \approx 17$ the difference of the shifts of different states is small and the fitted curves agree well with the black squares, where individual peaks can not be resolved. All data points (except those with lowest n values) agree perfectly with the model (Equation 5.1), demonstrating the Rydberg character of the Cs–He_N system. The fit results for the ionization energies of the Cs–He_N system are in excellent agreement and the average value is $E_{\mathrm{I,dr}} = 31355(1)\,\mathrm{cm}^{-1}$. This corresponds to a decrease of the ionization energy compared to the bare atom of $\Delta E_{\mathrm{I}} = -52(1)$ cm^{-1}, which is approximately half the value reported for the Na–He_N system [164], which was found to be droplet size dependent. It has to be taken into account that in our case the ground state for the second excitation step is the $6^2\mathrm{P}_{1/2}$ ($6^2\Pi_{1/2}$) state, which has its equilibrium at larger distances to the droplet than the $6^2\mathrm{S}_{1/2}$ state (c.f. the similar situation in Rb [2]). This might result in a smaller value of ΔE_{I} as compared to excitations from the $6^2\mathrm{S}_{1/2}$ state. However, a lowering of E_{I} is perfectly reasonable because of polarization effects and the resulting attractive interaction between the Cs^+ core and the He_N. In contrast, the differences in the droplet induced changes of the quantum defect Δd_{dr} are not surprising

because of the strong mixing of configurations in highly excited states [178], which can be assumed to be different for the individual states. The decrease of d_{dr}, which is the case for all states, and which has also been reported for Na–He_N [164], indicates that the configuration mixing at high states, after all, decreases the electron probability inside the positive core.

Finally, it is instructive to compare the radii of bare Cs* atoms with the droplet radius, especially for values of n where the Cs*–He_N potential starts to become attractive. Expectation values for orbital radii can be obtained from $\langle r \rangle = \frac{a_0}{2}[3n^{*2} - l(l+1)]$ (ref [120]), where $n^* = n - d_{\mathrm{at}}$ is the effective quantum number, a_0 is the Bohr radius, and d_{at} is the quantum defect as listed in Table 5.2. These radii are $r \approx 6.4\,\mathrm{nm}$ (S state, $n = 13$), $r \approx 3.2\,\mathrm{nm}$ (P ($\Pi_{1/2}$, $\Pi_{3/2}$) states, $n = 10$), $r \approx 5.5\,\mathrm{nm}$ (P ($\Sigma_{1/2}$) state, $n = 12$), $r \approx 4.3\,\mathrm{nm}$ (D (Δ) state, $n = 10$), and $r \approx 8.6\,\mathrm{nm}$ (D (Π) state, $n = 13$). These radii compare to a mean helium droplet radius of $r_{\mathrm{dr}} \approx 5\,\mathrm{nm}$, as obtained with the source conditions used here. A certain measure for the orbital penetration into the Cs^+–He_N core would be the inner turning point of the l orbitals. We find that for a D state the inner turning point is calculated as $3a_0$ only (Equation (2.25) Chapter 2 in ref [120]). Large l on the order of 13 or 14 would be required to guarantee zero penetration. On the other hand, plotting the radial parts of wavefunctions for $n = 20$ and $l = 2$ to 10 yields probabilities around 2 % that the electron spends inside a radius of $100a_0$. The angular dependence is neglected in this estimate. We believe that intermediate l will show interesting results that relate to the scattering of orbital electrons from the finite size superfluid.

5.1.4 Summary and Conclusions

By two-step laser excitation through the well-defined intermediate state $6^2P_{1/2}$, nS, nP, and nD states of Cs atoms bound to a helium nanodroplet could be explored. Excitations were monitored via LIF for principal quantum numbers $n \leq 10$ and via R3PI-TOF spectroscopy for higher states. For n up to 10, excited states are well represented by the pseudo-diatomic model, in which the droplet and the Cs atom each take the role of an atom in a diatomic with an "internuclear" quantization axis for the electronic angular momentum (Σ, Π, Δ, ...). Beyond $n = 10$, the Λ-substates start to merge. At the same time, the evaluation of the energies in terms of a quantum defect shines additional light on the character of the states. Around $n = 15$, Λ has practically lost its importance, the states have merged to S, P, and D series whose on-droplet energies are given by a Rydberg formula, in which the known free-atom quantum defects are reduced by a constant value and the on-droplet ionization limit is reduced by about $52\,\mathrm{cm}^{-1}$. Also around $n = 10$, the on-droplet states start to be lower in energy than the corresponding free-atom states, which indicates the beginning of a strong attraction of the Cs^+ core towards the interior of the droplet as has been observed as snowball formation after ionization [1]. The reported experiments represent an important step towards the preparation of the mentioned superatom consisting of a positive alkali ion inside a superfluid helium nanodroplet with an electron in a large orbital outside. Electronic states with larger orbital angular momenta will have to be excited in order to reduce the penetration of the electron into the helium.

5.1.5 Acknowledgments

We gratefully acknowledge the experimental advice of Prof. L. Windholz, who also loaned us his home made Ti:S laser. This work is supported by the Austrian Science Fund (FWF) under Grant FWF-E-1511P19759.

5.2 The Cs 7P state manifold on helium nanodroplets

The 7P states of Cs atoms were one of the first investigated higher excited states on helium droplets. First results were presented in the master thesis of R. Huber [162] and the first spectrum, including calculations of spectral peak positions, was published in 2010 [161]. The 7P state of Cs on He_N splits into the three molecular sub-levels $^2\Pi_{1/2}$, $^2\Pi_{3/2}$, and $^2\Sigma_{1/2}$. From the $6^2S_{1/2}(^2\Sigma_{1/2})$ ground state of the Cs–He_N system transitions into all three sub-levels are possible. Upon direct excitation of the 7P state from the ground state, a second photon from the same laser is sufficient to ionize the complex. For the 7P state experiments shown in the following, a Radiant Dyes DL-Midi (0.5-2 mJ) laser was used. 40% of the XeCl pump laser of the FL 3002 were used to pump the DL-Midi laser. As laser dyes in this spectral range, Coumarin 440 and Coumarin 2 were used. The advantages of a two-photon ionization compared to three-photon ionization are the relatively high ion signal, because only one intermediate state is excited, and the simple experimental setup, because only one laser is needed.

Previous investigations of this state were restricted to LIF spectroscopy experiments and a fixed droplet size [6, 161]. In this section R2PI spectroscopy signals are shown, which allow to study the dynamics of the system on the basis of the formation of exciplexes after excitation (Section 5.3). In addition, the droplet size dependence of the 7P state spectra is investigated.

Figure 5.5 shows the excitation spectrum of the 7P state manifold for different droplet sizes. The signals are smoothed and scaled to the maximum of the $^2\Pi_{3/2}$ state for the sake of a better comparability. The $^2\Sigma_{1/2}$ substate exhibits the strongest blue shift. The spin-orbit splitting between the $^2\Pi_{1/2}$ and the $^2\Pi_{3/2}$ states is well resolved. The broadening and the blue shift of the transition increases with the droplet size. This is the same behavior as it was found for Rb–He_N (next chapter). When states of atoms on helium droplets are compared to

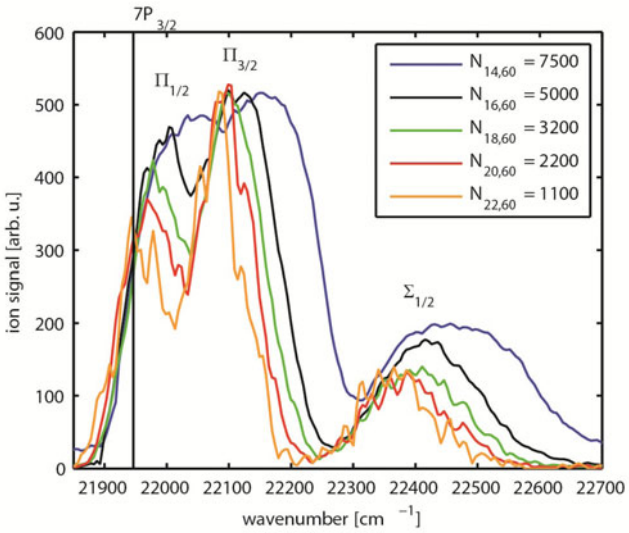

Figure 5.5: Cs–He_N R2PI excitation spectrum for different droplet sizes. The spectrum is recorded by monitoring the Cs^+–He_m ($m = 1-6$) ion yield as a function of the laser wavenumber. The signals are scaled to the maximum of the $\Pi_{3/2}$ state.

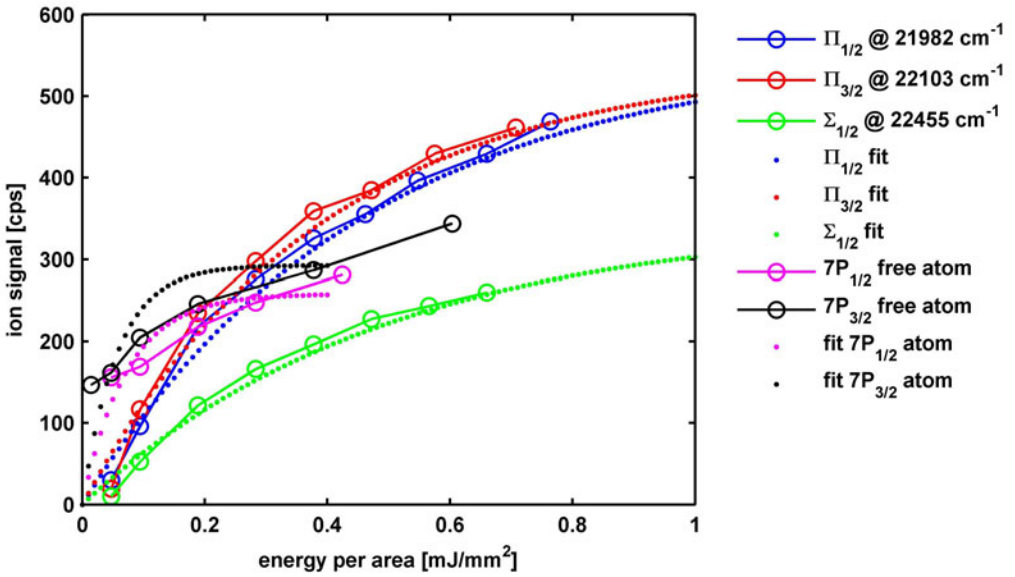

Figure 5.6: Dependence of the Cs–He_N and free atom 7P state signals on the laser pulse energy. The solid lines connect the data points. The dotted lines are the fit results to the data points.

free-atom states, the potential minimum of the ground state has to be taken into account (Rb, Cs: $< 20\text{cm}^{-1}$). The starting point for Cs–He_N R2PI spectroscopy is thus lower in energy. Accounting for this effect in the spectrum would correspond to a blue shift of the atomic lines. But since the exact value of the minimum is not known we neglect this effect. From Figure 5.5 it can be seen that all three potentials of the 7P state manifold are strongly repulsive.

5.2.1 Saturation effects and photoionization cross sections

For the Cs–He_N 7P $^2\Pi_{1/2}$, $^2\Pi_{3/2}$, and $^2\Sigma_{1/2}$ molecular sub-states, the dependence of the photo-ion signal on the laser pulse energy was investigated. This is shown in figure 5.6, where the photo-ion yield as a function of laser pulse energy per area is plotted. The on-droplet transitions are compared to the laser pulse energy dependence of transitions into the two spin-orbit split free atom states. The solid lines represent the measured data points, at wavenumbers 21982 cm^{-1}, 22103 cm^{-1} and 22455 cm^{-1}, corresponding to the $^2\Pi_{1/2}$, $^2\Pi_{3/2}$, and $^2\Sigma_{1/2}$ states, respectively. All monomer related ion masses are recorded (Cs-He_m, $m = 0 - 6$). The laser cross-section at the interaction zone with the doped droplet beam is approximately $1\,\text{mm}^2$. The signal is obtained for droplets of size $\hat{N}_{15,60} = 6200$. The free atom ion signal starts to increase in the μJ regime. In contrast, more laser pulse energy is needed if the atoms are on the surface of helium droplets. The signal starts to increase in the 0.01-0.1 mJ/mm^2 regime, where the slope of the curve is very steep. From Figure 5.6 it is evident that the on-droplet signal is not fully saturated, because the signal keeps increasing with the laser pulse energy. The transition on the droplet requires more laser pulse energy because it is spread out over a wide wavenumber range compared to the free atom transition.

For free atoms, absolute ionization cross sections has been deduced from laser pulse energy versus photo-ion yield measurements. The method is described in refs. [186, 187] and was

recently also applied for the lowest nP states of Rb [188] and Cs [189]. According to this method, the data in Figure 5.6 can be modeled with the following equation

$$N = N_0 \left[1 - \exp\left(-\frac{\sigma_{PI} U}{2\hbar\omega A}\right)\right]. \tag{5.2}$$

U/A is the pulse energy per area, $2\pi\omega$ is the laser frequency, N_0 is the number of atoms in the ionization volume and σ_{PI} is the photoionization cross section of the intermediate state. The fit results are shown in Figure 5.6. The formula is only strictly valid, if the intermediate state is saturated [189]. This is not the case in our experiment, hence the results are only a rough estimation. The number of atoms in the ionization volume also depends on the detection efficiency, which is not known exactly, but the detection efficiency for ions is usually close to unity. Assuming an interaction volume of $(0.5\,\mathrm{x}\,0.75\,\mathrm{x}\,5)\,\mathrm{mm}^3$, the asymptotic value of the photo-ion yield in Figure 5.6 corresponds to the situation where the laser ionizes all N_0 atoms on the helium droplets in this volume. From this value, the particle density at the interaction volume can be calculated for example with $\sim 3\,\mathrm{x}\,10^9$ atom doped droplets per unit volume for $N_0 = 550$ obtained for the $^2\Pi_{3/2}$ state. In addition to other effects, the broadened lines and especially the droplet induced inhomogeneous line broadening will also contribute to the underestimation of the calculated particle density and to the differences in the asymptotic photo-ion yield values. If the laser is set to a certain wavenumber, the effect of inhomogeneous line-broadening is due to the fact that predominantly atoms of one corresponding droplet size will be ionized. Not all atoms on the droplets are excited and ionized with the same efficiency. Thus the given calculated particle density is only an estimation for a lower limit.

Another result from the fit of the data points to Equation 5.2 is the absolute photoionization cross sections. The fit results for the atomic transition are very uncertain because of insufficient data points at low laser pulse energy. The fit results for the ionization cross section from the atomic states are $\sigma_{PI} = 1.6\,\mathrm{Mb}$ ($7^2\mathrm{P}_{1/2}$) and $\sigma_{PI} = 2\,\mathrm{Mb}$ ($7^2\mathrm{P}_{3/2}$). These values can be compared with more accurate measurements in reference [190], where values of $\sigma_{PI} = 6.2\,\mathrm{Mb}$ ($7^2\mathrm{P}_{1/2}$) and $\sigma_{PI} = 8.8\,\mathrm{Mb}$ ($7^2\mathrm{P}_{3/2}$) were reported. They are in the same order of magnitude, but they show the bad accuracy of the free atom fits. However, the fit results are more accurate for the transitions on the droplet and the results are: $\sigma_{PI} = 0.25\,\mathrm{Mb}$ ($^2\Pi_{1/2}$), $\sigma_{PI} = 0.3\,\mathrm{Mb}$ ($^2\Pi_{3/2}$) and $\sigma_{PI} = 0.23\,\mathrm{Mb}$ ($^2\Sigma_{1/2}$). Those values are more than one order of magnitude lower than the free atom literature values.

This rough estimation demonstrates that more laser energy is required for excitation of on-droplet states than for free-atom atom states. On droplet transitions are not fully saturated, even if pulsed lasers are used.

5.3 Excited state dynamics

Upon excitation of an excited state, alkali atoms usually desorb from the helium droplet. So far, no evidence for surface bound states of alkali atoms, except for the first excited P states in Rb and Cs, was found.

The dynamics of the desorption process can be investigated by mass resolved excitation spectra. In the Cs–$\mathrm{He_N}$ R3PI excitation spectrum in Figure 5.2, only the sum of Cs-He_m ($m = 1 - 6$) ion yield was presented. However, a comparison of different Ak^+ and Ak^+-He_m

ion masses in various spectral ranges gives additional information about the fragmentation dynamics of the Ak-He_N system and the assignment of excited states. The Cs 7P state in the Cs–He_N system is ideally suited for such investigations because of its well separated states. Figure 5.7 shows a mass resolved excitation spectrum with the fragment ions, which are formed upon excitation and ionization of the different molecular sub-states of the 7P state manifold. The spectrum was recorded for droplets consisting of $N_{16,60} = 5000$ helium atoms. It can be seen that an ionization via the $^2\Pi_{1/2}$ and $^2\Pi_{3/2}$ states leads to the formation of exciplexes. The highest signal is monitored for the Cs*-He exciplex. In contrast an ionization via the $^2\Sigma_{1/2}$ state leads predominantly to the desorption of bare Cs atoms, but also a small number of Cs*-He exciplexes is detected.

Note that in this spectrum, the 6D (Δ) state is not observed (see ref. [6]) because this transition is forbidden from the ground state. This observation demonstrates the validity of the diatomic selection rules for the Cs–He_N system. For alkali atoms on helium droplets it is known that for lower Rydberg states an ionization via an high molecular substate leads to an increased probability for the formation of exciplexes [7, 165, 166]. In ref. [7] this was shown for the Rb–He_N 5D (Δ) state manifold. In contrast no exciplex formation was found, when ionizing Li and Na via the $(n+1)$s$\leftarrow n$s transition. Only a small fraction of Ak atoms desorb from the surface when a Σ molecular substate is involved in the ionization path. These findings and general trends for the exciplex formation in Ak-He_N systems are in excellent agreement with our results on the 7P state. The observed mass dependence is also in agreement with the explanation based on orbital orientations to the droplet surface in chapter 4.2. For the 7P state this means that in the case of the two Π states, the 7P orbitals are oriented parallel to the surface. The helium atoms are accommodated near the waste of the excited Cs atom, where the electron density is lower. In contrast, in the case of the Σ state, the 7P orbital points straight towards the droplet, and hence it experiences a stronger repulsive interaction and the formation of exciplexes is suppressed.

Rydberg state desorption dynamics

When the principal quantum number gets higher and the intermediate Rydberg region goes over into the higher Rydberg state region, the Λ dependence of the exciplex formation vanishes and the exciplex formation probability increases independent of the molecular substate. This transition from one region into the other lies in the spectral region of about 19300 cm^{-1} to 20000 cm^{-1} for Rb–He_N and 18700 cm^{-1} to 19300 cm^{-1} for Cs. This is approximately the region where the blue shift of the states goes over into the red shift and the size of the electron orbital becomes larger than the droplet. The energy spacing between adjacent energy levels is in the order of < 200 cm^{-1} and mixing of states becomes more important. Above this region, exciplex formation is independent of the intermediate state. This can be seen in Figure 5.2 by the increase in the Cs^+-He_m signal. This effect was also observed for Na–He_N in ref. [164]. There it was concluded from ZEKE and REMPI experiments that the observation of larger exciplexes indicates that the atoms excited into higher Rydberg states remain longer on the He_N surface. Figure 5.8 shows the mass resolved excitation spectrum for the Cs-He_N system for droplets with $\hat{N}_{60,14} = 7500$. The Cs^+ and Cs^+-He_m ($m = 1, 2, 3, 4$) ion yield is plotted as a function of the wavenumber of laser L2. The molecular substates have merged completely above 19550 cm^{-1} and the Rydberg transitions form a hydrogen like series of progressive peaks.

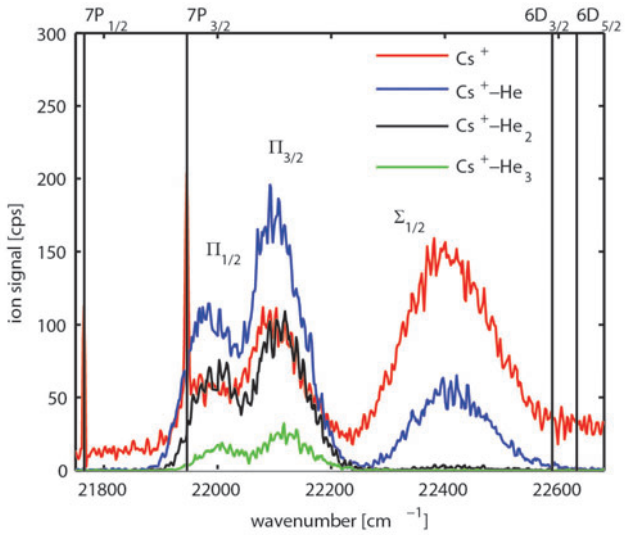

Figure 5.7: Cs–He$_N$ R2PI excitation spectrum for droplets with $N_{16,60} = 5000$. The ion yield for Cs^+–He$_m$ $m = (0, 1, 2, 3)$ is monitored as a function of the laser wavenumber. Free atom lines are depicted as solid vertical lines. The spin-orbit split $\Pi_{1/2}$ and $\Pi_{3/2}$ molecular-substates are well separated. The two Π components are followed by the energetically higher $\Sigma_{1/2}$ state.

The formation of exciplexes is increased for all states. This increased probability of exciplex formation and the observed red-shift of the states indicates that the attractive interaction between the helium droplet and the Ak ion core pull the ion core into the droplet when the electron is far away.

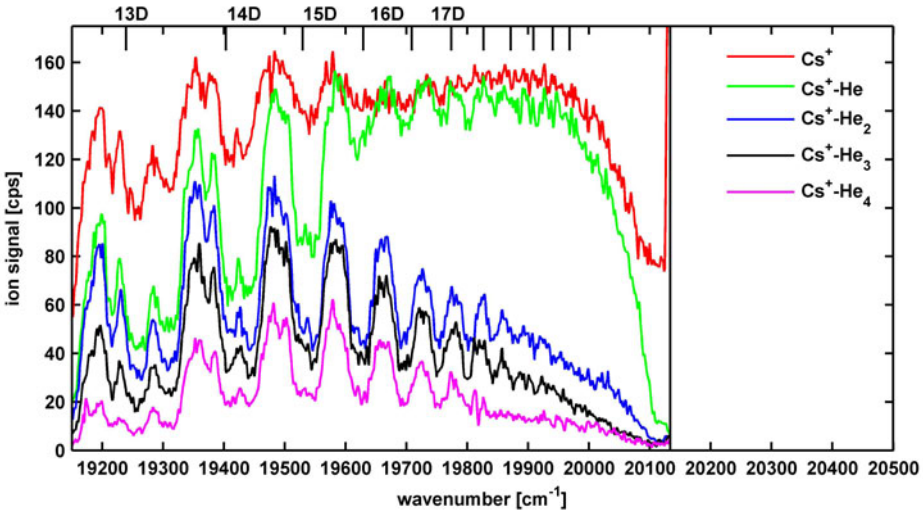

Figure 5.8: Cs^+ and Cs^+-He$_m$ $(m = 1, 2, 3, 4)$ ion yield for Cs-He$_N$ high Rydberg states. The excitation spectrum was recorded for $\hat{N}_{60,14} = 7500$ droplets. For high Rydberg states exciplex formation is independent of the Λ quantum number of the molecular substate. Positions of atomic states and the field corrected ionization threshold are indicated as vertical solid lines. The steep increase of the Cs^+ at the threshold is caused by the ionization of free Cs atoms.

5.4 Droplet size effects

The Cs–He_N excitation spectrum in section 5.1 was recorded for a fixed droplet size. Later experiments with Rb–He_N, in which the droplet size dependence of excited states was investigated, revealed that there is a systematic behavior of the droplet size dependent variation of spectral positions of observed transitions. This section shows similar results for the Cs–He_N system, which demonstrates the similarity between both systems.

As an example for lower states we show the droplet size dependence of the spectral position of the Cs–He_N 7D (Δ) state in Figure 5.9. The excitation spectrum was recorded by LIF spectroscopy. The transition is blue-shifted with respect to the free-atom line. The blue shift is stronger for large droplets. Also the width of the spectral peak decreases with the droplet size. This is similar to the corresponding 6D (Δ) state in Rb, which is discussed in the next chapter.

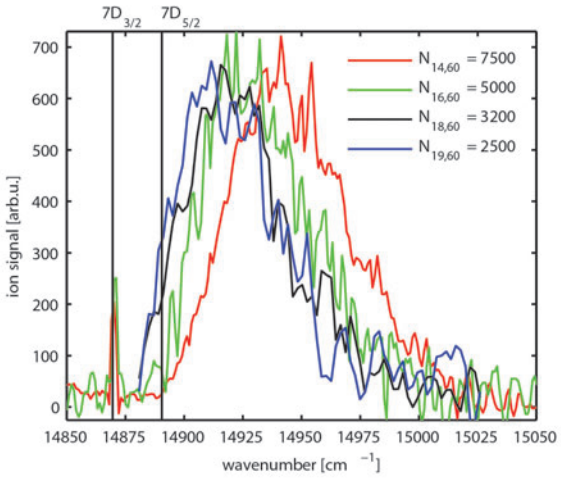

Figure 5.9: LIF two-step excitation spectra of the Cs–He_N 7D (Δ) state for different droplet sizes. The signals are scaled so that the maxima of the 7D (Δ) peak are equal to the peak maximum of the Cs–He_{7500} signal. Atomic lines are drawn as vertical solid lines.

5.4.1 Droplet induced line-broadening

The fact that ionization via the 7P ($\Sigma_{1/2}$) state does not lead to a desorption of $CsHe_m$ with $m > 1$ can be exploited for an investigation of the droplet induced line-broadening effect. In this optical-optical double resonance (OODR) experiment [191] one laser (DL-Midi) is scanned across the 7P ($\Pi_{1/2}$) and ($\Pi_{3/2}$) state while the $CsHe_{2-5}$ signal is monitored. A second laser (FL3002) is kept at 22503 cm^{-1} at the 7P ($\Sigma_{1/2}$) state. The signal in Figure 5.5 suggests that at this wavelength predominantly atoms on large droplets are excited and ionized. Thus the second laser is expected to selectively deplete the large droplet signal. The exclusion of the $CsHe_m$ with $m \leq 1$ signal guarantees that no background signal is caused by the second laser and all counts are related to the laser which scans across the 7P ($\Pi_{1/2}$) and ($\Pi_{3/2}$) states. The difference between the depletion laser "off" and depletion laser "on" signal is a measure for the depletion (a higher signal corresponds to a higher depletion). The result is shown in Figure 5.10. The experiment was repeated (Me 1 and Me 2) and is reproducible. It shows the

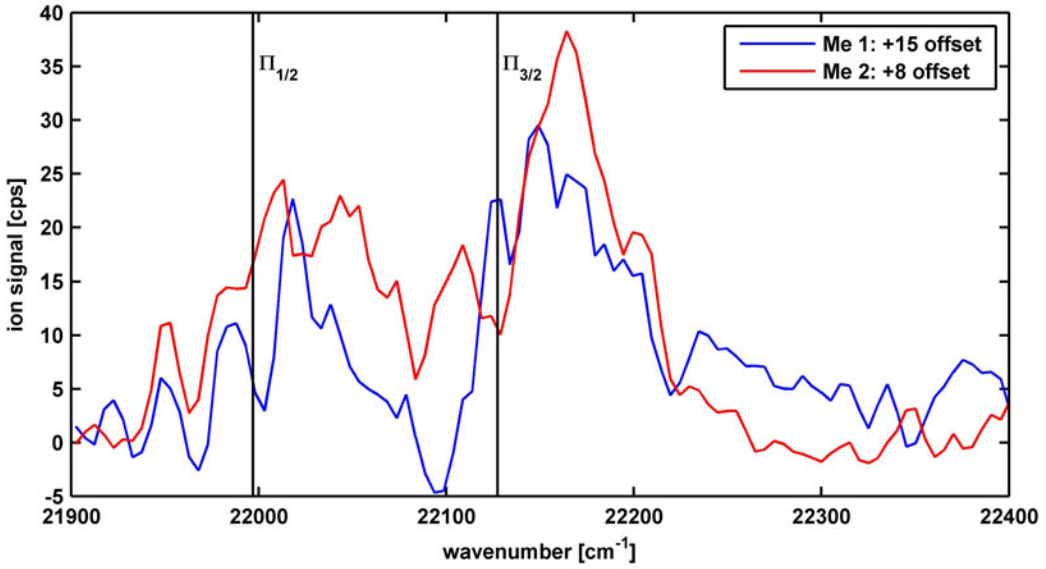

Figure 5.10: Investigation of the droplet induced line-broadening of the Cs–He_N 7P state. One laser is scanned across the 7P ($\Pi_{1/2}$) and ($\Pi_{3/2}$) states (the peak center is shown as vertical line) while the $CsHe_{2-5}$ signal is monitored. A second laser is kept fixed at 22503 cm^{-1} at the 7P ($\Sigma_{1/2}$) state. The signal shows the difference between the signal without and with the depletion laser and it was offset corrected so that the signal on the left and right end of the scale is at zero cps. An increased signal is detected slightly to the right of the center of the Π components, indicating a depletion of large droplets. The two different signals (Me 1 and Me 2) show the same experiment with the same lasers but at different times to test the reproducibility.

expected behavior: If the depletion laser is set to the large droplet part of the 7P ($\Sigma_{1/2}$) state, the depletion of large droplets is detected at slightly higher wavenumbers than the peak centers of the 7P ($\Pi_{1/2}$) and ($\Pi_{3/2}$) state. Unfortunately this experiment has several disadvantages. The spatially overlapped and synchronized lasers can cause unwanted effects. For example the second laser can contribute to the ionizing step of the first laser. Also the broad transition into the 7P ($\Sigma_{1/2}$) state is a disadvantage because due to the steep repulsive potential of this state, the contribution of different droplet sizes will overlap. And in addition, the signal is very low and the signal to noise ratio is relatively high because of the exclusion of the $CsHe_m$ with $m \leq 1$ signal. These results show that a more sophisticated experiment which uses cw lasers to allow spatial separation of the lasers and a more suitable (narrower) transition for the depletion will give much better signals. However, the current data demonstrate that the droplet size distribution is one of the origins of the inhomogeneous line-broadening effect.

5.4.2 High Rydberg states

In contrast to lower states, higher Cs–He_N Rydberg states are red-shifted with respect to free-atom states. This is shown in Figure 5.11 for the Cs–He_N system for droplets consisting of $\hat{N}_{60,15} = 6200$ and $\hat{N}_{60,17} = 4100$ helium atoms. We observe a similar behavior for Cs–He_N

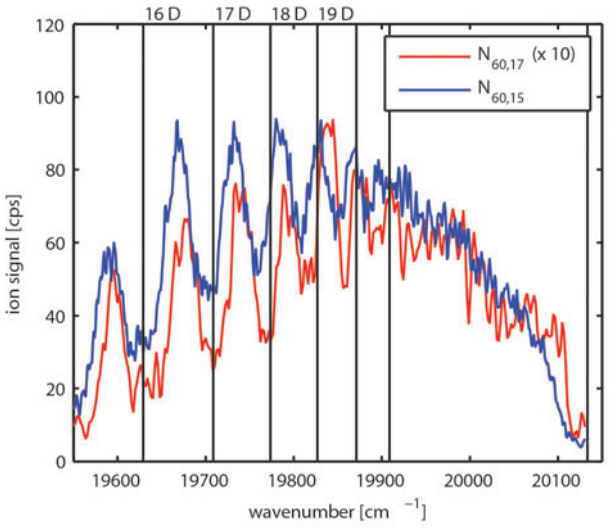

Figure 5.11: Cs–He_N excitation spectrum of high Rydberg sates monitored on the masses of Cs^+-He_m $(n = 1 - 6)$ for droplets sizes of $\hat{N}_{60,15} = 6200$ and $\hat{N}_{60,17} = 4100$. The vertical lines represent atomic transition and the field corrected ionization threshold.

as it was found for Rb [7], which suggests that our findings might be valid for other surface-bound atoms as well. At high Rydberg states the molecular axis has lost its importance. All molecular sub-states have merged and form a hydrogen-like series of Rydberg states. The states converge to the ionization threshold, which depends on the droplet size, but not on the molecular substate. This is reasonable since the intermolecular axis is no longer important for those states. All states are red shifted with respect to free-atom states. The red shift and the linewidth depend on the droplet size and the influence of the droplet is stronger for large droplets. The highest state which could be identified corresponds to the 20D free atom state. Above this state no individual transitions could be resolved and the states form a continuum. In Figure 5.11 also the decrease of the ionization threshold for different droplet sizes can be seen. The threshold is lower for larger droplets, which is in agreement with the results obtained from the Rydberg formula fits [6] and measurements of the Cs–He_N ionization threshold by monitoring the production of Cs^+–He_N ion complexes.

5.5 Comparison of LIF and R3PI spectra

LIF spectra were recorded with cw lasers, which have a photon density at the interaction volume between laser and the He_N beam much smaller than the photon density of the pulsed laser systems used in the R3PI experiments with pulse energies in the mJ range. The use of pulsed lasers allows to draw conclusions about the dynamics of the Ak–He_N system. Thus the differences in the LIF and R3PI spectra can give information about the duration of relaxation processes and saturation effects. The findings about the relaxation process of the intermediate state in section 4.3 are supported by the comparison of LIF and R3PI spectra. In Figure 5.12 and 5.13 the Cs-He_m $(m = 1 - 6)$ signal is plotted and compared to the LIF signal (from Figure 5.2). The spin-orbit split 6P $(\Pi_{1/2})$ and $(\Pi_{3/2})$ components are well separated.

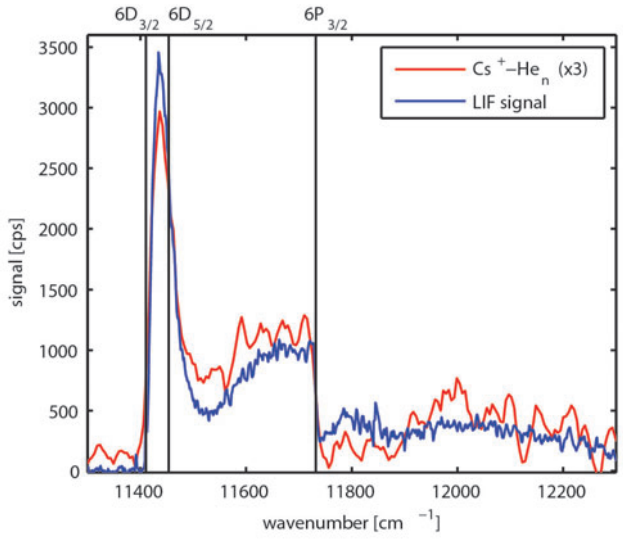

Figure 5.12: Comparison of the Cs–He_N LIF and R3PI-TOF excitation spectrum for the 6D state manifold. The R3PI-TOF spectrum is obtained by recording the Cs^+-He_n ($n = 0 - 4$) ion yield as a function of L2. The 6D (Δ) state is followed by a second maximum, which could not be recorded fully because of a resonance of L2 with the D2 transition. The $6^2P_{3/2}$ state is depicted as vertical line, where the spectral position refers to the ground state.

The 6P ($\Sigma_{1/2}$) state is much more blue shifted than the Π states and it is followed by the transition into the 7D (Δ). No significant differences are noticed between both signals. The R3PI excitation spectra are obtained by using pulsed lasers with a full width at half duration (FWHD) of 30 ns. From Figure 5.12 and 5.13 it can be seen that peak positions obtained with the two different techniques coincide. Slight differences occur because the cw LIF signal reflects the portion of desorbed atoms due to the suppression of exciplex emission by the used filter. Thus we conclude that the relaxation process has to take place on a few-nanosecond or sub-nanosecond time scale, much shorter than the duration of the laser pulse. Otherwise a difference between the cw and pulsed laser experiments should have been observed. This difference can be estimated by the sum of the excess energy of the laser and the depth of the $n^2P_{1/2}$ ($^2\Pi_{1/2}$) potential and would be in the order of approximately $10 - 15\,cm^{-1}$. This estimation is in agreement with comparisons between a two-photon one color and a two-step excitation of the Rb–He_N 5D state manifold [2]. For the Cs–He_N system comparisons of LIF and R3PI spectra are shown in Figure 5.12 for the 6D state manifold and in Figure 5.13 for the 7D and 6P state manifold. For lower states the signal obtained by LIF spectroscopy is superior because of the higher duty cycle of the cw laser. The Cs–He_N 6D state is the analogon to the Rb–He_N 5D state (i.e. the second lowest D state). Comparing both species, the splitting between the Δ and Π, Σ molecular substates is larger in the Cs–He_N system. The abrupt decrease of the Cs–He_N signal, which coincides with the free atom $6^2P_{3/2}$ state is caused by the excitation of the $6^2P_{3/2}(^2\Pi_{3/2})$ transition, which competes with the excitation into the $6^2P_{1/2}(^2\Pi_{1/2})$ intermediate state (see Section 5.1).

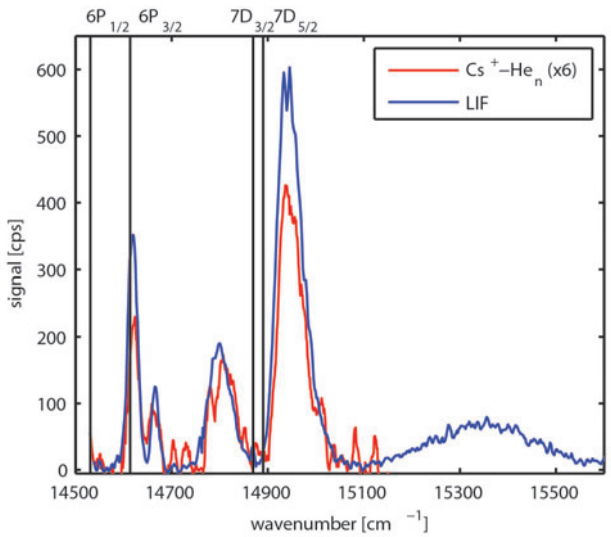

Figure 5.13: Comparison of the Cs–He_N LIF and R3PI-TOF excitation spectrum for the 6P and 7D state manifold. The R3PI-TOF spectrum is obtained by recording the Cs^+-He_n ($n = 1-6$) ion yield as a function of L2. The spin-orbit split 6P $\Pi_{1/2}$ and $\Pi_{3/2}$ components are well separated. The 6P ($\Sigma_{1/2}$) state is much more blue shifted than the Π states. The intense 7D (Δ) state is followed by the Π substate, which was only recorded with LIF spectroscopy.

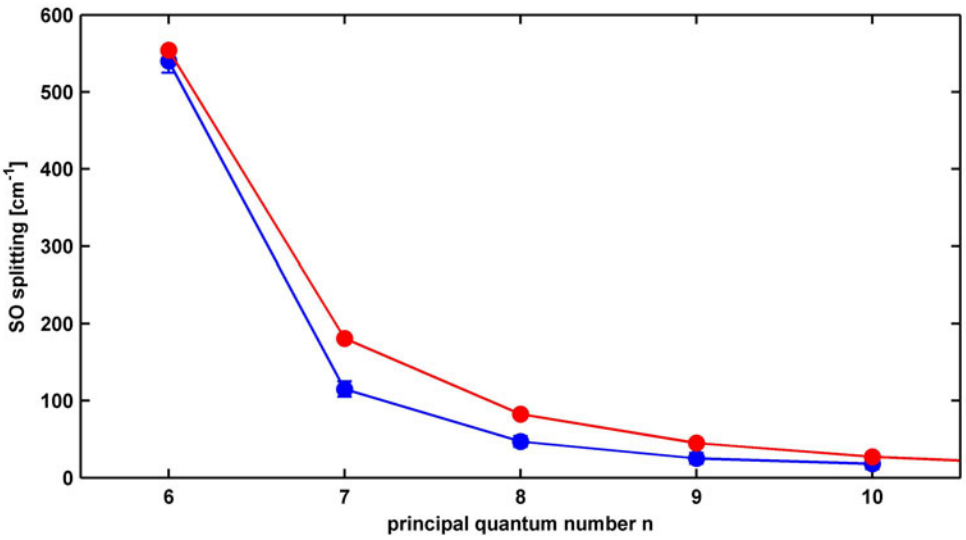

Figure 5.14: Comparison of the spin-orbit split Cs–He_N nP $\Pi_{1/2}$ and $\Pi_{3/2}$ components and the free atom $n^2P_{1/2}$ and $n^2P_{3/2}$ states.

5.6 Spin-orbit splitting of the Cs $n^2P_{1/2,3/2}$ states on helium nanodroplets

Among the Ak–He_N systems the Cs–He_N complex is the only one where the spin-orbit splitting of the nP $\Pi_{1/2}$ and $\Pi_{3/2}$ components can be studied (up to $n = 10$). For all other systems, the droplet induced line broadening is larger than the spin-orbit splitting. This is shown in Figure 5.14. It can be seen that the separation between the $\Pi_{1/2}$ and $\Pi_{3/2}$ is smaller than the separation of the free atom $n^2P_{1/2}$ and $n^2P_{3/2}$ states.

Chapter 6

Spectroscopy of Rb atom Rydberg States on He Nanodroplets

The main part of this chapter corresponds to the J. Phys. Chem. Lett. 3, 1404-1408 (2012) article (ref. [6]). This work includes the complete Rb-He_N excitation spectrum. It includes an investigation of the droplet size dependence of Rydberg series. Excitation spectra are obtained by using R3PI-TOF mass spectroscopy. This article corresponds to the first section in this chapter. The following sections include additional detailed studies of the excitation spectrum and the droplet induced line shifts, as well as detailed two-photon ionization studies of the 4D states, which will be published in ref. [8].

6.1 Rubidium on Helium Droplets: Analysis of an Exotic Rydberg Complex for $n^* < 20$ and $0 \leqslant l \leqslant 3$

Rubidium atom Rydberg states perturbed by helium droplets of different sizes provide insight into the role of a nanosized dielectric on the Coulomb potential. The observation of droplet size dependent shifts of excited states with respect to bare atom states is explained by a decreased quantum defect and a lowered ionization threshold. Within the scope of a Rydberg model we demonstrate that quantum defects and ionization potentials are constant for each specific Rydberg series, which confirms the Rydberg character of excited Rubidium states on helium droplets. A set of six Rydberg series could be identified. Individual Rydberg states are observed with effective principal quantum numbers up to $n^* \approx 19$ and $l \leqslant 3$, for which the expectation value of the electron orbital radius is about ten times larger than the droplet radius.

6.1.1 Introduction

Rydberg state spectroscopy provides important insights into the charge distribution of an ionic core through its interaction with a single outer electron. From the hydrogen atom to small molecules [192, 193] and clusters [123], Rydberg states are found in a wide variety of systems. Most recently, the Rydberg state concept has been applied to the "heavy Bohr atom" [124], a H^+H^- ion-pair system, bound by the Coulombic $1/r$ potential. The extraordinary

properties of Rydberg atoms enable the formation of ultralong-range Rydberg molecules where the rubidium (Rb) macrodimer has recently been characterized spectroscopically [194].

We report on a comprehensive and systematic investigation of nS, nP, nD, and nF Rydberg series of the Rb-helium nanodroplet (Rb–He_N) complex, which forms a new type of exotic Rydberg system. When an alkali metal (Ak)–He_N cluster is excited into states where the diameter of the valence electron orbital becomes large compared to the droplet diameter, recent experiments indicate that the system consists of an Ak ion immersed inside the He_N surrounded by a Rydberg electron [5, 6]. This exceptional configuration of Ak–He_N is of fundamental interest and questions about its properties and stability are of importance [6, 164, 165, 183, 195]. In this letter we focus on the Rb–He_N system, which exhibits a favorable electronic structure and provides essential advantages in terms of accessibility of states with high orbital angular momentum quantum number l and in terms of the assignment of D and F states. We provide evidence for the excitation of a Ak–He_N system into a nF state. In addition, we present the new application of a method for the assignment of Ak–He_N Rydberg states, which is similar to a method for the assignment of Rydberg states in l-mixed supercomplexes [192, 193]. Excited states are organized into Rydberg series, allowing the determination of series specific ionization thresholds (IT) and quantum defects (QD). We find that the IT and the QD are lowered due to the presence of the He_N and both depend on the number of He atoms in the droplet. The droplet size dependence of the QD gives information about the l value of the atomic state from which the observed Rb–He_N states originate. The advantage of the bound $5^2P_{1/2}$ ($^2\Pi_{1/2}$) Rb–He_N state [174] as intermediate state in a two-step excitation scheme [2] is that it enables access to states with high l. High l and n states are of interest because the electron wavefunction is spread out and the penetration of the Rydberg electron into the He_N is reduced. Due to the smaller overlap of high-l orbitals with the core of the Rb–He_N complex, one should expect longer lifetimes of the high-l states. Lower electronically excited states of Ak atoms, which reside on the surface of He_N, have been investigated since the early days of helium nanodroplet isolation spectroscopy [18]. The D lines of the Ak atoms, from Li [159] to Rb [160] and Cs [89] are among the best investigated electronic transitions in doped He_N. In contrast, relatively little work has been done on the characterization of higher excited states [2, 161, 166] and Rydberg states [6, 164, 165]. Only Na–He_N [164, 165] and Cs–He_N [6] Rydberg states were investigated so far. The lack of a bound intermediate state in the Na–He_N system restricts the investigations to Π and Σ states (see below). For the Cs–He_N system, where the use of a two-step excitation scheme is possible [2], no investigation of droplet size dependent effects was performed and the experimental detection scheme forbids the complete recording of the 6D state manifold. The Rb–He_N complex provides the ideal Ak–He_N system for following complete Rydberg series up to the IT.

For characterization of the observed Rydberg states, we use the well-established pseudo-diatomic model for the Ak–He_N system [159], where the He_N is treated as one atom in a diatomic molecule and the molecular axis is defined by the connection between the center of the droplet and the Ak nucleus. In this picture the projection Λ of the valence electron's angular orbital momentum onto the molecular axis is a conserved quantity, and the diatomic selection rules for electronic transitions apply ($\Delta\Lambda = 0, \pm 1$).

6.1.2 Experimental

A detailed description of the experimental setup and the excitation scheme can be found in Chapter 2 and in ref. [6, 76, 196]. In brief, helium droplets are produced in a supersonic jet expansion of high purity helium gas through a cold 5 μm nozzle ($p_0 = 60$ bar, $T_0 = 14$ - 20 K) into vacuum. The droplet sizes follow a log-normal distribution and the distribution maxima $\hat{N}_{p_0,T_0}$ are $\hat{N}_{60,20} = 2000$, $\hat{N}_{60,18} = 3200$, $\hat{N}_{60,16} = 5000$, and $\hat{N}_{60,14} = 7500$, corresponding to droplet radii of 28 Å, 33 Å, 38 Å, and 44 Å, respectively [14]. The He_N are doped by means of a resistively heated pickup cell, containing a small amount of Rb metal. A resonant three-photon-ionization (R3PI) scheme is applied. The ion yield is monitored with a time-of-flight (TOF) mass spectrometer (Jordan D-850 AREF). A pulsed Ti:Sapphire laser L1 (Coherent Indigo-S, 30 ns pulse duration, 0.15 mJ pulse energy) excites the Rb–He_N system into the $5^2P_{1/2}$ ($^2\Pi_{1/2}$) intermediate state (1st step). L1 is spatially overlapped and synchronized with a tunable pulsed dye laser L2 (Lambda Physik FL 3002, 26 ns, $\sim$6 mJ), which induces a transition to Rb–He_N Rydberg states (2nd step). A third photon of either L1 or L2 ionizes the complex and the resulting ions are counted while L2 is scanned. The counter is set to a time window, corresponding to the mass range of Rb^+–He_m ($m = 1-6$). This mass range was found not to be influenced by parasitic signals arising from, e.g., fragmented Rb dimers or bare Rb atoms. The obtained ion signal is smoothed and the spectra obtained with different dyes are scaled to match each other. Thus intensities of different peaks can not be compared. For the investigation of high Rydberg states ($\tilde{\nu}_{L2} > 20250\,cm^{-1}$) the TOF extraction field was turned off during the laser pulse and activated 2 μs afterwards in order to avoid distortions (Stark-effect).

6.1.3 Results and Discussion

Rb–He_N excitation spectra obtained with different droplet sizes are presented in Figure 6.1. The spectra are plotted as a function of the laser L2 wavenumber. They begin at the 5D state manifold and continue to the IT. The highest resolved Rydberg state has an effective principal quantum number of $n^* \approx 19$ (the effective principal quantum number is defined as the difference between the principal quantum number and the quantum defect). The recorded spectrum clearly shows a regular pattern of states, which repeats with integer steps of n^*. Thus we organize the observed states into Rydberg series, as indicated on top in Figure 6.1. Considering Rb–He_N sub-states arising from Rb nS, nP, nD, and nF bare atom states, nine allowed transitions into the molecular sub-levels S(Σ), P(Π, Σ), D(Δ, Π, Σ), and F(Δ, Π, Σ) are expected. The assignment is helped by a procedure that was applied by the Field group for the identification of CaF [192] and BaF [193] Rydberg states. The effective principal quantum number n^* of each of the 9 subseries should differ by approximately 1 for consecutive members. With this condition, six sequences could be assigned without prior knowledge of absolute quantum numbers. Assuming a constant QD and IT for the higher members, absolute quantum numbers could be determined. These values were confirmed by following down a series to its lowest members that agree well with the experimental results in ref. [2] (5D state manifold) and with the calculations (states up to the 7P manifold) in ref. [178].

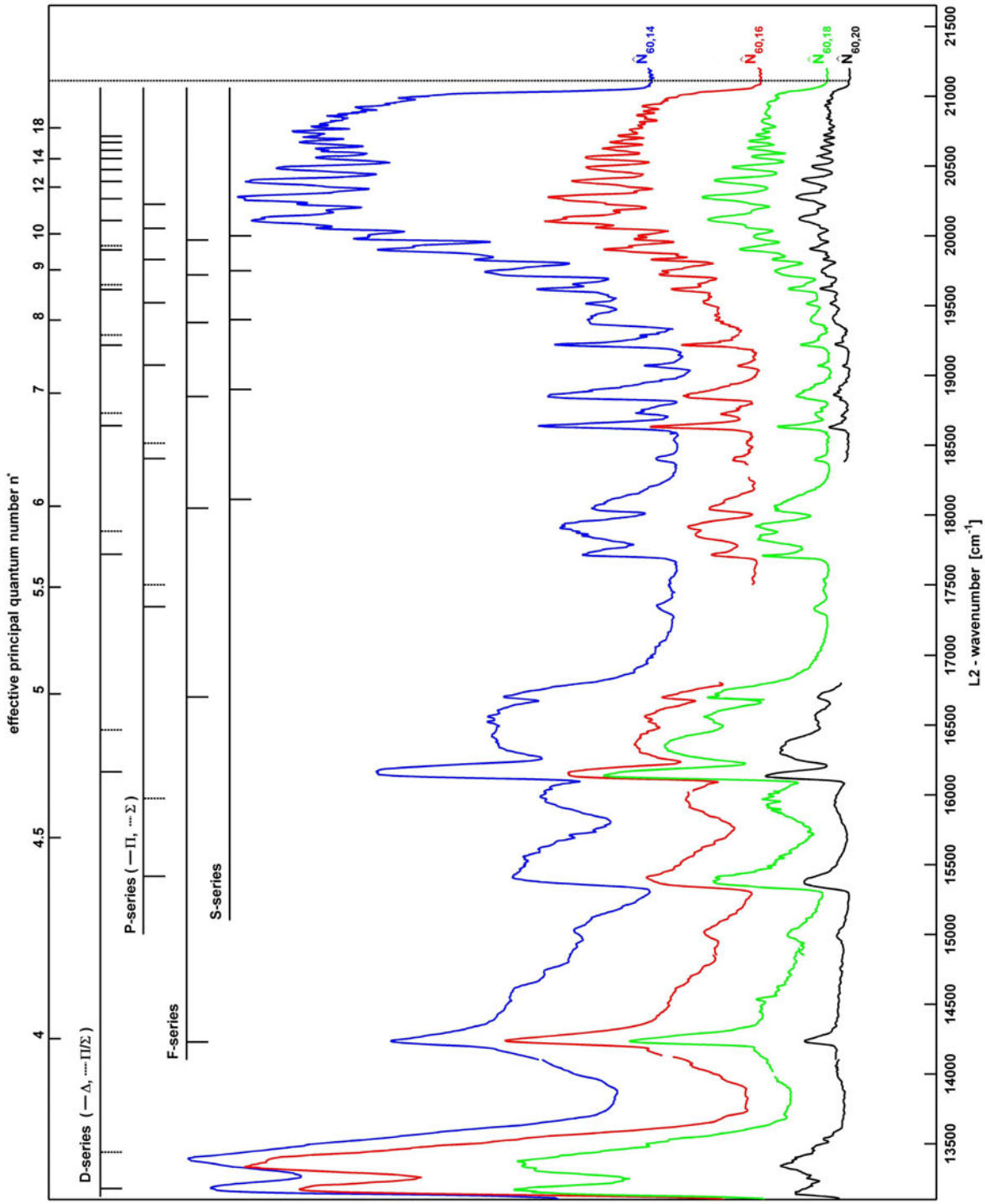
effective principal quantum number n*
4
4.5
5
5.5
6
7
8
9
10
12
14
18
D-series (—Λ, ···Π/Σ)
P-series (—Π, ···Σ)
F-series
S-series
$\hat{N}_{60,14}$
$\hat{N}_{60,16}$
$\hat{N}_{60,18}$
$\hat{N}_{60,20}$
13500
14000
14500
15000
15500
16000
16500
17000
17500
18000
18500
19000
19500
20000
20500
21000
21500
L2 - wavenumber [cm^{-1}]

Figure 6.1 *(facing page)*: Excitation spectra of Rb–He_N recorded with R3PI-TOF spectroscopy for droplet sizes of $\hat{N}_{60,20} = 2000$ (black), $\hat{N}_{60,18} = 3200$ (green), $\hat{N}_{60,16} = 5000$ (red), and $\hat{N}_{60,14} = 7500$ (blue) as a function of the laser L2 wavenumber. Laser L1 excites the $5^2P_{1/2}$ ($^2\Pi_{1/2}$) intermediate state (fixed at $12600\,cm^{-1}$). From this state the second laser L2 is scanned across Rydberg states. A third photon ionizes the complex. The signal is obtained by monitoring the ion yield of the most abundant Rb^+–He_m ($m = 1-6$) complexes with a TOF mass spectrometer. The states are grouped into Rydberg series as indicated on top. The vertical dashed line marks the ionization threshold of the bare atom and the top scale shows the effective principal quantum number n^* of the bare atom.

The D(Δ)-features appear close to the bare atom nD lines, which is important for the confirmation of F states (see below). Table 6.1 shows the dependence of the D(Δ)-feature on the droplet size and the principal quantum number. The peak shift and the line width for lower states increases with the droplet size. The lower states are strongly blueshifted. For $n \geq 8$ the D(Δ)-peak shift is negative, which corresponds to a redshift of the Rb-He_N below the bare atom state. The D(Π) and D(Σ) peaks merge to one peak for $n^* > 6$, hence we refer to

Table 6.1: D(Δ) peak positions, peak shifts compared to the $n^2D_{3/2}$ state and peak width for different droplet sizes $\hat{N}$ and principal quantum numbers n.

$\hat{N}$	n	position / cm^{-1}	shift / cm^{-1}	width / cm^{-1}
7500	5	13181±5	60±5	80±10
7500	6	16174±10	66±10	78±7
7500	7	17725±15	24±15	52±15
7500	8	18636±6	-7±6	38±6
7500	9	19218±3	-25±3	29±7
7500	10	19615±3	-34±3	24±7
3200	5	13166±5	44±5	62±7
3200	6	16152±5	44±5	57±5
3200	7	17719±10	18±10	40±10
3200	8	18631±5	-12±5	31±6
3200	9	19216±5	-27±5	19±7
3200	10	19617±5	-32±5	22±7

this series as D(Π/Σ) series. Similarly we assign the P(Π), P(Σ), S(Σ) and F series. For the F series it was not possible to resolve different Λ substates because the F states have very small QDs. For higher n, l-coupling to the pseudo-molecular axis becomes weaker and molecular states merge to one single peak and form a hydrogen-like Rydberg series converging to the attractive potential curve of the ion in/on the droplet. The Rydberg potentials are very similar to the potential curve of the ion and an attractive force acts on the ionic core of the Rb atom [5]. Figure 6.2 shows a portion of the spectrum at the highest resolved Rydberg states (TOF E-field 240 V/cm). The E-field influences only the position of the IT and not the position of the resolvable peaks up to $n^* = 19$. All Λ-substates have merged and for large droplets the high Rydberg states are broader and the redshift is stronger than for small droplets.

Additional information is extracted from our observation that the probability for exciplex formation upon excitation into a Rb–He_N Rydberg state increases with Λ, at least for lower n. Consequently, the amount of observed Rb^+–He_m ($m = 1, 2, 3$) allows to conclude about the Λ (and thus l) character of the Rb–He_N state. The Rb^+–He_m ($m = 1, 2, 3$) ion yields in the section of the spectrum containing the 5D, 7S, and 4F manifolds are shown in Figure 6.3 for droplets of $\hat{N}_{60,14} = 7500$. Most striking is the difference between Rb^+–He and Rb^+–$He_{2/3}$ signals. The 5D(Δ) state is known to be closer to the bare atom line than the 5D(Π) and 5D(Σ) state [2]. We thus conclude that for lower states an increased Rb^+–$He_{2/3}$ signal indicates high $\Lambda(l)$ states. The Rb^+–He signal on the blue side of the bare atom 7S state is due to a combination of 7S(Σ) and 4F(Δ, Π, Σ). We interpret the Rb^+–$He_{2/3}$ peak at 14240 cm^{-1} as being due to the high Λ component, i.e. 4F(Δ). This demonstrates that high l states are

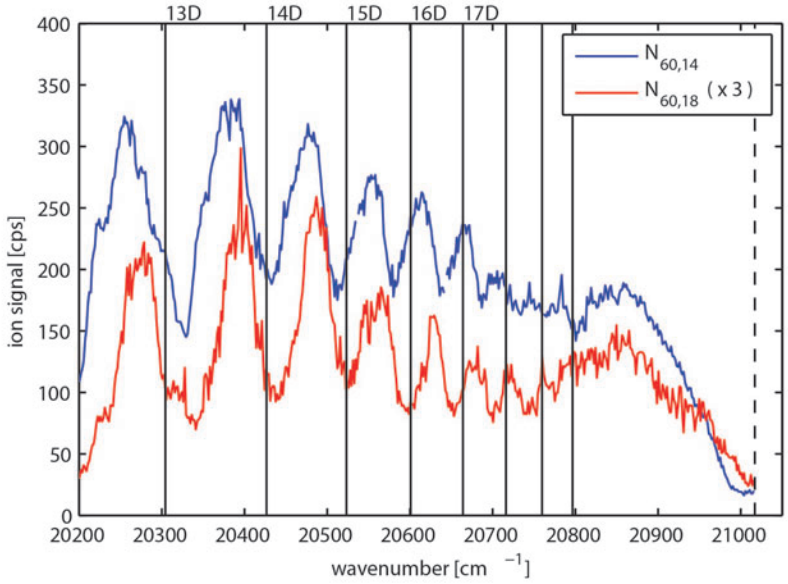

Figure 6.2: Excitation spectrum of high Rydberg states monitored on the masses of Rb^+–He_m ($m = 1 - 6$) for droplet sizes of $\hat{N}_{60,14} = 7500$ and $\hat{N}_{60,18} = 3200$. Lines are broader and the red shift is stronger for larger droplets. The vertical dashed line at $21017\,\mathrm{cm}^{-1}$ marks the field corrected ionization threshold. Bare atom nD line positions are indicated as vertical lines.

accessible with our two-step excitation scheme. We can identify higher S and F states by comparing the Rb^+ and Rb^+–He_m signals for lower states. For $n^* \gtrsim 8.5$ this Λ dependence vanishes and Rb^+–He_m complexes are detected regardless of the intermediate state.

In order to model the droplet size dependence of spectral features in Figure 6.1, we use a Rydberg approach. The Rb^+–He_N energy levels $E_{\Lambda,\hat{N}}(IT, n^*)$ are represented by the Rydberg formula [120]:

$$E_{\Lambda,\hat{N}}(IT, n^*) = IT_{\Lambda,\hat{N}} - \frac{R_\infty}{\left(n^*_{\Lambda,\hat{N}}\right)^2}, \tag{6.1}$$

$$n^*_{\Lambda,\hat{N}} = n - d_{\Lambda,\hat{N}}. \tag{6.2}$$

All states of a given series can be described by two parameters, the ionization threshold ($IT_{\Lambda,\hat{N}}$) and the effective principal quantum number $n^*_{\Lambda,\hat{N}}$ (which is related to the quantum defect $d_{\Lambda,\hat{N}}$). Note that IT and d depend on the droplet size $\hat{N}$. R_∞ denotes the Rydberg constant and in good approximation we can treat the quantum defect as independent of n. The $E_{\Lambda,\hat{N}}(IT, n^*)$ are obtained from the spectra as maxima of Gaussian fits to the spectral peaks, neglecting the shallow minimum ($\approx 5\,cm^{-1}$) [5] of the $5^2P_{1/2}(^2\Pi_{1/2})$ potential. A non-linear least squares fit is used to determine $IT_{\Lambda,\hat{N}}$ and $n^*_{\Lambda,\hat{N}}$ from Equation 1. Only peaks with $n^* > 5.2$ are included in the fit because for lower states the peak positions deviate from the model [6]. The strength of our method is that it is not based on an initial correspondence with bare atom states. Conclusions about the IT and the QD include only n^*. For bare atoms the QD for series of nl states is approximately constant. From Equation 2 it is evident that the remainder of n^*, which is obtained by the modular arithmetic operation "$n^*\,mod\,1$", is

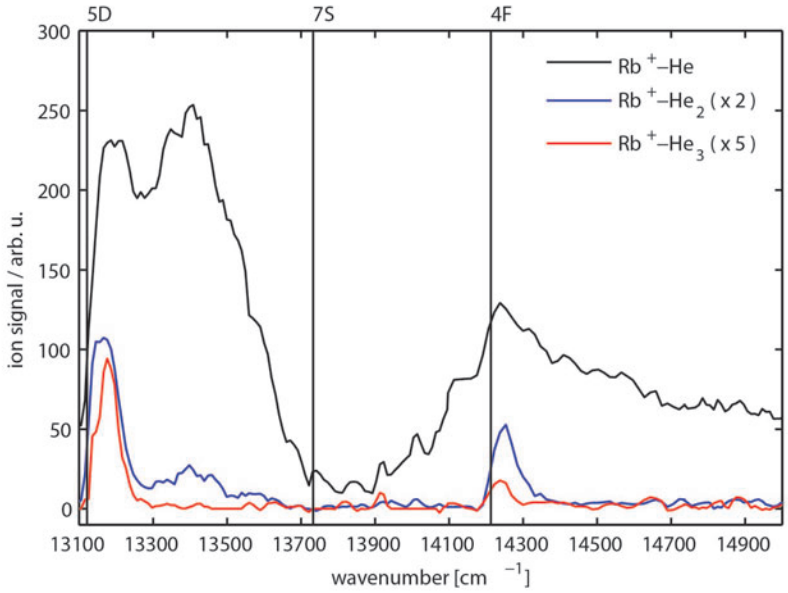

Figure 6.3: Excitation spectrum monitored on the masses of Rb^+–He_m ($m = 1, 2, 3$) for droplet sizes of $\hat{N}_{60,14} = 7500$. Bare Rb atom line positions are marked by vertical bars. Exciplex formation is strongly enhanced for high Λ states (e.g. 5D(Δ), close to the bare atom line [2]). Increased exciplex formation is also monitored close to the 4F state, indicating the high-Λ character of this state.

constant for each nl series. For Cs–He_N [6] and Na–He_N [164] the QDs are smaller than the bare atom values. In Figure 6.4b it is shown that the Rb–He_N QD is also lowered by the droplet, additionally we validated here that the quantum defect is droplet size dependent. The bare atom QDs are indicated as horizontal lines and the Rb–He_N QDs are plotted in colors. For example, for $d_D = 1.35$ it follows from Equation 2 that $n^* \, mod \, 1 = 0.65$ (horizontal line in Figure 6.4b). The $1 - (n^* \, mod \, 1) = 0.35$ operation (right scale) provides the remainder of the QD. For the D(Δ) series $1 - (n^* \, mod \, 1) \approx 0.27$, which corresponds to a decreased QD $d_{D(\Delta)} = 1.27$ ($\Delta d_{D(\Delta)} = -0.08$) if one assumes that the Rb-He_N QD lies in the range of the free atom.

All QDs are lowered by the influence of the He_N and show a trend toward the related bare atom values with decreasing $\hat{N}$. This demonstrates that our method allows the allocation of transitions according to their $l(\Lambda)$ character. The observed decrease of the QD may be due to a shielding of the Rb^+ ionic core from the Rydberg electron. This corresponds to an increase in energy, which is manifested in the spectra as a blue shift of lines for low n*, where the influence of the QD is most pronounced. Figure 6.5 shows the quantum defects, obtained upon ascription of the true quantum numbers (using the terminology of G. Herzberg in ref. [197]) to the observed states from the effective principal quantum numbers.

The IT of the Rb–He_N system is found to be droplet size dependent and lowered in comparison to bare Rb (Figure 6.4a). This is in agreement with previous experiments [5, 164]. The lowered IT is explained by the attractive interaction of the He_N and the positive alkali core due to polarization [5]. Our values (Figure 6.4a) are in good agreement with ref. [5], where an IT lowering of $37 - 55\,cm^{-1}$ for droplet sizes in a similar range as here is reported.

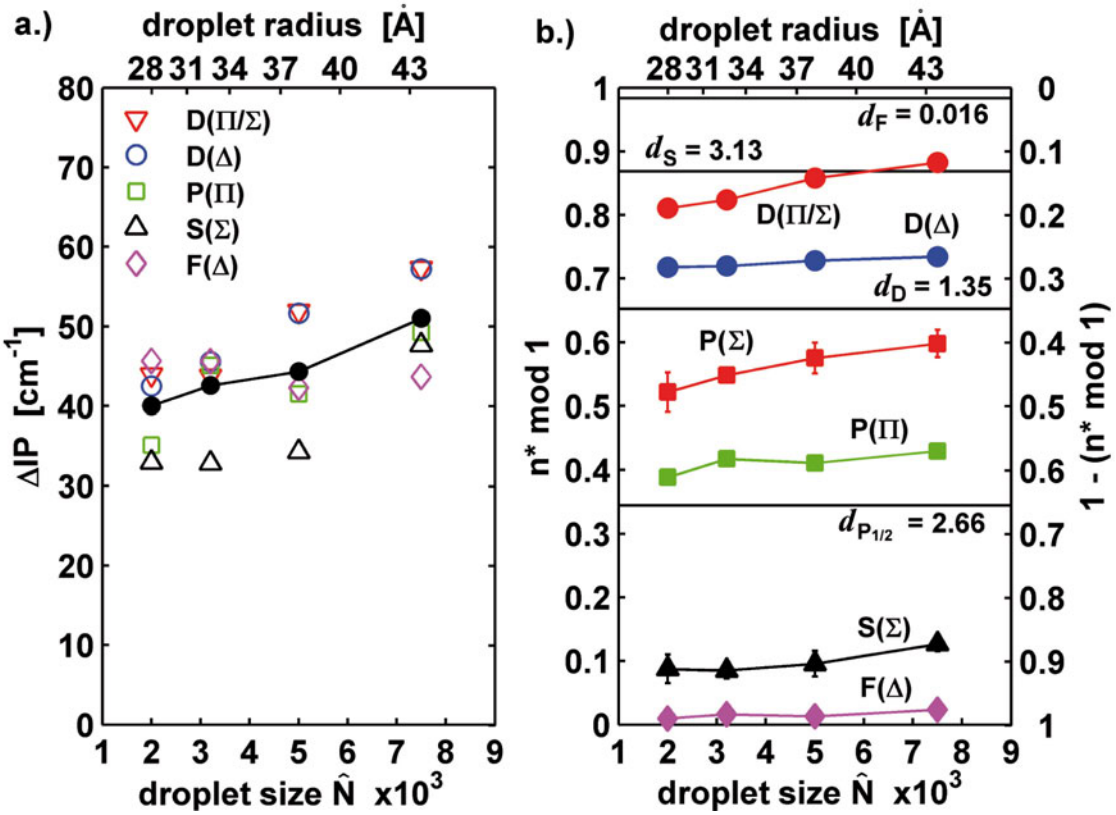

Figure 6.4: Decrease of the ionization thresholds (a) and effective principal quantum number $n^* \, mod \, 1$ (b) as a function of droplet size. Both parameters show a trend towards atomic values [151]. The solid line in (a) represents the mean value of the IT shift for each droplet size and the uncertainties of the IT values are smaller than $\pm 10\,\mathrm{cm}^{-1}$.

The ITs show no significant l and Λ dependence and show a trend towards the bare atom value for decreasing $\hat{N}$. In light of this discussion, we can describe the droplet size dependent line broadening effect by the log-normal distribution of the droplet size. Each size has its specific $IT_{\Lambda,\hat{N}}$ and $d_{\Lambda,\hat{N}}$ and thus necessarily a different spectral position. The breadth of the distribution at low nozzle temperature is reflected by broad spectral peaks.

6.1.4 Conclusion

In conclusion, we have demonstrated the Rydberg character of excited states of Rb atoms on helium nanodroplets. A complete excitation spectrum from the 5D state manifold to the ionization threshold is presented for various droplet sizes. The highest resolved states have an orbital radius, which is approximately ten times larger than the He_N. Within a Rydberg model we analyze the observed droplet size dependent effects of peak shift, line broadening and red shift of ionization threshold. In addition we show evidence for the excitation of previously unobserved nF states, demonstrating the possibility of transitions into high l states. Our findings support a qualitative picture in which the helium nanodroplet forms a dielectric around the Ak^+ reducing the binding energy and the interaction of the outer electron with the Ak^+ core orbitals, thus resulting in a lower ionization threshold and a smaller quantum defect.

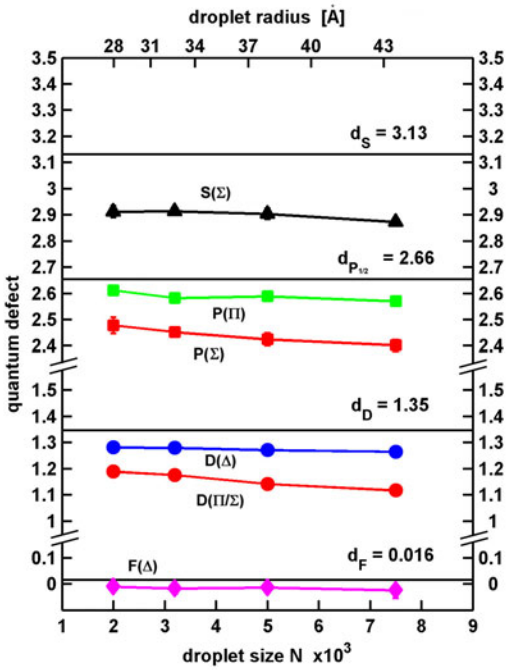

Figure 6.5: Decrease of the quantum defect as a function of droplet size. The quantum defects show a trend towards atomic values [151] with decreasing droplet size.

In a more refined model, the Pauli exclusion due to the helium should lead to a reduced core penetration of the Rydberg electron. In this limit, the helium may be modeled as dielectric around the Ak^+ ionic core [183].

Acknowledgments

This research is supported by the Austrian Science Fund (FWF) under Grant FWF-E-P19759 and the EFRE Program of the European Union and the Region of Styria.

6.2 The Rb 4D states on helium nanodroplets

Starting from the $5^2S_{1/2}$ ($^2\Sigma_{1/2}$) ground state, transitions into the Rb–He_N 4D Π and Σ molecular sub-states are allowed according to the pseudo-diatomic model. These transitions are presented in the excitation spectrum in Figure 6.6 for droplets consisting of $\hat{N}_{60,14} = 7500$ He atoms. The signals are obtained with R2PI spectroscopy. The Rb^+ and Rb^+-He_m ion yield is monitored as a function of the laser wavenumber. In addition the Rb_2^+ dimer [96] signal is shown. The free-atom transitions from the $5^2S_{1/2}$ ground state into the $4^2D_{3/2,5/2}$ states [198] at 19355.2 cm^{-1} and 19355.7 cm^{-1}, respectively, are forbidden according to the dipole selection rules. For the Rb–He_N system this spectral range was previously published in ref. [166] and the results therein agree well with ours.

In the excitation spectrum Rb–He_N, which is shown in Figure 6.6, we see the influence of fragmenting dimers on the Rb monomer signal. The Rb_2–He_N excitation spectrum shows two maxima. Comparing the Rb^+ and Rb^+-He_m signal, they differ significantly in the high wavenumber part. This is because the 4D (Σ) state is expected to produce mainly Rb ions [166], but there is also a contribution from fragmented dimers. Note that the dimer maximum is in the range of the bump in the Rb^+ signal at 20000 cm^{-1}. Also the rising edge in the Rb^+-He_m signal is much sharper than in the Rb^+ signal, which can as well be explained by the dimer influence. In contrast, we do not observe a correlation between the Rb^+-He_m and the dimer signal, neither in this spectral range, nor in any other recorded spectral range, which leads to the conclusion that dimers predominantly fragment into Rb atoms without attached He atoms after excitation followed by ionization. Because of this dimer contribution to the monomer signal, we excluded the Rb^+ signal in our previous publications, although it is only a problem when large droplets are used and pickup temperatures for a maximum monomer signal are chosen.

In ref. [166] the dynamics and Rb^+-$He_{1,2}$ exciplex formation for the Rb–He_N 4D Π and Σ states were discussed. Here we show a study of the droplet size dependence of the excitation spectra for those states. The Rb^+-He_m signals for different droplet sizes are shown in Figure 6.7. The spectra is smoothed and scaled to the maximum of the $\hat{N}_{60,14} = 7500$ signal. The broadening of the transition gets larger with increasing droplet size. The large droplet signal extends to much higher energies than that for small droplets. Compared to other transitions in the Rb–He_N system, this one is very broad and it extends over several hundred wavenumbers. The 4D state is the energetically lowest D state of the Rb atom. The expectation value of the 4D free atom orbital is 4 Å, thus the electron is located close to the Rb ion core. The shift and broadening of low states (up to effective principle quantum number $n^* < 5$) differ in behavior from higher states and do not fit well into the Rydberg model (see Section 6.4). Their shift with respect to the free atom states is not as strong as one would expect from the results of higher states. As will be discussed in Chapter 7, the smaller energy shift indicates that the probability to find the electron inside the core increases, which causes a higher (i.e. closer to the free atom value) quantum defect. Also the droplet size dependence of the 4D state is small, indicating that the perturbation is predominantly caused by the helium atoms close to the Rb atom, for which the wavefunction is sensitive.

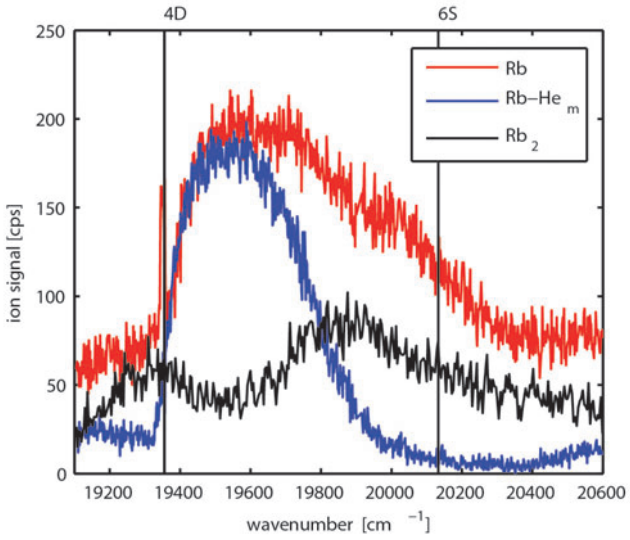

Figure 6.6: Recorded R2PI excitation spectrum of the Rb-He$_N$ 4D state manifold. The laser is scanned while monitoring the Rb^+, Rb^+-He$_m$ and Rb_2^+ ion yield. The difference in the Rb^+ and Rb^+-He$_m$ ($m = 1 - 6$) signal at 20000 cm^{-1} is caused by the 4D (Σ) state, which leads predominantly to the desorption of single Rb atoms and the influence of fragmenting dimers (Rb_2^+ signal).

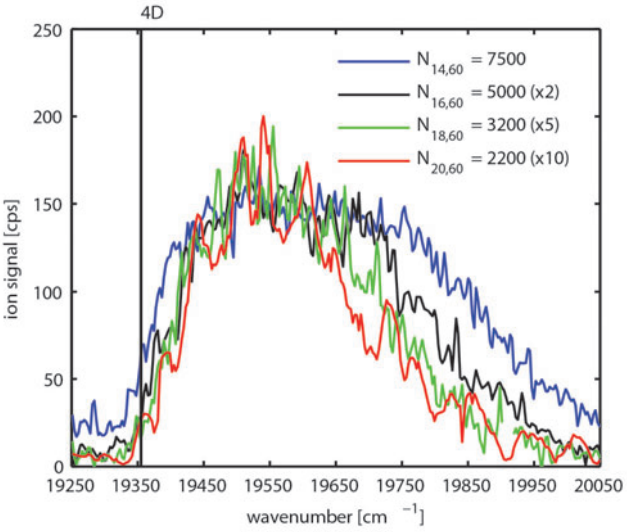

Figure 6.7: Excitation spectra of the Rb-He$_N$ 4D state manifold for different droplet sizes as obtained by monitoring the Rb^+-He$_m$ ($m = 1-6$) signal as a function of the laser wavenumber.

6.3 Excited state dynamics

This section discusses mass resolved excitation spectra of the Rb-He_N system, similar to the discussion about Cs-He_N in section 5.3. The spectra in Figure 6.1 were recorded by monitoring the Rb^+-He_m ($m = 1$ - 6) ion signal as a function of laser L2. The Rb^+ ion mass was excluded, because at low nozzle temperatures (14 K) the resulting broad droplet size distribution leads to an increased probability for the formation of dimers (and larger oligomers) [3, 73] on the droplet, especially when pickup temperatures for maximum monomer signals are chosen. Using smaller droplets, the influence of dimers decreases and the Rb^+ signal is more reliable. Although experiments where the droplet size dependence of Rb-He_N Rydberg states was investigated includes spectra of Rb on small droplets in Figure 6.1, for the sake of consistence with the large droplet spectrum the Rb^+ signal was excluded. However, a comparison of different Rb^+ and Rb^+-He_m ion masses in various spectral ranges gives additional information about the dynamics of the Rb-He_N system and the assignment of excited states.

In Figure 6.8 the Rb^+ and Rb^+-He_m ion yield for transitions into intermediate and high Rydberg states for the Rb-He_N system are shown. The excitation spectrum was recorded for small droplets with $\hat{N}_{18,60} = 3200$. The vertical lines mark the position of free atom transitions from the $5^2P_{1/2}$ state into nS (green), nP (red), nD (blue), and nF (black) states. Keep in mind that there is an uncertainty when free atom states are compared to on droplet states caused by the shallow minimum ($< 10\,cm^{-1}$) in the $5^2P_{1/2}(^2\Pi_{1/2})$ potential. Accounting for this effect would correspond to a slight red-shift of the free atom lines (or a blue-shift of transitions of atoms on the droplet). But since the exact depth of the potential is not known we neglect this small effect in the comparison between atoms and atoms on He_N. Closer inspection of the spectrum in Figure 6.8 reveals the differences between the desorption of atoms in states with high and low Λ. The state corresponding to the free atom 9P state (18350 - 18570 cm^{-1}) consists of the Π and Σ molecular sub-state. The energetically higher state is assigned to the 9P(Σ) state and the lower one to the 9P(Π)[7]. Due to the relatively small spin-orbit splitting (11 cm^{-1}) [198] of the 9P state compared to the peak width of the states on the droplet, the spin-orbit components of the Π molecular sub-state could not be resolved. The formation of exciplexes is suppressed at the Σ state with the maximum at (18522±10) cm^{-1}, which is immediately evident when the Rb^+ and Rb^+-He_m signals are compared. Following adjacent members of the nP (Σ) Rydberg series up to $n = 11$, the highest one which could be resolved before the peaks start to merge, it can be seen that the probability for the formation of exciplexes during the desorption process after the excitation into a Σ molecular substate is very low.

The difference between the Rb^+ and Rb^+-He_m ion yield can also be used to distinguish between transitions into molecular substates of nS and nF states. The spectral position of the free-atom Rb 9S state is 17921 cm^{-1} and the 6F state is located at 18049 cm^{-1}, measured from the $5^2P_{1/2}$ state [198]. The free atom states are followed by a double-peak structure. The lower and narrower peak at (18027±5) cm^{-1} is attributed to the 6F state [7]. The influence of the helium droplet on the quantum defect of the F series was found to be very small. At low states the decreased quantum defect is mainly responsible for the blue shift of the peaks. This means that a relatively small shift of F states on the droplets from the atomic state is expected at low states. At high Rydberg states the decreased ionization threshold is prevailing and causes a redshift, which explains the observed peak positions.

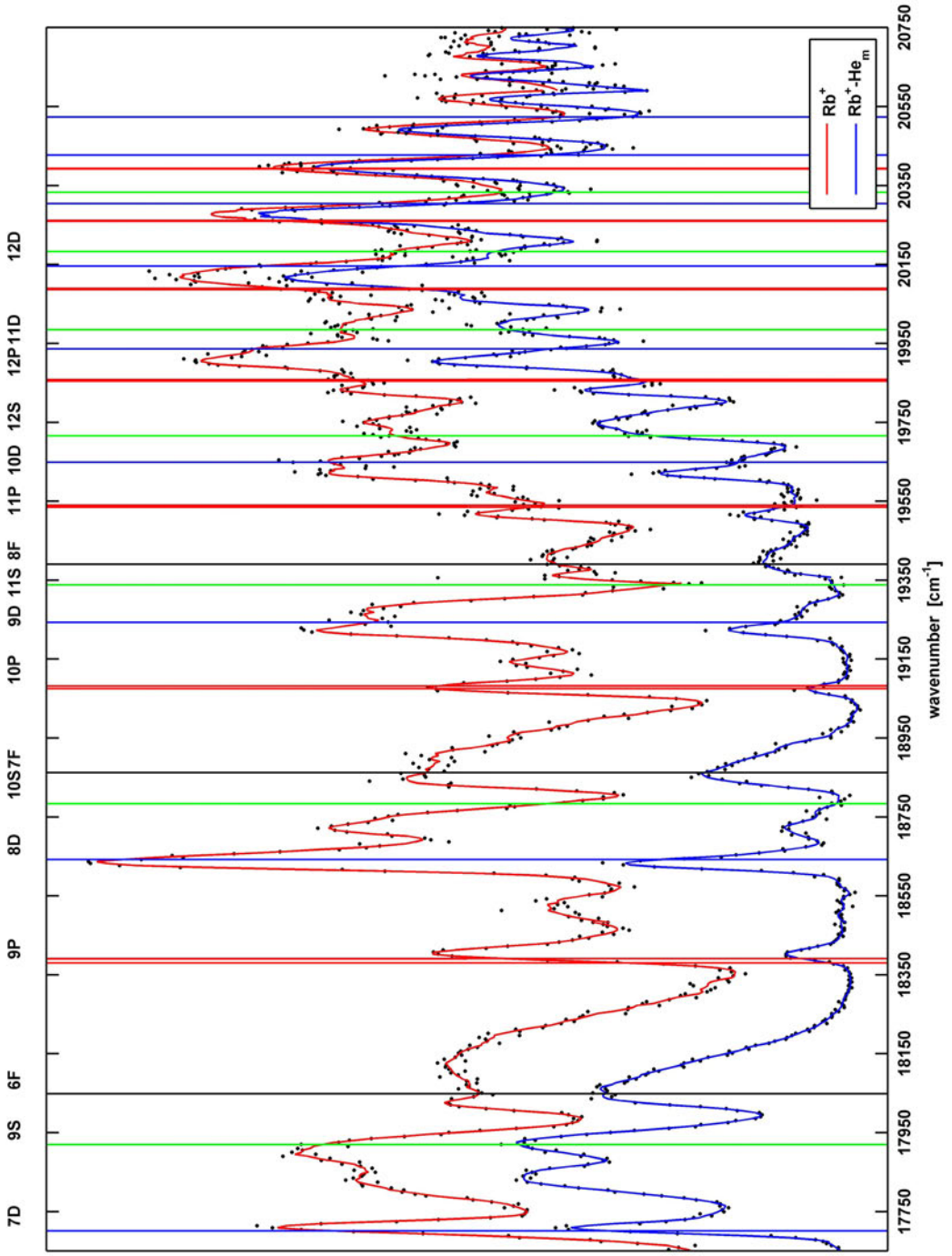
Rb+
Rb+-Hem
wavenumber [cm-1]
20750
20550
20350
20150
19950
19750
19550
19350
19150
18950
18750
18550
18350
18150
17950
17750
12D
12P 11D
12S
10D
11P
9D 11S 8F
10P
10S7F
8D
9P
6F
9S
7D

The three allowed molecular substates nF (Δ, Π, Σ) can not be resolved. The second peak, at higher energy, is attributed to the 9S (Σ) state. Exciplex formation is suppressed when ionizing via this Σ state. For adjacent states with increasing n the same double peak structure could be resolved till the S and F states start to merge. The 8F and 12S states are not included into our analysis because they are overlaid and distorted by a two-photon ionization when laser L2 scans across the 4D(Π, Σ)$\leftarrow 5^2S_{1/2}(^2\Sigma_{1/2})$ transition (See section. 6.2), which is accidently in the same spectral region. Also at the nD molecular substates we see differences in the exciplex formation. An excitation into a Δ molecular sub-state leads to an increased probability for the formation of exciplexes. In contrast the probability is smaller when a Π or Σ sub-state is excited. Unfortunately the Π and Σ state can not be assigned unambiguously and they start to merge at relatively low states ($n \geq 8$). At the 7D state the three components of the molecular substates can be resolved. The peak close to the free atom state is assigned to the Δ state. On the basis of the observation of an increased Rb^+ signal at the energetically higher peak and the above discussion of the Λ dependence of the exciplex formation, the energetically lower peak is most probably the 7D(Π) state and the higher one is the 7D(Σ) state.

Figure 6.9 shows the mass resolved excitation spectrum of Rb-He_N for Rydberg states close to the ionization threshold, recorded by using the pulsed extraction field (field free conditions). Unfortunately the scan speed of the FL3002 laser was very fast, which is responsible for the bad resolution. Despite this disadvantage, the quality is sufficient to demonstrate the increased exciplex formation probability at high Rydberg states in the Rb-He_N system. The formation of larger exciplexes, consisting of Rb* with two or three He atoms attached, starts to increase between $19300\,cm^{-1}$ to $20000\,cm^{-1}$. This is very similar to what was observed in the mass resolved spectra of Cs-He_N in section 5.3. This is approximately the region where the blue shift of the states goes over into the red shift and the size of the electron orbital becomes larger than the droplet. A dependence of the exciplex formation on the molecular sub-state is not observed above this region.

In summary, we could show that the probability of exciplex formation increases with Λ, which goes along with an increase of L, for lower Rydberg states. For high Rydberg states the exciplex formation increases for all transitions independent of the molecular sub-state. The above discussion shows again the similarities of the Rb-He_N and Cs-He_N systems.

6.4 Rydberg series and spectral trends

In Figure 6.10 the shifts of the observed Rb–He_N transitions with respect to the corresponding free-atom transitions are presented for different droplet sizes. The position of spectral peaks is obtained by fitting Gaussian functions to the peaks in the Rb^+ and Rb^+-He_m spectra. The transitions are assigned with the procedure presented in section 6.1. The solid lines are

Figure 6.8 *(facing page)*: Comparison of the Rb^+ and Rb^+-He_m ion yield in the intermediate and high Rydberg state range of the Rb-He_N system for small droplet sizes ($\hat{N}_{18,60} = 3200$). The vertical lines mark the position of free atom transition from the $5^2P_{1/2}$ state into nS (green), nP (red), nD (blue), and nF (black) states.

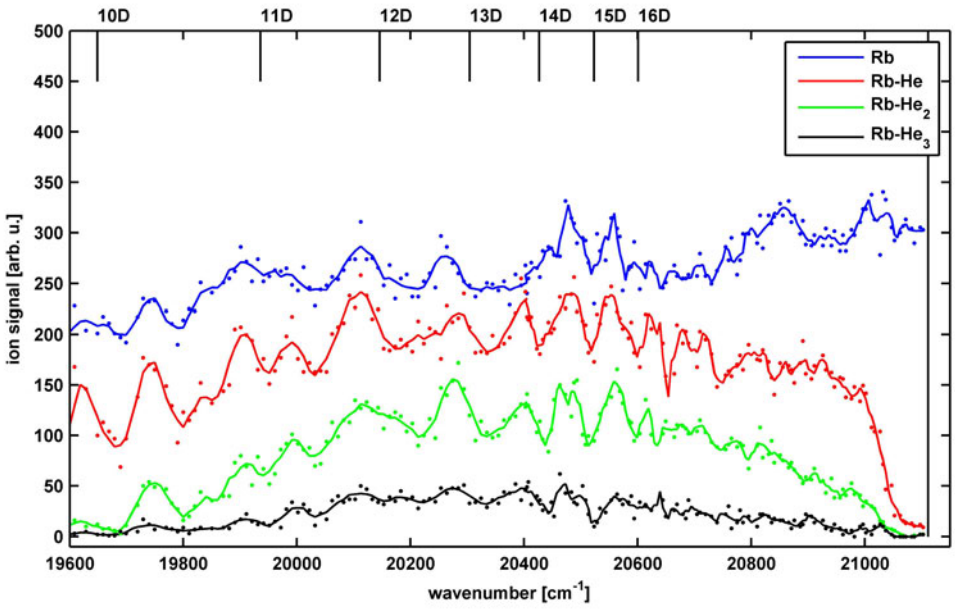

Figure 6.9: Rb^+ and Rb^+-He_m ($m = 1, 2, 3$) ion yield for Rb-He_N high Rydberg states. The excitation spectrum was recorded for $\hat{N}_{60,14} = 7500$ droplets. For high Rydberg states exciplex formation is independent on the Λ quantum number of the molecular substate. Positions of atomic states and the ionization threshold are indicated as vertical solid lines.

obtained from the Rydberg formula using the quantum defects and ionization thresholds from section 6.1. Best results are obtained for the nD (Λ) and nP (Λ) series, where many individual transitions could be resolved. The nD (Π) and nD (Σ) series could not be unambiguously separated for $n > 7$ and thus they are treated as nD (Π, Σ) series. For the nP(Σ) only a few peaks at low n could be resolved, thus for the determination of the droplet size dependent quantum defects of this series the ionization thresholds obtained for the nP (Π) series was taken. For the highest resolved Rydberg states the assignment is not unambiguously possible. Those states are depicted in the lower left panel together with the nD (Λ) series in gray. Although they are excluded from the fit procedure, they fit into this series. The Rb–He_N shifts behave similar as the one found for the Cs–He_N system [6].

From Figure 6.10 it is evident that for all Rydberg series the lower members are blue shifted and higher members are red shifted. The blue-shift of the lower states is strongly dependent on the droplet size. At the crossing point of the solid lines for different droplet sizes the size dependence reaches a minimum. The shift of adjacent members of each Rydberg series converge to a asymptotic value. This value corresponds to the difference between the ionization threshold of atoms on He_N and the free atom ionization threshold. The ionization threshold is decreased by the influence of the helium droplet and depends also on the droplet size [5]. The S (Σ) states experiences the strongest shift (note the different scale in the upper left panel). In this case the repulsive interaction of the S orbital and the droplet is very large. In contrast, states with high orbital angular momentum do not experience such a strong shift. For a fixed orbital angular momentum the shift depends on the molecular sub-state Λ. With increasing Λ the shift and thus the perturbation by the droplet gets weaker. This can be seen

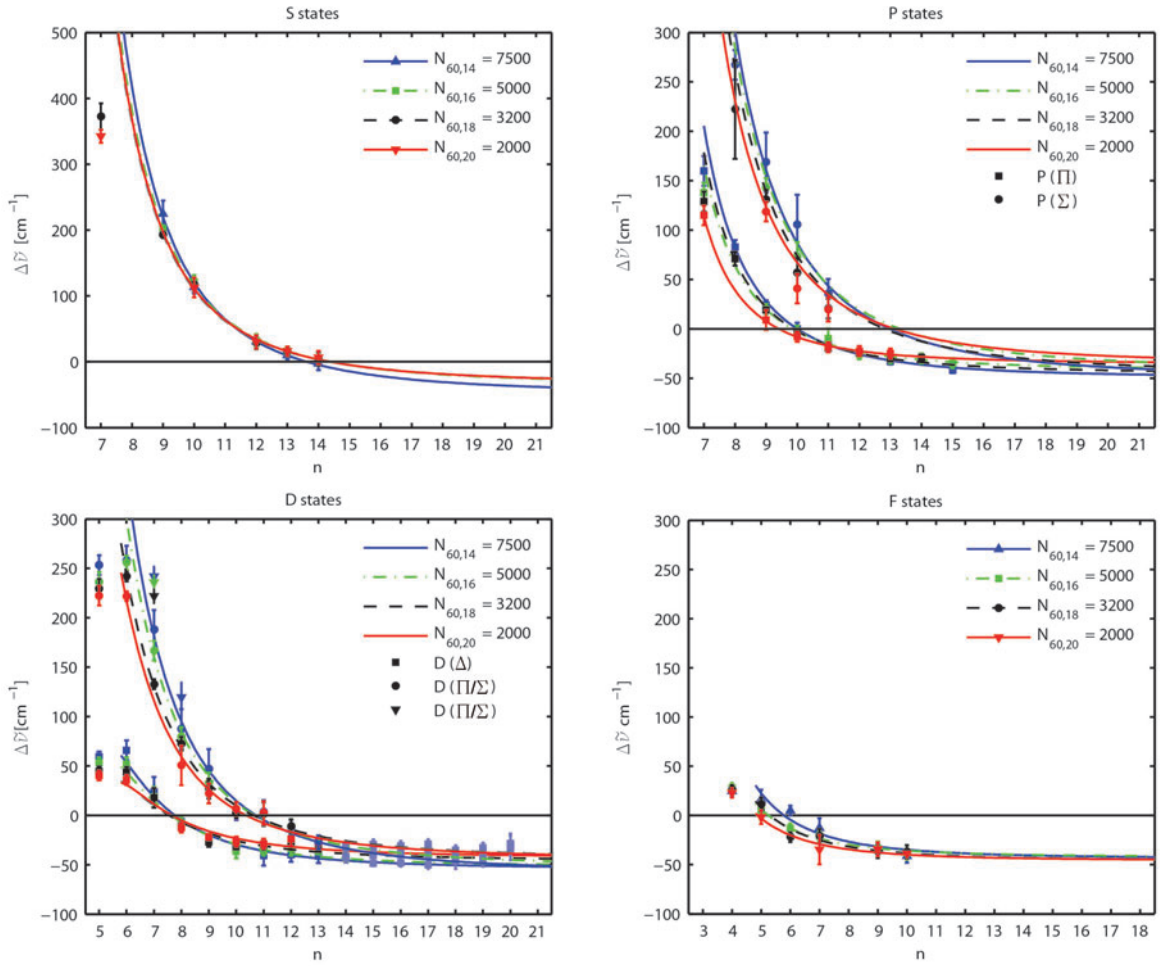

Figure 6.10: Shift of the recorded Rb–He_N transitions with respect to the corresponding free-atom transitions for nS (Σ), nP (Π, Σ), nD (Δ, Π, Σ), and nF Rydberg series. The shifts are shown for different droplet sizes. The solid lines are obtained from the Rydberg formula with the droplet size dependent quantum defects and ionization thresholds.

in the upper right panel where the nP (Π) and nP (Σ) Rydberg series are shown. The nP (Σ) is much more shifted than the nP (Π) series. This suggests the qualitative picture in which the overlap between the helium droplet and the unperturbed wavefunction is a measure for the interaction between droplet and dopant on the surface. Considering an S (Σ) orbital with its spherical symmetry, the overlap of wavefunction and droplet will be large. A P(Π) orbital, where the two lobes are aligned perpendicular to the pseudo molecular axis (i.e. a P (Π) state) does not have such a large overlap. In contrast, if one lobe points towards the helium droplet (P(Σ) state) the shift is strong. These observations and especially the droplet size dependent effects are well described by the Rydberg formula (see Chapter 3):

$$E_{\Lambda,\hat{N}}(IT, n^*) = IT_{\Lambda,\hat{N}} - \frac{R_\infty}{\left(n^*_{\Lambda,\hat{N}}\right)^2}, \tag{6.3}$$

$$n^*_{\Lambda,\hat{N}} = n - d_{\Lambda,\hat{N}}. \tag{6.4}$$

With the Rydberg formula, the positions of the energy levels $E_{\Lambda,\hat{N}}(IT, n^*)$ are described by the interplay of ionization threshold ($IT_{\Lambda,\hat{N}}$) and the quantum defect $d_{\Lambda,\hat{N}}$, which defines the effective principal quantum number $n^*_{\Lambda,\hat{N}}$. The presence of the droplet causes a red shifted ionization threshold and a decreased quantum defect. It was found that for larger droplets both, the ionization threshold and the quantum defect, are lower than for smaller droplets. According to the Rydberg formula the quantum defect has a dominant effect on the spectral position of lower states, where the principal quantum number n is not much larger than the quantum defect. The effect of a lower quantum defect in Figure 6.10 will be an increase in the curvature of the solid lines. A horizontal line would correspond to an unperturbed (free-atom) quantum defect. In contrast, for high n, the dominant parameter in the Rydberg formula is the ionization threshold. This explains the droplet size dependent evolution from low to high n states in Figure 6.10. At low n states the decreased quantum defect causes a blue shift of the observed transitions. This blue shift is stronger for atoms on large droplets because the decrease of the quantum defect is larger. At high Rydberg states the red-shift of the ionization threshold dictates the spectral position. The ionization threshold is more red-shifted for Rb atoms on large droplets and thus the red-shift of the high Rydberg states is larger. This shows that for atoms on large droplets the perturbation of low and high Rydberg states is stronger.

Details of the Rydberg excitation spectrum

After this general discussion of spectral trends we present a detailed study of the evolution of Rydberg states on the example of the Rb-He_N nD (Δ) series. States with $n = 6$, 8, 10, and 11 are shown in Figure 6.11 for different droplet sizes. Except for the $\hat{N}_{60,22} = 1100$ data, the excitation spectra are shown in Figure 6.1, but here they are scaled so that the maxima of the D (Δ) peaks are at the same high as the Rb–He_{7500} D (Δ) peak maximum. This allows a better comparability of the peak positions and linewidths for different droplet sizes. At the lowest state with $n = 6$ the blue shift of the D(Δ) state compared to the $6^2D_{3/2,5/2}$ states is large. The linewidth increases rapidly with increasing droplet size. For Rb–He_{7500} the peak maximum is at (16174±10) cm^{-1}, which corresponds to a shift of (+66±10) cm^{-1} to the $6^2D_{3/2}$ free-atom state. In contrast, for He_{1100} droplets the peak is located at (16128±5) cm^{-1}, which corresponds to a shift of only +20±5 wavenumbers. The line width of these two transitions are (+78±10) cm^{-1} for Rb–He_{7500} and (+43±10) cm^{-1} for Rb–He_{1100}. In this spectral range the electron wavefunction is very sensitive to the droplet size. The corresponding droplet radii are $\hat{R}_{60,14} = 44$ Å and $\hat{R}_{60,22} = 23$ Å. Comparing those radii to the radial expectation value $\langle R \rangle = 16$ Å of the electrons 6D wavefunction we see that both values are in the same order of magnitude. Only in this energy range we observe such strong blue shifts. The next higher state in Figure 6.11 is the 8D (Δ) state. Here the transition for $\hat{N}_{60,14} = 7500$ is at the same position as the free atom transition, shifted only for (-7±6) cm^{-1}. Note that this is in the range of the depth of the $5^2P_{1/2}(^2\Pi_{1/2})$ potential. The transition appears red shifted for the $\hat{N}_{60,14} = 2000$ cluster size compared to the $\hat{N}_{60,14} = 7500$ and (-13±5) cm^{-1} to the free atom state. These values are much smaller than the one for $n = 6$ before. At the 10D(Δ) and 11D(Δ) states all peaks are strongly red-shifted. The red-shift is stronger for atoms on large droplets, which is the reverse behavior than at lower states. This effect is explained within the Rydberg picture (Equation (6.3)) in the following.

The quantum defects and ionization thresholds obtained for the identified Rydberg series

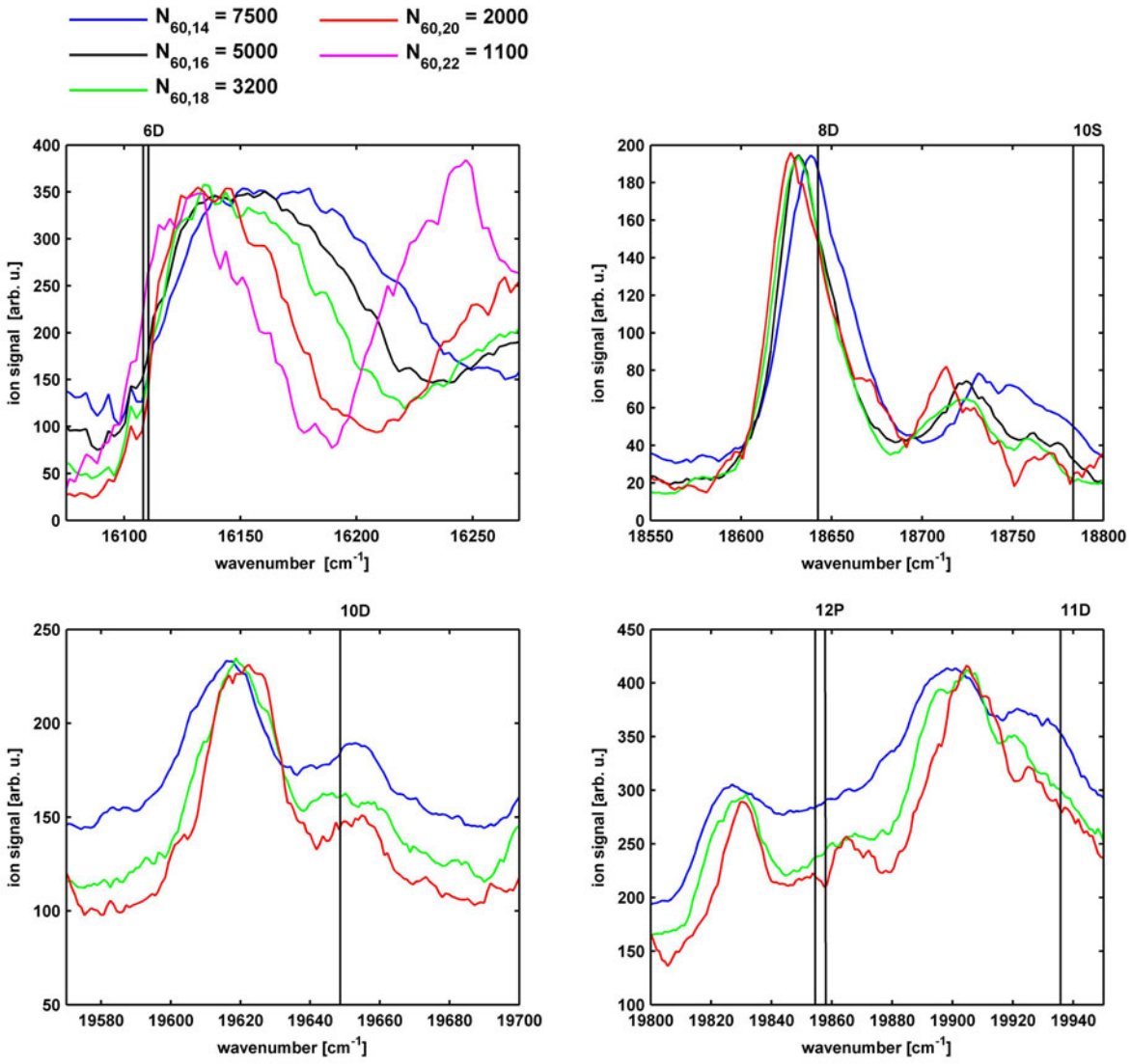

Figure 6.11: Excitation spectra of the nD (Δ) state for n =6, 8, 10, and 11. The signals are scaled so that all maxima of the D (Δ) peaks are at the same high as the $N_{60,14} = 7500$ maximum. Atomic lines are drawn as vertical solid lines. At the lower right panel in addition to the 11D (Δ) states starts to merge with the 11D (Π, Σ) state and the 12P (Π) and for $N_{60,14} = 2000$ the 12P (Σ) states are shown.

are summarized in Table 6.2 and 6.3. They are obtained by fitting observed transitions to the Rydberg formula (Equation 6.3) as discussed above. The ionization thresholds are given with respect to the free-atom $5^2S_{1/2}$ ground state. The quantum defects for the nD (Δ) series are noted in the first line in Table 6.3. In the lower left panel in Figure 6.10 the shifts of all members of the nD(Δ) Rydberg series are displayed. The point of intersection between the curves for different nozzle temperatures is in the region around $n = 8$. For example, the $d_{\Delta,7500}$ quantum defect is smaller than the $d_{\Delta,3200}$ quantum defect. According to the Rydberg formula, a lower

Table 6.2: Fit results for the Rb-He_N ionization threshold for different droplet sizes.

droplet size $\hat{N}$	7500	5000	3200	2000	atom
D(Δ)	33634±6	33639 ±9	33645± 12	33648 ±9	33690.80
D(Π/Σ)	33633 ±14	33639± 16	33647± 13	33647± 19	33690.80
P(Π)	33642± 4	33649± 5	33646± 6	33656± 3	33690.80
P(Σ)	-	-	-	-	33690.80
S(Σ)	33643± 12	33656± 24	33658±14	33658± 16	33690.80
F-series	33647± 20	33648 ±5	33645±14	33645± 16	33690.80

Table 6.3: Fit results for the Rb-He_N quantum defects for different droplet sizes.

droplet size $\hat{N}$	7500	5000	3200	2000	atom
D(Δ)	1.27± 0.02	1.27± 0.02	1.28± 0.02	1.28± 0.01	1.347
D(Π/Σ)	1.12± 0.03	1.14± 0.03	1.18± 0.02	1.19± 0.02	1.347
P(Π)	2.57± 0.01	2.59± 0.01	2.58± 0.01	2.61± 0.01	2.655
P(Σ)	2.40± 0.04	2.42± 0.05	2.45± 0.02	2.48± 0.06	2.655
S(Σ)	2.87± 0.02	2.90± 0.04	2.91± 0.03	2.91± 0.04	3.131
F-series	-0.024± 0.023	-0.014± 0.015	-0.017± 0.018	-0.011± 0.018	0.016

quantum defect gives a higher energy level, but only if the ionization thresholds are the same. The ionization threshold $IT_{\Delta,7500}$ is lower than the ionization threshold for smaller droplets $IT_{\Delta,3200}$. This means that in this region the influence of the decreased ionization threshold $IT_{\Delta,\hat{N}}$ counteracts the decreased $d_{\Delta,\hat{N}}$ quantum defect which causes the blue shift. With higher quantum number the influence of the quantum defect on the energy levels decreases. They are predominantly determined by the ionization threshold to which the Rydberg series converges. This can be seen in the two lower panels in Figure 6.11 where the 10D (Δ) and 11D (Δ) states are shown. In this spectral region the peaks obtained for large droplets are more red shifted because the influence of the decreased ionization threshold is dominant. In light of the discussion above we can explain the observed peak positions by droplet size dependent ionization thresholds and quantum defects within the scope of a Rydberg model.

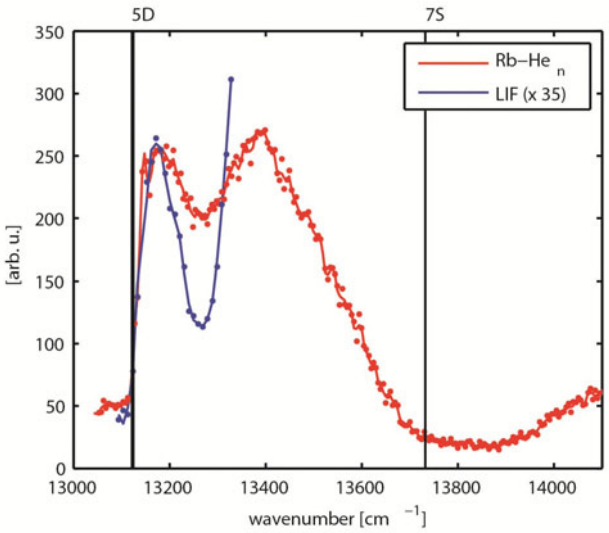

Figure 6.12: Comparison of the Rb–He_N LIF and R3PI-TOF excitation spectrum for the 5D state manifold. LIF data (blue) are taken from reference [2]. The R3PI-TOF spectrum is obtained by recording the Rb^+He_m ($m = 1 - 6$) ion yield as a function of L2 wavenumber.

6.5 Comparison of LIF and R3PI spectra

Similar to Section 5.5 for Cs–He_N, LIF spectra can be compared to R3PI spectra for the Rb–He_N system. This is shown in Figure 6.12 for the 5D state manifold. The LIF signal is described in our article ref. [2]. The differences between the LIF and R3PI signals in Figure 6.12 are caused by saturation effects due to the different laser intensities. The R3PI signal was recorded using much more energy in order to ionize the atoms efficiently. Thus the peak seems broader and the minimum is not so pronounced than it is in the LIF signal. The rising edge, the peak maximum and the following minimum are not significantly affected by this effect.

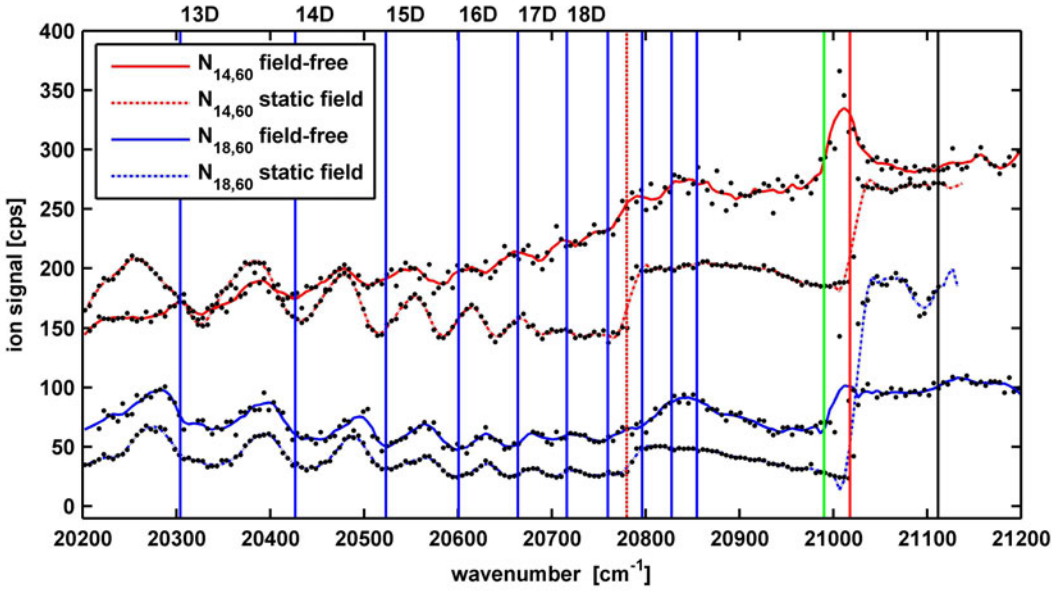

Figure 6.13: Comparison of the Rb^+ photo-ion yield for high Rydberg states of Rb–He_N at static field and field-free conditions for different droplet sizes. The free atom ionization threshold is shown as solid black vertical line. The field corrected free-atom ionization threshold (static field: 236 V/cm, pulsed field: 394 V/cm) measured from the $5^2P_{1/2}$ state is shown as vertical red line and as vertical green line, respectively. The field corrected ionization threshold measured from the $5^2P_{3/2}$ state is shown as dashed red line.

6.6 Excitations at field-free versus static field conditions

In this section excitation spectra recorded in field-free space and static electrical fields are compared for high Rydberg states and the ionization threshold. The spectra are shown in Figure 6.13 for the Rb^+ ion yield and in Figure 6.14 for the Rb^+-He_m ($m = 1 - 6$) photo-ion yield. These Figures show that, as long as individual states can be resolved, the presence of an (relatively weak) electrical field does not significantly affect the peak position and the peak width of the recorded transitions. In contrast it does affect the position of the ionization threshold. The field-free atomic ionization threshold is shown as vertical solid black line in the Figures. The field corrected free-atom ionization threshold (236 V/cm, measured from the $5^2P_{1/2}$ state) is shown as vertical red line and as dashed red line the ionization threshold measured from the $5^2P_{3/2}$ state is shown. For the pulsed field experiment, an extraction field of 394 V/cm was used (vertical green line). The Rb^+ signal shows an interesting feature. Two steps are visible in the spectrum, one of them corresponds exactly to the field-corrected IT measured from the $5^2P_{1/2}$ state. This is caused by atoms which desorb in one of the intermediate states as free atoms. These atoms are then ionized by the laser. The other edge matches exactly the field-corrected IT measured from the $5^2P_{3/2}$ state. Since the intermediate $5^2P_{1/2}$ state is energetically lower than the $5^2P_{3/2}$ state, this signal must be caused by atoms which desorb as free atoms upon excitation into a Rydberg state.

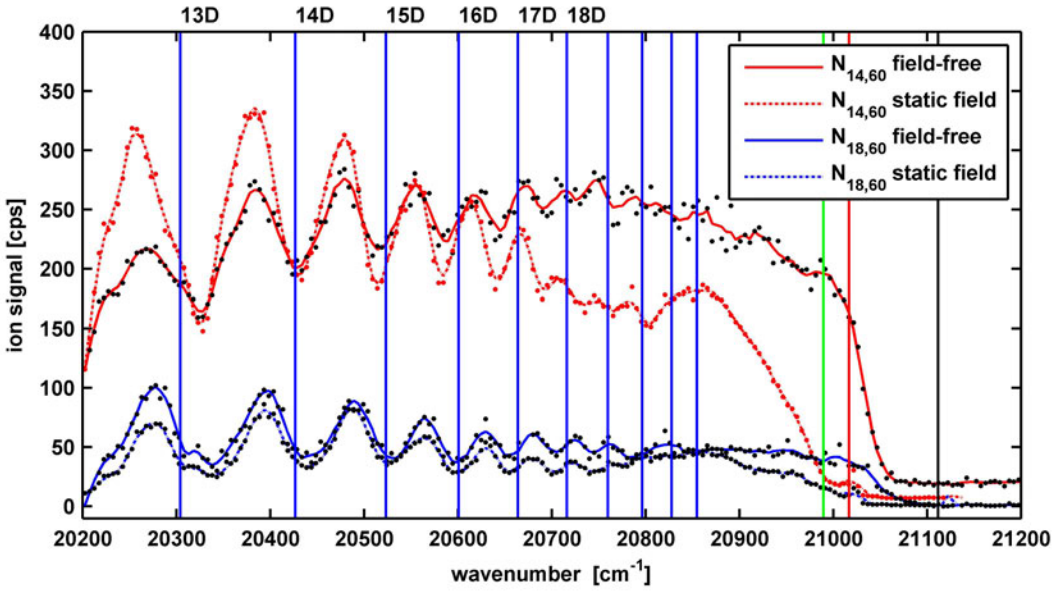

Figure 6.14: Comparison of the Rb^+-He_m ($m = 1-6$) photo-ion yield for high Rydberg states of Rb–He_N at static field and field-free conditions for different droplet sizes. The free atom ionization threshold is shown as solid vertical line. The field corrected free-atom ionization threshold (static field: 236 V/cm, pulsed field: 394 V/cm) measured from the $5^2P_{1/2}$ state are shown as vertical red line and as vertical green line, respectively.

Chapter 7

Rydberg States and Rydberg Series of Atoms on He Nanodroplets

In the previous chapters of this thesis, excitation spectra of alkali atom Rydberg states on helium nanodroplets were presented. Spectral positions of the recorded transitions were analyzed with a Rydberg model. In this chapter a more sophisticated Rydberg-Ritz model is presented, which is able to explain deviations of lower Rydberg states from the simple Rydberg model. In section 7.2 different methods for the determination of ionization thresholds of alkali atoms on helium droplets are compared. Section 7.2 discusses the relation between various Rydberg systems, which are perturbed by rare gas atoms, and the Rb-He$_N$ Rydberg system. In addition, high Rydberg states of atoms on helium nanodroplets are discussed in Section 7.4, including a description of the so called "Sekatskii-atom", an ion core solvated into a helium droplet with an orbiting electron.

7.1 Alkali atom Rydberg series on helium nanodroplets

In the course of this thesis, different Rydberg approaches were used to describe the experimentally determined energy levels of the investigated Ak-He$_N$ systems.

In Chapter 5, which is about Cs–He$_N$, a model was introduced which assumes a similar behavior of atomic quantum defects and on-droplet quantum defects. In this model, the lowest transitions were excluded from the fit procedure because they do not fit well into this kind of model. A disadvantage of this method is that the recorded transitions have to be related to free-atom transitions prior to the fit procedure. In the case of Cs–He$_N$ this prior assignment was possible because of the well resolved transitions, especially the spin-orbit split lower nP states and the available calculation for the lowest series members. The fact that the lower states do not fit well into this Rydberg model shows that the behavior of the on-droplet quantum defects differs from free atom quantum defects. In contrast to Rb-He$_N$, it was not possible for Cs-He$_N$ to distinguish between nS and nF states as discussed in Chapter 5. The line positions in the nS series might be influenced by the overlapping nF states.

Another ansatz was used in Chapter 6 for the Rb-He$_N$ system. Spectral peaks, which differ in their effective quantum numbers n^* by integer steps were organized into Rydberg series. In Chapter 3 it was shown that this is the condition which must be fulfilled by members of a Rydberg series. The results of the fit procedure for each Rydberg series were the ionization

threshold IT and the value of $n^*\ mod\ 1$, since the true quantum numbers [197] are not known a priori. For Rb-He_N it is also possible to assign on-droplet states on the basis of extrapolation from lower known states and calculations, similar to Cs–He_N, but it was not required prior the fit procedure with this ansatz. From the comparison of the $n^*\ mod\ 1$ fit parameters and the modulo of the free atom quantum defects, additional information for the identification of spectral peaks was obtained and molecular-substates were assigned to the corresponding free atom states from which they are arising. The advantage of this method compared to the former is that prior assignment of spectral peaks to free atom states is not necessary. However, the method also failed to describe the lowest energy levels of the Rydberg series accurately, which were therefore excluded from the fit procedure.

The two methods are able to describe states for which the quantum defect has essentially settled down to a constant value. Therefore the first few members of a Rydberg series were excluded from the fit procedure. This is a valid and frequently used method for the determination of asymptotic quantum defects. However, since the lowest members of a Rydberg series include also some information, a Rydberg-Ritz fit model which is able to reproduce deviations of lower Rydberg states and their quantum defects should be the method of choice.

7.1.1 Rydberg-Ritz formula for alkali atom Rydberg series on helium nanodroplets

The Rydberg-Ritz formula (Equation 3.41) was discussed in Section 3.4. The previous analysis of Rb-He_N and Cs–He_N includes only the first Rydberg-Ritz coefficient, which reduces the equation to the form of the ordinary Rydberg formula. In order to describe deviations from a constant quantum defect, at least the second Rydberg-Ritz coefficient b of the modified quantum defect (Equation 3.42) must be considered. However, because of the relatively few resolved transitions, too many free parameters will increase the uncertainty of the fit parameters and will thus decrease the reliability of the Rydberg-Ritz model. In addition, since the observed transitions are very broad, their spectral position can not be determined very accurately.

In light of these arguments, the best choice will be a modified Rydberg-Ritz model which includes the second order Rydberg-Ritz coefficient b. This modified Rydberg-Ritz formula can be written as:

$$E_n = IT - \frac{Ry}{\left(n - \left(a + \frac{b}{(n-a)^2}\right)\right)^2}. \tag{7.1}$$

Note that the Rydberg-Ritz parameter a corresponds to the asymptotic quantum defect d_Λ and should not differ significantly from the fit results of the other Rydberg models in the previous chapters.

In the following, the Rydberg-Ritz fit model is applied to Rb–He_N and Cs–He_N.

7.1.2 Rydberg-Ritz model for Cs atoms on helium nanodroplets

We start the discussion with a re-analysis of the Cs–He_N system within the scope of a Rydberg-Ritz model. The new insights gained by this approach are discussed and afterwards used for the more complex experimental (because of the droplet size dependence studies) Rb–He_N results.

The least squares fit of the observed transition wavenumbers E_n to the modified Rydberg-Ritz formula gives values for the ionization threshold IT, the Rydberg-Ritz parameter a, which corresponds to the asymptotic quantum defect d_Λ and the Rydberg-Ritz parameter b, which accounts for deviations from the asymptotic quantum defect at low n. However, once the IT and true quantum numbers are known, the quantum defects can be calculated from the experimentally determined energy levels $E_{n,\Lambda}$:

$$d_\Lambda(n^*) = n - n^* = n - \sqrt{\frac{Ry}{IT - E_{n,\Lambda}}}. \tag{7.2}$$

Quantum defects

The quantum defects calculated with Equation 7.2 are shown in Figure 7.1 for the $n\mathrm{S}(\Sigma)$ Rydberg series, in Figure 7.2 for the $n\mathrm{P}(\Pi,\Sigma)$ series and in Figure 7.3 for the $n\mathrm{D}(\Delta,\Pi,\Sigma)$ series. These plots shine light on several important features of Rydberg series perturbed by helium droplets.

The uncertainties of the quantum defects increase with the principal quantum number. The quantum defect determines predominantly the spectral position of lower states, whereas the spectral position of states with high n is dictated by the IT. The increase of the uncertainty of the quantum defects with n is immediately seen from Equation 7.2: The larger $E_{n,\Lambda}$, which is subtracted from the IT in the denominator, the larger is the value of the square root which is subtracted from n and hence the larger is the influence of the uncertainty of the energy levels on the uncertainty of the quantum defect. This explains the increase of the size of the error bars in the Figures. Depending on the Rydberg series, beyond a certain n the quantum defects calculated with Equation 7.2 become unreliable. For the Cs–$\mathrm{He_N}$ Rydberg series, the only series where the manifestation of this effect is important is the nP series beyond $n = 15$. The quantum defects of all other states fit well into the series.

Another way to plot the obtained quantum defects was introduced by B. Edlén in ref. [154]. If the quantum defect (or $n - n^*$) is plotted versus $1/n_{eff}^2$ (here we use $n_{eff}(= n^*)$, in analogy to B. Edlén), the resulting plots are straight lines (which is obvious from Equation 7.1). This is a frequently used method to depict quantum defects and the plots are referred to as Edlén-plots. They are shown in Figure 7.4 for the $n\mathrm{S}(\Sigma)$ Rydberg series, in Figure 7.5 for the $n\mathrm{P}(\Pi,\Sigma)$ series and in Figure 7.6 for the $n\mathrm{D}(\Delta,\Pi,\Sigma)$ series.

Rydberg-Ritz fit results

Table 7.1 shows the least-squares fit results obtained with the Rydberg-Ritz model. The $n\mathrm{D}(\Sigma)$ states were fitted with the Rydberg-Ritz formula, but this series shows a very high uncertainty because there are only four resolved states of this series in the spectrum. The assignment of the $n\mathrm{D}(\Sigma)$ and $n\mathrm{D}(\Pi)$ series is based on the findings on the energetic ordering of molecular sub-states as described in Chapter 5 and Chapter 6, where the state which is higher in energy is associated with the $\mathrm{D}(\Sigma)$ state. The mean value for the ionization threshold obtained from the values in Table 7.1 is $(31349\pm10)\,\mathrm{cm}^{-1}$. The value obtained for the threshold obtained from the model in Chapter 5 is $(31355\pm1)\,\mathrm{cm}^{-1}$. The reason for the higher uncertainty in the Rydberg-Ritz model for the IT are the values of the $\mathrm{D}(\Sigma)$ (which was not determined in Chapter 5) and of the $\mathrm{S}(\Sigma)$ series, which have a higher uncertainty. The mean value without

Table 7.1: Rydberg-Ritz model least-squares fit results for the asymptotic quantum defect d_Λ (Rydberg-Ritz coefficient a), ionization threshold IT and the Rydberg-Ritz coefficient b for Cs–He_N Rydberg series.

D(Δ)	D(Π)	D(Σ)	P($\Pi_{1/2}$)	P($\Pi_{3/2}$)	P($\Sigma_{1/2}$)	S(Σ)
ionization threshold						
31344±4	31345±10	31377±575				
			31351±4	31346±5	31350±8	
						31333±25
quantum defect d_Λ - Rydberg-Ritz coefficient a						
2.35±0.01	2.16±0.04	2.2±1.5				
			3.51±0.01	3.48±0.02	3.41±0.03	
						3.79±0.07
Rydberg-Ritz coefficient b						
1.36±0.11	1.6±1	-2.5±26				
			0.8±0.3	1±0.4	1.4±0.7	
						3.6±1.4

those two series is $(31347\pm3)\,\mathrm{cm}^{-1}$, which is also very close to the previous value. This will correspond to a red-shift of the ionization threshold of $(59.5\pm3)\,\mathrm{cm}^{-1}$ with respect to the bare atom threshold at $31406.5\,\mathrm{cm}^{-1}$ [151].

The obtained values for the asymptotic quantum defect (Rydberg-Ritz coefficient a) for different Rydberg series are in good agreement with the fit results presented in Chapter 5 (Table 5.2). Considering the relatively small amount of available resolved transitions, the agreement between the two different models is remarkable and demonstrates the Rydberg character of the Ak–He_N systems. The uncertainties are slightly higher (depending on the Rydberg series) in the Rydberg-Ritz model. If a modified Rydberg-Ritz formula of higher order is used, the uncertainties increase and the model becomes unreliable.

We have seen that the results of the two different fit models are in good agreement. The Rydberg-Ritz model is preferable because it can explain the spectral position of lower Rydberg series members. In the following we discuss this advantage in more detail by explaining the physical meaning (within the frame of QDT) of deviations of the quantum defect for the lowest n states.

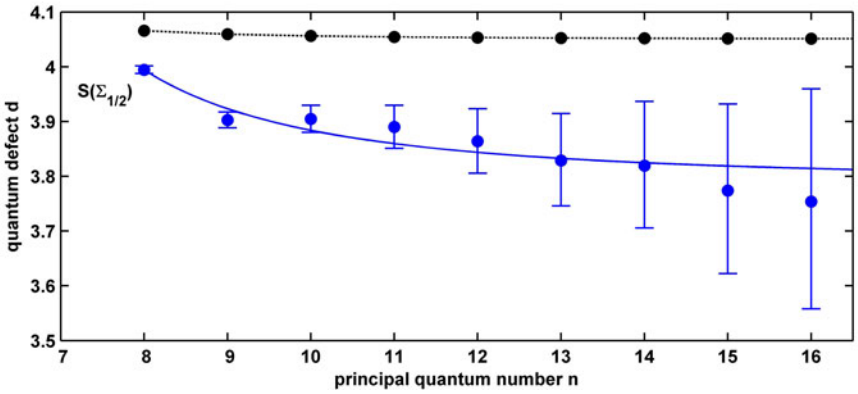

Figure 7.1: Quantum defects of the Cs–He_N nS(Σ) series. The solid blue line is obtained by using a Rydberg-Ritz model. The black line shows the free atom nS series.

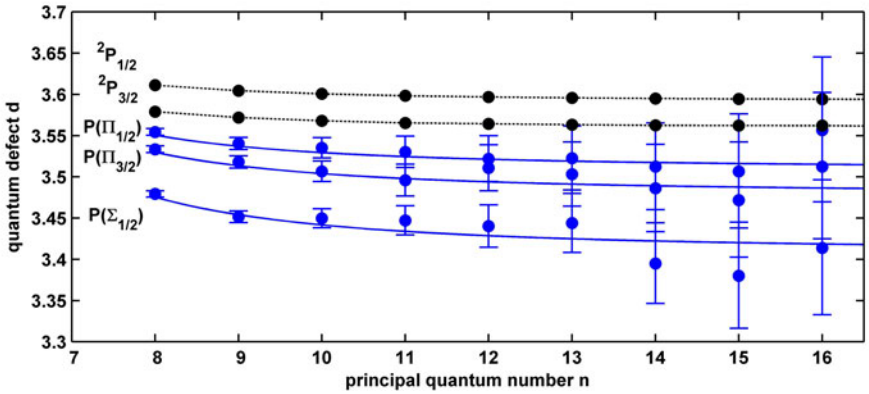

Figure 7.2: Quantum defects of the Cs–He_N nP(Π, Σ) series. The solid blue lines are obtained by using a Rydberg-Ritz model. The black lines show the free atom $n\mathrm{P}_{1/2,3/2}$ series.

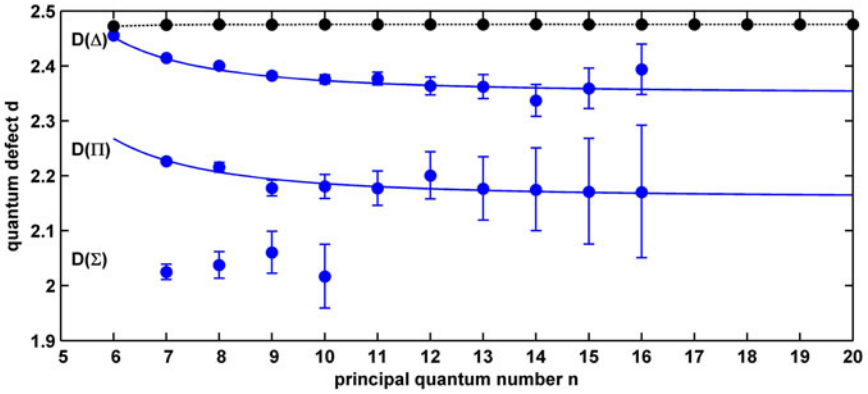

Figure 7.3: Quantum defects of the Cs–He_N nD(Δ, Π, Σ) series. The solid blue lines are obtained by using a Rydberg-Ritz model. The black line shows the free atom $n\mathrm{D}_J$ series.

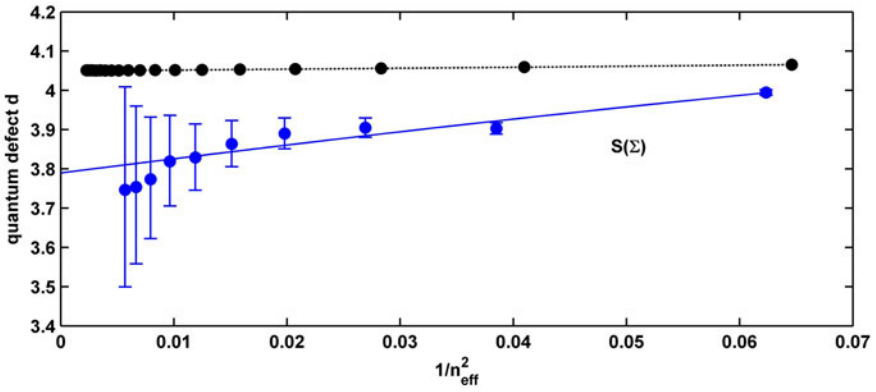

Figure 7.4: Edlén-plots of the quantum defects of the Cs–He_N nS(Σ) series. The solid blue line is obtained by using a Rydberg-Ritz model. The black line shows the free atom $n\mathrm{S}_{1/2}$ series.

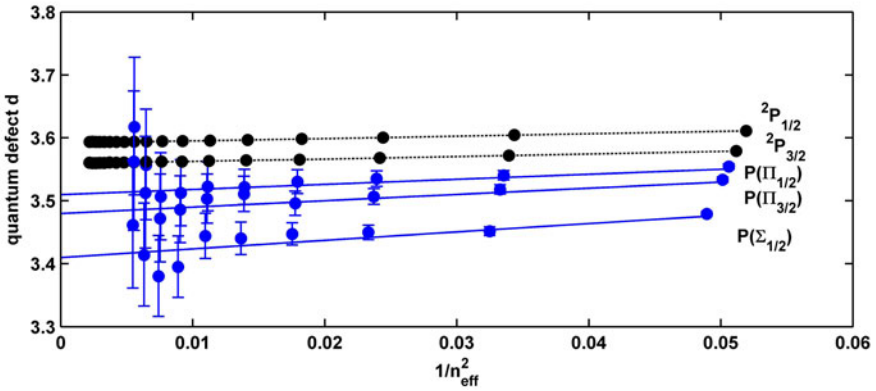

Figure 7.5: Edlén-plots of the quantum defects of the Cs–He_N nP(Π, Σ) series. The solid blue lines are obtained by using a Rydberg-Ritz model. The black line shows the free atom $n\mathrm{P}_{1/2,3/2}$ series.

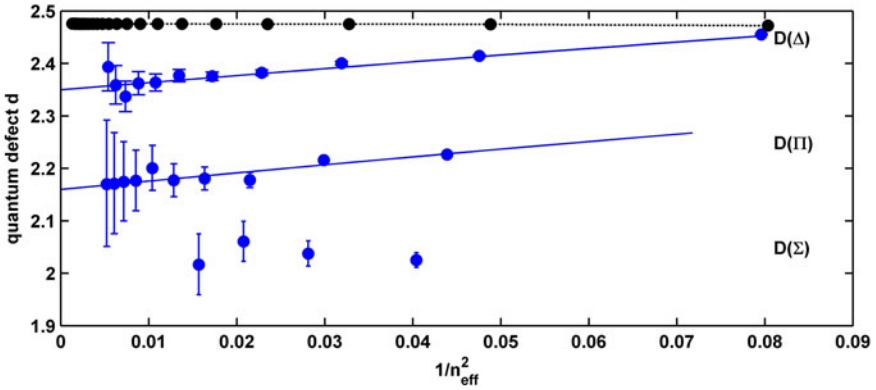

Figure 7.6: Edlén-plots of the quantum defects of the Cs–He_N nD(Δ, Π, Σ) series. The solid blue lines are obtained by using a Rydberg-Ritz model. The black line shows the free atom $n\mathrm{D}_J$ series.

Discussion

Before we start to interpret the findings from the quantum defect plots (Figure 7.1 - 7.3), the Edlén-plots (Figure 7.4 - 7.6) and the fit results in Table 7.1, we summarize some of the insights into the nature of the quantum defect we gained from single channel QDT in Chapter 3.

A higher quantum defect means that the electron has a higher probability to be found inside the core orbitals of the atom. Thinking of the normalization constant for the radial wave function, which scales with $n^{*-3/2}$, an increase of the quantum defect at low n is reasonable because the electron spends more time (higher probability) in the core. On the energy scale, an increased quantum defect corresponds to a higher binding energy caused by the higher net charge experienced by the electron in the core. The consequence are lowered energy levels compared to hydrogenic energy levels (which are approximately represented by nF energy levels in the Rb and Cs atom). It is characteristic for these core-penetrating states, that if n increases, the quantum defect decreases and rapidly settles down to its asymptotic value. The deviation from the asymptotic value is highest at the lowest n states.

In contrast, non-penetrating states show the reversed behavior, their quantum defect increases slightly with n. For non-penetrating states the quantum defects are determined by core polarization effects. As discussed in Chapter 3, the Cs $n\mathrm{D}_J$ series is an exception because its lower states behave core non-penetrating and its quantum defects increase with n, but the quantum defect reaches a maximum around $n = 10$ and starts to decrease for higher n.

Thus, according to the Rydberg-Ritz formula, a core-penetrating series has a positive Rydberg-Ritz coefficient b and this corresponds to monotonically increasing (with $1/n_{eff}^2$) quantum defects in the Edlén-plots. Hence, by introducing the Rydberg-Ritz model for atoms on helium droplet, we can learn about the effects of the perturbation by helium atoms on the expectation value of the electron in the alkali atom core.

A general finding for all observed Ak–$\mathrm{He_N}$ Rydberg series is that the quantum defect is decreased by the presence of the helium droplet. From the perspective of QDT this means that the electron spends less time inside the core than compared to the free atom. The helium screens the electron from the charge of the atom core. As it was already mentioned earlier, the lower states differ in their behavior from the higher states. The reason can be seen from the Figures 7.1 - 7.3 where the quantum defects are shown as a function of the principal quantum number n. All states on the droplet show a relatively (compared to atoms) strong increase of the quantum defects at low n and therefore a deviation from the behavior of free atom quantum defects (black lines). Hence it becomes clear why these low n states can not be fitted with the model presented in Chapter 5, where the same behavior of low n free-atom and on-droplet quantum defects is assumed.

Especially from the nD series it becomes evident that the core-penetrating character becomes dominant at low n for Cs states on helium droplets. The slight increase of the free-atom quantum defect at low n members of this series has changed to a monotone decrease of the quantum defect. From the Edlén-plots, it can be seen that all series have the same slope and increase with $1/n_{eff}^2$. This is equivalent with the finding of monotone decreasing quantum defects with n, which is also reflected by the signs of the Rydberg-Ritz coefficients b (Table 7.1) which are positive (within the uncertainty) for all Rydberg series.

In conclusion it can be stated that the presence of the helium forces the electrons to spend

more time outside the core of the atom. The helium droplet screens the atom core from the valence electron. At low n where the electron's wavefunction is confined in a small space around the helium droplet and the alkali atom core, the behavior of the lower n states is different and the quantum defects increase with decreasing n, but do not reach the free atom value. As n increases and the orbital gets larger, a decreasing percentage of the orbital will overlap with the droplet and the core (this is related to the $n^{*-3/2}$ scaling of the normalization constant). The quantum defects settle down rapidly to the constant asymptotic value.

7.1.3 Rydberg-Ritz model for Rb atoms on helium nanodroplets

For Rb–He_N, in contrast to Cs–He_N discussed above, excitation spectra for different droplet sizes were recorded. The Rydberg-Ritz model, which has been described in the last section can be used for droplet size dependence studies of the quantum defects of Rydberg series in the Rb–He_N system.

A least-squares fit of observed Rydberg state energy levels to the modified Rydberg-Ritz formula (Equation 7.1) gives values for the ionization threshold, the Rydberg-Ritz parameter a, which corresponds to the asymptotic quantum defect d_Λ and the Rydberg-Ritz parameter b, which accounts for deviations from the asymptotic quantum defect at low n. Similar to Cs–He_N, we can calculate quantum defects from the IT with Equation 7.2.

Quantum defects

The different droplet sizes used in this section are $\hat{N}_{60,14} = 7500$, $\hat{N}_{60,16} = 5000$, $\hat{N}_{60,18} = 3200$ and $\hat{N}_{60,20} = 2000$. We start the discussion with the results for the quantum defects (Equation 7.2) obtained from the fit results of the ionization thresholds from Chapter 6 within the simple Rydberg formula model. These quantum defects are shown in Figure 7.7 for the $n\mathrm{S}(\Sigma)$ series, in Figure 7.8 for the $n\mathrm{P}(\Pi, \Sigma)$ series, in Figure 7.9 for the $n\mathrm{D}(\Delta, \Pi, \Sigma)$ series and in Figure 7.10 for the nF series. The quantum defects therein are compared to free atom quantum defects (black-lines).

The quantum defects calculated with the simple Rydberg formula appear as horizontal lines in these plots. It can be seen that the quantum defects of lower n states deviate from these straight lines (i.e. the simple Rydberg model), similar to what we have observed in the last section for Cs–He_N. These data points were excluded from the least-squares fit, but they can be included in the fit procedure if a Rydberg-Ritz model is used, which is demonstrated in the following.

Rydberg-Ritz fit results

The fit results are shown for different droplet sizes in Figure 7.11 for the $n\mathrm{P}(\Pi, \Sigma)$ series, in Figure 7.12 for the $n\mathrm{D}(\Delta, \Pi, \Sigma)$ series and in Figure 7.13 for the nF series. The Rydberg-Ritz model was used only when possible, which means where the least squares fit gives reliable results. It was not possible to fit the $n\mathrm{S}(\Sigma)$ series with this model, which is evident from Figure 7.7, because there is only one data point (and only for the $\hat{N}_{60,18} = 3200$ and $\hat{N}_{60,20} = 2000$ cluster sizes) which deviates from the series. In addition, for some n in this series it was not possible to assign a spectral peak and for the $n\mathrm{P}(\Sigma)$ series it was not possible to use the Rydberg-Ritz model because of the few available data points.

Edlén-plots for the obtained quantum defects are presented in Figure 7.14 for the nS(Σ) series, in Figure 7.15 for the nP(Π, Σ) series, in Figure 7.16 for the nD(Δ, Π, Σ) series and in Figure 7.17 for the nF series.

The fit results for the least squares fit of the observed transitions are shown for the ionization thresholds in Table 7.2, for the asymptotic quantum defects in Table 7.3 and for the Rydberg-Ritz coefficients b in Table 7.4. The fit results are in good agreement with the ionization thresholds and quantum defects obtained by a fit to the ordinary Rydberg formula, except for slight deviations of the quantum defect in the nD(Π, Σ) series (see Section 6.4, Table 6.2 and 6.3). Because of the small number of resolved spectral peaks in the nP(Σ) series, the ionization threshold of the nP(Π) series was taken for the fit procedure in order to decrease the number of fit parameters, which makes the result more reliable.

Table 7.2: Rydberg-Ritz model fit results for Rb–He_N ionization thresholds for different droplet sizes.

droplet size $\hat{N}$	7500	5000	3200	2000	atom
D(Δ)	33630±8	33638±8	33645±10	33652±9	33690.80
D(Π/Σ)	33624±19	33623±22	33628±24	33627±48	33690.80
P(Π)	33636±10	33647±6	33639±15	33655±5	33690.80
P(Σ)	-	-	-	-	33690.80
S(Σ)	-	-	-	-	33690.80
F	33637±14	33645±5	33643±22	33645±23	33690.80

Table 7.3: Rydberg-Ritz model fit results for Rb–He_N asymptotic quantum defects for different droplet sizes, which correspond to the Rydberg-Ritz coefficient a.

droplet size $\hat{N}$	7500	5000	3200	2000	atom
D(Δ)	1.25±0.02	1.27±0.02	1.28±0.02	1.30±0.02	1.347
D(Π/Σ)	1.04±0.05	1.05±0.05	1.09±0.05	1.11±0.11	1.347
P(Π)	2.53±0.03	2.57±0.02	2.54±0.05	2.61±0.01	2.654
P(Σ)	-	-	-	-	2.655
S(Σ)	-	-	-	-	3.131
F	-0.063 ±0.063	-0.026± 0.010	-0.029±0.046	-0.013±0.051	0.016

Table 7.4: Rydberg-Ritz model fit results for Rb–He_N Rydberg-Ritz coefficients b for different droplet sizes.

droplet size $\hat{N}$	7500	5000	3200	2000
D(Δ)	0.24±0.23	0.01±0.24	-0.13±0.30	-0.32±0.29
D(Π/Σ)	2.73±0.76	2.60±0.79	2.03±0.83	1.75±1.61
P(Π)	1.12±0.63	0.59±0.42	1.18±0.91	0.15±0.25
P(Σ)	-	-	-	-
S(Σ)	-	-	-	-
F	0.86±0.66	0.27±0.21	0.31±0.5	0.08±0.43

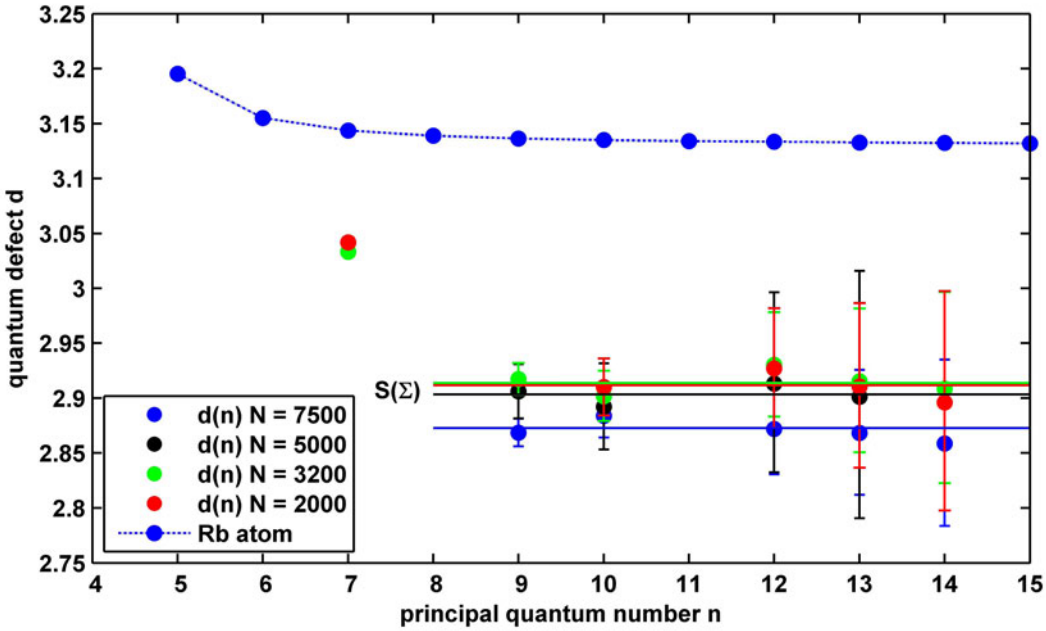

Figure 7.7: Quantum defects of the Rb–He_N nS(Σ) series. The solid lines are obtained by using a Rydberg model. Atomic quantum defects (nS$_{1/2}$ states) are shown as dashed blue line.

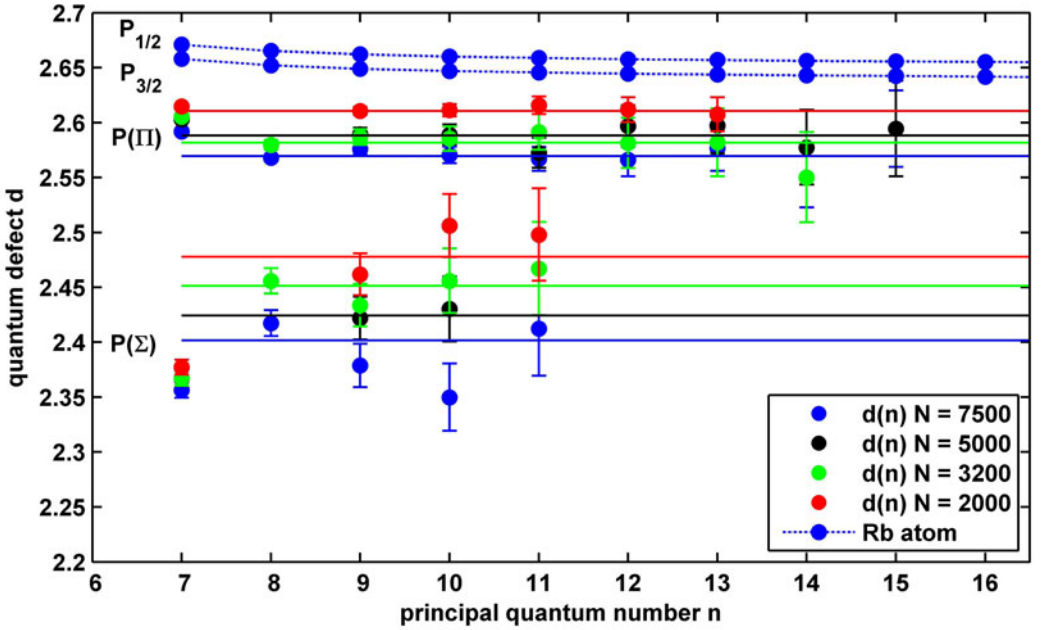

Figure 7.8: Quantum defects of the Rb–He_N nP(Π, Σ) series. The solid lines are obtained by using a Rydberg model. Atomic quantum defects (nP$_{1/2}$ and nP$_{3/2}$ states) are shown as dashed blue lines.

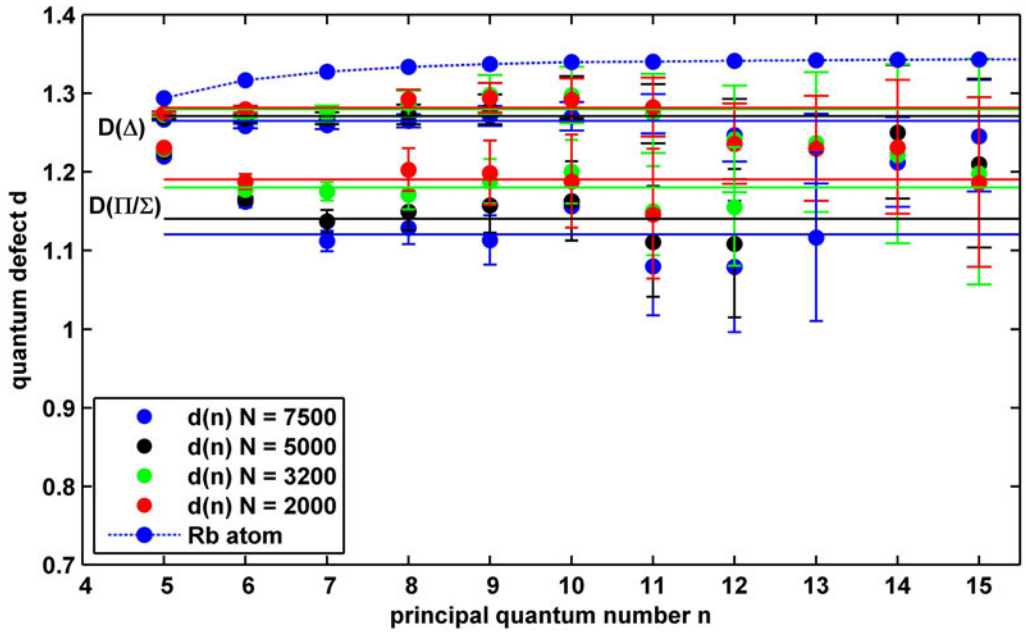

Figure 7.9: Quantum defects of the Rb–He_N nD(Δ, Π, Σ) series. The solid lines are obtained by using a Rydberg model. Atomic quantum defects (nD$_J$ states) are shown as dashed blue line.

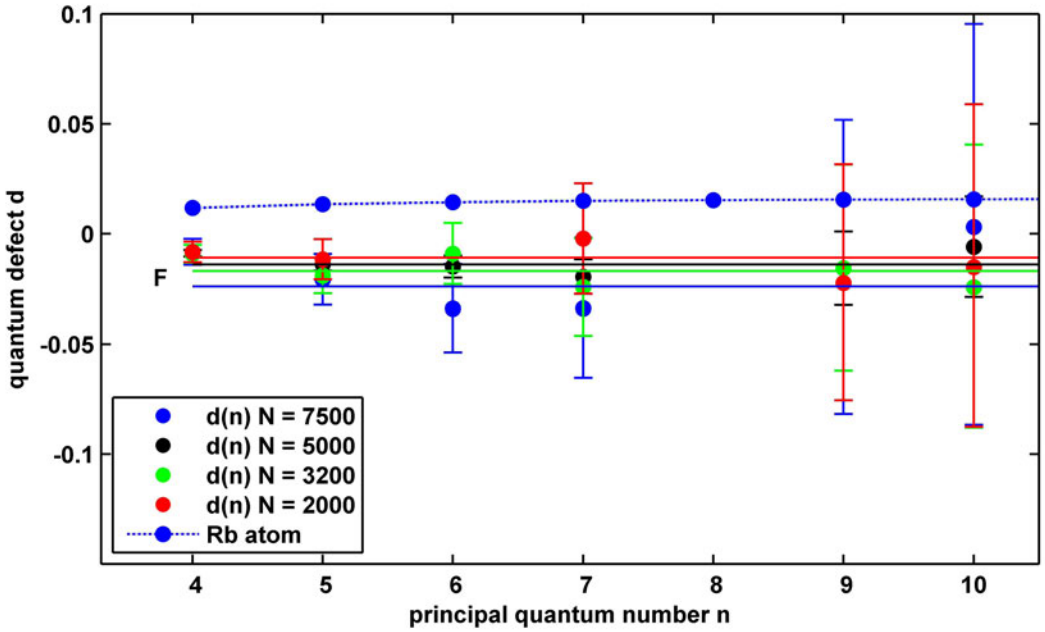

Figure 7.10: Quantum defects of the Rb–He_N nF series. The solid lines are obtained by using a Rydberg model. Atomic quantum defects (nF$_J$ states) are shown as dashed blue line.

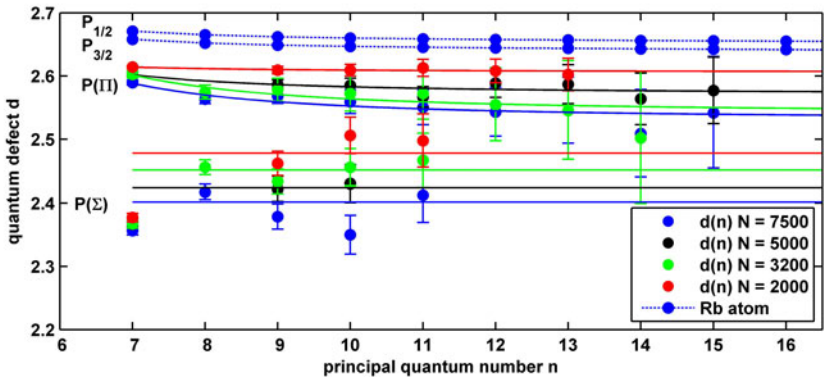

Figure 7.11: Quantum defects of the Rb–He_N nP(Π) series. The solid lines are obtained by using a Rydberg-Ritz model. For the P(Σ) series, a simple Rydberg model was used. Atomic quantum defects ($n\mathrm{P}_{1/2}$ and $n\mathrm{P}_{3/2}$ states) are shown as dashed blue lines.

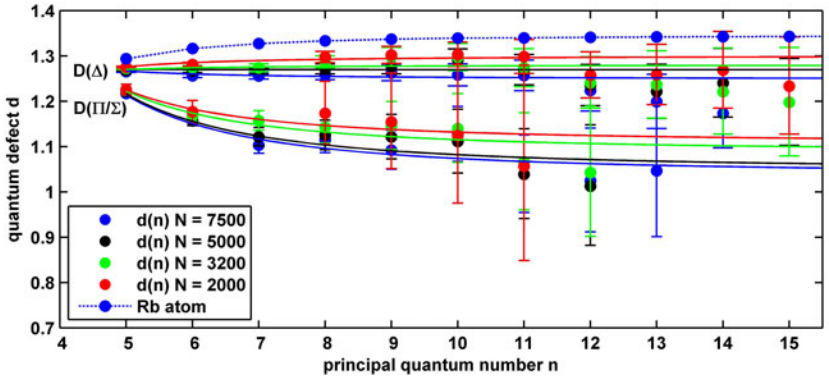

Figure 7.12: Quantum defects of the Rb–He_N nD(Δ, Π, Σ) series. The solid lines are obtained by using a Rydberg-Ritz model. Atomic quantum defects ($n\mathrm{D}_J$ states) are shown as dashed blue line.

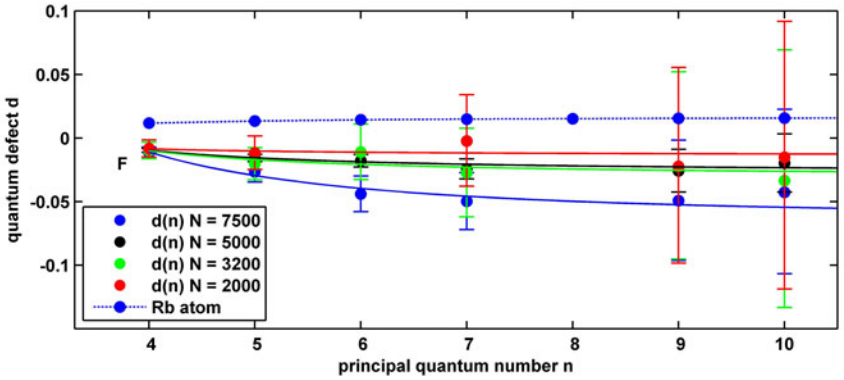

Figure 7.13: Quantum defects of the Rb–He_N nF series. The solid lines are obtained by using a Rydberg-Ritz model. Atomic quantum defects ($n\mathrm{F}_J$ states) are shown as dashed blue line.

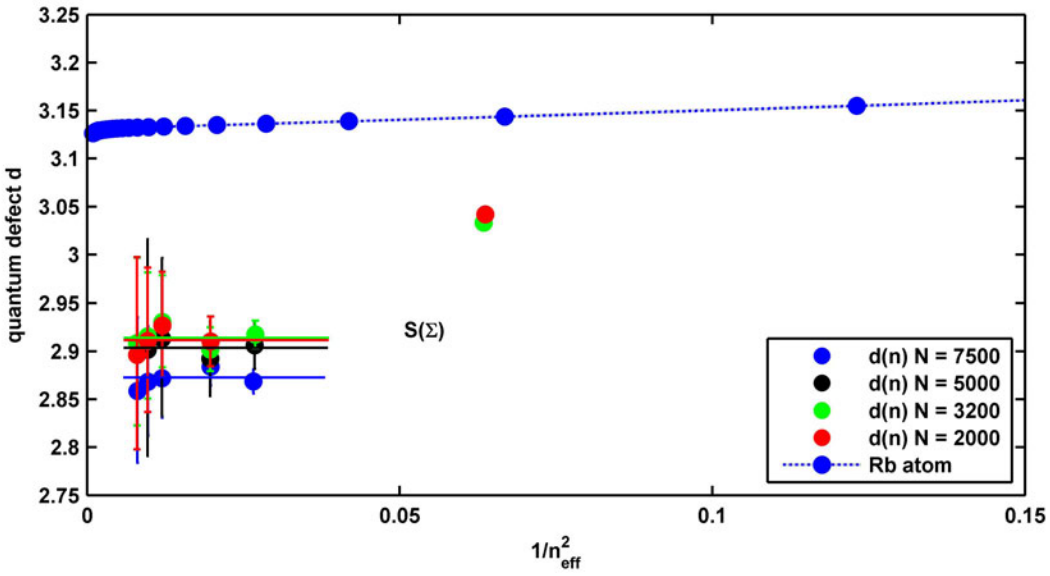

Figure 7.14: Edlén-plots for the Rb–He_N nS(Σ) series. The horizontal solid lines are obtained by using a Rydberg model. Atomic quantum defects ($nS_{1/2}$ states) are shown as dashed blue line.

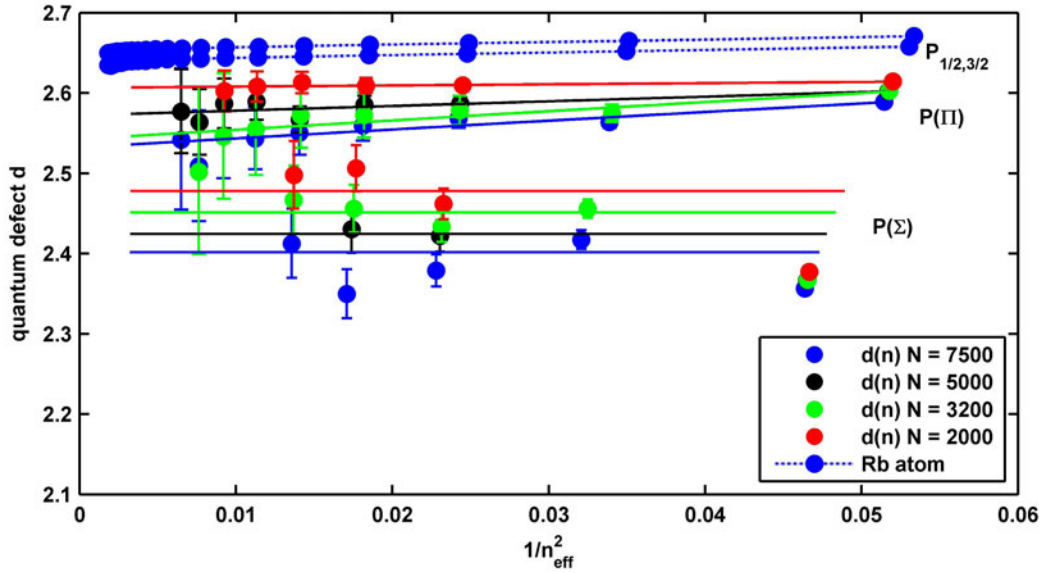

Figure 7.15: Edlén-plots of the Rb–He_N nP(Π) series. The solid lines are obtained by using a Rydberg-Ritz model. For the P(Σ) series, a simple Rydberg model was used. Atomic quantum defects ($nP_{1/2}$ and $nP_{3/2}$ states) are shown as dashed blue lines.

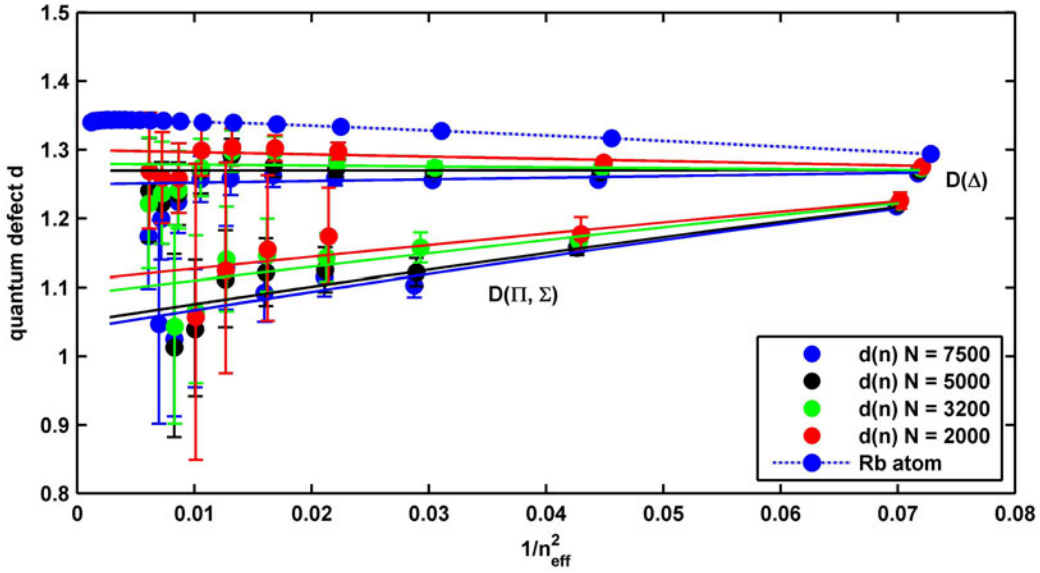

Figure 7.16: Edlén-plots for the Rb–He_N nD(Δ, Π, Σ) series. The solid lines are obtained by using a Rydberg-Ritz model. Atomic quantum defects (nD$_J$ states) are shown as dashed blue line.

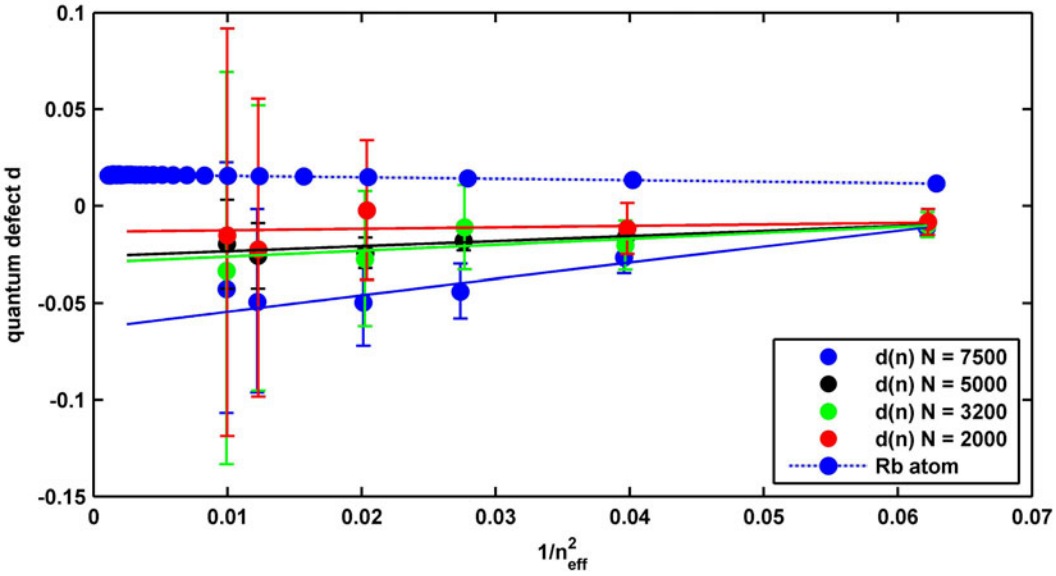

Figure 7.17: Edlén-plots for the Rb–He_N nF series. The solid lines are obtained by using a Rydberg-Ritz model. Atomic quantum defects (nF$_J$ states) are shown as dashed blue line.

Discussion

The figures in which the quantum defects are depicted show that the Rb–He_N system is very similar to Cs–He_N and we can tie up to the discussion in Section 7.1.2 for Cs–He_N. The comparison between the ordinary Rydberg and the Rydberg-Ritz model demonstrates the advantage of the Rydberg-Ritz formula.

A general finding is that the quantum defects are lowered by the presence of the helium droplet. The quantum defects increase at the lowest members of each Rydberg series, but to not reach the free atom values. This is seen by the deviation from straight lines in the plots of the quantum defects in Figure 7.7 - 7.10. The Rydberg-Ritz model, by using the second order Rydberg-Ritz coefficient b, is able to describe this observation. The deviation of the quantum defect at low n is reflected by a positive Rydberg-Ritz coefficient b. This corresponds to the slope of the Edlén-plots, which increase with $1/n_{eff}^2$. Similar to Cs–He_N we can conclude that the increased quantum defects of Rb–He_N at low n are caused by an increased probability of the electron to penetrate the core. Note that the overall core-penetration is lowered, which is reflected by the decreased Rb–He_N quantum defects with respect to the free atom quantum defects. An exception seems to be the 7P(Σ) state, which shows the reverse behavior at low n, but due to the low number of resolved states of this series the fit is not very accurate. This is most probably explained by the fact that for the fit of this series the ionization threshold of the nP(Π) series was taken in order to lower the number of fit parameters.

Additional information can be drawn from the comparison of quantum defects for different droplet sizes. The most striking observation is that the influence of the droplet size is relatively small at low n states. The quantum defects seem to be insensitive to the droplet sizes at these states. When n increases into the region where the orbital sizes are in the same order of magnitude than the droplet sizes, the quantum defects for different droplet sizes differ more strongly. This is reasonable because a small orbital will experience only the helium atoms which are close to the Rb atom core. The majority of He atoms in the droplet is far away from the orbital. Hence the deformation of the orbital, which leads in the end to shifted energy levels, is dominated by the short-range He atoms which are related to the shape of the dimple in which the Rb atom resides in the intermediate state. The dimple structure is not expected to differ strongly for the studied droplet size region and thus the environment for the electron also does not depend much on the droplet size. The situation is different for Rydberg orbitals of higher states, which are larger than the droplet. It is reasonable that a large droplet can shield the electron from the core more effectively, which explains the lower quantum defects and the more hydrogenic behavior for larger droplets.

An interesting exception from these general findings is the nD(Δ) series. The perturbation of the quantum defect of the lowest member of this series ($n = 5$) is so weak, that the core non-penetrating character of this state is preserved, which is reflected in a small negative Rydberg-Ritz coefficient b.

Spectral trends of Rb atoms on helium nanodroplets

In Figure 7.18-7.20 the shifts of observed on-droplet states with respect to bare atom states are shown (see Section 6.4). The solid lines represent the calculated energy levels within a Rydberg-Ritz model 6.4. The new model affect only the lowest n sates of each Rydberg series. The Figures demonstrate the effect of the Rydberg-Ritz parameter b. It can be seen that the Rydberg-Ritz model is able to reproduce the observed spectral position of the recorded states. The Rydberg-Ritz model was not used for the nS(Σ) series, therefore it is not shown here.

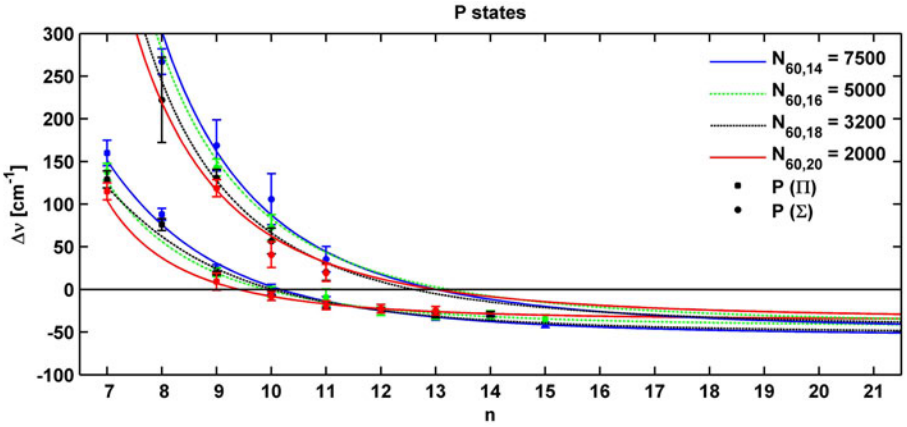

Figure 7.18: Shifts of the nP(Π, Σ) states with respect to the free atom $n\mathrm{P}_{1/2}$ state. The solid lines are calculated with the Rydberg-Ritz formula using the values listed in Table 7.2 - 7.4.

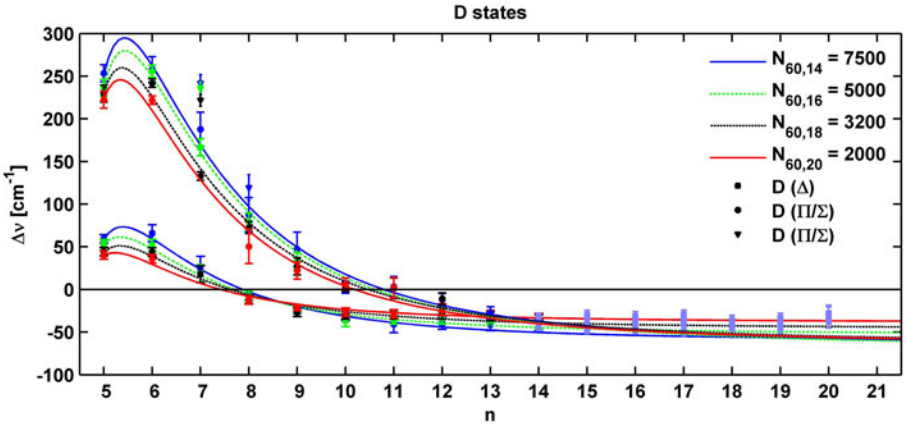

Figure 7.19: Shifts of the nD(Δ, Π, Σ) states with respect to the free atom nD states. The solid lines are calculated with the Rydberg-Ritz formula using the values listed in Table 7.2 - 7.4.

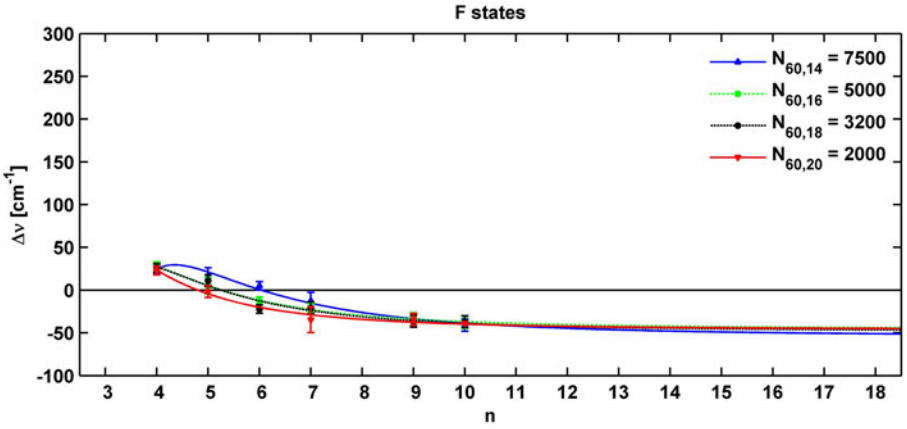

Figure 7.20: Shifts of the nF states with respect to the free atom nF states. The solid lines are calculated with the Rydberg-Ritz formula using the values listed in Table 7.2 - 7.4.

7.2 Ionization thresholds of alkali atoms on helium nanodroplets

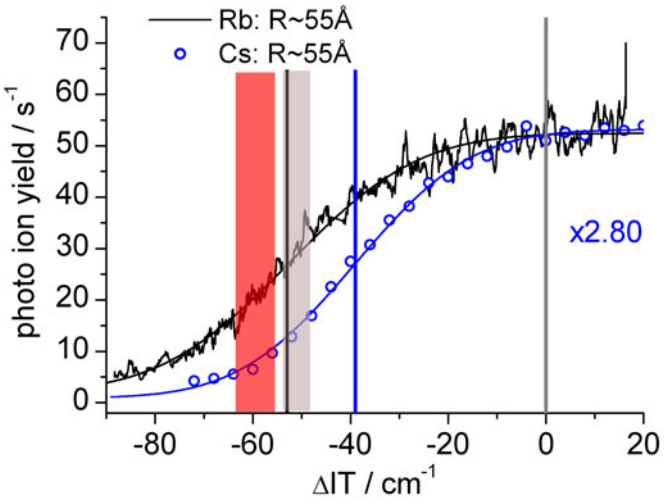

Figure 7.21: Ionization thresholds of Rb (black) and Cs (blue) atoms on helium nanodroplets with respect to the free atom ionization thresholds (vertical gray line). The signal is obtained by keeping one laser fixed at the D1 transition and a second laser is scanned across the ionization threshold while the photo-ion yield of heavy Ak^+–He_N complexes is monitored. The red (Cs) and gray (Rb) areas mark the position of the ionization thresholds obtained from the Rydberg series fits. The vertical blue (Cs) and black (Rb) lines correspond to the ionization thresholds as obtained by a least-squares fit of the data to a Gaussian error function. (figure from ref. [5], modified)

In this section, different methods for the determination of ionization thresholds of alkali atoms on helium nanodroplets are compared to each other.

The first method uses a two-step ionization scheme in which one laser excites the D1 transition and the second laser is scanned across the ionization threshold while the photo-ion yield of heavy Ak^+–He_N complexes is monitored. This method is presented in our article ref. [5]. The Ak^+–He_N is formed upon ionization when the Ak ion immerses into the helium droplet [1]. The ionization thresholds obtained with this method are red shifted with respect to the free atom threshold and the values are $\Delta IT_{Rb} = -53^{+13}_{-8}\,\mathrm{cm}^{-1}$ and $\Delta IT_{Cs} = -39^{+13}_{-8}\,\mathrm{cm}^{-1}$ for droplets consisting of He $\hat{N}_{60,14} = 7500$ atoms. ΔIT is the difference between the threshold of free atoms and atoms on the droplets. These values are obtained by fitting the experimental data to a Gaussian error function. The static extraction field of the TOF mass spectrometer was used for these experiments.

The second method was presented in the previous chapters and exploits the fact that Rydberg states are stepping stones towards ionization [158]: the determination of ionization threshold from Rydberg series.

A comparison of the results of both methods is shown in Figure 7.21. The heavy ion yield is shown for Rb–He_N (black) and Cs–He_N (blue). The lowering of the IT obtained from the Rydberg series extrapolation is shown as red area (Rb–He_N, $\Delta IT_{Rb} = -59 \pm 10\,\mathrm{cm}^{-1}$,

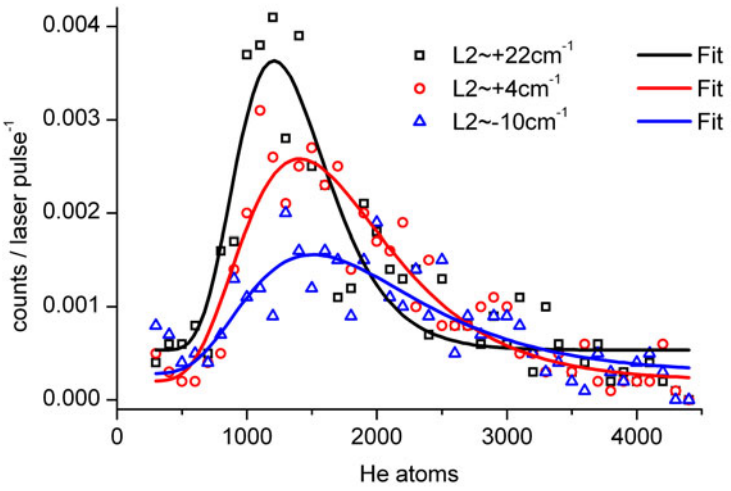

Figure 7.22: TOF mass spectra of Cs^+–He_N complexes for different ionization laser wavenumbers with respect to the ionization threshold as obtained by a least-squares fit of the data to an error function. (figure from ref. [5])

Rydberg-Ritz model, see Section 7.1.3) and gray area (Cs–He_N, $\Delta IT_{Cs} = -52 \pm 5\,\mathrm{cm}^{-1}$, Rydberg model [6], see Section 5.1). Despite the great difference between the two approaches, the results agree very well. Note that the Gaussian error function does not account for the log-normal distribution. The agreement is better in the case of Rb–He_N.

Another interesting finding from the heavy ion yield is the droplet size dependence of the ionization threshold. The larger the droplets, the lower the ionization threshold. This is in good agreement with the finding from the Rydberg and Rydberg-Ritz models. The effect can be seen in Figure 7.22 for Cs–He_N: If the laser is set to lower wavenumbers, e.g. -10 cm^{-1} below the threshold (as obtained from the fit), predominantly large Cs^+–He_N complexes are detected. In contrast, for higher wavenumbers, also small Cs^+–He_N complexes are detected. The reason for the lowered ionization threshold is explained by polarization effects. The helium atoms close by the Ak ion core are polarized by the positive charge. This polarization causes an attractive force acting on the Ak ion core, which manifests in a decreased ionization potential. In this picture, the attractive force draws the Ak ion core towards the droplet. The detection of Ak^+–He_N complexes demonstrates the stability of these systems, because the time from the creation of the system to the impact on the detector is in the order of 100 μs. The IT determined with these two methods corresponds to the value of the "vertical ionization threshold", which depends on the equilibrium position of the Ak atom. From ref. [199] it can be estimated that the total energy drop, if the ion submerges into the droplet, corresponds to approximately 2000 cm^{-1}. The Ak ions are surrounded by a few layers of increased helium density [200, 201]. The Ak ion surrounded by these layers is referred to as "snowball" because the helium density in the first shell is locally well above the freezing density and a solid order is expected. The total binding energy released by the submersion of the Ak ion depends on the droplet size: the larger the droplets, the larger is the total binding energy and hence the lower is the observed vertical ionization threshold [199]. Also the trend from heavy to light Ak atoms, where the ionization threshold is lower for the lighter species, is in agreement with ref.

[199]. Calculations of the electrostatic potential, which is produced by the dielectric response of the helium to an ionic impurity [202], show that the Ak ion will migrate to the center of the droplet. This motion of the ion can be influenced by the external static E-field in the TOF, but for field strength less than 200 V/cm it was reported that the ion mobility in liquid helium is field independent [201, 203].

7.3 The Ak-He$_N$ Rydberg complex in comparison to other Rydberg systems

A comparison of the results obtained for the Ak–He$_N$ complexes to other Rydberg systems shines light onto the Ak–He$_N$ Rydberg systems from a different viewpoint. Similarities between different systems strengthen the conclusions drawn in the previous chapters. For example, lowered ionization thresholds due to polarization of nearby rare gas atoms by positive ions or broadened and shifted Rydberg states are observed in various systems in which rare gas (RG) atoms interact with atoms or molecules.

In the following, some examples of atoms and molecules interacting with single RG atoms, clusters and matrices are discussed and the similarities between them and the Ak–He$_N$ system are worked out and highlighted. In addition to alkali atoms interacting with those species the NO molecule is treated, which is the "alkali atom" of the molecules due to its single, unpaired electron outside of filled molecular orbitals [204]. Spectroscopy of NO is dominated by Rydberg transitions and it is very well characterized.

7.3.1 Rare gas induced collisional broadening and line shifts of alkali atom Rydberg states

The first observations of broadened and shifted alkali atom Rydberg states upon interaction with rare gas atoms date back to the 1930's [205, 206]. Absorption and excitation spectra are obtained with cells containing mixtures of Ak atoms and rare gas. Fermi developed a theory which is able to explain the observed shift and broadening of spectral lines [207]. According to Fermi's theory the displacement of Rydberg terms is caused by two different effects: the polarization of rare gas atoms in the field of the alkali core and the scattering of the valence electron on the rare gas atoms [206, 208]. The important point is that the polarization effect causes a red-shift of the spectral lines similar to the polarization of the nearby He atoms due to the Ak core on the helium droplet.

7.3.2 Rydberg states in rare gas matrices

The great difference between helium nanodroplet isolation spectroscopy and rare gas matrix isolation spectroscopy is the relatively weak interaction between the helium droplet and the dopant. Due to the small size of the helium nanodroplet the electron can spread out into the surrounding vacuum, whereas in a matrix with, from the viewpoint of the atom, almost infinite size, the electron is located in the matrix. This causes very large perturbations of the Rydberg states and only the lowest states can be identified. However, the Rydberg approach also works to characterize these systems and some similarities between them and the Ak-He$_N$ complex can be found.

Relatively little work has been done on the characterization of Rydberg transitions of alkali atoms in RG matrices [209–211]. Only the first few transitions could be resolved, higher Rydberg states start to merge and form a continuum. The ionization threshold is strongly red-shifted because of polarization effects, much more than we observe on helium droplets. It is theoretically explained [212] that for this reason experimentally no higher series members could be observed, because the whole series of higher states merge and the states are squeezed into a very tiny energy interval below the adiabatic ionization continuum. An interesting point which connects the matrix isolated atoms to the Sekatskii-atom (see Section 7.4) is the model presented in ref. [212, 213]: The potential far away from the alkali core is described by a Coulomb potential shielded by the dielectric constant ϵ of the rare gas matrix. As will be shown in Section 7.4, this screening effect is also present in the Ak^+–He_N + e system (although it is weaker because the dielectric constant decreases from Xe to He). This suggests the possibility of the investigation of the properties of a nanoscaled dielectric, i.e. the liquid helium droplet containing a positive charge, surrounded by a negative electron.

Even more similarities are found between Ak–He_N and NO Rydberg states in RG matrices [214]. It was found that low n states will be blue shifted because of the repulsive interaction between the first layer of surrounding atoms in matrix (Pauli repulsion) and the large electron density of small orbitals, which overlap with this nearby atoms. The blue shift increases with the density of the RG matrix. At these low n states the confined electron density screens the positive ion core from the matrix, thus preventing the core from polarizing the surrounding RG atoms. Higher states are found to be red shifted, because of the polarization effect described above. The higher states converge to the shifted IT (the molecular ion ground state potential) which causes a compression of the Rydberg series. Also a lowering of the quantum defect was proposed (but experimentally not found) because of the dielectric screening of the electron against the ionic core, thus reducing further the penetration of the electron into the core [214].

7.3.3 Rydberg states of NO-rare gas van der Waals complexes

According to Ch. Jungen [215] the NO molecule is the "sodium atom" among the diatomic molecules, and as such hosts a prototype system of Rydberg states. Its s(σ), p(σ, π), d(σ, π, δ) and f($\sigma, \pi, \delta, \phi$) Rydberg series (compare to Ak–He_N) are the first which have been fully characterized for a molecule [216]. In addition the Rydberg series for this systems were analyzed within a Rydberg model [217].

The simplest NO-RG van der Waals complex consists of the NO molecule and a single RG atom (e.g. see [204, 218]). It was pointed out that the orientation of the molecular orbitals to the RG atom is very important for the term energy of Rydberg states. Moreover, even the lowest Rydberg orbitals are large enough to accommodate an RG atom within its orbit [219]. The IT is red-shifted and this shift increases with the polarizability of the RG partner. The polarization effect is dominant and all observed Rydberg states are red-shifted. The energy levels are affected by the Pauli repulsion between the RG atom and the electron which decreases the penetration of the electron into the core of the molecule (screening effect). According to QDT this corresponds to a decreased quantum defect. Interestingly, the energy ordering of the d(Δ, Π, Σ) series in NO-RG is the same than we found for Ak–He_N d(Δ, Π, Σ) Rydberg series.

With increasing number m of rare gas atoms in the NO-RG$_m$ system [220, 221], the pertur-

bations (shift and broadening) of the states becomes larger. For small van der Waals clusters the size of the Rydberg orbital is sufficiently large to accommodate several RG atoms within the electrons orbit even for low n. Such systems were theoretically studied also for small $NaAr_n^*$ clusters [222]. For example, two different types of interactions are found for the NO-Ar_m ($m = 1-6$) system: If the atoms are inside the Rydberg orbital, the electron is partially screened from the core by the RG atoms. Whereas, if the RG atoms are outside the orbital, the RG atom is screened from the NO^+ by the Rydberg electron.

NO Rydberg states on helium nanodroplets

The only helium nanodroplet Rydberg system besides Na–He_N, Rb–He_N, Cs–He_N and Ba–He_N which has been investigated is the NO–He_N complex [223]. In its $X^2\Pi$ ground state it resides inside the helium nanodroplet. Upon excitation of the strongly blue shifted $A^2\Pi \leftarrow X^2\Pi$ transition the NO* molecule migrates to the surface of the droplet and is hence very similar to a Ak–He_N complex. The authors of ref. [223] propose that for low Rydberg states, the increased electron density close to the NO^+ core prevents the formation of NO*-He_k exciplexes (except for very small k) and high Rydberg levels are supposed to form NO^+-He_k very efficiently. In the latter case the He rushes towards the NO^+ core rapidly because of the low electron density between the droplet and the molecule. This scenario is similar to what we observe for Ak–He_N: for high Rydberg states the probability of exciplex formation increases independent of the molecular sub-state. This can also be explained by the decreased electron density and the attractive interaction between polarized He atoms and the Ak ion core.

7.4 On the nature of Rydberg electrons attached to positively charged helium droplets - the Sekatskii-atom

The situation where a positively charged ion is located inside a helium nanodroplet is in literature often referred to as Sekatskii-atom, superatom or Scolium [195]. This system was theoretically investigated by Golov and Sekatskii [183]. Experiments strongly suggest that the formation of these systems is possible, although a direct experimental verification of the Sekatskii-atom failed so far.

VUV-spectroscopy of small pure helium clusters with synchrotron radiation show that the Rydberg electron tends to move outside the cluster [224, 225]. Experiments with Ak doped helium nanodroplets presented in this thesis show that the excitation of very high Rydberg states is possible, but a last proof is missing that the ion core immerses into the droplet upon the Rydberg excitation. On one hand, the observation of red-shifted states shows the attractive interaction between the helium droplet and the ion core of the Rydberg atom. The fact that Ak^+–He_N could be detected with the TOF demonstrates that the helium droplet and the ion core form a stable complex if the electron is completely removed. On the other hand, life time measurements of Na–He_N [164] show that high Rydberg states with $n = 100$ are only stable on a micro-second time scale. Also our preliminary results (see next Chapter) of pulsed field ionization experiments with Ak–He_N in high Rydberg states failed to show the appearance of heavy Ak^+–He_N complexes below the ionization threshold, which would be a verification for the Sekatskii-atom (see Section 8.1). These results suggest that the Rydberg

electron recombines rapidly with the ion core either due to tunneling of the electron into the droplet (only important for small droplets) or because of the attraction of the ion to the electron. The latter effect is suggested to cause the short lifetime of the Sekatskii-atom by theoretical calculation in ref. [195]. The results therein suggest that smaller Sekatskii-atoms with fairly large solid core (snowball) are stable on a longer timescale.

The experimental realization of a Sekatskii atom will open a unique possibility to study the influence of a confined superfluid dielectric on a nanosized scale, but it remains a challenging task for future experiments.

Overlap between hydrogenic radial wavefunctions and a helium droplet

It is instructive to study the overlap between the unperturbed wavefunction of an electron and the helium droplet as a function of the principal quantum number. The smaller the electron density which overlaps with the droplet, the smaller is the repulsive part of the interaction. A schematic comparison of the size of radial hydrogen d-wavefunctions ($l = 2$) with $n = 10$ (red) and $n = 14$ (blue) with a helium droplet with a diameter of $d = 56\,\text{Å}$ is shown in Figure 7.23. It reflects the situation with an atom located on the surface of the droplet. The vertical

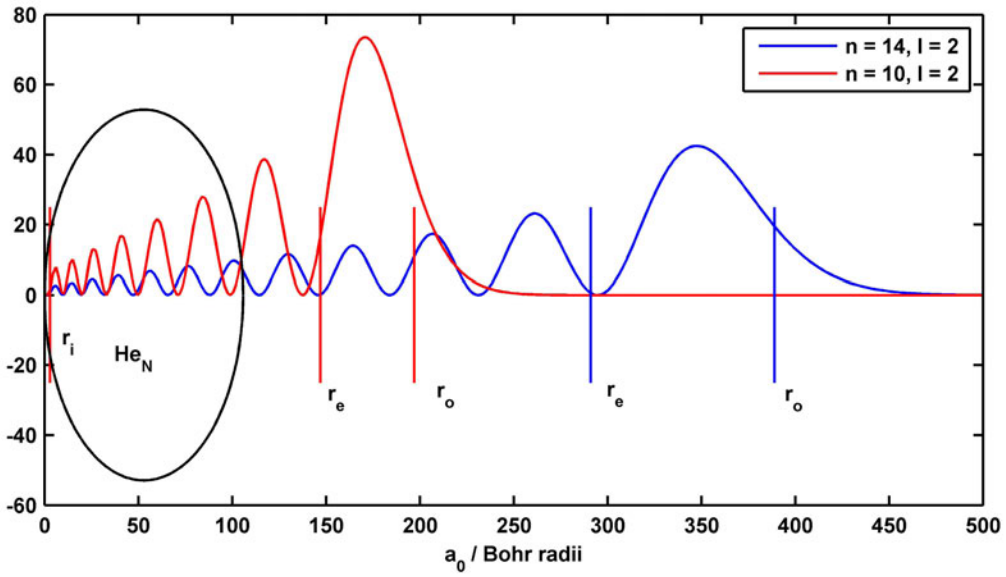

Figure 7.23: Schematic comparison of the size between the radial d-wavefunctions ($l = 2$) with a helium droplet with a diameter of $d = 56\,\text{Å}$. The $n = 10$ (red) and $n = 14$ (blue) wavefunctions are shown. The vertical lines correspond to the inner turning point r_i (which can not be separated for the two wavefunctions), the expectation value r_e and the outer turning point r_o.

lines in Figure 7.23 correspond to (from left to right, color coded for $n = 10$ and $n = 14$) the inner turning point r_i, the expectation value r_e and the outer turning point r_o. The inner turning point is approximately constant for different n. The two depicted wavefunctions are normalized. The position of the knots of the inner part of the wavefunction is approximately constant. With increasing n, additional knots and loops are added to the long range part of

the wavefunction. This is expressed by Mullikan's famous analogy between embryology and atomic Rydberg orbitals [226]: "Ontology recapitulates phylogeny". A developing organism, once started, goes through a series of stages resembling successive evolutionary precursors (in biology this theory is nowadays just a historic side note and is now defunct [227]). Similar for atomic orbitals, the nth orbital recapitulates the inner loops and knots of the $(n-1)$th orbital. One further node and loop are added for each unit increase in n. The Rydberg orbitals (e.g. Cs: 10s) have precursors in the core, where the occupied orbitals in the core are referred to as "real precursors" (e.g. Cs: 1s to 6s) and the not occupied as "virtual precursors" (e.g. Cs: 7s or 8s).

For our problem this means that the number of oscillations of the alkali wavefunction which overlap with the droplet is constant for a Rydberg series. The amplitudes of these innermost lobes which overlaps with the droplet scale as $\sim n^{*-3/2}$ (normalization constant) and thus the probability to find the electron outside the droplet increases with n. As a simple model to

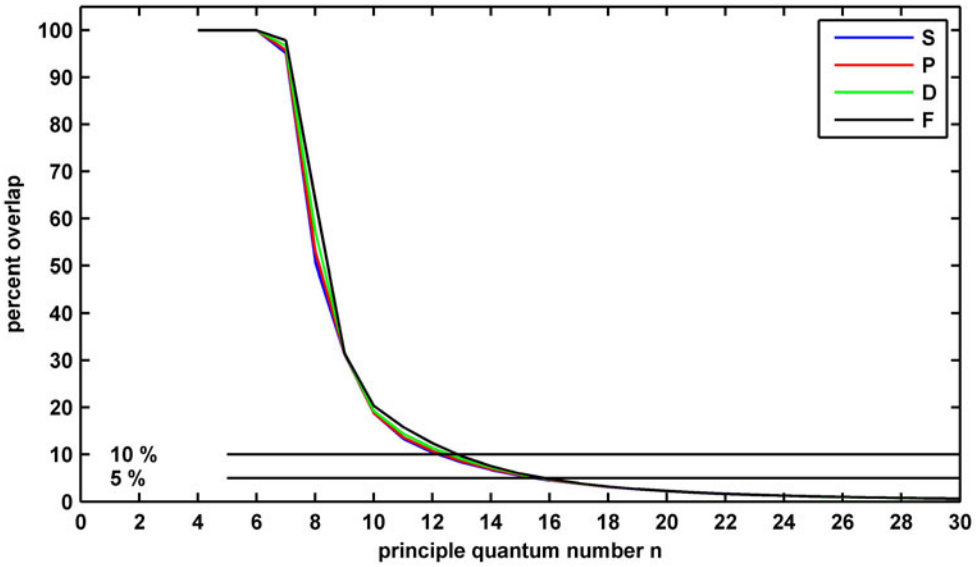

Figure 7.24: Integral over the hydrogenic radial wavefunction from zero to the droplet diameter $d = 56$ Å. The percentage of the electron density which overlap with the helium droplet is given as a function of the principal quantum number n.

estimate the overlap we integrate hydrogenic radial wavefunctions (Equation 3.9) from zero to the droplet diameter $d = 56$ Å. This estimation gives an upper boundary for the overlap, but it neglects the orientation of the orbital to the droplet (the angular part). This is shown in Figure 7.24. It can be seen that at $n > 6$ the overlap drops rapidly and it drops below 5 % for $n > 16$. Alkali atoms will show the same behaviour because their wavefunction is also hydrogenic, except for inside the core which is accounted for with the quantum defect. For alkali atoms the n scale must be replaced by the effective quantum number n^*.

A small fraction of the wavefunction remains overlapped with the helium droplet as the constant inner turning point suggests. In order to create a wavefunction without an overlap with the droplet, very high $l \sim 15$ states would be required. According to the electronic selection rules a preparation of such high l states with laser excitation of Ak–He_N is not

possible.

The Golov and Sekatskii model

In the following we will discuss these Rydberg states based on the simple approach presented by Golov and Sekatskii [183, 228]. It should be mentioned that the idea of this system has been proposed earlier in 1988 (see [229]). The Golov and Sekatskii model was refined later and an up to date calculation can be found in ref. [195].

In this model a positive charge (e.g. an Ak ion core) is assumed to be located in the center of a helium droplet. It was shown later by calculations of potentials of ionic impurities in helium droplets that an ion will reside at the center [202]. The positive charge is surrounded by a helium droplet with radius r_0. The radius is the most important parameter for the spectrum of bound states. The calculations are valid for $r_0 > 20\,\text{Å}$, which is a radius where the Coulomb attraction at the droplet surface is much less than the barrier which prevents the electron from penetrating into the droplet $V_0 \sim 1\,\text{eV}$. The geometry of the problem enables the use of a centrally symmetric potential which simplifies the calculation. The electron potential is different inside and outside the droplet. Inside the droplet the potential is given by the sum of the potential barrier and the Coulomb potential in a dielectric (in atomic units):

$$V = V_0 - \frac{1}{\epsilon r}, \tag{7.3}$$

where the $\epsilon = 1.057$ is the dielectric constant of liquid helium. This potential ignores the density fluctuation due to electrostatic effects inside the droplet, but because of the high barrier V_0 the penetration of the electron into the droplet is small and thus the inner structure does not affect the electronic structure. Outside the droplet the potential has the form of the ordinary Coulomb potential

$$V = -\frac{1}{r}. \tag{7.4}$$

The Schrödinger equation with this potential can be solved analytically and gives the spectrum of allowed energies which can be calculated with the following set of equations:

$$\lambda = \frac{1}{\sqrt{2(V_0 - 1/\epsilon r_0)}} \tag{7.5}$$

$$k = M - \frac{3}{4} + \frac{\sqrt{8r_0}}{\pi} + \frac{1}{\pi}\arctan\left(\sqrt{\frac{r_0}{2}}\left(\frac{1}{\lambda} + \frac{1}{r_0}\right)\right) \tag{7.6}$$

$$E_{M,l,r_0,\epsilon} = -\frac{Ry}{k^2}. \tag{7.7}$$

Equation 7.7 is the Rydberg formula for the Sekatskii-atom. The quantum number M is an integer, where $M > \sqrt{r_0/2}$ must be fulfilled. Due to the potential barrier the electron's wavefunction is damped inside the helium droplet. The energy level dependence on the orbital angular momentum l is very small. In the case of an impenetrable potential barrier V_0 the states are degenerated in l, because only the pure Coulomb part of the potential remains. With this set of equations the energy levels as a function of the quantum number M can be calculated. The calculated energy levels as a function of the droplet size are shown in Figure 7.25 for $M = 14, 16, 18$ and 20 and $l = 0$.

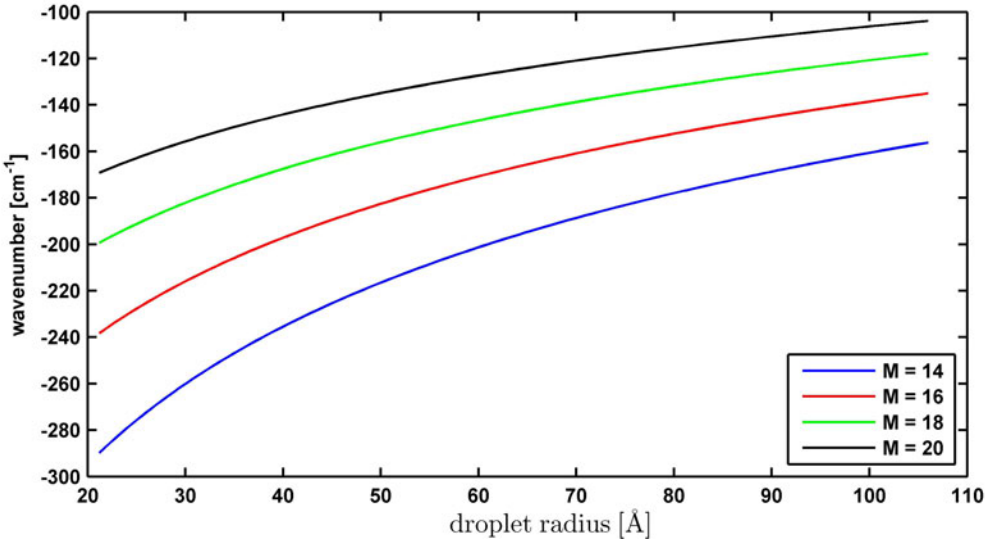

Figure 7.25: Energy levels of the Sekatskii atom for $M = 14, 16, 18$ and 20 and $l = 0$ as a function of the droplet size with respect to the ionization threshold.

Beyond the Golov and Sekatskii model

We can use the findings on the Sekatskii atom above and combine it with the conclusions from the spectroscopy of the Ak–He_N system. Ak–He_N Rydberg states and the Ak–He_N ionization threshold were found to be droplet size dependent. Similarly the Rydberg states of a Sekatskii-atom, created in a droplet beam experiment are suggested to be convoluted by the log-normal droplet size distribution. This is shown in Figure 7.26 for droplets with $\hat{N}_{60,18} = 3200$. The calculation suggests that the spectroscopy of Sekatskii-atom Rydberg states with microwave spectroscopy (e.g. chirped-pulse millimeter-wave Rydberg state spectroscopy [230]) is hardly possible. Transitions between these states will most probably not lead to a spectrum with resolvable peaks [231].

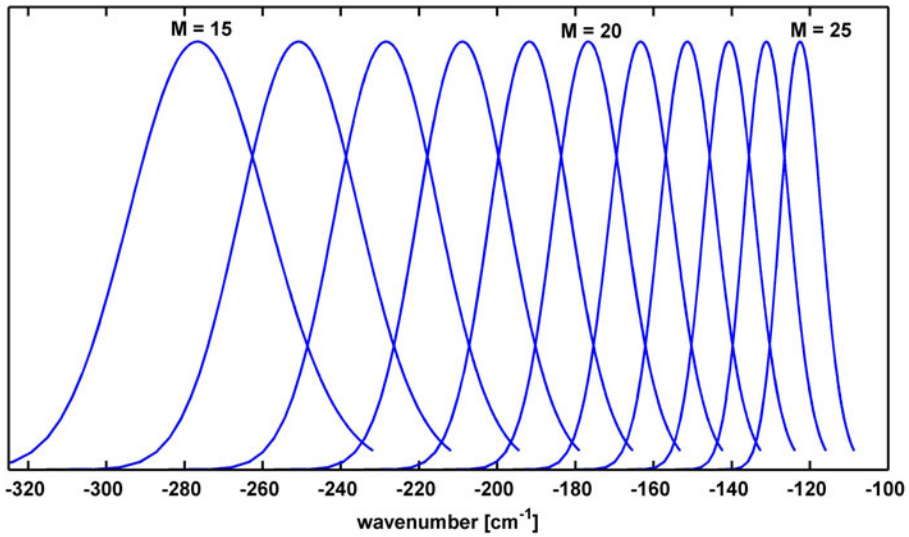

Figure 7.26: Calculated energy levels of the Sekatskii-atom from $M = 15$ to 25 and $l = 0$ for a log-normal droplet size distribution of droplets with $\hat{N}_{60,18} = 3200$. The origin of the energy scale is the ionization threshold.

Chapter 8

Preliminary Results and Outlook

This section discusses two important preliminary findings which suggest new experiments beyond this thesis. These are, in the fist section, experiments with the pulsed extraction field source. On the basis of the findings presented in this section experiments for the possible direct verification of a Sekatskii-atom are suggested, which might lead to fruitful results. Furthermore, the knowledge of excited states and Rydberg states are the foundation of photo-induced chemical reactions. First results on this topic are presented in the second section of this chapter.

8.1 On the experimental verification of the Sekatskii-atom

A possible method to verify the successful excitation of a system with an Ak ion core attached to a helium droplet and an orbiting electron would be the detection of Ak^+–He_N complexes slightly below the ionization threshold of Ak–He_N upon field-ionization. This will demonstrate the immersion of an ion core while the atom is excited into a high Rydberg state. So far, it is only known that the ion core immerses into the droplet upon ionization [1]. A time delay between excitation and field-ionization of this high Rydberg state would be a proof of the stability of the system. In order to access these fragile Rydberg states, the TOF mass spectrometer was equipped with a pulsed extraction field.

Test measurements presented in this section were done with the Cs–He_N system. A two-step excitation scheme was applied with the Cs–He_N $6^2P_{1/2}(^2\Pi_{1/2})$ state as intermediate state. A second laser was scanned across high Rydberg states and the ionization threshold while the Cs^+–He_N (and Cs^+–He_m) ion yield was recorded. The laser pulse energies were optimized for field ionization and different delays of the pulsed field were tested. Unfortunately it turned out that this system was not the best choice. As can be seen from Figure 7.21 in Section 7.2 and Figure 8.3, the Cs^+–He_N signal is very low compared to Rb^+–He_N. This makes it very hard to detect the Cs^+–He_N signal ($\sim$ 15 cps with the pulsed field) and it has a bad signal to noise ratio. This forbids serious interpretation of the ion yield slightly below the ionization threshold.

Lighter alkali atoms on helium droplets would probably be a better choice for this kind of experiment. The mass of the Ak atom is important for the experiment. In the case of the inertial heavy Cs atom, the light He atoms which surrounds the Cs atom in the dimple rush rapidly to the atom, which keeps its position relatively far from the droplet. The situation would be different for example in the case of Li on the droplet. The attractive polarization

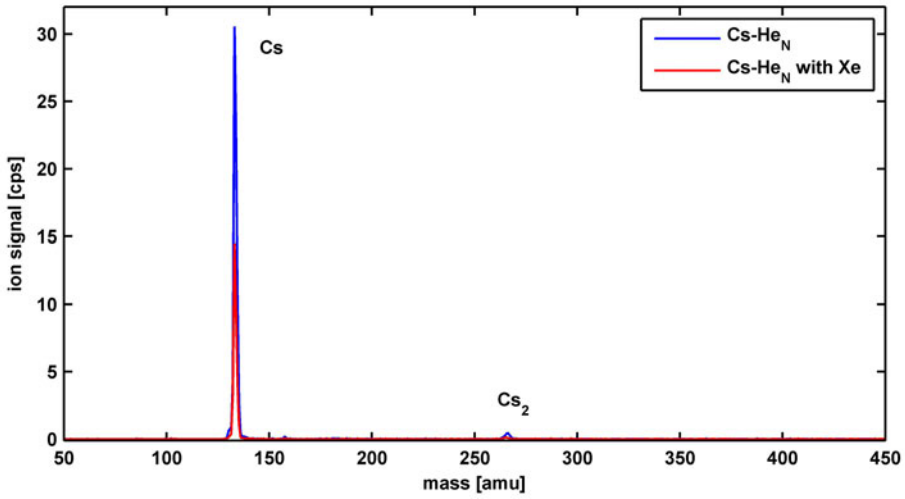

Figure 8.1: Difference between the mass spectra of Cs–He_N and Cs–He_N upon additional doping with Xe atoms.

potential pulls the Li atom towards the droplet much faster than the other alkalis. This argumentation can also explain the differences in the ion yields between Rb^+–He_N and Cs^+–He_N, where the first gives a three times higher ion yield (although the equilibrium distance to the droplet in the intermediate state might also play an important role). Ionization of the Li–He_N system is hence most probably a better choice for this kind of experiment.

However, the attraction between the ion core of the Cs Rydberg atom and the helium matrix can be increased by adding Xe atoms to the droplet as the following discussion will show.

8.1.1 Increasing the Cs^+–He_N ion yield with Xe atoms

Rare gas atoms reside inside the helium nanodroplet [232, 233] and form a "subcluster". The idea of adding Xe atoms to the droplet is to use the long-range van der Waals attraction to pull the ion core of the Cs atom towards the droplet, similar to the experiment presented in ref. [234]. Therein Xe atoms were used to pull Ba atoms into the droplet to enhance the $Ba + N_2O \rightarrow BaO^* + N_2$ reaction inside the droplet. Here the Xe atoms were expected to assist and stabilize the formation of the Sekatskii atom due to the increased attraction acting on the ion core.

In order to avoid coagulation of Xe and Cs atoms at the surface, the Xe atoms were added first. The effect of Xe atoms on the low mass part of the obtained TOF mass spectrum is shown in Figure 8.1 for droplets with a size of $\hat{N}_{14,60} = 7200$. The voltage adjustments of the TOF are chosen for heavy ion detection, but in order to monitor the low and high mass range at the same time the VXY voltage was set to 0 V. This has the disadvantage that not the full range of the heavy ion yield is covered, only the onset of this signal. The pulsed field was used with 1 μs delay.

Upon additional Xe pickup the Cs^+ and Cs_2^+ signals decrease to approximately 1/2 of the original signal. This is partly explained by the decreased pickup cross section of the helium

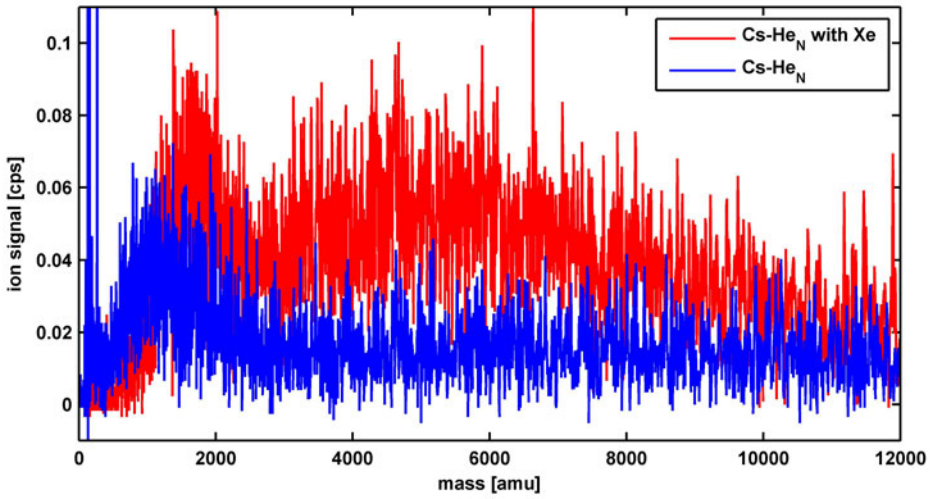

Figure 8.2: Same spectrum as shown in Figure 8.1 but with different scaling so that the Cs^+–He_N yield can be seen.

droplet, which decreases upon the doping with Xe atoms, but it also shows that another channel is enhanced for the Cs ions upon ionization as will be shown in the following. The heavy ion yield for Cs^+–He_N is shown in Figure 8.2. Due to the zero VXY voltage, only the onset of the signal can be seen (hence it does not reflect the droplet size distribution). Note that the mass spectra in Figure 8.1 and 8.2 are identical, but with different scaling. The heavy ion signal is strongly enhanced by the Xe atoms in the center of the droplet. The double peak structure can not be explained so far. It is probably an artifact caused by the detector and the not optimized VXY voltage. A similar structure has been observed for Ba on helium droplets in ref. [176], where it was related to the initial velocity of the ions parallel to the detector surface in combination with a spatial variation of the sensitivity of the micro-channel plate detector.

Additional information is gained by monitoring the Cs^+–He_N ion yield while the laser is scanned across high Rydberg states and the ionization threshold. This is shown in Figure 8.3. The red spectrum is taken in a static field of 1180 V/cm. The black signal shows the ion yield by using the pulsed field with 1 μs delay. The blue and the green signal are obtained by adding Xe atoms to the droplet for different positions of the leak valve (small Xe clusters: 1.25, larger Xe clusters: 1.75). The Xe atoms increase the ion yield by a factor of x5. The fact that the ionization threshold is not influenced by the Xe atoms in the droplet suggests the following explanation: We conclude from the findings of rare gas matrix experiments (see 7.3, e.g. ref. [212]) that if the two species would be close to each other, the different polarizability of the Xe atoms compared to He atoms would decrease the ionization potential. Since this is not the case, we conclude that initially the Cs atoms are on the surface of the droplet and the Xe atoms are inside and both species are well separated. This conclusion is verified by the fact that no $CsXe_m$ complexes could be observed in Figure 8.1. Also the fact that the two step ionization still works, shows that there are no large effects on the D1 transition. The fact that the ion yield increases for heavy ions shows that the ion core is attracted after the ionization into the droplet. Unfortunately no significant increase in the heavy ion signal below

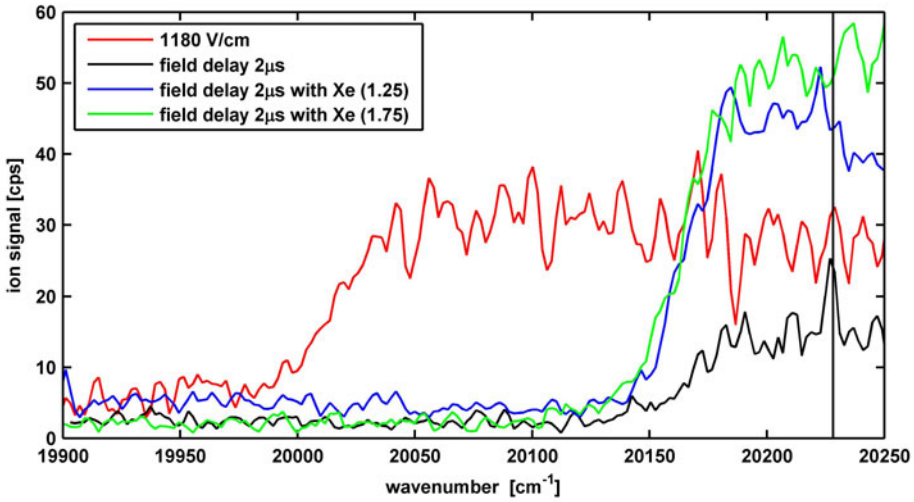

Figure 8.3: Two-step ionization via the D1 transition of Cs atoms on helium nanodroplets. The Cs^+–He_N ion yield is monitored as a function of the laser wavelength. The red spectrum is obtained upon ionization in a static electric field. The black signal is obtained for Cs atoms on helium droplets using the pulsed extraction field (field-free excitation). The heavy ion yield is strongly enhanced if Xe atom are added to the droplet (green and blue signal). The vertical black line indicates the position of the free atom ionization threshold.

the ionization threshold could be observed.

This discussion shows that Xe atoms can be used to pull the Ak ion core into the droplet. In experiments with lighter alkalis and a higher ion yield, Xe atoms could be used to increase the signal and thus the probability for the realization of the Sekatskii-atom.

8.2 Photoinduced chemical reactions on/in helium nanodroplets

Helium nanodroplets have been used to stabilize free radicals and complexes in transition states for infrared spectroscopy [235, 236]. Due to the low temperature and the high cooling rate of helium nanodroplets they provide a unique environment to study chemical reactions. This has been exploited to study the chemical reactions $Ba + N_2O$ [234], $Ak + (H_2O)_m$ [237], $Mg + O_2$ [238], $Si + O_2$ [239] $Al + O_2$ and $Ak + H_2O$ [240] at a temperature of 0.38 K. These reactions are all exothermic and reaction products are detected by mass spectrometric methods or by the detection of chemiluminescence light.
In this outlook section, two photoinduced chemical reactions for future experiments are proposed. Photoinduced reactions have been triggered with infra-red lasers [241]. Here endothermic reactions which are triggered by electronic excitations with lasers in the visible and UV range are discussed.

8.2.1 Transition state spectroscopy on helium nanodroplets

Due to the low temperature, helium droplet can serve as a tool to freeze transition states of chemical reactions. A possible test for this application would be the $Na\cdots FH$ van der Waals molecule reaction upon excitation of the Na atom, or a similar reaction. Due to photoexcitation (1.5-2.3 eV) of the sodium atom the following charge exchange reaction (harpoon type reaction [242, 243]) is triggered $Na\cdots FH + h\nu \rightarrow [Na^*\cdots FH]^\ddagger \rightarrow [Na^+\cdots FH^-]^\ddagger \rightarrow NaF + H$ (or $Na + FH$). This reaction has been studied in crossed molecular beam experiments [244, 245]. In these experiments the photo-depletion of $Na\cdots FH$ ($m/z = 43$) as a function of a second laser ($\lambda_2 = 550$ - 850 nm) was monitored. The $Na\cdots FH$ complex can be ionized in a single photon process with $\lambda_2 = 248$ nm (frequency doubled Coumarin 307). It should be possible to study this reaction in our apparatus on the helium droplet with the TOF mass-spectrometer and the FL3002 (using the FL 35 frequency doubling stage) synchronized with the DL-Midi laser.

8.2.2 The photoinduced $Cs^* + H_2 \rightarrow CsH + H$ reaction on helium droplets

In this section some preliminary results on the photo-induced chemical reaction $Cs^* + H_2 \rightarrow CsH + H$ on helium nanodroplets are presented. Although the formation of the Cs-H_2 complex on the droplet could be demonstrated with TOF and QMS mass spectroscopy and an influence of hydrogen doping on the excitation spectrum could be shown, so far it was not possible to unambiguously attribute the recorded signals to the reaction.

The $Cs^* + H_2 \rightarrow CsH + H$ reaction

Among the photoinduced $Ak^* + H_2 \rightarrow AkH + H$ reactions the Ak = Cs reaction has been exhaustively studied in theory as well as in experiments. The reaction was first observed accidently during an optical-pump experiment in 1975. In this experiment, a laser passed a Cs vapor cell that contained a small amount of hydrogen. Small micron sized crystals were observed in this chamber and soon it was realized that this so called "laser snow" consists of CsH, which has been formed in a photoinduced chemical reaction [246]. The absorption spectrum of CsH is known since 1938 and was characterized by Almy and Rassweiler [247]. The

absorption spectrum of CsD can be found in ref. [248]. An extensive review on the spectroscopy and structure of AkH diatomic molecules is given in ref. [249] and an introduction into this reaction can be found in ref. [250].

The first systematic experiments characterize the CsH $X^1\Sigma^+$ ground state [251] and the $A^1\Sigma^+ \leftarrow X^1\Sigma^+$ transition [252]. In the 1980's and 1990's the reaction was characterized in many crossed beam experiments [253–258]. The energetics of the reaction is explained with

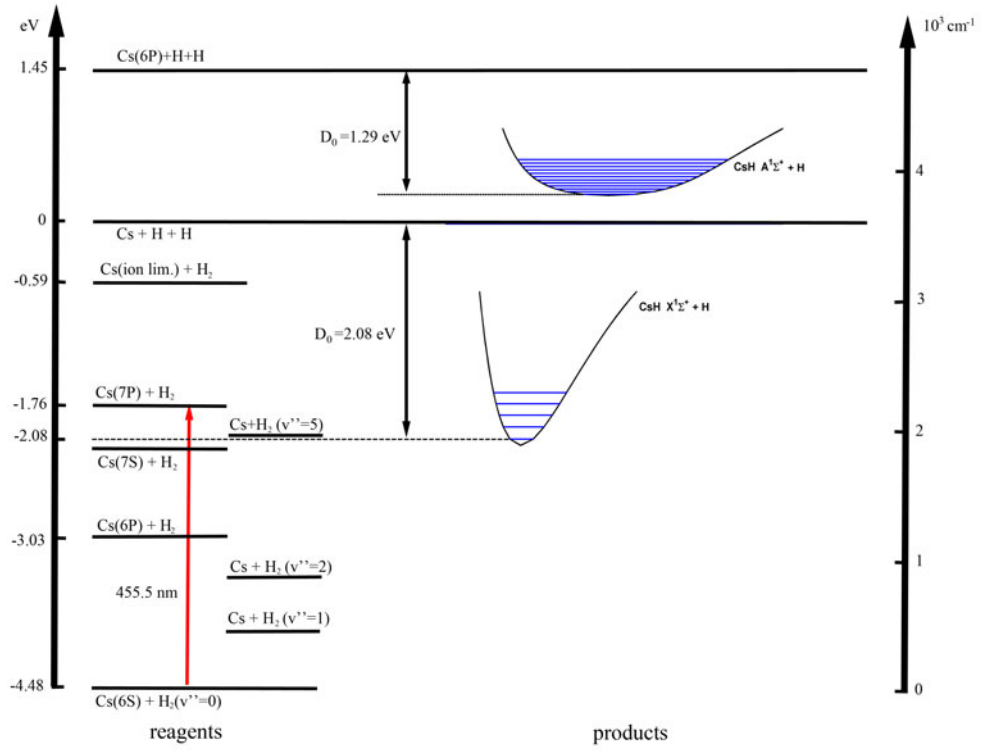

Figure 8.4: Relevant Energy levels for the Cs* + H_2 → CsH + H reaction.

Figure 8.4 (see ref. [259]). The energy needed to trigger the reaction is given with 2.08 eV. This energy can be provided by exciting the Cs atom into the 7P states or higher. In this type of reaction, the electron of the Cs atom is thought to move to the hydrogen molecule at relatively large distances (5 to 10 Å). Due to the attractive Coulomb forces between the oppositely charged ions, the intermediate $[Cs^+\text{-}H_2^-]^\ddagger$ transition state is formed. During the attraction process a stable CsH molecule is formed and one H atom is ejected. The valence electron acts as a harpoon with which the hydrogen molecule is pulled towards the Cs atom. This reaction type model was suggested by Polanyi [242] for reactions between Ak atoms and halogen molecules. It should be mentioned that recently questions about the applicability of the harpoon mechanism to the alkali hydrogen reactions have been raised [260].

The reaction cross section upon excitation of the $7^2P_{1/2}$ state is about five times higher than for the $7^2P_{3/2}$ state. The excess energy is very low (lower than 0.03 eV [253] for the $7^2P_{1/2}$ state) so that the CsH molecule is produced in its vibronic ground state. The $X^1\Sigma^+$ and $A^1\Sigma^+$ state potentials are shown in the right panel of Figure 8.4.

The Cs* + H_2 reaction on helium droplets - preliminary results

The first challenge in the experimental realization of the Cs* + H_2 reaction on the helium droplet is to bring both species together on the droplet. Hydrogen molecules and clusters have been studied on helium droplets by several groups, most noticeable is the work of the Scheier group in Innsbruck who did a lot of work on the characterization of hydrogen molecules in helium droplets using mass spectroscopic techniques [261, 262]. It was found that $He_xH_y^+$ complexes consisting of an odd number of hydrogen atoms are much more stable upon electron impact ionization on helium droplets. Also fragmentation processes play an important role. Another problem is that H_4 has the same mass as the He atom. These considerations show that it is not straight forward to obtain a pickup statistic of H_2 on helium droplets with a QMS. Hence to characterize the pickup we use the adjustment of the leak valve for the discussion of this preliminary results. The leak valve position $v = 1.75$ corresponds approximately to monomer pickup, $v = 1.5$ to 1.25 correspond to medium hydrogen pickup and beyond $v = 1.0$ hydrogen clusters are formed and the droplet beam is noticeably attenuated.

The hydrogen molecule is very weakly bound to the helium inside the droplet [263] because of its small size. It is thought that it can move inside the droplet. So it is not clear a priori what happens if helium nanodroplets are doped with single hydrogen molecules and surface atoms. In contrast, hydrogen clusters are known to reside in the center of the droplet [264].

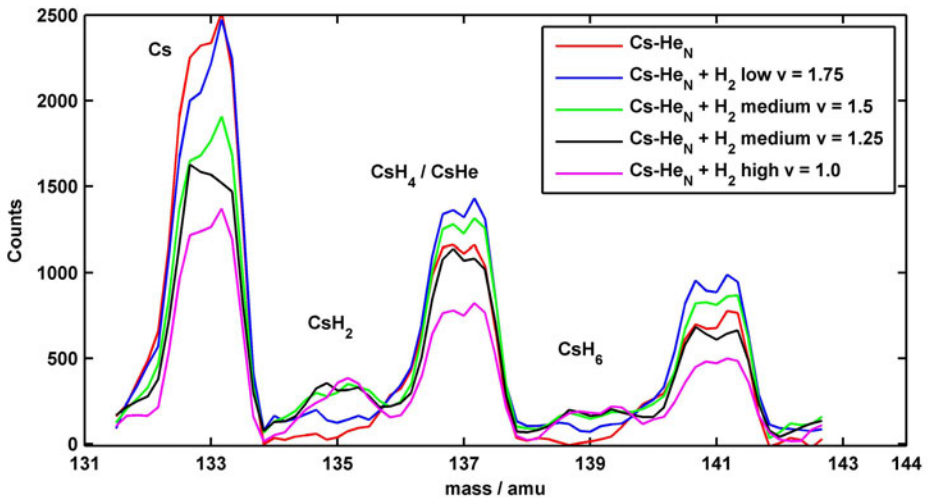

Figure 8.5: Quadrupole mass spectrum of Cs and hydrogen doped helium nanodroplets from 130 to 144 amu. With increasing pickup pressure (low to high pressure) the peaks corresponding to CsH_{2m}^+ grow while the Cs^+ mass decreases.

A quadrupole mass spectrum of Cs and hydrogen doped helium nanodroplets from 130 to 144 amu is presented in Figure 8.5. With increasing pickup pressure (low to high pressure) the peaks corresponding to CsH_{2m}^+ grow while the Cs^+ mass decreases. This demonstrates that upon electron impact ionization (60 eV) the two species find each other and appear together in the mass spectrum. Figure 8.6 shows the same result for the deuterium molecule. The deuterium molecule has the disadvantage that it has the same mass as the helium atom, which makes it almost impossible to take a pickup statistic with our QMS. However the electron

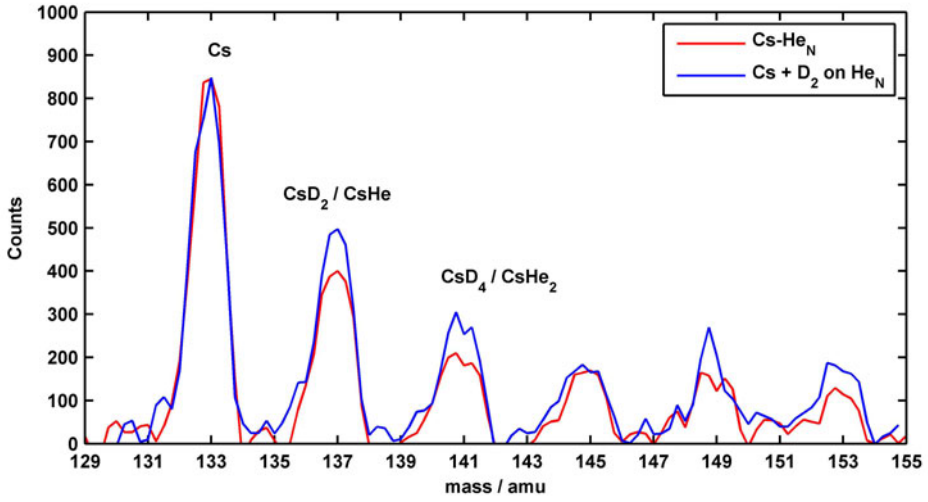

Figure 8.6: Quadrupole mass spectrum of Cs and deuterium doped helium nanodroplets from 129 to 155 amu. The signal with deuterium is scaled so that the two signals match each other at $m/z = 133$ (x 1.2). If deuterium is present in the pickup cell the peaks corresponding to CsD^+_{2m} grow.

impact ionization brings a lot of excess energy into the system and it can also ionize the hydrogen molecule.

Compared to electron impact ionization, laser ionization is very "soft" and is capable to ionize only the Cs atom on the droplet. This is shown in Figure 8.7. With increasing pickup pressure the peak corresponding to CsH^+_2 between the Cs and $CsHe_m$ peaks begins to grow. This finding suggests that the two species are relatively close to each other, since large droplets were used in this experiment ($\hat{N}_{16,60} = 5000$). In contrast, experiments with Xe, which is known to be strongly bound in the center of the droplet, reveal no $CsXe_m$ complexes upon photoionization. This shows that hydrogen behaves differently.

The mass spectrum was acquired with one laser (DL-Midi) at the $7^2P_{1/2}$ ($\Pi_{1/2}$) state (22079 cm^{-1}) and a second laser (FL3002) was scanned across the CsH $A^1\Sigma^+ \leftarrow X^1\Sigma^+$ transition (480 - 525 nm). The Franck-Condon factors (FCF) for this transition were calculated with the Level 8.0 code from LeRoy [265] and it was assumed that the molecule is initially in its vibronic ground state $X^1\Sigma^+$ ($v" = 0$). This is shown in Figure 8.8. Unfortunately CsH^+ was not observed (generated in a REMPI process) in the mass spectrum, which would be a verification for the reaction. Also the additional usage of a third laser (308 nm XeCl, ~2 mJ) overlapped and synchronized with the DL-Midi (Coumarin 2) and the FL3002 (Coumarin 307) did not lead to the observation of CsH^+. The attempt to use the frequency doubling stage (FL 35) of the FL3002 with frequency doubled Coumarin 2 at 235 nm and 200 μJ (fundamental: 453 nm, 0.5 mJ,) instead of Coumarin 307 was also not fruitful. It turned out that the intense Cs^+ signal makes it difficult to resolve a small CsH^+ signal. The situation would be better if deuterium is used, because CsD^+ could be clearly resolved. This would be a suggestion for future experiments. However, a different indirect approach is presented in the following.

An indirect verification for the reaction would be a variation in the Cs^+ signal as a function of the probe laser when hydrogen is present, if one assumes that the CsH molecule fragments

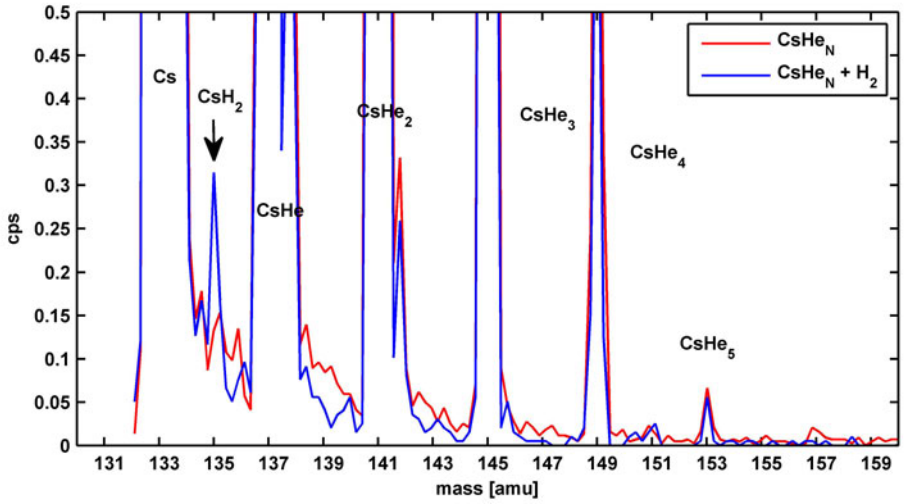

Figure 8.7: TOF mass spectrum of Cs and hydrogen doped helium nanodroplets from 130 to 144 amu. With increasing pickup pressure the peak corresponding to CsH_2^+ begins to grow. The mass spectrum was acquired with one laser at the $7^2P_{1/2}$ ($\Pi_{1/2}$) state and a second laser scanning across the CsH $A^1\Sigma^+ \leftarrow X^1\Sigma^+$ transition (480 - 525 nm). Unfortunately CsH^+ was not observed in the mass spectrum.

upon ionization. The probe laser scans across the CsH $A^1\Sigma^+ \leftarrow X^1\Sigma^+$ transition (480 - 525 nm). This is shown in Figure 8.9 for the case without hydrogen pickup (red), low hydrogen pressure (blue) and medium hydrogen pressure (black) in the pickup cell. The Cs^+ signal is monitored as a function of the laser L2 which is supposed to excite the CsH $A^1\Sigma^+ \leftarrow X^1\Sigma^+$ transition. Laser L1 is fixed at the $7^2P_{1/2}$ ($\Pi_{1/2}$) state (22079 cm^{-1}). A large contribution to the signal is caused from the laser L1 which ionizes the Cs atom in a two-photon process. This causes a relatively large background signal. However there is a slight difference in the signals in the high energy range, but unfortunately this can not be related unambiguously to the reaction.

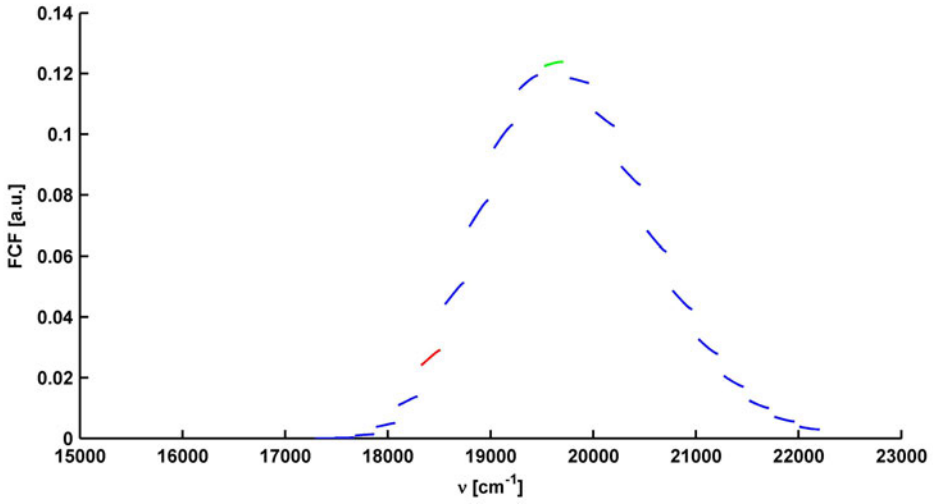

Figure 8.8: Franck-Condon factors for the CsH $A^1\Sigma^+ \leftarrow X^1\Sigma^+$ transition calculated with the Level 8 code from LeRoy [265]. The potentials were taken from ref. [249] and it was assumed that the molecule is in its vibronic ground state $X^1\Sigma^+$ ($v" = 0$).

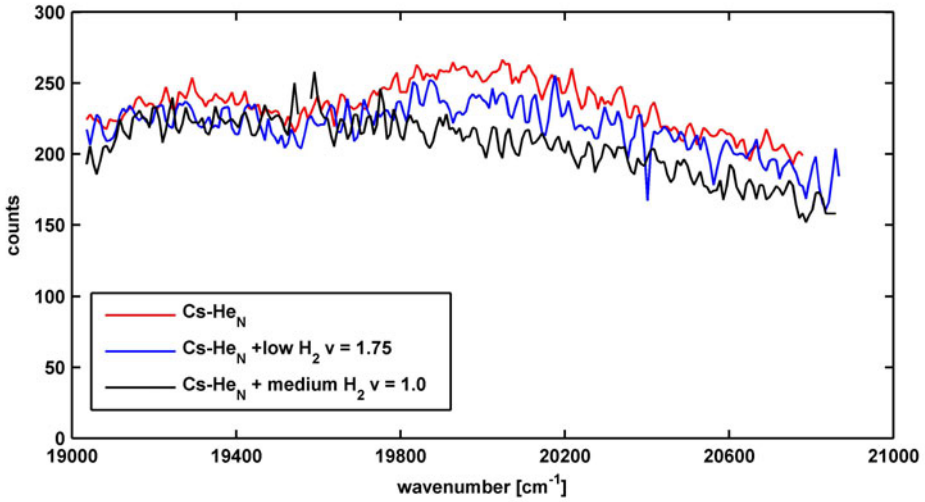

Figure 8.9: Cs^+ signal monitored as a function of the probe laser which is supposed to excite the CsH $A^1\Sigma^+ \leftarrow X^1\Sigma^+$ transition.

Summary

The object of this thesis is the spectroscopy of rubidium (Rb) and cesium (Cs) atoms on the surface of helium nanodroplets (He_N). For the first time, complete excitation spectra of these atoms on helium droplets have been recorded. This thesis includes Rb–He_N and Cs–He_N spectra from the lowest transitions up to Rydberg states and the ionization threshold.

Superfluid helium nanodroplets consisting of 10^3 to 10^4 helium atoms are produced in a supersonic jet expansion ($T_0 = 14 - 22\,\mathrm{K}$, $p_0 = 60\,\mathrm{bar}$). Upon production they cool down rapidly to 0.38 K by evaporative cooling and hence provide a low temperature matrix for spectroscopy. Helium droplets are doped by passing pickup cells, loaded with the desired species as gas/vapor.

Resonance-enhanced multi-photon ionization time-of-flight (REMPI-TOF) mass spectroscopy and multi-photon laser induced fluorescence (LIF) spectroscopy were used as spectroscopic tools to investigate these Rydberg systems in this thesis. A large variety of laser systems (pulsed and cw) and laser dyes were used in the course of this thesis in order to cover the spectral range from the UV to the near IR.

A special two-step excitation technique was developed, which exploits the fact that Rb and Cs atoms stay bound to the droplet surface upon excitation into their lowest $n^2P_{1/2}(^2\Pi_{1/2})$ state. For the Cs atom, the bound character of this state was found during the work on this thesis. The two-step excitation scheme is fundamental for this thesis and was investigated in detail. The bound intermediate $n^2P_{1/2}(^2\Pi_{1/2})$ (Rb: $n = 5$, Cs: $n = 6$) state serves as a springboard for the excitation of Rydberg states.

The spectroscopy of Rb and Cs atom Rydberg states on helium nanodroplets revealed that the observed transitions could be explained within the pseudo-diatomic model as long as individual states could be resolved. In this work the Rydberg character of these systems is demonstrated. The recorded transitions could be organized into Rydberg series, thus giving quantum defects and ionization thresholds. In addition, the dependence of these Rydberg states on the droplet size was investigated.

It was found that the ionization threshold and the quantum defects are lowered by the influence of the helium droplet and the perturbation increases with the droplet size. The lowered ionization threshold is explained by polarization of helium atoms close by the ion core of the alkali atom. The lowered quantum defect indicates the screening of the Rydberg electron from ionic core by the helium droplet, which acts as a nanosized dielectric.

Rydberg states with electron orbitals much larger than the helium droplet could be observed.

States with effective principal quantum numbers $n^* < 20$ could be resolved, beyond this region the states form a continuum. Such highly excited Rydberg atoms can accommodate the helium droplet within the orbital of the electron. The attractive interaction between the alkali ion core and the helium droplet suggests the formation of a system known in literature as "Sekatskii-atom": a positive charged alkali ion core surrounded by a liquid helium droplet and an orbiting electron.

This thesis gives new insights into the nature of Rydberg states of atoms on the surface of helium droplets. On the basis of the results new experiments are proposed which go beyond the scope of this thesis. The knowledge of excited states is a basic ingredient for the experimental realization of photo-induced chemical reactions on/inside helium nanodroplets, which are discussed in the outlook section of this thesis.

Appendix A

Appendix

A.1 Droplet sizes

In this section the calculated parameters for the log-normal droplet size distributions are listed. The parameters are calculated for a fixed nozzle diameter ($d_0 = 5\mu$m) and various source pressures p_0 and source temperatures T_0. For the calculation of the parameters for $p_0 < 30$ bar a fixed $\delta = 0.625$ parameter is used [54]. The method for the calculation is described in section 1.4.1. Listed are values for $1000 < \bar{N} < 20000$. In addition the corresponding droplet radii are given (see section 1.4.1).

Table A.1: Calculated parameters for the log-normal droplet size distribution.

$p_0 = 20$ bar

T_0	$\bar{N}$	$\bar{R}$	$\Delta N_{1/2}$	$\hat{N}$	$\hat{N}$	N_{Median}	R_{Median}	μ	σ
11	16960	57	15181	9440	47	13951	53	9.54	0.625
12	11622	50	10403	6469	41	9560	47	9.17	0.625
13	8083	45	7235	4499	37	6649	42	8.8	0.625
14	5735	40	5134	3192	33	4718	37	8.46	0.625
15	4155	36	3720	2313	29	3418	33	8.14	0.625
16	3046	32	2727	1696	26	2506	30	7.83	0.625
17	2271	29	2033	1264	24	1868	27	7.53	0.625
18	1722	27	1541	958	22	1416	25	7.26	0.625
19	1323	24	1185	737	20	1089	23	6.99	0.625
20	1032	22	923	574	18	849	21	6.74	0.625

$p_0 = 30$ bar

T_0	$\bar{N}$	$\bar{R}$	$\Delta N_{1/2}$	$\hat{N}$	$\hat{N}$	N_{Median}	R_{Median}	μ	σ
12	17735	58	14953	12558	52	15808	56	9.67	0.48
13	13073	52	10252	10108	48	11999	51	9.39	0.41
14	9722	47	7006	7994	44	9108	46	9.12	0.36
15	7303	43	4954	6196	41	6914	42	8.84	0.33
16	5527	39	3676	4730	37	5248	39	8.57	0.32
17	4230	36	2962	3533	34	3984	35	8.29	0.35

18	3273	33	2507	2581	30	3024	32	8.01	0.4
19	2561	30	2137	1843	27	2295	29	7.74	0.47
20	2025	28	1783	1290	24	1742	27	7.46	0.55
21	1617	26	1447	885	21	1322	24	7.19	0.63
22	1303	24	1140	596	19	1004	22	6.91	0.72
23	1060	23	874	394	16	762	20	6.64	0.81

$p_0 = 40$ bar

T_0	$\bar{N}$	$\bar{R}$	$\Delta N_{1/2}$	$\hat{N}$	$\hat{N}$	N_{Median}	R_{Median}	μ	σ
13	16857	57	14967	8375	45	13351	53	9.5	0.68
14	12911	52	11503	6599	42	10323	48	9.24	0.67
15	9978	48	8891	5108	38	7982	44	8.98	0.67
16	7749	44	6895	3914	35	6171	41	8.73	0.67
17	6064	40	5368	2955	32	4772	37	8.47	0.69
18	4783	37	4188	2195	29	3689	34	8.21	0.72
19	3807	35	3263	1602	26	2853	31	7.96	0.76
20	3055	32	2529	1150	23	2206	29	7.7	0.81
21	2470	30	1945	813	21	1705	27	7.44	0.86
22	2014	28	1479	565	18	1319	24	7.18	0.92
23	1653	26	1112	388	16	1019	22	6.93	0.98

$p_0 = 50$ bar

T_0	$\bar{N}$	$\bar{R}$	$\Delta N_{1/2}$	$\hat{N}$	$\hat{N}$	N_{Median}	R_{Median}	μ	σ
13	19882	60	17002	8294	45	14856	55	9.61	0.76
14	15505	55	13366	6663	42	11700	50	9.37	0.75
15	12190	51	10522	5265	39	9215	47	9.13	0.75
16	9628	47	8292	4123	36	7257	43	8.89	0.75
17	7669	44	6544	3175	33	5716	40	8.65	0.77
18	6142	41	5162	2418	30	4501	37	8.41	0.79
19	4958	38	4064	1813	27	3545	34	8.17	0.82
20	4025	35	3187	1343	24	2792	31	7.93	0.86
21	3295	33	2484	979	22	2199	29	7.7	0.9
22	2713	31	1922	706	20	1732	27	7.46	0.95
23	2248	29	1474	502	18	1364	25	7.22	1
24	1874	27	1120	353	16	1074	23	6.98	1.06
25	1572	26	843	245	14	846	21	6.74	1.11

$p_0 = 60$ bar

T_0	$\bar{N}$	$\bar{R}$	$\Delta N_{1/2}$	$\hat{N}$	$\hat{N}$	N_{Median}	R_{Median}	μ	σ
14	17713	58	15171	7432	43	13261	53	9.49	0.76
15	14133	54	12159	6027	40	10638	49	9.27	0.75
16	11247	50	9736	4914	38	8534	45	9.05	0.74
17	9051	46	7817	3917	35	6846	42	8.83	0.75
18	7342	43	6284	3074	32	5492	39	8.61	0.76
19	5986	40	5051	2387	30	4406	36	8.39	0.78
20	4915	38	4053	1828	27	3535	34	8.17	0.81
21	4062	35	3240	1382	25	2836	31	7.95	0.85

22	3372	33	2578	1035	22	2275	29	7.73	0.89
23	2816	31	2039	766	20	1825	27	7.51	0.93
24	2366	30	1600	560	18	1464	25	7.29	0.98
25	1998	28	1245	406	16	1174	23	7.07	1.03
26	1695	26	961	291	15	942	22	6.85	1.08

$p_0 = 70$ bar

T_0	$\bar{N}$	$\bar{R}$	$\Delta N_{1/2}$	$\hat{N}$	$\hat{N}$	N_{Median}	R_{Median}	μ	σ
14	19648	60	17109	8795	46	15030	55	9.62	0.73
15	15726	56	13869	7491	43	12282	51	9.42	0.7
16	12626	52	11226	6341	41	10036	48	9.21	0.68
17	10236	48	9125	5264	39	8201	45	9.01	0.67
18	8360	45	7454	4305	36	6701	42	8.81	0.67
19	6873	42	6116	3476	34	5476	39	8.61	0.67
20	5687	40	5035	2770	31	4475	37	8.41	0.69
21	4734	37	4148	2181	29	3656	34	8.2	0.72
22	3958	35	3413	1703	27	2988	32	8	0.75
23	3330	33	2799	1313	24	2441	30	7.8	0.79
24	2814	31	2285	1003	22	1995	28	7.6	0.83
25	2389	30	1854	759	20	1630	26	7.4	0.87
26	2039	28	1493	569	18	1332	24	7.19	0.92

$p_0 = 80$ bar

T_0	$\bar{N}$	$\bar{R}$	$\Delta N_{1/2}$	$\hat{N}$	$\hat{N}$	N_{Median}	R_{Median}	μ	σ
15	17246	57	15437	9584	47	14179	54	9.56	0.63
16	13955	53	12420	8440	45	11802	51	9.38	0.58
17	11388	50	10010	7309	43	9823	48	9.19	0.54
18	9357	47	8121	6243	41	8176	45	9.01	0.52
19	7747	44	6681	5251	39	6805	42	8.83	0.51
20	6454	41	5571	4364	36	5665	40	8.64	0.51
21	5405	39	4699	3588	34	4715	37	8.46	0.52
22	4547	37	3995	2923	32	3924	35	8.27	0.54
23	3849	35	3420	2353	30	3266	33	8.09	0.57
24	3269	33	2924	1880	27	2719	31	7.91	0.61
25	2790	31	2494	1489	25	2263	29	7.72	0.65
26	2392	30	2118	1168	23	1884	27	7.54	0.69

Danksagung

Am Ende meiner Doktorarbeit angelangt, blicke ich zurück auf drei eindrucksvolle und erfüllte Jahre des Experimentierens. An dieser Stelle seien nun einige Worte des Dankes an diejenigen gerichtet, welche mich im Laufe meiner Arbeit begleitet und unterstützt haben.
Prof. Wolfgang Ernst möchte ich dafür danken, dass er mir die Möglichkeit gegeben hat meine Arbeit nach meiner Diplomarbeit in seiner Arbeitsgruppe fortzusetzen. Er war stets fördernd und motivierend und hatte immer ein offenes Ohr für meine Anliegen. Durch die zahlreichen Auslandsaufenthalte im Rahmen der Teilnahme an diversen Tagungen hatte ich die Möglichkeit etwas von der Welt zusehen.
Günter Krois sei gedankt für die Gesellschaft die er mir in den vergangenen Jahren geleistet hat und dafür, dass er bereit ist, auch noch um drei Uhr morgens mit mir Laser-Spiegelsätze und Farbstoffe zu wechseln um ein noch besseres Signal zu erhalten.
Bedanken möchte ich mich auch bei Markus Koch für die zahlreichen Diskussionen beim täglichen Espresso, so wie seine Hilfe in allen möglichen Bereichen, vom Verfassen von Publikationen bis zum Steuern von Segelboten.
Gedankt sei auch meinen vormaligen Laborkollegen Moritz Theisen.
Wenn ich in der Danksagung meiner Diplomarbeit unsere Arbeitsgruppe als ultimative Matrix für den Spektroskopiker bezeichnet habe, so kann ich dies an dieser nur nochmal wiederholen. Es war und ist mir eine Freude in solch einer freundschaftlichen Umgebung zu arbeiten. Die vielen Gespräche wissenschaftlicher als auch nicht-wissenschaftlicher Natur beim einen oder anderen Kaffee/Bier/Glühwein sorgten für eine erfrischende und kurzweilige Atmosphäre, auch im Leben abseits der Physik.
Reinhard Dämon, Josef Friedrich und Christian Neureiter sei gedankt für den Bau der vielen Geräte sowie für ihre schnelle Hilfe bei plötzlich auftretenden Problemen der elektronischen Art, die uns den einen oder anderen Messtag gerettet haben.
Für die Anfertigung so mancher Bauteile sowie die raschen Reperaturen möchte ich mich bei Rupert Maierhofer, Werner Luttenberger und Uwe Seidl bedanken.
Ich danke meinen Eltern für ihre Unterstützung in den letzten 28 Jahren und dafür, dass ihr mir mein Studium ermöglicht habt.
Mein größter Dank gilt aber meiner noch recht jungen Familie. Danke Alexandra, dass du mir den notwendigen Rückhalt gibst sowie für dein Verständnis für meine oft etwas längeren Arbeitstage im Labor. Und zu guter Letzt möchte ich meiner Tochter Lena danken, dafür dass sie da ist.

Bibliography

[1] M. Theisen, F. Lackner, and W. E. Ernst. Forming Rb^+ snowballs in the center of He nanodroplets. *Phys. Chem. Chem. Phys.*, 12(12):14861–14863, 2010. i, 65, 77, 89, 144, 155

[2] M. Theisen, F. Lackner, F. Ancilotto, C. Callegari, and W. E. Ernst. Two-step excitation of Rb atoms on He nanodroplets. *Eur. Phys. J. D*, 61(2):403–408, 2011. i, 61, 68, 69, 77, 78, 83, 85, 88, 99, 104, 105, 108, 110, 123

[3] M. Theisen, F. Lackner, and W. E. Ernst. Rb and Cs Oligomers in Different Spin Configurations on Helium Nanodroplets. *J. Phys. Chem. A*, 115(25):7005–7009, 2011. i, 5, 17, 20, 115

[4] M. Theisen, F. Lackner, and W. E. Ernst. Cs atoms on helium nanodroplets and the immersion of Cs^+ into the nanodroplet. *J. Chem. Phys.*, 135(7):074306, 2011. i, 61, 68, 69, 72, 76, 77, 83

[5] M. Theisen, F. Lackner, G. Krois, and W. E. Ernst. Ionization Thresholds of Alkali Metal Atoms on Helium Droplets. *J. Phys. Chem. Lett.*, 2(21):2778–2782, 2011. i, 104, 108, 109, 110, 118, 144, 145

[6] F. Lackner, G. Krois, M. Theisen, M. Koch, and W. E. Ernst. Spectroscopy of nS, nP, and nD Rydberg series of Cs atoms on helium nanodroplets. *Phys. Chem. Chem. Phys.*, 13:18781–18788, 2011. i, 61, 76, 91, 94, 98, 103, 104, 105, 109, 110, 118, 145

[7] Lackner, F. and Krois, G. and Koch, M. and Ernst, W. E. Rubidium on Helium Droplets: Analysis of an Exotic Rydberg Complex for n* < 20 and 0 <= l <= 3. *J. Phys. Chem. Lett.*, 3(10):1404–1408, 2012. i, 72, 94, 98, 115

[8] F. Lackner; G. Krois, and W. E. Ernst. Excited States and Rydberg Series of Alkali Atoms on Helium Nanodroplets. *in preparation*, 2013. i, 61, 76, 103

[9] Z.J. Jakubek and R.W. Field. Core-penetrating Rydberg series of BaF: Single-state and two-state fits of new electronic states in the 4.4 <= n* <= 14.3 region. *J. Mol. Spectrosc.*, 205(2):197–220, 2001. 1

[10] J. Nagl. *Spectroscopic investigations of homo- and heteronuclear molecules of K and Rb on the surface of argon and helium clusters.* PhD thesis, TU Graz, 2008. 3, 14, 19, 21

[11] M. Koch. *Magnetic Resonance Spectroscopy of Single Alkali-Metal Atoms Isolated in Superfluid Helium Nanodroplets.* PhD thesis, TU Graz, 2009. 7

[12] G. Krois. Heavy alkali and alkaline earth metals on cold helium droplets: First comparison of excitation spectra. Master's thesis, TU Graz, 2011. 22, 23, 25, 26

[13] F. Lackner. Laserspektroskopie und Flugzeitmassenspektrometrie an Rubidium-dotierten Heliumnanotröpfchen. Master's thesis, TU Graz, 2009. 3, 4, 29, 30, 32

[14] J. P. Toennies and A. F. Vilesov. Superfluid Helium Droplets: A Uniquely Cold Nanomatrix for Molecules and Molecular Complexes. *Angew. Chem. Int. Edit.*, 43(20):2622–2648, 2004. 3, 5, 6, 7, 8, 13, 18, 105

[15] F. Stienkemeier and K. K Lehmann. Spectroscopy and dynamics in helium nanodroplets. *J. Phys. B: At. Mol. Opt.*, 39(8):R127, 2006.

[16] M. Y. Choi, G. E. Douberly, T. M. Falconer, W. K. Lewis, C. M. Lindsay, J. M. Merritt, P. L. Stiles, and R. E. Miller. Infrared spectroscopy of helium nanodroplets: novel methods for physics and chemistry. *Int. Rev. Phys. Chem.*, 25(1-2):15–75, 2006. 3, 18

[17] Special issue. *J. Chem. Phys.*, 115, 2001. 3

[18] C. Callegari and W. E. Ernst. *Handbook of High-Resolution Spectroscopy,* eds. M. Quack and F. Merkt. 2011. 3, 5, 7, 18, 76, 104

[19] W.H. Keesom. *Helium.* Elsevier, 1942. 3

[20] Davide R. Lide, editor. *CRC Handbook of Chemistry and Physics.* CRC - Press, 77 edition, 1996. 3, 7, 15

[21] James F. Annett. *Superconductivity, Superfluids and Condensates.* Oxford University Press, 2004. 3

[22] D. van Delft. Little cup of helium, big science. *Phys. Today*, 61(3):36–42, 2008. 3

[23] P. Kapitza. Viscosity of liquid helium below the λ-point. *Nature*, 141:74, 1938. 3

[24] J. F. Allan and A.D. Misener. Flow of liquid helium II. *Nature*, 141:75, 1938. 3

[25] M. H. Anderson, J. R. Ensher, M. R. Matthews, C. E. Wieman, and E. A. Cornell. Observation of bose-einstein condensation in a dilute atomic vapor. *Science*, 269(5221):198–201, 1995. 4

[26] K. B. Davis, M. O. Mewes, M. R. Andrews, N. J. van Druten, D. S. Durfee, D. M. Kurn, and W. Ketterle. Bose-einstein condensation in a gas of sodium atoms. *Phys. Rev. Lett.*, 75:3969–3973, 1995. 4

[27] F. Dalfovo and S. Stringari. Helium nanodroplets and trapped Bose-Einstein condensates as prototypes of finite quantuum fluids. *J. Chem. Phys.*, 115:10078–10089, 2001. 4

[28] C.A. Swenson. The Blocked Capillary Method for Determining Melting Pressures: The Melting Curve of Helium from 1.5 K to 4 K. *Phys. Rev.*, 89:538, 1953. 4

[29] C.A. Swenson. The Liquid-Solid Transformation in Helium near Absolute Zero. *Phys. Rev.*, 79:626, 1950.

[30] G. Schmidt and W.H. Keesom. New meassurements of liquid helium temperatures II: The vapour pressure curve of liquid helium. *Physica*, 4:971–977, 1937.

[31] R.A. Erickson, L.D. Roberts. The Measurement and Calculation of Liquid Helium Vapor Pressure-Temperatur Scale frpm 1 K to 4.2 K. *Phys. Rev.*, 93:957, 1954.

[32] P. R. Roach. Pressure-Density-Temperature Surface of ^{4}He near the critical Point. *Phys. Rev.*, 170:213, 1968. 4

[33] G. Scoles, editor. *Atomic and Molecular Beam Methods Volume 1.* Oxford University Press, 1988. 4

[34] Klingelhofer R. Lohse P. Becker, E.W. Strahlen aus kondensiertem Helium im Hochvakuum. *Z. Naturforsch. A*, 16:1259, 1961. 4, 18

[35] H. Buchenau, E. L. Knuth, J. Northby, J. P. Toennies, and C. Winkler. Mass spectra and time-of-flight distributions of helium cluster beams. *J. Chem. Phys.*, 92(11):6875–6889, 1990. 4, 5

[36] H. Buchenau, J. P. Toennies, and J. A. Northby. Excitation and ionization of ^{4}He clusters by electrons. *J. Chem. Phys.*, 95(11):8134–8148, 1991. 4

[37] E. Loginov, L. F. Gomez, N. Chiang, A. Halder, N. Guggemos, V. V. Kresin, and A. F. Vilesov. Photoabsorption of Ag_N (N $\sim$ 6 - 6000) Nanoclusters Formed in Helium Droplets: Transition from Compact to Multicenter Aggregation. *Phys. Rev. Lett.*, 106:233401, 2011. 5

[38] G.D. Stein. Cluster beam sources: predictions and limitations of the nucleation theory. *Surf. Sci.*, 156:44–56, 1985. 5

[39] M. Hartmann, R.E. Miller, J.P. Toennies and A. Vilesov. Rotationally Resolved Spectroscopy of SF_6 in Liquid Helium Clusters: A Molecular Probe of Cluster Temperature. *Phys. Rev. Lett.*, 75:1566–1569, 1995. 5, 76

[40] J. Harms, M. Hartmann, J. P. Toennies, A. F. Vilesov, and B. Sartakov. Rotational Structure of the IR Spectra of Single SF_6 Molecules in Liquid ^{4}He and ^{3}He Droplets. *J. Mol. Spectrosc.*, 185:204, 1997.

[41] M. Hartmann and N. Pörtner and B. Sartakov and J. P. Toennies and A. F. Vilesov. High resolution infrared spectroscopy of single SF_6 molecules in helium droplets. I. Size effects in ^{4}He droplets. *J. Chem. Phys.*, 110(11):5109–5123, 1999. 5, 7, 8

[42] G. Auböck, J. Nagl, C. Callegari, and W. E. Ernst. Triplet State Excitation of Alkali Molecules on Helium Droplets: Experiments and Theory. *J. Phys. Chem.*, A 2007, 111:7404–7410, 2007. 5, 17, 19

[43] S. Grebenev, J.P. Toennies, A.F. Vilesov. Superfluidity Within a Small Helium-4 Cluster: The Microscopic Andronikashvili Experiment. *Science*, 279:2083 – 2086, 1998. 5

[44] Tang, J. and Xu, Y. and McKellar, A. R. W. and Jäger, W. Quantum solvation of carbonyl sulfide with helium atoms. *Science*, 297(5589):2030–2033, 2002. 5

[45] McKellar, A. R. W. and Xu, Y. and Jäger, W. Spectroscopic exploration of atomic scale superfluidity in doped helium nanoclusters. *Phys. Rev. Lett.*, 97:183401, 2006. 5

[46] M. N. Slipchenko, S. Kuma, T. Momose, and A. F. Vilesov. Intense pulsed helium droplet beams. *Rev. Sci. Inst.*, 73(10):3600–3605, 2002. 5, 7

[47] M. Lewerenz, B. Schilling, and J.P. Toennies. A new scattering deflection method for determining and selecting the sizes of large liquid clusters of 4he. *Chem. Phys. Lett.*, 206(1-4):381 – 387, 1993. 5, 6, 7

[48] J. Chaiken, J. Goodisman, Oleg Kornilov, and J. Peter Toennies. Application of scaling and kinetic equations to helium cluster size distributions: Homogeneous nucleation of a nearly ideal gas. *J. Chem. Phys.*, 125(7):074305, 2006. 5

[49] E. L. Knuth and U. Henne. Average size and size distribution of large droplets produced in a free-jet expansion of a liquid. *J. Chem. Phys.*, 110(5):2664–2668, 1999. 5, 6, 7

[50] U. Henne and J. P. Toennies. Electron capture by large helium droplets. *J. Chem. Phys.*, 108(22):9327–9338, 1998. 5

[51] T. Jiang and J. A. Northby. Fragmentation clusters formed in supercritical expansions of ^{4}He. *Phys. Rev. Lett.*, 68:2620–2623, 1992. 5

[52] J. Harms, J. P. Toennies, and F. Dalfovo. Density of superfluid helium droplets. *Phys. Rev. B*, 58:3341–3350, 1998. 6, 7, 8, 9, 10, 11

[53] J. Harms, J. P. Toennies, M. Barranco, and M. Pi. Experimental and theoretical study of the radial density distributions of large ^{3}He droplets. *Phys. Rev. B*, 63:184513, 2001. 6

[54] O. Kornilov and J.P. Toennies. The determination of the mean sizes of large he droplets by electron impact induced attenuation. *Int. J. Mass Spectrom.*, 280(1-3):209 – 212, 2009. 6, 7, 8, 167

[55] M. Farnik, U. Henne, B. Samelin, and J.P. Toennies. Comparison between positive and negative charging of helium droplets. *Z. Phys. D: Atom. Mol. Cl.*, 40:93–98, 1997. 6

[56] L. F. Gomez, E. Loginov, R. Sliter, and A. F. Vilesov. Sizes of large he droplets. *J. Chem. Phys.*, 135(15):154201, 2011. 6, 11

[57] P. Claas, S.-O. Mende, and F. Stienkemeier. Characterization of laser ablation as a means for doping helium nanodroplets. *Rev. Sci. Inst.*, 74(9):4071–4076, 2003.

[58] E.L. Knuth. Size correlations for condensation clusters produced in free-jet expansions. *J. Chem. Phys.*, 107(21):9125–9132, 1997. 7

[59] E. Loginov. *Photoexcitation and Photoionization Dynamics of doped liquid Helium-4 Nanodroplets.* PhD thesis, Ecole Polytechnique Federale de Lausanne, 2008.

[60] F. Bierau, P. Kupser, G. Meijer, and G. von Helden. Catching proteins in liquid helium droplets. *Phys. Rev. Lett.*, 105:133402, 2010. 7

[61] R. E. Grisenti and J. P. Toennies. Cryogenic microjet source for orthotropic beams of ultralarge superfluid helium droplets. *Phys. Rev. Lett.*, 90:234501, 2003.

[62] T. M. Falconer, W. K. Lewis, R. J. Bemish, R. E. Miller, and G. L. Glish. Formation of cold ion-neutral clusters using superfluid helium nanodroplets. *Rev. Sci. Inst.*, 81(5):054101, 2010.

[63] U. Even, J. Jortner, D. Noy, N. Lavie, and C. Cossart-Magos. Cooling of large molecules below 1 K and He clusters formation. *J. Chem. Phys.*, 112(18):8068–8071, 2000.

[64] D. Pentlehner, R. Riechers, B. Dick, A. Slenczka, U. Even, N.Lavie, R. Brown, and K. Luria. Rapidly pulsed helium droplet source. *Rev. Sci. Inst.*, 80(4):043302, 2009.

[65] S. Yang, S. M. Brereton, and A. M. Ellis. Controlled growth of helium nanodroplets from a pulsed source. *Rev. Sci. Inst.*, 76(10):104102, 2005.

[66] Shengfu Yang and Andrew M. Ellis. Selecting the size of helium nanodroplets using time-resolved probing of a pulsed helium droplet beam. *Rev. Sci. Inst.*, 79(1):016106, 2008. 7

[67] R. D. McCarty. Thermodynamic Properties of Helium 4 from 2 to 1500 K at Pressures to 10^8 Pa. *J. Phys. Chem. Ref. Data*, 2(4):923–1042, 1973. 7

[68] T. Fliessbach. *Statistische Physik*. Elsevier, 4 edition, 2007. 7

[69] R. J. Donnelly and C. F. Barenghi. The observed properties of liquid helium at the saturated vapor pressure. *J. Phys. Chem. Ref. Data*, 27(6):1217–1274, 1998. 11

[70] T. E. Gough, M. Mengel, P. A. Rowntree, and G. Scoles. Infrared spectroscopy at the surface of clusters: SF_6 on Ar. *J. Chem. Phys.*, 83(10):4958–4961, 1985. 13

[71] A. Scheidemann, B. Schilling, J.P. Toennies, and J.A. Northby. Capture of foreign atoms by helium clusters. *Physica B*, 165-166(0):135 – 136, 1990. 13, 18

[72] S. Stringari and J. Treiner. Systematics of liquid helium clusters. *J. Chem. Phys.*, 87(8):5021–5027, 1987. 14, 17

[73] M. Lewerenz, B. Schilling, and J. P. Toennies. Successive capture and coagulation of atoms and molecules to small clusters in large liquid helium clusters. *J. Chem. Phys.*, 102(20):8191–8207, 1995. 14, 16, 115

[74] O. Bünermann and F. Stienkemeier. Modeling the formation of alkali clusters attached to helium nanodroplets and the abundance of high-spin states. *Eur. Phys. J. D*, 61:645–655, 2011. 14, 15, 16, 17

[75] F. Ancilotto, E. Cheng, M. W. Cole and F. Toigo. The binding of alkali atoms to the surfaces of liquid helium and hydrogen. *Z. Phys. B: Con. Mat.*, 98(3):323–329, 1995. 17, 19, 62, 76

[76] J. Nagl, G. Auböck, A. W. Hauser, O. Allard, C. Callegari, and W. E. Ernst. High-spin alkali trimers on helium nanodroplets: Spectral separation and analysis. *J. Chem. Phys.*, 128(15):154320, 2008. 17, 19, 105

[77] O. Allard, J. Nagl, G. Auböck, C. Callegari and W. E. Ernst. Investigation of KRb and Rb_2 formed on cold helium nanodroplets. *J. Phys. Chem. B*, 39(19):1169, 2006. 17, 19

[78] A. Scheidemann, J. P. Toennies, and J. A. Northby. Capture of neon atoms by ^{4}He clusters. *Phys. Rev. Lett.*, 64:1899–1902, 1990. 18

[79] S. Goyal, D. L. Schutt, and G. Scoles. Vibrational spectroscopy of sulfur hexafluoride attached to helium clusters. *Phys. Rev. Lett.*, 69:933–936, 1992. 18

[80] R. Fröchtenicht and J.P. Toennies and A. Vilesov. High-resolution infrared spectroscopy of SF_6 embedded in He clusters. *Chem. Phys. Lett.*, 229(1-2):1–7, 1994. 18

[81] M. Hartmann, R. E. Miller, J. P. Toennies, and A. F. Vilesov. High-resolution molecular spectroscopy of van der waals clusters in liquid helium droplets. *Science*, 272(5268):1631–1634, 1996. 18

[82] K. K. Lehmann and G. Scoles. The ultimate spectroscopic matrix? *Science*, 279(5359):2065–2066, 1998. 18

[83] Y. Kwon, P. Huang, M. V. Patel, D. Blume, and K. B. Whaley. Quantum solvation and molecular rotations in superfluid helium clusters. *J. Chem. Phys.*, 113(16):6469–6501, 2000. 18

[84] M. Hartmann, F. Mielke, J. P. Toennies, A. F. Vilesov, and G. Benedek. Direct spectroscopic observation of elementary excitations in superfluid he droplets. *Phys. Rev. Lett.*, 76:4560–4563, 1996. 18

[85] A. Bartelt, J.D. Close, F. Federmann, K. Hoffmann, N. Quaas, and J.P. Toennies. The UV-absorption of europium atoms embedded in helium nanodroplets. *Z. Phys. D: Atom. Mol. Cl.*, 39:1–2, 1997. 18

[86] A. Bartelt, J. D. Close, F. Federmann, N. Quaas, and J. P. Toennies. Cold metal clusters: Helium droplets as a nanoscale cryostat. *Phys. Rev. Lett.*, 77:3525–3528, 1996. 18

[87] F. Federmann, K. Hoffmann, N. Quaas, and J. D. Close. Rydberg states of silver: Excitation dynamics of doped helium droplets. *Phys. Rev. Lett.*, 83:2548–2551, 1999. 18, 68

[88] F. Ancilotto, P. B. Lerner, and M. W. Cole. Physics of solvation. *J. Low Temp. Phys.*, 101:1123–1146, 1995. 19, 62, 64

[89] O. Bünermann, G. Droppelmann, A. Hernando, R. Mayol, and F. Stienkemeier. Unraveling the absorption spectra of alkali metal atoms attached to helium nanodroplets. *J. Phys. Chem. A*, 111(49):12684–12694, 2007. 19, 61, 62, 68, 104

[90] Y. Takahashi, K. Sano, T. Kinoshita, and T. Yabuzaki. Spectroscopy of alkali atoms and molecules in superfluid helium. *Phys. Rev. Lett.*, 71:1035–1038, 1993. 19

[91] Gerald Auböck. *Spectroscopy of Alkali-Metal Atoms and their High-Spin Oligomers on Helium Nanodroplets in External Magnetic Fields.* PhD thesis, TU Graz, IEP, 2008. 19, 63, 64

[92] G. Auböck, J. Nagl, C. Callegari, and W. E. Ernst. Observation of relativistic E x e vibronic coupling in Rb_3 and K_3 quartet states on helium droplets. *J. Chem. Phys.*, 129(11):114501, 2008. 19

[93] J. Nagl, G. Auböck, A. W. Hauser, O. Allard, and W. E. Callegari, C.and Ernst. Heteronuclear and Homonuclear High-Spin Alkali Trimers on Helium Nanodroplets. *Phys. Rev. Lett.*, 100:063001, 2008.

[94] G. Auböck and M. Aymar and O. Dulieu and W. E. Ernst. Reinvestigation of the $Rb_2(2)^3\Pi_g$ - $a^3\Sigma_u^+$ band on helium nanodroplets. *J. Chem. Phys.*, 132(5):054304, 2010. 19

[95] J. Higgins, C. Callegari, J. Reho, F. Stienkemeier, W. E. Ernst, K. K. Lehmann, and G. Gutowski, M.and Scoles. Photoinduced chemical dynamics of high-spin alkali trimers. *Science*, 273(5275):629–631, 1996. 19

[96] F. R. Brühl, R. A. Miron, and W. E. Ernst. Triplet states of rubidium dimers on helium nanodroplets. *J. Chem. Phys.*, 115(22):10275–10281, 2001. 19, 113

[97] M. Mudrich, Ph. Heister, T. Hippler, Ch. Giese, O. Dulieu, and F. Stienkemeier. Spectroscopy of triplet states of Rb_2 by femtosecond pump-probe photoionization of doped helium nanodroplets. *Phys. Rev. A*, 80:042512, 2009.

[98] A. W. Hauser and W. E. Ernst. Homo- and heteronuclear alkali metal trimers formed on helium nanodroplets. Part I. Vibronic spectra simulations based on ab initio calculations. *Phys. Chem. Chem. Phys.*, 13(42):18762–18768, 2011.

[99] C. Giese, F. Stienkemeier, M. Mudrich, A. W. Hauser, and W. E. Ernst. Homo- and heteronuclear alkali metal trimers formed on helium nanodroplets. Part II. Femtosecond spectroscopy and spectra assignments. *Phys. Chem. Chem. Phys.*, 13(42):18769–18780, 2011. 19

[100] W. E. Ernst, R. Huber, S. Jiang, R. Beuc, M. Movre, and G. Pichler. Cesium dimer spectroscopy on helium droplets. *J. Chem. Phys.*, 124(2):024313, 2006. 19, 80

[101] O. Bünermann, M. Mudrich, M. Weidemüller and F. Stienkemeier. Spectroscopy of Cs attached to helium nanodroplets. *J. Chem. Phys.*, 121(18):8880, 2004. 19, 61, 66, 76, 80

[102] C. P. Schulz, P. Claas, D. Schumacher, and F. Stienkemeier. Formation and stability of high-spin alkali clusters. *Phys. Rev. Lett.*, 92:013401, 2004. 20

[103] C. Stark and V. V. Kresin. Critical sizes for the submersion of alkali clusters into liquid helium. *Phys. Rev. B*, 81:085401, 2010. 20

[104] L. an der Lan and P. Bartl and Ch. Leidlmair and H. Schöbel and R. Jochum and S. Denifl and T. D. Märk and A. M. Ellis and P. Scheier. The submersion of sodium clusters in helium nanodroplets: Identification of the surface –> interior transition. *J. Chem. Phys.*, 135(4):044309, 2011. 20

[105] An der Lan, L. and Bartl, P. and Leidlmair, Ch. and Schöbel, H. and Denifl, S. and Märk, T. D. and Ellis, A. M. and Scheier, P. Submersion of potassium clusters in helium nanodroplets. *Phys. Rev. B*, 85:115414, 2012. 20

[106] K. Hauffe. Gegen Flusssäure korrosionsbeständige Werkstoffe. *Materialwissenschaft und Werkstofftechnik*, 16(8):259–270, 1985. 25

[107] J. Nagl. Aufbau und Test einer Düsenstrahlapparatur zur Spektroskopie an alkalimetalldotierten Edelgasclustern. Master's thesis, TU Graz, IEP, 2004. 25, 26

[108] Lackner F. Laserspektroskopie und Flugzeitmassenspektrometrie an Rubidium-dotierten Heliumnanotrpfchen. Master's thesis, TU Graz, 2009. 26

[109] W.C. Wiley and I.H. McLaren. Time-of-flight mass spectrometer with improved resolution. *Rev. Sci. Inst.*, 26:1150, 1955. 30

[110] H. Pauly. *Atom, Molecule, and Cluster Beams I.* Springer, 2000. 31

[111] R. Weinkauf, K. Walter, C. Weickhardt, U. Boesl, E.W. Schlag. Laser Tandem Mass Spectrometry in a Time of Flight Instrument. *Z. Naturforsch.*, 44a:1219, 1989.

[112] U. Boesl, R. Weinkauf and E.W. Schlag. Reflectron time-of-flight mass spectrometry and laser excitation for the analysis of neutrals, ionized molecules and secundary fragments. *Int. J. Mass Spectrom.*, 112:121–166, 1992. 31

[113] C.A. Flory, R.C. Taber, G.E. Yefchak. Analytic expression for the ideal one-dimensional mirror potential yielding perfect energy focusing in TOF mass spectrometry. *Int. J. Mass Spectrom.*, 152:177–184, 1996. 31

[114] T. Bergmann, T. P. Martin, and H. Schaber. High-resolution time-of-flight mass spectrometers: Part I. Effects of field distortions in the vicinity of wire meshes. *Rev. Sci. Inst.*, 60:347, 1989. 31

[115] B.A. Mamyrin. Laser assisted reflectron time-of-flight mass spectrometry. *Int. J. Mass Spectr.*, 131:1–19, 1993. 31

[116] R.M. Jordan Company. *Instruction Manual, AREF Time of flight power supply.* 32, 34

[117] Alexandra Pifrader. Pulsed laser spectroscopic investigations of rubidium atoms attached to helium nanodroplets. Master's thesis, TU Graz, Institut für Experimentalphysik, 04 2009. 35, 61

[118] M. Krug. A matlab program to control a time-of-flight multichannel analyzer and test experiments on caesium. Master's thesis, Bachelorthesis, TU Graz, 2010. 37

[119] Robert W. Boyd. *Nonlinear Optics.* Elsevier, 2008. 39

[120] T. F. Gallagher. *Rydberg Atoms.* Cambridge University Press, 1 edition, 1994. 43, 45, 46, 55, 58, 88, 89, 109

[121] R. Pohl, A. Antognini, F. Nez, F. D. Amaro, F. Biraben, J.M. R. Cardoso, D. S. Covita, A. Dax, S. Dhawan, L. M. P. Fernandes, A. Giesen, T. Graf, T. W. Haensch, P. Indelicato, L. Julien, C.-Y. Kao, P. Knowles, E.-O. Le Bigot, Y.-W. Liu, J. A. M. Lopes, L. Ludhova, C. M. B. Monteiro, F. Mulhauser, T. Nebel, P. Rabinowitz, J. M. F. dos Santos, L. A. Schaller, K. Schuhmann, C. Schwob, D. Taqqu, J. F. C. A. Veloso, and F. Kottmann. The size of the proton. *Nature*, 466(7303):213–216, 2010. 44, 46

[122] J.-P. Connerade. *Highly Excited Atoms.* Cambridge University Press, 1 edition, 1997. 44, 45, 46, 50, 60

[123] R. Neuhauser, K. Siglow, and H. J. Neusser. Hydrogenlike rydberg electrons orbiting molecular clusters. *Phys. Rev. Lett.*, 80:5089–5092, 1998. 45, 103

[124] M. O. Vieitez, T. I. Ivanov, E. Reinhold, C. A. de Lange, and W. Ubachs. Observation of a Rydberg Series in H^+H^-: A Heavy Bohr Atom. *Phys. Rev. Lett.*, 101:163001, 2008. 45, 103

[125] E. Reinhold and W. Ubachs. Heavy Rydberg states. *Mol. Phys.*, 103(10):1329–1352, 2005. 45

[126] F.E. Maas, B. Braun, H. Geerds, K. Jungmann, B.E. Matthias, G. zu Putlitz, I. Reinhard, W. Schwarz, L. Willmann, L. Zhang, P.E.G. Baird, P.G.H. Sandars, G.S. Woodman, G.H. Eaton, P. Matousek, W.T. Toner, M. Towrie, J.R.M. Barr, A.I. Ferguson, M.A. Persaud, E. Riis, D. Berkeland, M.G. Boshier, V.W. Hughes, and K.A. Woodle. A measurement of the 1s-2s transition frequency in muonium. *Phys. Lett. A*, 187(3):247 – 254, 1994. 45

[127] M. S. Fee, S. Chu, A. P. Mills, R. J. Chichester, D. M. Zuckerman, E. D. Shaw, and K. Danzmann. Measurement of the positronium $1\,^3s_1$–$2\,^3s_1$ interval by continuous-wave two-photon excitation. *Phys. Rev. A*, 48:192–219, 1993. 45

[128] G. Gabrielse, N. S. Bowden, P. Oxley, A. Speck, C. H. Storry, J. N. Tan, M. Wessels, D. Grzonka, W. Oelert, G. Schepers, T. Sefzick, J. Walz, H. Pittner, T. W. Hänsch, and E. A. Hessels. Driven production of cold antihydrogen and the first measured distribution of antihydrogen states. *Phys. Rev. Lett.*, 89:233401, 2002. 45

[129] J. J. Balmer. Notiz über die Spectrallinien des Wasserstoffs. *Ann. Phys.*, 261(5):80–87, 1885. 45

[130] I. Martinson and L.J. Curtis. Janne Rydberg - his life and work. *Nucl. Inst. Meth. B*, 235(1-4):17 – 22, 2005. 45

[131] J.R. Rydberg. Recherches sur la constitution des spectres d'emission des elements chimique. *Den Kungliga Svenska Vetenskapsakademiens Handlingar*, 23, 1889. 46

[132] H. Haken, H.C. Wolf. *Atom- und Quantenphysik.* Springer, 6 edition, 1996. 46, 49

[133] I.V. Hertel and C.-P. Schulz. *Atome, Moleküle und optische Physik 1.* Springer, 2008. 50, 53

[134] B.H. Bransden and C.J. Joachain. *Physics of Atoms and Molecules.* Pearson Education Limited, 2 edition, 2003.

[135] Robert D. Cowan. *The Theory of atomic structure and spectra.* University of California Press, 1981. 46, 49

[136] M.S. Child. *Theory of Molecular Rydberg States.* Cambridge University Press, 2011. 46, 50, 51, 52, 54

[137] Walter R. Johnson. *Atomic Structure Theory.* Springer, 2007. 48

[138] M. J. Seaton. Quantum defect theory. *Rep. Prog. Phys.*, 46:167, 1983. 50, 51, 52

[139] C. H. Greene and Ch. Jungen. Molecular Application of Quantum defect theory. *Adv. Atom. Mol. Phys.*, 21:51–123, 1985. 50

[140] M. J. Seaton. Quantum defect theory I. General formulation. *P. Phys. Soc.*, 88(4):801, 1966. 50

[141] U. Fano. Quantum Defect Theory of l Uncoupling in H_2 as an Example of Channel-Interaction Treatment. *Phys. Rev. A*, 2:353–365, 1970. 50, 52

[142] C. H. Greene, A. R. P. Rau, and U. Fano. General form of the quantum-defect theory. II. *Phys. Rev. A*, 26:2441–2459, 1982. 50, 52

[143] Arnold Sommerfeld. *Atombau und Spektrallinien.* Vieweg & Sohn, Braunschweig, 1924. 52, 55

[144] C. Fabre, M. Gross, J. M. Raimond, and S. Haroche. Measuring atomic dimensions by transmission of Rydberg atoms through micrometre size slits. *J. Phys. B: At. Mol. Phys.*, 16(21):L671, 1983. 54

[145] D. B. Branden, T. Juhasz, T. Mahlokozera, C. Vesa, R. O. Wilson, M .Zheng, A. Kortyna, and D. A. Tate. Radiative lifetime measurements of rubidium Rydberg states. *J. Phys. B: At. Mol. Opt.*, 43(1):015002, 2010. 55

[146] T. F. Gallagher, R. M. Hill, and S. A. Edelstein. Resonance measurements of $d-f-g-h$ splittings in highly excited states of sodium. *Phys. Rev. A*, 14:744–750, 1976. 56

[147] Walter Ritz. Zur Theorie der Serienspektren. *Ann. Phys.*, 317(10):264–310, 1903. 57

[148] R. Jastrow. On the Rydberg-Ritz Formula in Quantum Mechanics. *Phys. Rev.*, 73:60–67, 1948. 57

[149] D. R. Hartree. The wave mechanics of an atom with a non-Coulomb central field Part III Term values and intensities in series an optical spectra. *Proc. Chamb. Philos. Soc.*, 24:426–437, 1928. 57

[150] W. C. Martin. Series formulas for the spectrum of atomic sodium (Na I). *J. Opt. Soc. Am.*, 70(7):784–788, 1980. 57

[151] C.-J. Lorenzen and K. Niemax. Quantum Defects of the $n^2P_{1/2,3/2}$ Levels in ^{39}K I and ^{85}Rb I. *Phys. Scripta*, 27(4):300, 1983. 57, 111, 112, 130

[152] B. Sanguinetti, H. O. Majeed, M. L. Jones, and B. T. H. Varcoe. Precision measurements of quantum defects in the $nP_{3/2}$ Rydberg states of ^{85}Rb. *J. Phys. B: At. Mol. Opt.*, 42(16):165004, 2009. 57

[153] K.-H. Weber and C. J. Sansonetti. Accurate energies of nS, nP, nD, nF, and nG levels of neutral cesium. *Phys. Rev. A*, 35(11):4650–4660, 1987. 58, 59, 88

[154] Bengt Edlen. *Handbuch der Phyik*, chapter Atomic Spectra, pages 80–220. Springer, 1964. 58, 129

[155] C. J. Lorenzen and K. Niemax. Precise quantum defects of nS, nP and nD Levels in Cs I. *Z. Phys. A Hadron. Nucl.*, 315:127–133, 1984. 58

[156] Robert S. Freud. *Rydberg states of atoms and molecules*, chapter 10 - High-Rydberg molecules, pages 355–392. Cambridge University Press, 1983. 60

[157] F. Merkt. Molecules in high Rydberg states. *Ann. Rev. Phys. Chem.*, 48:675–709, 1997. 60

[158] R. S. Mulliken. Rydberg states and Rydbergization. *Accounts Chem. Res.*, 9(1):7–12, 1976. 60, 144

[159] F. Stienkemeier, J. Higgins, C. Callegari, S. I. Kanorsky, W. E. Ernst, G. Scoles. Spectroscopy of alkali atoms (Li, Na, K) attached to large helium clusters. *Z. Phys. D: At., Mol. Clusters*, 38(3):253–263, 1996. 61, 62, 66, 76, 77, 104

[160] F. R. Brühl, R. A. Trasca, and W. E. Ernst. Rb–He exciplex formation on helium nanodroplets. *J. Chem. Phys.*, 115(22):10220–10224, 2001. 61, 65, 66, 76, 104

[161] A. Pifrader and O. Allard and G. Auböck and C. Callegari and W. E. Ernst and R. Huber and F. Ancilotto. One- and two-photon spectroscopy of highly excited states of alkali-metal atoms on helium nanodroplets. *J. Chem. Phys.*, 133(16):164502, 2010. 61, 62, 77, 83, 84, 85, 91, 104

[162] R. Huber. Spectroscopic studies of higher excited states of heavy alkali atoms on helium nanodroplets. Master's thesis, Pennsylvania State University, 2003. 61, 91

[163] A. Hernando, M. Barranco, M. Pi, M. Loginov, E.and Langlet, and M. Drabbels. Desorption of alkali atoms from ^{4}He nanodroplets. *Phys. Chem. Chem. Phys.*, 14:3996–4010, 2012. 61

[164] E. Loginov and M. Drabbels. Unusual Rydberg System Consisting of a Positively Charged Helium Nanodroplet with an Orbiting Electron. *Phys. Rev. Lett.*, 106(8):083401, 2011. 61, 77, 88, 89, 94, 104, 110, 148

[165] E. Loginov, C. Callegari, F. Ancilotto, and M. Drabbels. Spectroscopy on Rydberg States of Sodium Atoms on the Surface of Helium Nanodroplets. *J. Phys. Chem. A*, 115:6779–6788, 2011. 61, 77, 85, 94, 104

[166] L. Fechner, B. Gruner, A. Sieg, C. Callegari, F. Ancilotto, F. Stienkemeier, and M. Mudrich. Photoionization and imaging spectroscopy of rubidium atoms attached to helium nanodroplets. *Phys. Chem. Chem. Phys.*, 14:3843–3851, 2012. 61, 94, 104, 113

[167] E. Cheng, M. W. Cole, W. F. Saam, and J. Treiner. Wetting transitions of classical liquid films: A nearly universal trend. *Phys. Rev. B*, 48:18214–18221, 1993. 62

[168] F. Meier F. Stienkemeier and H. O. Lutz. Alkaline earth metals (Ca, Sr) attached to liquid helium droplets: Inside or out? *J. Chem. Phys.*, 107:10816, 1997. 62

[169] Y. Ren and V. V. Kresin. Surface location of alkaline-earth-metal-atom impurities on helium nanodroplets. *Phys. Rev. A*, 76:043204, 2007. 62

[170] Gerhard Herzberg. *Molecular Spectra and Molecular Structure.* VNR, 1959. 63

[171] J. Reho, J. Higgins, C. Callegari, K. K. Lehmann, and G. Scoles. Alkali-helium exciplex formation on the surface of helium nanodroplets. I. Dispersed emission spectroscopy. *J. Chem. Phys.*, 113(21):9686, 2000. 65, 76

[172] J. Reho, J. Higgins, K. K. Lehmann, and G. Scoles. AlkaliâĂŞhelium exciplex formation on the surface of helium nanodroplets. ii. a time-resolved study. *J. Chem. Phys.*, 113(21):9694, 2000. 76

[173] M. Mudrich, F. Stienkemeier, G. Droppelmann, P. Claas, and C. P. Schulz. Quantum interference spectroscopy of rubidium-helium exciplexes formed on helium nanodroplets. *Phys. Rev. Lett.*, 100:023401, 2008. 65, 68

[174] G. Auböck, J. Nagl, C. Callegari, and W. E. Ernst. Electron Spin Pumping of Rb Atoms on He Nanodroplets via Nondestructive Optical Excitation. *Phys. Rev. Lett.*, 101(3):035301, 2008. 68, 69, 72, 76, 104

[175] A. Kautsch, M. Hasewend, M. Koch, and W. E. Ernst. Fano resonances in chromium photoionization spectra after photoinduced ejection from a superfluid helium nanodroplet. *Phys. Rev. A*, 86:033428, Sep 2012. 68

[176] E. Loginov and M. Drabbels. Spectroscopy and dynamics of barium-doped helium nanodroplets. *J. Chem. Phys.*, 136(15):154302, 2012. 68, 157

[177] X. Zhang and M. Drabbels. Communication: Barium ions and helium nanodroplets: Solvation and desolvation. *J. Chem. Phys.*, 137(5):051102, 2012. 68

[178] C. Callegari and F. Ancilotto. Perturbation method to calculate the interaction potentials and electronic excitation spectra of atoms in he nanodroplets. *J. Phys. Chem. A*, 115(25):6789–6796, 2011. 69, 77, 83, 84, 85, 86, 89, 105

[179] J. Reho, C. Callegari, J. Higgins, W. E. Ernst, K. K. Lehmann, and G. Scoles. Spin-orbit effects in the formation of the Na-He excimer on the surface of He clusters. *Faraday Discuss. 1997*, 108:161–174, 1997. 76

[180] M. Koch, G. Auböck, C. Callegari, and W. E. Ernst. Coherent Spin Manipulation and ESR on Superfluid Helium Nanodroplets. *Phys. Rev. Lett.*, 103(3):035302, 2009. 76

[181] M. Koch, J. Lanzersdorfer, C. Callegari, J. S. Muenter, and W. E. Ernst. Molecular Beam Magnetic Resonance in Doped Helium Nanodroplets. A Setup for Optically Detected ESR/NMR in the Presence of Unresolved Zeeman Splittings. *J. Phys. Chem. A*, 113(47):13347, 2009.

[182] M. Koch, C. Callegari, and W. E. Ernst. Alkali-metal electron spin density shift induced by a helium nanodroplet. *Mol. Phys.*, 108(7):1005–1011, 2010. 76

[183] A. Golov, S. Sekatskii. A new type of excimer atom: electron + ionized helium cluster. *Z. Phys. D: Atom. Mol. Cl.*, 27(4):349–355, 1993. 77, 104, 112, 148, 151

[184] C.-J. Lorenzen, K.-H. Weber, and K. Niemax. Energies of the n^2S_{12} and $n^2D_{3/2,5/2}$ states of Cs. *Opt. Commun.*, 33(3):271 – 276, 1980. 85, 88

[185] C.-J. Lorenzen and K. Niemax. New measurements of the $n^2P_{1/2,3/2}$ energy levels of Cs(I). *J. Quant. Spectrosc. Radiat. Transfer*, 22(3):247 – 252, 1979. 85, 88

[186] C. E. Burkhardt, J. L. Libbert, Jian Xu, J. J. Leventhal, and J. D. Kelley. Absolute measurement of photoionization cross sections of excited atoms: Application to determination of atomic beam densities. *Phys. Rev. A*, 38:5949–5952, 1988. 92

[187] L.-W. He, C. E. Burkhardt, M. Ciocca, J. J. Leventhal, and S. T. Manson. Absolute cross sections for the photoionization of the $6s\ 6p\ ^1P$ excited state of barium. *Phys. Rev. Lett.*, 67:2131–2134, 1991. 92

[188] A. Nadeem and S. U. Haq. Photoionization from the $^2 5p_{3/2}$ state of rubidium. *Phys. Rev. A*, 83:063404, 2011. 93

[189] S. U. Haq and A. Nadeem. Photoionization from the $6p\ ^2P_{3/2}$ state of neutral cesium. *Phys. Rev. A*, 81:063432, 2010. 93

[190] U. Heinzmann, D. Schinkowski, and H. Zeman. Comment on measuring photoionization cross sections of excited atomic states. *Appl. Phys. A: Mater.*, 12:113–113, 1977. 93

[191] H. Lefebvre-Brion and R.W. Field. *The spectra and dynamics of diatomic molecules.* Elsevier, 2004. 96

[192] J. E. Murphy, J. M. Berg, A. J. Merer, N. A. Harris, and R. W. Field. Rydberg states and ionization potential of calcium monofluoride. *Phys. Rev. Lett.*, 65:1861–1864, 1990. 103, 104, 105

[193] Z. J. Jakubek and R. W. Field. Core-penetrating Rydberg Series of BaF: $s \sim p \sim d \sim f$ Supercomplexes. *Phys. Rev. Lett.*, 72:2167–2170, 1994. 103, 104, 105

[194] V. Bendkowsky, B. Butscher, J. Nipper, J. P. Shaffer, R. Loew, and T. Pfau. Observation of Ultralong-Range Rydberg Molecules. *Nature*, 458(7241):1005–1008, 2009. 104

[195] F. Ancilotto, M. Pi, R. Mayol, M. Barranco, and K. K. Lehmann. Squeezing a helium nanodroplet with a rydberg electron. *J. Phys. Chem. A*, 111(49):12695–12701, 2007. 104, 148, 149, 151

[196] J. Nagl and A. W. Hauser and G. Auböck and C. Callegari and W. E. Ernst. Optical spectroscopy of potassium-doped argon clusters. experiments and quantum-chemistry calculations. *J. Phys. Chem. A*, 111(49):12386–12397, 2007. 105

[197] Gerhard Herzberg. *Atomic spectra and atomic structure.* Dover Publications, 2 edition, 1945. 110, 128

[198] J. E. Sansonetti. Wavelength, Transition Propabilities, and Energy Levels for the Spectra of Rubidium (Rb I through Rb XXXVII). *J. Phys. Chem. Ref. Data*, 35:301–421, 2006. 113, 115

[199] D. E. Galli, D. M. Ceperley, and L. Reatto. Path Integral Monte Carlo Study of ^{4}He Clusters Doped with Alkali and Alkali-Earth Ions. *J. Phys. Chem. A*, 115(25):7300–7309, 2011. 145, 146

[200] D. E. Galli, M. Buzzacchi, and L. Reatto. Pure and alkali–ion-doped droplets of ^{4}He. *J. Chem. Phys.*, 115(22):10239–10247, 2001. 145

[201] K. R. Atkins. Ions in liquid helium. *Phys. Rev.*, 116:1339–1343, 1959. 145, 146

[202] K. K. Lehmann and J. A. Northby. Potential of an ionic impurity in a large ^{4}He cluster. *Molecular Physics*, 97:639–644, 1999. 146, 151

[203] L. Meyer and F. Reif. Mobilities of He Ions in Liquid Helium. *Phys. Rev.*, 110:279–280, 1958. 146

[204] J. C. Miller and W. C. Cheng. Multiphoton ionization of nitric oxide-rare gas van der Waals species. *J. Phys. Chem.*, 89(9):1647–1653, 1985. 146, 147

[205] E. Amaldi and E. Segre. Effect of pressure on high terms of alkaline spectra. *Nature*, 133:141, 1934. 146

[206] Tsi-Ze, N. and Shang-Yi, C. The displacement of principal series lines of rubidium by the addition of rare gases. *Phys. Rev.*, 51:567–571, 1937. 146

[207] E. Fermi. *Nuovo Cimento*, 11:157, 1934. 146

[208] W. L. Brillet and A. Gallagher. Inert-gas collisional broadening and shifts of Rb Rydberg states. *Phys. Rev. A*, 22:1012–1017, 1980. 146

[209] W. Weyhmann and F. M. Pipkin. Optical absorption spectra of alkali atoms in rare-gas matrices. *Phys. Rev.*, 137:A490–A496, 1965. 147

[210] L. C. Balling and J. J. Wright. Laser excitation of excited states of Rb and Cs atoms in an Ar matrix. *J. Chem. Phys.*, 78(1):592–593, 1983.

[211] J. Hormes. On Rydberg transitions of matrix isolated atoms. *Chem. Phys. Lett.*, 112(5):431 – 435, 1984. 147

[212] N. Schwentner and M. Chergui. A model potential for Rydberg states of alkali atoms in rare gas matrices. *J. Chem. Phys.*, 85(6):3458–3462, 1986. 147, 157

[213] L. Resca and R. Resta. Rydberg states in condensed matter. *Phys. Rev. B*, 19:1683–1688, 1979. 147

[214] F. Vigliotti and M. Chergui. Rydberg states in the condensed phase studied by fluorescence depletion spectroscopy. *Eur. Phys. J. D*, 10:379–390, 2000. 147

[215] R. Guerout, M. Jungen, and Ch. Jungen. Ab initio molecular quantum defect theory: II. Rydberg and continuum states of NO. *J. Phys. B: At. Mol. Opt.*, 37(15):3057, 2004. 147

[216] E. Miescher. Absorption spectrum of the NO molecule: Part VII. Extension of the Rydberg series of ns, np, nd, and nf - complexes. *J. Mol. Spectrosc.*, 20(2):130 – 140, 1966. 147

[217] Ch. Jungen. Rydberg Series in the NO Spectrum: An Interpretation of Quantum Defects and Intensities in the s and d Series. *J. Chem. Phys.*, 53(11):4168–4182, 1970. 147

[218] N. Shafizadeh and Ph. Bréchignac and M. Dyndgaard and J. H. Fillion and D. Gauyacq and B. Levy and J. C. Miller and T. Pino and M. Raoult. A, C, and D electronic states of the Ar–NO van der Waals molecule revisited: Experiment and theory. *J. Chem. Phys.*, 108(22):9313–9326, 1998. 147

[219] D. E. Bergeron, A. Musgrave, R. T. Gammon, V. L. Ayles, J. A. E. Silber, T. G. Wright, B. Wen, and H. Meyer. Electronic spectroscopy of the 3d Rydberg states of NO–Rg (Rg = Ne,Ar,Kr,Xe) van der Waals complexes. *J. Chem. Phys.*, 124(21):214302, 2006. 147

[220] D. E. Bergeron, A. Musgrave, V. L. Ayles, R. T. Gammon, J. A. E. Silber, and T. G. Wright. Electronic spectroscopy of NO–$(Rg)_x$ complexes (Rg = Ne,Ar) via the 4s and 3d Rydberg states. *J. Chem. Phys.*, 125(14):144319, 2006. 147

[221] B. Wen, H. Meyer, V. L. Ayles, A. Musgrave, D. E. Bergeron, J. A. E. Silber, and T. G. Wright. Electronic spectroscopy of the $\tilde{E} \leftarrow \tilde{X}$ transition of NO-Kr and shielding/penetration effects in Rydberg states of NO-Rg complexes. *Phys. Chem. Chem. Phys.*, 10:375, 2008. 147

[222] M. B. E. H. Rhouma, Z. B. Lakhdar, H. Berriche, and F. Spiegelman. Rydberg states of small $NaAr_n^*$ clusters. *J. Chem. Phys.*, 125(8):084315, 2006. 148

[223] E. Polyakova, D. Stolyarov, and C. Wittig. Multiple photon excitation and ionization of no in and on helium droplets. *J. Chem. Phys.*, 124(21):214308, 2006. 148

[224] K. von Haeften and T. Laarmann and H. Wabnitz and T. Müller. The electronically excited states of helium clusters: an unusual example for the presence of rydberg states in condensed matter. *J. Phys. B: At. Mol. Opt.*, 38(2):S373, 2005. 148

[225] von Haeften, K. and Laarmann, T. and Wabnitz, H. and Möller, T. and Fink, K. Size and Isotope Effects of Helium Clusters and Droplets: Identification of Surface and Bulk-Volume Excitations. *J. Phys. Chem. A*, 115(25):7316–7326, 2011. 148

[226] R. S. Mulliken. The Rydberg States of Molecules.1a Parts I-V1b. *J. Am. Chem. Soc.*, 86(16):3183–3197, 1964. 150

[227] S. Lovtrup. On von Baerian and Haeckelian Recapitulation. *Syst. Biol.*, 27(3):348–352, 1978. 150

[228] A. Golov and S. Sekatskii. Rydberg branch of electronic excitations of helium clusters. *Physica B*, 194-196:555–556, 1994. 151

[229] M.V.R. Krishna and K.B. Whaley. Excess-electron surface-states of helium clusters. *Phys. Rev. B*, 38(16, Part b):11839–11842, 1988. 151

[230] K. Prozument, A. P. Colombo, Y. Zhou, G. B. Park, V. S. Petrović, S. L. Coy, and R. W. Field. Chirped-pulse millimeter-wave spectroscopy of rydberg-rydberg transitions. *Phys. Rev. Lett.*, 107:143001, 2011. 152

[231] Robert W. Field. private communication. 152

[232] J. H. Kim, D. S. Peterka, C. C. Wang, and D. M. Neumark. Photoionization of helium nanodroplets doped with rare gas atoms. *J. Chem. Phys.*, 124(21):214301, 2006. 156

[233] J. Poms, A. W. Hauser, and W. E. Ernst. Helium nanodroplets doped with xenon and rubidium atoms: a case study of van der Waals interactions between heliophilic and heliophobic dopants. *Phys. Chem. Chem. Phys.*, pages –, 2012. 156

[234] E. Lugovoj, J. P. Toennies, and A. Vilesov. Manipulating and enhancing chemical reactions in helium droplets. *J. Chem. Phys.*, 112(19):8217–8220, 2000. 156, 159

[235] J. Kuepper and J. M. Merritt. Spectroscopy of free radicals and radical containing entrance-channel complexes in superfluid helium nanodroplets. *Int. Rev. Phys. Chem.*, 26(2):249–287, 2007. 159

[236] J. M. Merritt, S. Rudić, and R. E. Miller. Infrared laser spectroscopy of CH_3HF in helium nanodroplets: The exit-channel complex of the F + CH_4 reaction. *J. Chem. Phys.*, 124(8):084301, 2006. 159

[237] S. Müller, S. Krapf, Th. Koslowski, M. Mudrich, and F. Stienkemeier. Cold reactions of alkali-metal and water clusters inside helium nanodroplets. *Phys. Rev. Lett.*, 102:183401, 2009. 159

[238] S. A. Krasnokutski and F. Huisken. Ultra-Low-Temperature Reactions of Mg Atoms with O_2 Molecules in Helium Droplets. *J. Phys. Chem. A*, 114(27):7292–7300, 2010. 159

[239] S. A. Krasnokutski and F. Huisken. Oxidative reactions of silicon atoms and clusters at ultralow temperature in helium droplets. *J. Phys. Chem. A*, 114(50):13045–13049, 2010. 159

[240] S. A. Krasnokutski and F. Huisken. Low-Temperature Chemistry in Helium Droplets: Reactions of Aluminum Atoms with O_2 and H_2O. *J. Phys. Chem. A*, 115(25):7120–7126, 2011. 159

[241] T. Liang, S. D. Flynn, A. M. Morrison, and G. E. Douberly. Quantum Cascade Laser Spectroscopy and Photoinduced Chemistry of Al-$(CO)_n$ Clusters in Helium Nanodroplets. *J. Phys. Chem. A*, 115(26):7437–7447, 2011. 159

[242] H.-J. Schumacher. Atomic reactions. by michael polanyi. 64 seiten mit 22 figuren. verlag williams & norgate ltd., london. preis geh. 6 sh. *Z. Elektrochem. Angew. P.*, 39(6):405–405, 1933. 159, 160

[243] R. D. Levine and R. B. Bernstein. *Molekulare Reaktionsdynamik*. Teubner Stuttgart, 1991. 159

[244] M. S. Topaler, D. G. Truhlar, X. Y. Chang, P. Piecuch, and J. C. Polanyi. The photoabsorption spectrum of Na$\cdots$FH van der Waals molecule: Comparison of theory and experiment for a harpooning reaction studied by transition state spectroscopy. *J. Chem. Phys.*, 108(13):5378–5390, 1998. 159

[245] X. Y. Chang, R. Ehlich, A. J. Hudson, P. Piecuch, and J. C. Polanyi. Dynamics of harpooning studied by transition state spectroscopy Na $\cdots$ FH. *Faraday Discuss.*, 108:411–425, 1997. 159

[246] A. Tam, G. Moe, and W. Happer. Particle Formation by Resonant Laser Light in Alkali-Metal Vapor. *Phys. Rev. Lett.*, 35(24):1630–1633, 1975. 159

[247] G. M. Almy and M. Rassweiler. The absorption spectrum of caesium hydride. *Phys. Rev.*, 53:890, 1938. 159

[248] I. R. Bartky. The absorption spectrum of cesium deuteride. The $A^1\Sigma^+$ state of CsH. *J. Mol. Spectrosc.*, 21(1-4):25 – 28, 1966. 160

[249] W. C. Stwalley, W. T. Zemke, and S. C. Yang. Spectroscopy and structure of the alkali hydride diatomic molecules and their ions. *J. Phys. Chem. Ref. Data*, 20(1):153, 1991. 160, 164

[250] K.-C. Lin and R. Vetter. Alkali-hydrogen reactions. *Int. Rev. Phys. Chem.*, 21(3):357–383, 2002. 160

[251] A. C. Tam and W. Happer. Spectroscopy of the CsH($X^1\Sigma^+$) state by laser-excited fluorescence. *J. Chem. Phys.*, 64(6):2456, 1976. 160

[252] X. F. Gadea, G. H. Jeung, M. Pelissier, J. P. Malrieu, J. L. Picque, G. Rahmat, J. Verges, and R. Vetter. Preliminary Investigations about the Cs*+H_2 Collision. *Laser Chem.*, 2:361–372, 1983. 160

[253] G. Rahmat, F. Spiegelmann, J. Verges, and R. Vetter. The Cs(7P) + $H_2 \rightarrow$ CsH + H reaction at threshold energy. *Chem. Phys. Lett.*, 135(4,5):459, 1987. 160

[254] J.-M. L'Hermite, G. Rahmat, and R. Vetter. The Cs + $H_2 \longrightarrow$ CsH + H reaction. I. Angular scattering measurements by doppler analysis. *J. Chem. Phys.*, 93(1):434, 1990.

[255] J.-M. L'Hermite, G. Rahmat, and R. Vetter. The Cs + $H_2 \longrightarrow$ CsH + H reaction. II. Rotationally resolved total cross section. *J. Chem. Phys.*, 95(5):3347, 1991.

[256] J.-M. L'Hermite. The Cs(7P)+$H_2 \rightarrow$ CsH + H reaction. III. Quasiclassical trajectory study. *J. Chem. Phys.*, 97 (9):6215, 1992.

[257] X. Huang, J. Zhao, G. Xing, X. Wang, and R. Bersohn. The reaction of Cs(8^2P) and Cs(9^2P) with hydrogen molecules. *J. Chem. Phys.*, 104(4):1338–1343, 1996.

[258] V. Cavero, J.-M. L'Hermite, G. Rahmat, and R. Vetter. The Cs($6D_{3/2}$)+$H_2 \rightarrow$ CsH + H reaction. IV. Rotationally resolved total cross sections. *J. Chem. Phys.*, 110(7):3428, 1999. 160

[259] J. L. Picque, J. Verges, and R. Vetter. Resonant character of laser-induced formation of particles in a Cs-H_2 vapor. *J. Physique - Lett.*, 41:L–305–L308, 1980. 160

[260] G.-H. Jeung, H. S. Lee, K. H. Kim, and Y. S. Lee. Does the harpooning model apply to the alkali-dihydrogen reactions, Ak* + $H_2 \rightarrow$ AkH + H ? *Chem. Phys. Lett.*, 358(1-2):151 – 156, 2002. 160

[261] A. Bacher S. Denifl F. F. da Silva H. Schöbel O. Echt T.D. Märk M. Probst D. K. Bohme S. Jaksch, A. Mauracher and P. Scheier. Formation of even-numbered hydrogen cluster cations in ultracold helium droplets. *J. Chem. Phys.*, 129:224306–1, 2008. 161

[262] S. Denifl O. Echt T. D. Märk S. Jaksch, F. F. de Silva and P.Scheier. Experimental Evidence for the Existence of an Electronically Excited State of the Proposed Dihydrogen Radical Cation He-H-H-He^+. *Chem. Eur. J.*, 15:4190–4194, 2009. 161

[263] E. Coccia, E. Bodo, and F. A. Gianturco. Size-dependent solvation of p-H_2 in ^{4}He clusters: A quantum Monte Carlo analysis. *J. Chem. Phys.*, 130(9):094906, 2009. 161

[264] B. G. Sartakov J. P. Toennies S. Grebenev, E. Lugovoi and A. F. Vilesov. Spectroscopy of OCS-hydrogen clusters in He droplets. *Faraday Discuss.*, 118:19–32, 2001. 161

[265] R.J. LeRoy. Level 8.0: A computer program for solving the radial Schrödinger equation for bound and quasibound levels. Chemical Physics Research Report CP-663, 2007. see the Computer Programs link at http://leroy.uwaterloo.ca. 162, 164